

Photochromism and photoconductivity in rare-earth oxyhydride thin films

Colombi, G.

DOI

[10.4233/uuid:02389b85-8dff-4939-a8d2-826196d3ef58](https://doi.org/10.4233/uuid:02389b85-8dff-4939-a8d2-826196d3ef58)

Publication date

2022

Document Version

Final published version

Citation (APA)

Colombi, G. (2022). *Photochromism and photoconductivity in rare-earth oxyhydride thin films*. [Dissertation (TU Delft), Delft University of Technology]. <https://doi.org/10.4233/uuid:02389b85-8dff-4939-a8d2-826196d3ef58>

Important note

To cite this publication, please use the final published version (if applicable). Please check the document version above.

Copyright

Other than for strictly personal use, it is not permitted to download, forward or distribute the text or part of it, without the consent of the author(s) and/or copyright holder(s), unless the work is under an open content license such as Creative Commons.

Takedown policy

Please contact us and provide details if you believe this document breaches copyrights. We will remove access to the work immediately and investigate your claim.



**Photochromism and Photoconductivity
in Rare-Earth Oxyhydride Thin Films**

Giorgio Colombi

**PHOTOCHROMISM AND PHOTOCONDUCTIVITY IN
RARE-EARTH OXYHYDRIDE THIN FILMS**

Giorgio Colombi

PHOTOCHROMISM AND PHOTOCONDUCTIVITY IN RARE-EARTH OXYHYDRIDE THIN FILMS

Dissertation

for the purpose of obtaining the degree of doctor
at Delft University of Technology,
by the authority of the Rector Magnificus prof.dr.ir. T.H.J.J. van der Hagen,
chair of the Board for Doctorates to be defended publicly on
Wednesday 13 April 2022 at 10.00 o'clock

by

Giorgio COLOMBI

Master of Science in Material Science
University of Padua, Italy
Born in Rome, Italy

The dissertation has been approved by the promotor

promotor: prof. dr. B. Dam

promotor: Dr. ir. T.J. Savenije

Composition of the doctoral committee

Rector Magnificus,	chairperson
Prof. dr. B. Dam	Delft University of Technology (NL), promotor
Dr. ir. T.J. Savenije	Delft University of Technology (NL), promotor

Independent members:

Dr. S. Iimura	National Institute for Materials Science (JP)
Prof. dr. T.E. Norby	University of Oslo (NO)
Dr. A. Borgschulte	Swiss Federal Laboratories for Materials Science and Technology (CH)
Prof. dr. P. Dorenbos	Delft University of Technology (NL)
Prof. dr. A.J. Houtepen	Delft University of Technology (NL), reserve member

Other members:

Dr. ir. G.A. de Wijs	Radboud University (NL)
----------------------	-------------------------



Front cover artwork by: Giorgio Colombi

Printed by: Ridderprint | www.ridderprint.nl

Copyright © 2022 by G. Colombi

ISBN 978-94-6384-321-8

An electronic version of this dissertation is available at

<http://repository.tudelft.nl/>

The doctoral research has been carried out in the Materials for Energy Conversion and Storage (MECS) group, Department of Chemical Engineering, Faculty of Applied Sciences, Delft University of Technology. This work was performed in close collaboration with projects supported by the Mat4Sus Research Program with Project Number 680.M4SE034 and by the Open Technology research program with Project Number 13282; both financed by The Netherlands Organisation for Scientific Research (NWO).

*We were all delighted, we all realized we were leaving confusion and nonsense behind
and performing our one noble function of the time, move.*

Jack Kerouac, *On the Road* (1951)

CONTENTS

1	Introduction	1
1.1	Saving energy with smart windows	1
1.2	Photochromism of RE oxyhydride thin films	4
1.2.1	Hypothesis for the photochromic mechanism	6
1.3	This thesis	7
	References	9
2	Composition: REO_xH_{3-2x} oxyhydride nature	13
2.1	Introduction	14
2.2	Experimental	14
2.3	Results	15
2.3.1	Oxyhydride nature of RE-based photochromic thin films	15
2.3.2	O:H ratio and optical bandgap	19
2.4	Discussion	21
2.4.1	Composition limits of photochromism	21
2.5	Conclusions	21
	References	23
3	Structure: generalized anion-disordered model	27
3.1	Introduction	28
3.2	Experimental	29
3.3	Results	32
3.3.1	Optical properties and photochromism	32
3.3.2	XRD: fcc cation lattice	33
3.3.3	EXAFS: tetrahedral oxygen location	35
3.4	Discussion	38
3.4.1	Lattice energy and air oxidation	38
3.4.2	Generalized anion-disordered model	41
3.5	Conclusions	42
	References	43
	Appendix	47
3.A	XANES and edge position	48
3.B	EXAFS	50
3.B.1	EXAFS Theory	50
3.B.2	EXAFS self absorption	50
3.B.3	Additional details on EXAFS data analysis	51
3.B.4	Gd oxyhydride composition from EXAFS coordination numbers	52
3.C	X-ray diffraction reference patterns	53
	References	54

4	Energy, metastability and optical properties of $\text{REO}_x\text{H}_{3-2x}$ oxyhydrides	55
4.1	Introduction	56
4.2	Computational details	58
4.3	Results	61
4.3.1	Energy: relative stability of anion-disorder	61
4.3.2	Structures: compositional limit of anion-disorder	65
4.3.3	Optical properties	68
4.4	Discussion	70
4.4.1	Comparison to photochromic thin films	70
4.4.2	Comparison to experimentally reported oxyhydrides	73
4.5	Conclusions	74
	References	76
	Appendix	81
4.A	Structural Models	82
4.A.1	Anion-ordered RE oxyhydrides based on CaF_2 -type lattice	82
4.A.2	Anion-disordered SQS	82
4.B	DFT binding, formation and lattice energy	85
4.C	Comparison between mBJ and G_0W_0	86
4.D	Madelung Energy and Born-Landé correction	87
4.E	RE-RE, RE-O, and RE-H radial distribution function	88
4.F	Bandgap comparison	91
4.G	Refractive index comparison	92
	References	93
5	Influence of cation and O:H ratio on the photochromism of $\text{REO}_x\text{H}_{3-2x}$ thin films	95
5.1	Introduction	96
5.2	Experimental	96
5.3	Results	97
5.3.1	Influence of deposition pressure	97
5.3.2	Irreversible light-induced vacancy formation	100
5.4	Discussion	102
5.5	Conclusion	104
	References	105
	Appendix	109
5.A	Air oxidation	110
5.B	Transmission spectra and Energy bandgap	111
5.C	Ion-beam composition analysis	112
5.D	XRD Patterns	113
5.E	Photochromic effect	114
5.F	Details on DB-PAS analysis on $\text{YO}_x\text{H}_{3-2x}$	115
5.F.1	Al-capped $\text{YO}_x\text{H}_{3-2x}$ sputtered at 0.4 Pa	116
5.F.2	Al-capped $\text{YO}_x\text{H}_{3-2x}$ sputtered at 0.5 Pa	118
5.F.3	Al-capped $\text{YO}_x\text{H}_{3-2x}$ sputtered at 0.6 Pa	120
	References	122

6	Photochromism and photoconductivity in $\text{REO}_x\text{H}_{3-2x}$	123
6.1	Introduction	124
6.2	Experimental	125
6.3	Results	127
6.3.1	Gd oxyhydride temperature stability	127
6.3.2	Gd oxyhydride transport properties	129
6.3.3	Relation between photoconductivity and photochromism	133
6.4	Discussion	136
6.4.1	Hypothesis of long living small defects	137
6.4.2	Hypothesis of metallic phase segregation	139
6.5	Conclusion	142
	References	144
	Appendix	149
6.A	Additional details on transport measurements	150
6.B	Photochromism and photo-conductivity	159
7	Reflection & future outlook	161
	Summary	163
	Samenvatting	165
	Acknowledgements	169
	Curriculum Vitae	175
	List of Publications	177

1

INTRODUCTION

Human ingenuity expresses itself in many colourful ways, not least, in the construction of complex structures and objects starting from raw materials. In this endeavour, most often the paradigm is that the material properties should be resilient to small external stimuli, and not change throughout the lifetime of the object. Many application with an high technological content, however, rely on the opposite paradigm and are enabled by a comparatively narrow group of materials (hereafter, *dynamic materials*) that are designed to have at least one property that can be changed in a controlled fashion by external stimuli, such as stress, light, temperature, pH, magnetic or electric fields, chemical compounds, etc.. Field effect transistors, optical modulators, and all types of sensors are only some examples of artificial, dynamic materials that are fundamental to life as we know it. On a more fundamental level, the investigation of dynamic properties is arguably one of the main areas that have been propelling the field of material science in the last century.

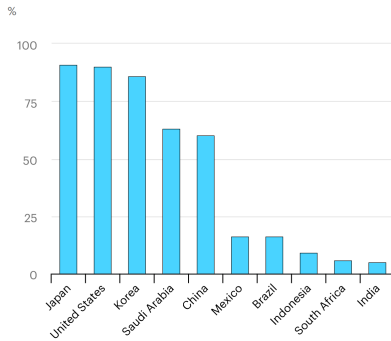
It is therefore not surprising that a large research campaign started when, in 2011, large and reversible photo-conductivity and photochromism were accidentally discovered in "*oxygen containing YH₂ thin films*".^[1] Immediately, the material was identified as a promising candidate for photochromic smart windows, an application that we describe in the following.

1.1. SAVING ENERGY WITH SMART WINDOWS

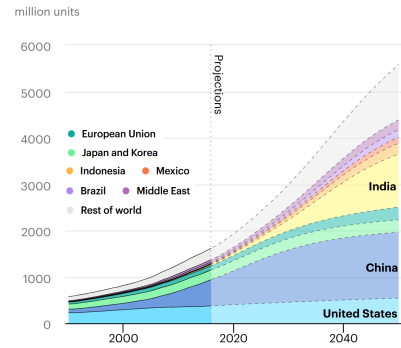
Energy, water, food, and land security are arguably four of the most essential pillars that sustain any developed human society. At present, however, our energy consumption poses a treat to the other three pillars, and the implementation of new concepts of energy production, storage, and usage is a prerequisite to sustain further growth in the medium-long term.^[8]

The challenge of net-zero emissions has no single, simple solution and every mitigating action is worth of consideration. In this sense, to increase the energy efficiency of buildings, which in EU account for approximately 40% of the energy consumption

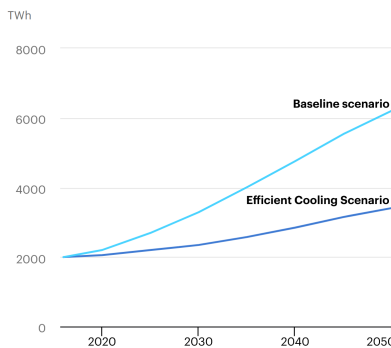
a) Percentage of households equipped with AC in selected countries, 2018



b) Global air conditioner stock, 1990-2050



c) Space cooling energy demand growth and savings potential, baseline and cooling scenario, 2016-2050



d) Share of global electricity demand growth to 2050

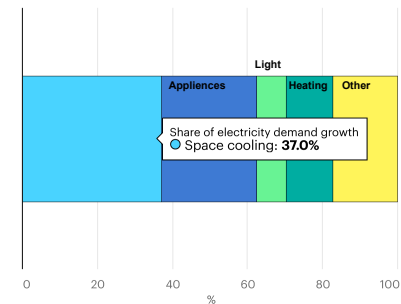


Figure 1.1: Present and future of cooling demand according to the International Energy Agency. *a)* Percentage of household equipped with air conditioning in selected countries, in 2018. *b)* Projection of the energy demand for cooling up to year 2050, with and without mitigating actions. *c)* Share of the growth of global electricity demand as projected up to year 2050. Accounting for 37%, space cooling is the single biggest driver of the rising energy demand of the future. *d)* Projected number of air conditioning units, in selected countries, up to year 2050. All panels are reproduced from ref. [2].

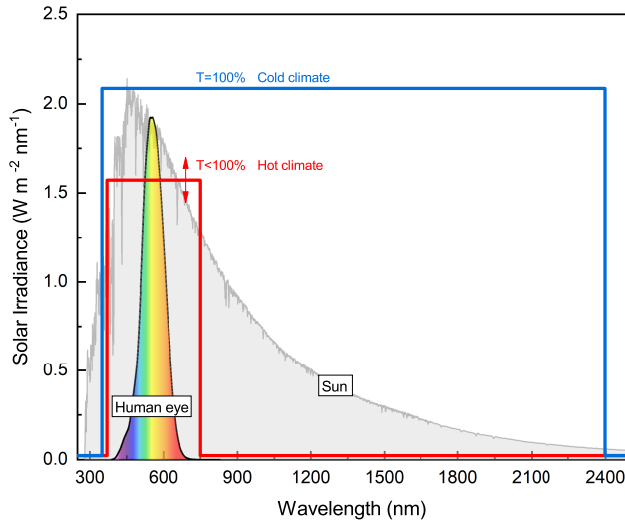


Figure 1.2: portion of solar spectrum ideally transmitted through a window for two limit scenarios: a cold climate with insufficient solar light (blue line), and an hot climate with excessive solar light (red line). The shown solar spectral irradiance corresponds to the ASTM G-173-03 terrestrial standard, [3] while the coloured area gives the spectral sensitivity of the human eye. [4].

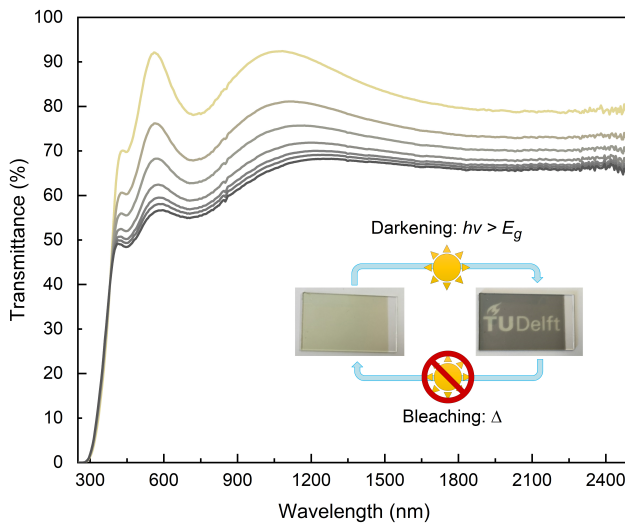


Figure 1.3: Example of transmittance at different stages of the photo-darkening process of a RE oxyhydride thin film. While this example is given for a ~ 300 nm thick Y oxyhydride film, comparable trends have been reported for Sc,Dy,Er,Gd, and Nd based oxyhydrides, [5-7] and photochromism is likely to be a general feature of other RE oxyhydrides as well. In the figure, the oscillation of the transmittance are due to thin-film interference; the fact that they reach the theoretical maximum of $\sim 92\%$ indicates negligible absorption at energies below the bandgap.

and 36% of the CO₂ emissions, [9] is a potentially very effective action and yet one of the Sustainable Development Goals (SDGs) that progress most slowly. In this sense the technology of windows appears particularly important, as they are estimated to contribute for approximately 60% of the buildings energy loss in the form of heat exchange with the outside environment. [10]

At present, the energy demand for heating in buildings slightly overweighs the demand for cooling, but this only reflects the current distribution of wealth (Fig. 1.1a), and globally the world is set on a different trajectory. [11] The energy demand for heating is in fact projected to stabilize this decade, [11] while the rising demand for air conditioning is, in the words of IEA Executive Director, Faith Birol, "one of the most critical blind spots in today's energy debate." [2] As the access to air conditioning becomes more widespread (Fig. 1.1b), it is estimated that without mitigating actions the demand for cooling will roughly triplicate by 2050 (Fig. 1.1c), becoming the single biggest driver behind the overall rise of the electricity demand (Fig. 1.1d). [2]

In a cold environment, thermal conduction due to the net temperature difference between inside and outside is the only mechanism of relevance for the insulating performance of a window. However, in an environment with a hot or mixed climate, the heat transferred in the form of solar radiation (also known as solar thermal gain) becomes important as well. Fig. 1.2 schematically shows the portion of solar spectrum ideally transmitted through a window for two limit scenarios. First, a cold climate with insufficient solar light, where all the visible and infrared radiation is desirable to minimize the need of artificial illumination and heating. Second, a hot climate with excessive solar light, where one wants to modulate the visible fraction of the transmitted light to a comfortable level, and completely cut the infrared radiation to minimize the need of cooling.

In this context, in hot and mixed-climates, smart windows that adapt their transmittance to the environment would offer an optimal modulation of the visible and infrared light for any condition of outside luminosity and temperature. As recently reviewed by Baetens *et al.* [12], three different technologies are commonly considered an option for smart windows: chromic (dynamic) materials, liquid crystals and electrophoretic or suspended-particle devices. The chromic materials are further distinguished into electrochromic, gasochromic, photochromic, and thermochromic on the basis of the external stimuli that trigger the dynamic response.

1.2. PHOTOCHROMISM OF RE OXYHYDRIDE THIN FILMS

The focus of this thesis is on photochromic rare-earth (RE) oxyhydride thin films, of which Fig. 1.3 reports an example of their transmittance before and during photo-darkening. Notably, the decrease of transmittance extends from the UV up to the mid-IR, showing that these materials are not only suitable for visible light-modulation but they also contribute to tune the solar thermal gain of a window. At the time of writing, however, the actual application of photochromic RE oxyhydrides thin films as coating for smart windows and sensors remain under question, with their slow switching kinetics and their yet not assessed stability over prolonged time/use being the main challenges to overcome in future research. Considering the average lifetime of a window and the typical speed of

weather changes and cloud movement, we estimate the following to be requirements for application in smart windows: (i) a switching time in the order of ~ 1 min, and (ii) reproducible behaviour throughout a use of ~ 20 years at ambient temperature.

My research work on the topic started in 2018, 7 years and 2 PhD cycles after the first discovery of photochromism in Y oxyhydride thin films. The following briefly reviews the knowledge produced in these early years.

The discovery. Our story starts in 2011, when the photochromism of reactively-sputtered "oxygen containing YH_2 " was casually discovered by T. Mongstad, [1, 13] who showed that upon UV exposure the optical and electrical properties of these thin films were undergoing large and *mostly*-reversible changes.

The early phase. Reflecting the novelty of the topic, the works published in the following years are exploratory in nature, and often imprecise or inconclusive. Yet, their merit lies in the hypothesis that were raised.

In 2013 Maehlen *et al.* [14] performs time-resolved X-ray crystal diffraction during illumination, ruling out any phase transformation but reporting a progressive lattice contraction. The year after a NMR study by Chandran *et al.* [15] looks at the role of Hydrogen for the first time: the coexistence of three H species is proposed and the NMR signal of the most mobile one appears to be reversibly quenched upon UV exposure. While these two works are similarly affected by the lack of complementary optical data, and advocate for the need of better controlled samples and experimental conditions, they open to the idea that the photochromism is not only of electronic nature only but might involve some structural dynamics as well.

Shortly after, the hypothesis of tuning the band-gap through the O:H ratio is advanced for the first time, although not convincingly proven. [16, 17]

Recent works. New important insight arrived in 2017, when Montero *et al.* [18] proposed that the photochromism could be explained by the gradual growth, under illumination, of metallic domains within the initial semiconducting matrix – a claim supported by the successful modelling of ellipsometric data in terms of an effective medium approximation. Here, the optical properties of the hypothesised metallic domains were approximated as those of a reference, optically thick film which contained a mixture of different metallic (YH_2 , $\text{YH}_{0.667}$) and non-metallic (YO_xH_y) phases, possibly including optically active defects as well. Because of that, it remains an open question which of these species dominates the absorption of the photodarkened state, or if they are all relevant. In any case, the work of Montero *et al.* [18] makes a strong case for the segregation upon photodarkening of a secondary phase of largely metallic character.

In 2017, another important contribution was made by Nafezarefi *et al.* [5], who demonstrated that the occurrence of photochromism was a general feature in oxygen containing hydride films of several RE elements. Specifically, it was shown that Gd, Dy, and Er based oxyhydride have band gap, crystal structure, and photochromic properties similar to those of Y-based thin films. In this occasion, the term RE *oxyhydrides* was adopted to collectively describe these materials. Such term will be proven correct later on. [6]

Finally, a last paper worth quoting is the one from Plokker *et al.* [19], in 2018, which represents the first attempt to investigate the role of defects in the RE oxyhydride photochromism.

1.2.1. HYPOTHESIS FOR THE PHOTOCROMIC MECHANISM

One would not expect to read speculation already at pag. 6 of a PhD thesis, but such is the nature of a young research topic, where heuristic thinking and educated guesses are the prime instruments to direct the next steps. In particular, not many species can absorb (with minimal scattering and reflection) over the very broad wavelength range shown in fig. 1.3. Consequently, the identity of the optically absorbing species seemed confined to only two possibilities, namely (i) a large ensemble of structural defects, and (ii) plasmonic domains.

DEFECT HYPOTHESIS:

This model assumes the existence of a large ensemble of long-living defect to explain the absorption of the photo-darkened state. The inter-band absorption that initiates the photo-darkening is followed by the trapping of electrons in these defect levels, generating thus colour centres that absorb light of low energy. Notably, the reported increase of conductivity upon illumination is in agreement with the formation of long-living holes as implied by this model. On the other hand, the presence of an ensemble of defects so large to absorb from visible to mid-infrared radiation is not very convincing. In addition, in the transparent state there is no absorption at energies below the optical gap, meaning that either all the transitions towards the defect levels are forbidden (unlikely for a big ensemble) or that these defects form as a consequence of the UV exposure itself.

THE PLASMONIC HYPOTHESIS:

This model resembles the mechanism behind one of the first, and most common, Corning's photochromic glasses. In this case, the plasmonic resonance of photo-induced metallic domains is responsible for the absorption of the photo-darkened state. [20-24] Corning's glasses contain small crystallites of copper-doped silver chloride, the real responsible for the color change. Upon illumination an electron is excited from a chlorine ion to a silver ion (eq. 1.1) and, at this point, it hops from silver to silver until it reaches a trapping site. Such trapping sites lie mostly at the boundaries of the silver halide grains where, eventually, occurs the growth of metallic silver specks big enough to sustain plasmonic modes. Notably, a vacancy is left behind in the lattice for each silver atom reduced to the metallic state.



Being Cl^0 an extremely oxidising species, either an immediate charge recombination or irreversible formation of other Cl-based by-products would occur in the absence of the copper ions, which instead prevent these instances by acting as a trap for the hole (eq. 1.2). [25]



During the darkening, the net reaction is therefore:



It is here worth quoting the words of Araujo, arguably among the most important pioneers in the field of silver halides: [...] *there can be no reasonable doubt that an anisotropic speck of silver is responsible for the major part of the visible absorption induced when a photochromic glass is darkened.* [24] A strong claim requires strong evidence and, in this case, Araujo was referring to the studies of T.P. Seward and N. Borrelli. [26-28] Their work indirectly proved the existence of such silver specks via experiments of optical bleaching, where it was shown that (i) polarized light of energy lower than the AgCl bandgap could dissolve silver specks of a well defined orientation, and (ii) that specific wavelengths could selectively dissolve silver specks of a characteristic aspect ratio.

The hypothesis of plasmonic domains is today highly considered as a possible explanation for the photochromism of RE oxyhydrides, as it aligns with the work of Montero *et al.* [18] and in the a clear reason for the long time-scale of the process. On the other hand however, the chemical changes that would occur in the RE oxyhydrides are completely unknown, and differently from the Corning's glasses we could not induce *any* optical bleaching of the photo-darkened state.

1.3. THIS THESIS

With this background in mind, my hope is that this thesis and the connected publications might help the topic to transition from an early, largely exploratory phase, towards a more mature understanding of the relation between composition, structure, and material properties.

PART I: Basic material properties.

Chapter 2 reports on the composition of the RE-based, photochromic thin films. We find them to belong to the RE oxyhydride composition line $\text{REO}_x\text{H}_{3-2x}$, with the photochromism occurring over a wide range of O:H anion-ratios ($0.5 \leq x \leq 1.3$). Additionally, we show that the optical gap varies continuously with the anion ratio, demonstrating the potential for band gap tuning.

Chapter 3 reports on the location of the oxide anions within the RE oxyhydride crystal structure. We find that the oxide anions predominantly occupy the tetrahedral interstitial sites of the the fcc RE cation lattice, and rationalize such preference in terms electrostatic lattice energy minimization. With such insight, we propose a fcc-based anion-disordered model to link the RE oxyhydrides to the related binary compounds and describe how their site occupancy evolves upon the O:H ratio.

Chapter 4 explores *via* ab-initio DFT the largely unknown properties – and their dependency on the O:H ratio – of the anion-disordered RE oxyhydride phase. A comparison with anion-ordered polymorphs of the same composition shows that the anion-disordered phase is energetically favoured in the H-rich interval ($0.5 < x < 1$), although it is the cation size that determines the maximum H content that the structure can accommodate. In terms of optical properties, major differences occur between H-rich and O-rich compositions, as the octahedral H^- present for $x < 1$ form electronic states at the top

of the valence band, which reduce the energy bandgap and dominate the electronic transitions at lower energies, thus increasing the refractive index of the material in the VIS-nIR spectral range. Finally, comparing the DFT results with the experimental data on photochromic Y oxyhydride films, reinforces the hypothesis of anion-disorder in the H-rich films ($x < 1$), while it hints towards some degree of anion-ordering in the O-rich ones ($x > 1$).

PART II: Light-induced effects: photochromism and photo-conductivity.

Chapter 5 sets to correlate the optical properties of the RE oxyhydride thin films, and particularly the photochromic contrast and the speed of the colour change, with the RE cation (Sc, Y, Gd) and with the O:H anion-ratio. While we do not exclude that other factors can play a role, we prove that controlling the deposition conditions and thus the composition of the thin film allows to largely tune its properties; In particular, the bleaching speed can be reduced by an order of magnitude by increasing the O:H ratio. The influence of the cation under comparable deposition condition is then discussed, showing that REs of larger ionic radius form oxyhydrides that present larger photochromic contrast and faster bleaching speed, hinting to a dependency of the photochromic mechanism on the anion site-hopping.

Chapter 6 reports on the conduction property of Gd oxyhydride thin films, and particularly on the relation between photochromism and photo-conductivity. We find that these two phenomena show a comparable time-dependency and temperature-dependency, with a unique exponential relation appearing between the material photo-conductivity and its absorption coefficient. These aspects indicate beyond reasonable doubt that photochromism and photo-conductivity originate from the same process, and possibly even from a same optically absorbing and electron conductive specie formed upon illumination. This last idea is discussed in a semi-quantitative fashion in the context of the mechanisms proposed for the photochromism. In doing so, we show (i) that the *defect hypothesis* only holds if both electron and hole traps form upon illumination, and (ii) that the *plasmonic hypothesis* only holds if the metallic domains form a network percolating throughout the entire film.

Finally, the thesis is concluded by a short outlook and a summary.

REFERENCES

- [1] T. Mongstad, C. Platzer-Björkman, J. P. Maehlen, L. P. Mooij, Y. Pivak, B. Dam, E. S. Marstein, B. C. Hauback, and S. Z. Karazhanov, *A new thin film photochromic material: Oxygen-containing yttrium hydride*, *Sol. Energy Mater. Sol. Cells* **95**, 3596 (2011).
- [2] International Energy Agency (2018), *The future of cooling, IEA, Paris*. Online; accessed 02-Jan-2022.
- [3] American Society for Testing and Materials (ASTM), *Terrestrial reference spectra for photovoltaic performance evaluation, astm g173-03, global tilt*, Online; accessed 02-Jan-2022.
- [4] ISO/CIE 11664-1:2019, *Colorimetry – part 1: CIE standard colorimetric observers*, Online; accessed 12-Dec-2021.
- [5] F. Nafezarefi, H. Schreuders, B. Dam, and S. Cornelius, *Photochromism of rare-earth metal-oxy-hydrides*, *Appl. Phys. Lett.* **111**, 103903 (2017).
- [6] S. Cornelius, G. Colombi, F. Nafezarefi, H. Schreuders, R. Heller, F. Munnik, and B. Dam, *Oxyhydride nature of rare-earth-based photochromic thin films*, *The Journal of Physical Chemistry Letters* **10**, 1342 (2019).
- [7] D. Chaykina, F. Nafezarefi, G. Colombi, S. Cornelius, L. J. Bannenberg, H. Schreuders, and B. Dam, *Influence of crystal structure, encapsulation, and annealing on photochromism in nd oxyhydride thin films*, *The Journal of Physical Chemistry C* **126**, 2276 (2022).
- [8] V. Masson-Delmotte, P. Zhai, A. Pirani, S.L.Connors, C. Péan, S. Berger, N. Caud, Y. Chen, L. Goldfarb, M. Gomis, M. Huang, K. Leitzell, E. Lonnoy, J.B.R.Matthews, T. Maycock, T. Waterfield, O. Yelekçi, R. Yu, and B. Zhou, *IPCC, 2021: Climate change 2021: The physical science basis. contribution of working group i to the sixth assessment report of the intergovernmental panel on climate change*, Cambridge University Press. In press (2021).
- [9] European Commission, *Energy performance of buildings directive*, Online; accessed on 10-Dec-2021.
- [10] A. Gustavsen, B. P. Jelle, D. K. Arasteh, and C. Kohler, *State-of-the-Art Highly Insulating Window Frames - Research and Market Review*, Tech. Rep. Project report 6 (INTEF Building and Infrastructure, 2007).
- [11] M. Isaac and D. P. van Vuuren, *Modeling global residential sector energy demand for heating and air conditioning in the context of climate change*, *Energy Policy* **37**, 507 (2009).
- [12] R. Baetens, B. P. Jelle, and A. Gustavsen, *Properties, requirements and possibilities of smart windows for dynamic daylight and solar energy control in buildings: A state-of-the-art review*, *Solar Energy Materials and Solar Cells* **94**, 87 (2010).

- [13] T. Mongstad, C. Platzer-Björkman, S. Karazhanov, A. Holt, J. Maehlen, and B. Hauback, *Transparent yttrium hydride thin films prepared by reactive sputtering*, [Journal of Alloys and Compounds](#) **509**, S812 (2011), proceedings of the 12th International Symposium on Metal-Hydrogen Systems, Fundamentals and Applications (MH2010).
- [14] J. P. Maehlen, T. T. Mongstad, C. C. You, and S. Karazhanov, *Lattice contraction in photochromic yttrium hydride*, [J. Alloys Compd.](#) **580**, S119 (2013).
- [15] C. V. Chandran, H. Schreuders, B. Dam, J. W. G. Janssen, J. Bart, A. P. M. Kentgens, and P. J. M. van Bentum, *Solid state nmr studies of the photochromic effects of thin films of oxygen containing yttrium hydride*, [J. Phys. Chem. C](#) **118**, 22935 (2014).
- [16] C. C. You, T. Mongstad, J. P. Maehlen, and S. Karazhanov, *Engineering of the band gap and optical properties of thin films of yttrium hydride*, [Appl. Phys. Lett.](#) **105**, 031910 (2014).
- [17] A. Pishtshev and S. Z. Karazhanov, *Role of oxygen in materials properties of yttrium trihydride*, [Solid State Communications](#) **194**, 39 (2014).
- [18] J. Montero, F. A. Martinsen, M. García-Tecedor, S. Z. Karazhanov, D. Maestre, B. Hauback, and E. S. Marstein, *Photochromic mechanism in oxygen-containing yttrium hydride thin films: An optical perspective*, [Phys. Rev. B](#) **95**, 201301 (2017).
- [19] M. Plokker, S. Eijt, F. Naziris, H. Schut, F. Nafezarefi, H. Schreuders, S. Cornelius, and B. Dam, *Electronic structure and vacancy formation in photochromic yttrium oxy-hydride thin films studied by positron annihilation*, [Sol. Energy Mater. Sol. Cells](#) **177**, 97 (2018).
- [20] N. J. Kreidl, *Photochromic glasses*, [Leonardo](#) **3**, 429 (1970).
- [21] C. L. Marquardt, J. F. Giuliani, and R. T. Williams, *Darkening mechanisms in silver-halide photochromic glasses: Flash photolysis and esr studies*, [Journal of Applied Physics](#) **47**, 4915 (1976).
- [22] R. J. Araujo, *Photochromic glass*, in [Glass I: Interaction with Electromagnetic Radiation](#), Treatise on Materials Science and Technology, Vol. 12, edited by M. Tomozawa and R. H. Doremus (Elsevier, 1977) pp. 91–122.
- [23] R. Araujo, *Inorganic photochromic systems*, [Molecular Crystals and Liquid Crystals Science and Technology. Section A. Molecular Crystals and Liquid Crystals](#) **297**, 1 (1997).
- [24] R. J. Araujo, *Photochromism in glasses containing silver halides*, [Contemporary Physics](#) **21**, 77 (1980).
- [25] N. F. Borrelli, *Photosensitive Glass and Glass-Ceramics* (CRC Press, 2017).
- [26] T. P. Seward, *Thermally darkenable photochromic glasses*, [Journal of Applied Physics](#) **46**, 689 (1975).

- [27] T. Seward, *Coloration and optical anisotropy in silver-containing glasses*, [Journal of Non-Crystalline Solids](#) **40**, 499 (1980), proceedings of the Fifth University Conference on Glass Science.
- [28] N. F. Borrelli, J. B. Chodak, and G. B. Hares, *Optically induced anisotropy in photochromic glasses*, [Journal of Applied Physics](#) **50**, 5978 (1979).

2

COMPOSITION: OXYHYDRIDE NATURE OF RE-BASED PHOTOCHROMIC THIN FILMS

*In the realm of ideas everything depends on enthusiasm.
In the real world all rests on perseverance.*

Johann Wolfgang von Goethe

Thin films of rare-earth (RE)-oxygen-hydrogen compounds prepared by reactive sputtering show a unique color-neutral photochromic effect at ambient conditions. Despite the interest in their optical properties, however, the understanding of the relation between photochromism, composition, and structure is limited. Here we lay the ground to understand such relation, establishing a RE–O–H composition diagram. The photochromic films are identified as oxyhydrides with a wide composition range described by the formula REO_xH_{3-2x} where $0.5 \leq x < 1.5$. The optical band gap varies continuously with the anion ratio, demonstrating the potential of band gap tuning for reversible optical switching applications.

This chapter is an adaptation of:

S. Cornelius, G. Colombi, F. Nafezarefi, H. Schreuders, R. Heller, F. Munnik, and B. Dam, *Oxyhydride Nature of Rare-Earth-Based Photochromic Thin Films*, *J. Phys. Chem. Lett.* **10**, 1342 (2019).

The text is largely written by Steffen Cornelius, and here my contribution is small.

2.1. INTRODUCTION

In 2011, a remarkable photochromic effect at ambient conditions was discovered in reactively sputtered YO_xH_y thin films. [1] Initially, these semiconducting materials were referred to as oxygen-containing yttrium hydride, [1, 2] and it was speculated that their properties could be explained in analogy to the transparent $\gamma\text{-YH}_3$ phase stabilized in the fcc structure by incorporation of oxygen into the lattice. [2] A later study on sputtered YO_xH_y composition gradient thin films, which covers the transition from opaque to transparent state, reports atomic ratios of up to $\text{H}:\text{Y} \sim 3$ as measured by heavy-ion elastic recoil detection (ERD) and nuclear reaction analysis (NRA). [3] However, this result seemed rather questionable considering the low H_2 partial pressures during deposition. Follow-up studies clarified that the transparent YO_xH_y materials are in fact formed by air oxidation of as-deposited absorbing metallic $\beta\text{-YH}_2$ films. [4, 5] Further, it was reported that other rare-earth (RE) based thin films (with $\text{RE} = \text{Gd}, \text{Dy}, \text{Er}$) exhibit the same photochromic effect and fcc crystal structure as YO_xH_y . [5] Since then, the term rare-earth (RE) oxyhydrides was adopted for this group of materials. However, experimental evidence for the presence of H^- ions was scarce. Although a recent study by Moldarev et al. supports the concept of H^- in photochromic YO_xH_y films, they also had to assume multiple cation charge states and/or the presence of OH^- groups in order to obtain charge balance. [6] In this chapter, the open question of composition is addressed.

In Sec. 2.3.1 we show that the photochromic RE-based films are indeed *oxyhydrides* - clearly distinct from *hydroxides* - with a composition described by the formula $\text{REO}_x\text{H}_{3-2x}$. In Sec. 2.3.2 we show that the O:H anion-ratio influences the optical bandgap, which for increasing oxygen content continuously widens from $E_{g,\text{REH}_3} \sim 2.6$ eV to $E_{g,\text{RE}_2\text{O}_3} \sim 5.5$ eV. Finally, in Sec. 2.4.1 we discuss the compositional limits in which photochromism appears.

2.2. EXPERIMENTAL

SAMPLE PREPARATION

In a previous work, our group reported that metallic $\beta\text{-REH}_{1.9+\delta}$ dihydride thin films with $\text{RE} = \text{Y}, \text{Er}, \text{Dy}, \text{Gd}$ can be prepared by direct current (DC) reactive sputtering of metal targets in an Ar/H_2 atmosphere. [5] Above a certain material-dependent critical deposition pressure (p^*), the films air-oxidize at room temperature (RT) to form stable semiconducting transparent photochromic REO_xH_y . In order to obtain samples with a wide range of chemical compositions, we have extended our standard synthesis procedure as follows:

- (i) Sc is sputtered as the RE element with the smallest ionic radius.
- (ii) A variable amount of O_2 is added to the $\text{Ar}/\text{H}_2/\text{O}_2$ process gas (5N purity) resulting in a mixture containing (12.5-11.9)% of H_2 and (0-4.7)% of O_2 .
- (iii) Pulsed DC plasma excitation (50 kHz, 90% duty cycle) is used to avoid arcing.

- (iv) Al capping layers (20 nm) were sputtered onto selected samples directly or after timed air exposure to prevent further oxidation.

All samples were grown on unheated UV-grade fused silica (f-SiO₂) and polished glassy carbon substrates (HTW Germany).

In addition, A special set of Sc, Y, and Gd dihydride reference samples was prepared by hydrogenating Pd-capped (20 nm) metal layers (150 nm) in a pressure cell at 1 bar of H₂ at RT. Employing the hydrogenography method,^[7] the change in optical transmittance is used to verify that all films were initially loaded to H:RE ratios above the dihydride to trihydride phase transition, followed by unloading to dihydride in air after opening the pressure cell. Because of the tensile strain induced by hydrogen desorption,^[8] we expect that these dehydrogenated layers have a H:RE ratio corresponding to the lower end of the β-REH_x existence range, i.e., ScH_{1.68},^[9] YH_{1.90},^[8] and GdH_{1.80}.

MATERIAL CHARACTERIZATION

Chemical composition The chemical composition is determined by a combination of Rutherford backscattering spectrometry (RBS) and ERD analysis at the 2 MV Van-de-Graaff accelerator at Helmholtz-Zentrum Dresden-Rossendorf (Dresden, Germany). RBS (ERD) measurements were performed with a 1.7 MeV 4He⁺ beam at 0°(70°) incidence and 160°(30°) scattering angle using semiconductor detectors with a solid angle (calibrated thanks to the known dihydride samples) of 3.3 msr (5.6 msr) and an energy resolution of ~16 keV. The ERD detector was covered by a 6.6 μm Al stopper foil to discriminate recoiled H from forward scattered He. For each sample, the RBS and ERD spectra were fitted self-consistently using the SIMNRA program and the SRIM2013 stopping power database.

Optical properties. The transmittance was measured with a Perkin-Elmer Lambda 900 UV-VIS-NIR spectrometer with a wavelength range of 200-2500 nm. The optical bandgap, E_g , was determined using the Tauc plot method with an estimated error of about $\Delta E_g = 0.1$ eV. ^[10, 11]

To test for photochromism, photo-darkening of the oxyhydride was initiated by a low pressure Hg UV-lamp (Herolab GmbH) with an emission range of 245-400 nm and an integrated irradiance of 5000 μW cm⁻², which is comparable to that of the sun (4610 μW cm⁻²) in the same spectral range. ^[12]

2.3. RESULTS

2.3.1. OXYHYDRIDE NATURE OF RE-BASED PHOTOCROMIC THIN FILMS

Figure 1, is an example showing the experimental ion beam spectra and corresponding simulations of a set of YO_xH_y films with different O:H ratios. The areal densities (*atoms/cm²*) of Y and O are obtained from RBS data, taking into account the Al or Pd capping layers. The overall fit accuracy benefits from the nearly background-free oxygen signal with good counting statistics, which is achieved by the use of carbon instead of f-SiO₂ substrates. The H areal density is obtained from the ERD signal taking into account the energy loss and straggling of H recoils in the Al stopper foil as well as geometric

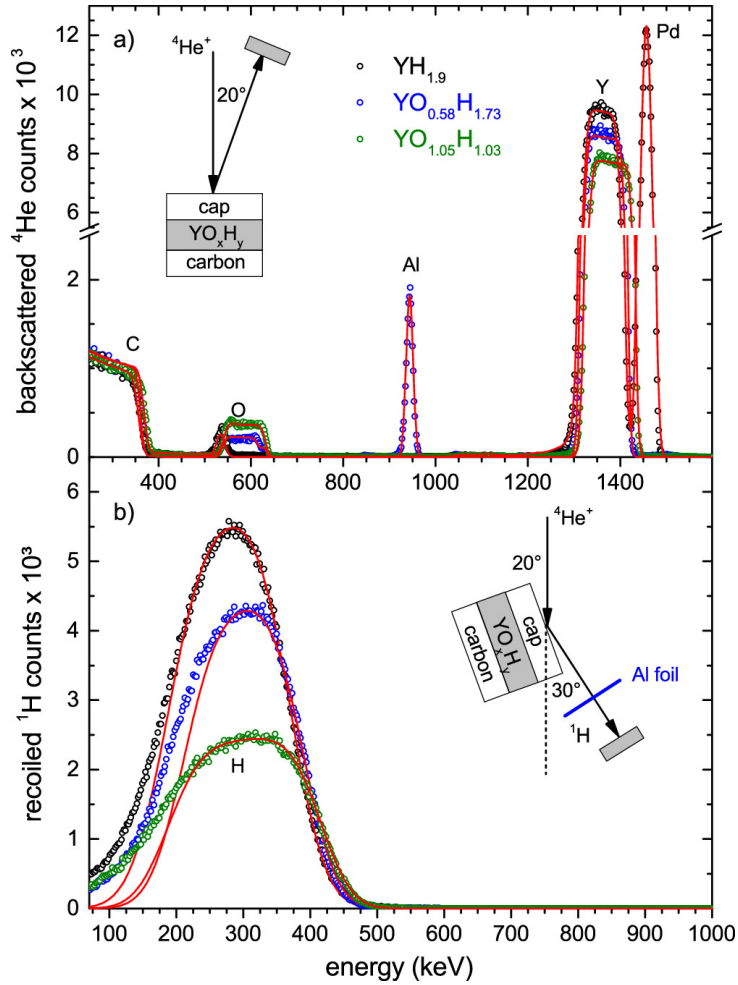


Figure 2.1: Comparison of (a) RBS and (b) ERD experimental spectra (open circles) and corresponding SIMNRA simulations (red lines) obtained by fitting of each combined data set. A series of samples (150 nm thickness) with increasing oxygen content is shown: Pd capped Y dihydride (black), Al-capped (blue), and uncapped Y oxyhydride (green). The broadening of the low-energy edge in the ERD spectrum is caused by thickness variations of the Al stopper foil.

straggling due to the variation of the scattering angle across the detector area. [13] The combined RBS and ERD analysis allows for a quantification of the element concentrations (in atom %) with an uncertainty below 2 atom %. The RBS spectrum of Pd-capped hydrogenated Y shows that the film contains no oxygen (O detection limit 1 atom %) except for a thin surface layer within the C substrate - possibly a result of surface polishing.

It is important to note here, that no other light elements, in particular F, could be detected in the REO_xH_y films discussed in this work. Together with the characteristic transmittance window (Fig. 2.3), [5] this increases the confidence that the RE hydride used for the calibration of the solid angle of the detectors are nearly ideal $\beta\text{-REH}_x$ reference materials. Besides oxygen, fluorine is a common impurity in rare-earth metals - especially in Y. [14] In the past, we observed high concentrations of O (up to 7 atom %) and F (up to 13 atom %) in many commercial Y metal sputter targets of nominal 99.9% purity. Such high F concentrations complicate the chemical analysis and obscure subsequent interpretation of charge balance and electronic properties. Hence, we use high-purity Y targets supplied by Stanford Advanced Materials (United States) to avoid these problems.

The RBS and ERD simulations shown in Fig. 2.1 confirm that the REO_xH_y film composition is homogeneous throughout the depth of the films. We have observed chemical gradients in a few samples prepared at deposition pressures far above the critical values of $p^* = 0.3$ Pa (Sc), 0.5 Pa (Y), and 0.7 Pa (Gd). [5] However, the interpretation of the composition-property relationships of such graded (and likely porous) films is rather ambiguous. Therefore, these samples were excluded from further analysis.

Fig. 2.2 shows the results of the ion beam chemical composition analysis of our $(\text{Sc,Y,Gd})\text{O}_x\text{H}_y$ thin films in a generalized ternary RE–O–H composition-phase diagram. This construction is based on the similar properties of the binary RE metal oxides and hydrides. At ambient conditions, the RE metals form stable RE_2O_3 sesquioxides (except CeO_2) with a cubic bixbyite ($Ia\bar{3}$) structure (except La, Pr, and Nd). [15] All RE metals readily dissolve hydrogen, forming a random interstitial $\alpha\text{-REH}_x$ alloy where H occupies a fraction of the tetrahedral sites in the hexagonal close-packed (hcp) RE lattice. Upon hydrogenation, a phase transition to the metallic fcc ($Fm\bar{3}m$) $\beta\text{-REH}_2$ occurs for all REs. Further hydrogenation leads to a metal to insulator transition near $\text{H/RE} = 3$. For most REs, this is accompanied by a structural phase transition to hcp $\gamma\text{-REH}_3$ (except Sc, La, Pr, Nd). Moreover, the REs form hcp $\text{RE}(\text{OH})_3$ hydroxides, [16] and various REOOH oxyhydroxide phases.

Our results show that the chemical composition of the Sc, Y, and Gd-based thin films follow the same general trends in the RE–O–H diagram. Two material groups can be clearly distinguished by considering the formal valencies and demanding charge neutrality (indicated by dashed lines). The RE oxyhydrides with a composition range of $\text{RE}^{3+}\text{O}_x^{2-}\text{H}_{3-2x}^-$ ($0.5 \leq x \leq 1.5$) are found on the line connecting REH_3 and RE_2O_3 . In particular, at $x = 1$ this includes the stoichiometric LnOH bulk compounds mentioned earlier. At $x = 0.5$, the data points deviate from the $\text{RE}^{3+}\text{O}_x^{2-}\text{H}_{3-2x}^-$ line toward REH_2 (hatched area). This is consistent with our previous work showing that as-deposited films sputtered in Ar/H₂ are metallic dihydrides that oxidize in air to form transparent photochromic films. [5] We obtain grey opaque films with compositions between REH_2 and $\text{REO}_{0.5}\text{H}_2$

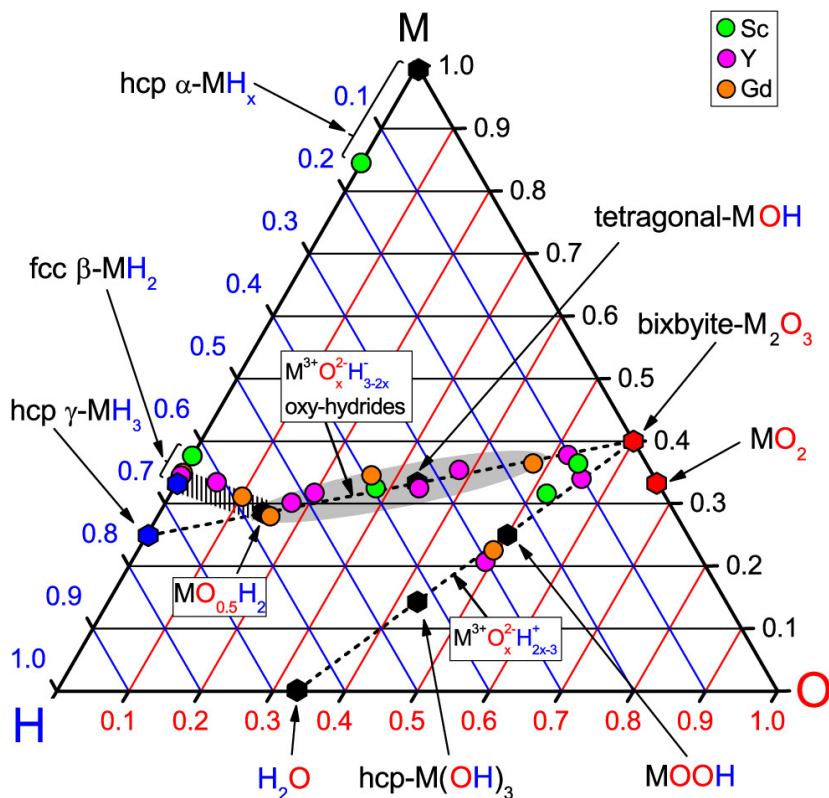


Figure 2.2: Ternary RE–O–H chemical composition and phase diagram where $M = \text{Sc, Y, La, Sm-Lu}$. Thick dashed lines indicate chemical compositions with the same charge state of cations (RE^{2+} , RE^{3+} , H^+) and anions (O^{2-} , H^-). Hexagons mark the (ideal) stoichiometric compounds that have been reported earlier: (i) binary compounds: REH_2 dihydride and REH_3 trihydride in blue as well as RE_2O_3 sesquioxides [15] and REO_2 in red; (ii) ternary compounds: REOH oxyhydrides, REOOH oxy-hydroxide, RE(OH)_3 hydroxide, and the hypothetical $\text{REO}_{0.5}\text{H}_2$ in black. Colored circles show the chemical compositions of REO_xH_y thin films obtained from ion beam analysis. Note that the diameter of the data points corresponds to a composition uncertainty of approximately ± 1 atom %. The region of photochromic materials is highlighted in grey.

by sputtering at pressures near p^* . Their composition range in the ternary RE–O–H diagram suggests that initially the air-oxidation proceeds via insertion of oxide ions into the REH_2 lattice accompanied by oxidation of RE^{2+} cations to RE^{3+} . The opaque character of these films is characteristic for intermixed metallic and dielectric phases indicating nucleation of semiconducting $\text{REO}_{0.5}\text{H}_2$ in $\beta\text{-REH}_2$. Note that $\text{REO}_{0.5}\text{H}_2$ ($x = 0.5$) marks the (ideal) composition where the conduction band is fully depleted of electrons (all cations are in the RE^{3+} state) resulting in a metal-insulator transition that is observed in terms of the appearance of an optical band gap. Increasing the pressure above p^* or adding small amounts of O_2 during deposition leads to the formation of transparent semiconducting oxyhydrides with compositions between $\text{REO}_{0.5}\text{H}_2$ and RE_2O_3 . In contrast, the RE hydroxides with the composition range $\text{RE}^{3+}\text{O}_x\text{H}_{3-2x}^-$ ($1.5 \leq x \leq 3$) are located on the line connecting RE_2O_3 and $\text{RE}(\text{OH})_3$. These transparent films were obtained by further increasing the O_2 fraction in the $\text{Ar}/\text{O}_2/\text{H}_2$ mixture during reactive sputtering.

2.3.2. O:H RATIO AND OPTICAL BANDGAP

Here we discuss the influence of the hydrogen content, as experimentally measured, on the electronic properties of the RE–O–H materials, namely their transmission spectra and optical bandgaps. Transmittance spectra of YO_xH_y films are presented as an example in Fig. 2.3.

The dense YH_x film prepared at $p = 0.3$ Pa (i.e., far below the critical deposition pressure for Y) shows a transmittance window centered around 700 nm characteristic of metallic in $\beta\text{-YH}_{1.9+\delta}$ dihydride, which is caused by a combination of weak interband and free-electron absorption. [18]

The RE oxyhydride and hydroxide films are transparent semiconductors. The optical band gap of Y oxyhydride increases continuously with increasing O^{2-} content from (2.5 ± 0.1) eV at $x = 0.7$ up to (4.9 ± 0.2) eV at $x = 1.4$ (Figure 2.4). An extrapolation of this nonlinear trend (dashed line) leads to good agreement with the band gaps of Y_2O_3 (5.6 eV) [17] and YH_3 (2.6 eV) [18], which are determined by the $\text{O}2p \rightarrow \text{Y}3d$ and $\text{H}1s \rightarrow \text{Y}3d$ interband transition, respectively. [19] Therefore, the upper valence band of the RE oxyhydrides is likely formed by a mixture of occupied H 1s and O 2p states where the valence band maximum (VBM) shifts to lower energies with increasing O^{2-} concentration because of the higher electronegativity of oxygen ($\chi_{\text{O}} = 3.44$) compared to hydrogen ($\chi_{\text{H}} = 2.20$). The resulting band gap widening of the Y oxyhydrides does not depend linearly on the anion composition. This “band gap bowing” effect also occurs in many other semiconducting multi-anion compounds such as oxysulfides, [20, 21] oxynitrides, [22] and III-V materials. [23] Its origin can be traced back to the mismatch in atomic orbital energy and (an)ion size, which leads to coupling of electronic states affecting the relative positions of the VBM and the conduction band minimum (CBM) in random alloys. [24] It seems plausible that these established principles also apply to the electronic structure of the oxyhydrides. However, comprehensive studies on this topic are still lacking.

Fig. 2.4 shows that the band gaps of the Sc and Gd oxyhydrides follow the same trend as $\text{YO}_x\text{H}_{3-2x}$, which is reasonable considering the similarity in band gaps of the oxides: Sc_2O_3 (~5.8 eV) [25] and Gd_2O_3 (5.4 eV) [26] as well as the trihydride GdH_3 (2.5 eV). [27] Slightly lower E_g values for RE = Sc, Gd are observed in oxyhydrides with low oxygen

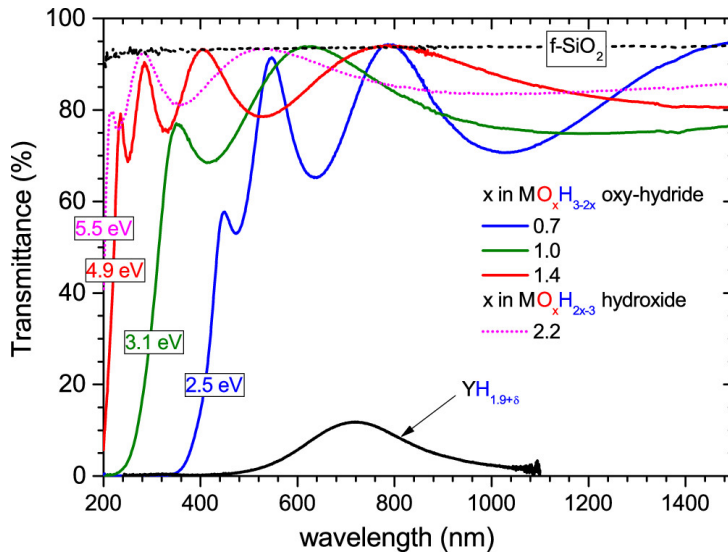


Figure 2.3: Transmittance spectra of Y-based ternary RE–O–H films corresponding with different compositions illustrating the metal-insulator transition from the dihydride $\text{YH}_{1.9+\delta}$ to the oxyhydride $\text{YO}_x\text{H}_{3-2x}$ phase followed by band gap widening with increasing O^{2-}/H^- ratio. The transmittance of a hydroxide-like film with a large H^+ concentration of ~ 30 atom % is shown for comparison. The optical band gap values as obtained from Tauc plots are given. The black dashed line is the transmittance of the bare fused silica substrate.

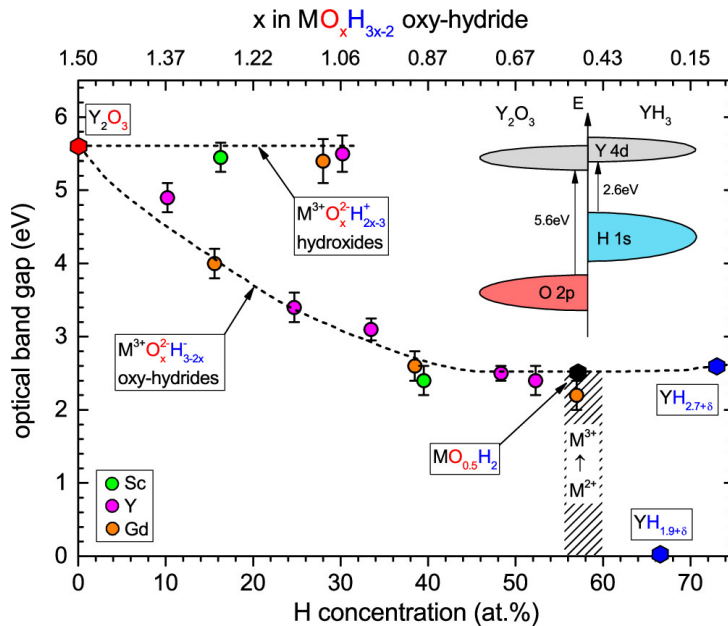


Figure 2.4: Dependence of the REO_xH_y optical band gap on the hydrogen concentration where $M = \text{Sc}, \text{Y}, \text{Gd}$ (colored circles). Reported band gap values of the binary compounds Y_2O_3 , $\text{YH}_{2.7+\delta}$ and metallic $\text{YH}_{1.9+\delta}$ are shown as colored hexagons. The metal-insulator transition upon oxidation of M^{2+} to M^{3+} with the hypothetical end point at $\text{MO}_{0.5}\text{H}_2$ is represented by the hatched region. Dashed lines are a guide to the eye and correspond to the charge-neutrality lines describing M^{3+} oxyhydrides and hydroxides in Fig. 2.2. The fundamental electronic transitions of the binary endmembers of the Y oxyhydrides are illustrated.

content ($x \sim 0.5$). This is in agreement with our work^[5] on REO_xH_y with RE= Y, Gd, Dy, Er and indicates that the effect of different RE cations on Eg is relatively weak compared to anion-alloying. Moreover, all RE hydroxide thin films have large optical band gaps ($E_g \sim 5.5$ eV) which are independent of the anion composition and similar in value to the sesquioxides, suggesting that the unoccupied H 1s orbitals do not interfere with the states at the VBM and CBM.

Given the chemical similarity of the RE elements, we suppose that the anion composition dependence of the optical band gap of most lanthanide oxyhydrides closely resembles the trend shown in Fig. 2.4. Notable exceptions are expected for M = Ce, Pr, Eu, Tb where the M 4f orbitals are located within the O 2p \rightarrow M 5d forbidden gap, resulting in a reduction of the M_2O_3 optical band gaps.^[26-28]

2.4. DISCUSSION

2.4.1. COMPOSITION LIMITS OF PHOTOCHROMISM

Having a well characterized set of RE oxyhydride materials that span most of the composition line from REH_3 to RE_2O_3 , we discuss here the relation between anion ratio and the presence of photochromism. We observe photochromism of the oxyhydrides over a wide composition range for both $x < 1$ and $x > 1$, as shown by the highlighted gray area in Fig. 2.2. However, the exact composition boundaries for photochromic $\text{REO}_x\text{H}_{3-2x}$ remain unclear.

Regarding the lower boundary, we did not obtain any oxyhydrides with $x < 0.5$ by either post-oxidation of metallic $\beta\text{-REH}_2$ films or direct growth using oxygen-poor Ar/O₂/H₂ gas mixtures. This suggests that, in contrast to what was reported by You et al.,^[3] H/RE ratios above 2 in RE oxyhydride films cannot be achieved by reactive sputtering. This is because the typical H₂ partial pressures in the order of 10 mPa during sputtering are far below the equilibrium pressure of the $\text{MH}_2 \rightarrow \text{MH}_3$ phase transition ($p\text{H}_2 \sim 0.1$ Pa)^[29, 30] and the addition of O₂ to the process gas favors further dehydrogenation. Therefore, we prepared a $\gamma\text{-YH}_{2.7+\delta}$ (i.e., $x \sim 0$) thin film by hydrogenation of a Pd-capped sputtered Y metal film at $p\text{H}_2 = 3.2$ kPa in a vacuum cell mounted into our in situ spectrometer. This trihydride did not show photochromism at RT, whereas air-oxidized RE dihydride films with $x \sim 0.5$ are photochromic. Hence, this value is marked as the O-poor boundary for photochromic RE oxyhydrides in Fig. 2.2.

Regarding the upper boundary, our ongoing photodarkening experiments with wavelength dependent excitation indicate that photon energies larger than E_g are required to trigger photochromism in RE oxyhydrides. Using UV excitation by Hg vapor lamps with $\lambda = 254$ nm, we observe weak photochromism in $\text{YO}_x\text{H}_{3-2x}$ oxyhydrides with band gaps up to 4.2 eV. According to Fig. 2.4, this corresponds to $x = 1.3$ ($c_H \sim 15$ atom %) which is marked as the oxygen-rich boundary for photochromism in Fig. 2.2.

2.5. CONCLUSIONS

In conclusion, we have established a ternary RE–O–H composition-phase diagram demonstrating that the previously reported photochromic Y-based thin films are O^{2-}/H^-

multi-anion compounds which are members of the $\text{REO}_x\text{H}_{3-2x}$ oxyhydrides material class including Sc and (most of) the lanthanides. These oxyhydride films are photochromic over nearly their entire range of composition ($0.5 \leq x \leq 1.5$), which implies that the presence of both oxide and hydride ions is crucial for the photochromic effect at ambient conditions. We notice a general trend toward decreased photochromic contrast and faster bleaching kinetics with increasing O:H ratio, in agreement with the report of Moldarev et al.^[6] Moreover, the RE oxyhydride optical band gap can be adjusted over a wide range by controlling the O:H anion ratio in order to adapt the photochromic response for applications such as energy-saving smart windows and adaptive eyewear. Further systematic investigation of the electronic structure and defect formation is required to clarify the origin and physical limitations of the photochromic effect in the REO_xH_y materials.

REFERENCES

- [1] T. Mongstad, C. Platzer-Björkman, J. P. Maehlen, L. P. Mooij, Y. Pivak, B. Dam, E. S. Marstein, B. C. Hauback, and S. Z. Karazhanov, *A new thin film photochromic material: Oxygen-containing yttrium hydride*, *Sol. Energy Mater. Sol. Cells* **95**, 3596 (2011).
- [2] T. Mongstad, C. Platzer-Björkman, S. Karazhanov, A. Holt, J. Maehlen, and B. Hauback, *Transparent yttrium hydride thin films prepared by reactive sputtering*, *Journal of Alloys and Compounds* **509**, S812 (2011), proceedings of the 12th International Symposium on Metal-Hydrogen Systems, Fundamentals and Applications (MH2010).
- [3] C. C. You, D. Moldarev, T. Mongstad, D. Primetzhofner, M. Wolff, E. S. Marstein, and S. Z. Karazhanov, *Enhanced photochromic response in oxygen-containing yttrium hydride thin films transformed by an oxidation process*, *Solar Energy Materials and Solar Cells* **166**, 185 (2017).
- [4] J. Montero, F. Martinsen, M. Lelis, S. Karazhanov, B. Hauback, and E. Marstein, *Preparation of yttrium hydride-based photochromic films by reactive magnetron sputtering*, *Sol. Energy Mater. Sol. Cells* **177**, 106 (2018).
- [5] F. Nafezarefi, H. Schreuders, B. Dam, and S. Cornelius, *Photochromism of rare-earth metal-oxy-hydrides*, *Appl. Phys. Lett.* **111**, 103903 (2017).
- [6] D. Moldarev, M. V. Moro, C. C. You, E. M. Baba, S. Z. Karazhanov, M. Wolff, and D. Primetzhofner, *Yttrium oxyhydrides for photochromic applications: Correlating composition and optical response*, *Phys. Rev. Materials* **2**, 115203 (2018).
- [7] R. Gremaud, M. Slaman, H. Schreuders, B. Dam, and R. Griessen, *An optical method to determine the thermodynamics of hydrogen absorption and desorption in metals*, *Appl. Phys. Lett.* **91**, 231916 (2007).
- [8] A. Remhof, J. W. J. Kerssemakers, S. J. van der Molen, R. Griessen, and E. S. Kooij, *Hysteresis in YH_x films observed with in situ measurements*, *Phys. Rev. B* **65**, 054110 (2002).
- [9] X. qiu Ye, T. Tang, B. yun Ao, D. li Luo, G. Sang, and H. zhi Zhu, *Thermodynamics of Sc–H and Sc–D systems: Experimental and theoretical studies*, *Journal of Fusion Energy* **32**, 254 (2013).
- [10] J. Tauc, R. Grigorovici, and A. Vancu, *Optical properties and electronic structure of amorphous germanium*, *physica status solidi (b)* **15**, 627 (1966).
- [11] M. Cesaria, A. P. Caricato, and M. Martino, *Realistic absorption coefficient of ultrathin films*, *J. Opt.* **14**, 105701 (2012).
- [12] American Society for Testing and Materials (ASTM), *Terrestrial reference spectra for photovoltaic performance evaluation, astm g173-03, global tilt*, Online; accessed 02-Jan-2022.

- [13] E. Szilágyi, *Energy spread in ion beam analysis*, *Nuclear Instruments and Methods in Physics Research Section B: Beam Interactions with Materials and Atoms* **161-163**, 37 (2000).
- [14] A. Takenouchi, T. Otomo, K. Niwa, M. Sakai, Y. Saito, T. Kirigane, M. Kosaka, S. Michimura, S. Hasegawa, and O. Nakamura, *Purification of commercial yttrium metal: Removal of fluorine*, *Journal of Crystal Growth* **468**, 701 (2017), the 18th International Conference on Crystal Growth and Epitaxy (ICCGE-18).
- [15] M. Zinkevich, *Thermodynamics of rare earth sesquioxides*, *Progress in Materials Science* **52**, 597 (2007).
- [16] G. Beall, W. Milligan, and H. A. Wolcott, *Structural trends in the lanthanide trihydroxides*, *Journal of Inorganic and Nuclear Chemistry* **39**, 65 (1977).
- [17] Adachi, Gin-ya, and N. Imanaka, *The binary rare earth oxides*, *Chem. Rev.* **98**, 1479 (1998).
- [18] A. T. M. van Gogh, D. G. Nagengast, E. S. Kooij, N. J. Koeman, J. H. Rector, R. Griessen, C. E. J. Flipse, and R. J. J. G. A. M. Smeets, *Structural, electrical, and optical properties of $La_{1-z}Y_zH_x$ switchable mirrors*, *Phys. Rev. B* **63**, 195105 (2001).
- [19] T. Miyake, F. Aryasetiawan, H. Kino, and K. Terakura, *GW quasiparticle band structure of YH_3* , *Phys. Rev. B* **61**, 16491 (2000).
- [20] B. K. Meyer, A. Polity, B. Farangis, Y. He, D. Hasselkamp, T. Krämer, and C. Wang, *Structural properties and bandgap bowing of $ZnO_{1-x}S_x$ thin films deposited by reactive sputtering*, *Applied Physics Letters* **85**, 4929 (2004).
- [21] C. Persson, C. Platzer-Björkman, J. Malmström, T. Törndahl, and M. Edoff, *Strong valence-band offset bowing of $ZnO_{1-x}S_x$ enhances p-type nitrogen doping of ZnO-like alloys*, *Phys. Rev. Lett.* **97**, 146403 (2006).
- [22] R.-J. Xie and H. T. (Bert) Hintzen, *Optical properties of (oxy)nitride materials: A review*, *Journal of the American Ceramic Society* **96**, 665 (2013).
- [23] I. Vurgaftman, J. R. Meyer, and L. R. Ram-Mohan, *Band parameters for III-V compound semiconductors and their alloys*, *Journal of Applied Physics* **89**, 5815 (2001).
- [24] S. Wei and A. Zunger, *Band offsets and optical bowings of chalcopyrites and Zn-based II-VI alloys*, *Journal of Applied Physics* **78**, 3846 (1995).
- [25] V. Afanas'ev, S. Shamuilina, M. Badylevich, A. Stesmans, L. Edge, W. Tian, D. Schlom, J. Lopes, M. Roeckerath, and J. Schubert, *Electronic structure of silicon interfaces with amorphous and epitaxial insulating oxides: Sc_2O_3 , Lu_2O_3 , $LaLuO_3$* , *Microelectronic Engineering* **84**, 2278 (2007), iNFOS 2007.
- [26] A. Prokofiev, A. Shelykh, and B. Melekh, *Periodicity in the band gap variation of Ln_2X_3 ($X = O, S, Se$) in the lanthanide series*, *Journal of Alloys and Compounds* **242**, 41 (1996).

- [27] M. W. Lee and C. H. Lin, *Determination of the optical constants of the γ -phase GdH_3 thin films*, [Journal of Applied Physics](#) **87**, 7798 (2000).
- [28] R. Gillen, S. J. Clark, and J. Robertson, *Nature of the electronic band gap in lanthanide oxides*, [Phys. Rev. B](#) **87**, 125116 (2013).
- [29] J. Huiberts, J. Rector, R. Wijngaarden, S. Jetten, D. de Groot, B. Dam, N. Koeman, R. Griessen, B. Hjörvarsson, S. Olafsson, and Y. Cho, *Synthesis of yttriumtrihydride films for ex-situ measurements*, [Journal of Alloys and Compounds](#) **239**, 158 (1996).
- [30] E. S. Kooij, A. T. M. van Gogh, and R. Griessen, *In situ resistivity measurements and optical transmission and reflection spectroscopy of electrochemically loaded switchable YH_x films*, [J. Electrochem. Soc.](#) **146**, 2990 (1999).

3

STRUCTURE: GENERALIZED ANION-DISORDERED MODEL

*The ability to play chess is the sign of a gentleman.
The ability to play chess well is the sign of a wasted life.*

Paul Charles Morphy

Rare-earth (RE) oxyhydride thin films prepared by reactive magnetron sputtering followed by air-oxidation show a color-neutral photochromic effect at ambient conditions within a wide composition range (REO_xH_{3-2x} where $0.5 \leq x < 1.5$). Due to the high degree of anion sublattice disorder present in these thin films, the structure models proposed for the related bulk materials are not directly applicable. Instead, we use a combination of EXAFS analysis and lattice energy calculations to establish a fcc-based model linking the oxyhydrides to the related binary compounds. The oxide anions are found to occupy predominantly the tetrahedral sites in the fcc structure which is attributed to electrostatic lattice energy minimization.

This chapter is an adaptation of:

G. Colombi, S. Cornelius, A. Longo, and B. Dam, *Structure Model for Anion-Disordered Photochromic Gadolinium Oxyhydride Thin Films*, J. Phys. Chem. C **124**, 13541 (2020).

3.1. INTRODUCTION

Multianion compounds are an emerging class of solid state materials due to their broad spectrum of functional properties. The wide range of different anion characteristics (electronegativity, polarizability, ionic radius, etc.) offers unprecedented degrees of freedom in the design of functional materials. In contrast, the local and electronic structure of single anion compounds, such as metal oxides, is determined to a large extent by the cation chemistry only. [1, 2]

Previously we have shown that rare-earth based oxyhydride thin films (with RE = Sc, Y, Gd, Dy and Er) can be synthesized via post-deposition air oxidation of RE dihydride films grown by reactive magnetron sputtering in Ar/H₂ atmosphere. [3, 4] Recently, this class of compounds gained attention in view of their peculiar reversible photochromic effect and related photoconductivity. [5] Most of the recent research, however, focused at the phenomenological aspects of these functional properties while the exact chemical composition and structure of the materials remained unclear. [6-9] The multianion nature of these films was established only in 2019 (see Chapter 2), when the photochromic effect and energy gap tunability (from 2.5 to 5.5 eV) were related to the oxyhydride RE³⁺O_x²⁻H_{3-2x}⁻ composition line which connects the trihydride (REH₃) to the oxide (RE₂O₃). To the best of our knowledge, these two binary compounds as well as the RE-hydroxides are not photochromic at ambient conditions, implying that photodarkening occurs only in presence of both O²⁻ and H⁻ anions. [4]

With this new compositional insight, it is worth noting that the technological potential of RE oxyhydrides thin films goes beyond applications in smart coatings for windows and sensors. Indeed, a new record for H⁻ ionic conductivity at intermediate temperatures was recently achieved LaO_xH_{3-2x} powders. [10] This finding introduced simple ternary systems with a cubic structure to the group of oxyhydride ionic conductors, a class of materials otherwise dominated by far more complex layered perovskites of the Ruddlesden-Popper type, such as La₂LiHO₃, LnSrCoO₃H_{0.7}, La_{2-x-y}Sr_{x+y}H_{1-x+y}O_{3-y} and La_{2-x-y}Sr_{x+y}LiH_{1-x+y}O_{3-y}. [11-14]

Given the analogous composition to LaO_xH_{3-2x}, we suppose that reactively sputtered RE oxyhydride thin films might be hydride-ion conductors as well. This property is likely tied to the still unclear mechanism of photodarkening, a process suggested to depend on the segregation of an optically absorbing phase during light exposure. [15, 16] The connection between the anion mobility and the photochromic effect remains an open question, with the only hint coming from a NMR study in which the photodarkening was shown to temporarily quench the signal of the most mobile hydrogen fraction. [17]

In this context, a deeper understanding of the crystal structure of the sputtered RE-O-H films is important not only to further explore the photo-initiated diffusion processes and solid state reactions, but also to assess the similarity to the other hydride-ion conductors.

Synthesized as powders via high temperature solid state reaction between oxide and trihydride precursors, the cubic LaO_xH_{3-2x} present a small tetragonal distortion (*P4/nmm*) in consequence of long range anion ordering. [10] Given the strain induced by the adhesion to the substrate and the fact that reactively sputtered photochromic RE oxyhydride thin films form via a process whose driving force and kinetics are inherently different from powder synthesis, it remains unclear to which extent they share the struc-

tural (and functional) properties of the bulk RE oxyhydrides.

Until now, due to the fact that neutron diffraction is not a viable option for thin films, experimental information on the location of the H^- and O^- anions was missing. In this chapter, we bridge this lack of evidence by measuring the extended X-ray absorption fine structure (EXAFS) of a subset of the samples studied in Chapter 2. We choose Gd-based samples because of (i) their high X-ray scattering cross section and (ii) the energy window of the XAS beamline we had access to; however the similar structural behaviour of other RE oxyhydrides^[3,4] and our energy calculations suggest that the result here discussed can be extended to other RE cations as well.

In Sec. 3.3.1 we use a combination of transmittance and photodarkening measurements to verify the identity (i.e., dihydride, oxyhydride, oxide, hydroxide) of each sample. In Sec. 3.3.2 XRD is used to probe the cation lattice, while In sec. 3.3.3 EXAFS is used to study the Gd local coordination. Here we verify that the local coordination of the in-situ sputtered GdH_2 resembles that of the well-known ex-situ hydrogenated RE dihydrides and that, upon air exposure, O^{2-} anions enter the tetrahedral sites of the fcc- GdH_2 lattice. In Sec. 3.4.1 we frame the experimental results in a broader discussion of the lattice energy, providing in addition a qualitative explanation of the driving force behind the air-mediated formation of the photochromic RE oxyhydrides. Finally, in Sec. 3.4.2 we propose an idealized structural model to describe the occupancy of each anion-site along the $\text{REO}_x\text{H}_{3-2x}$ composition line.

3.2. EXPERIMENTAL

SAMPLE PREPARATION

Gd-based thin films of thickness ~ 150 nm were prepared by reactive magnetron sputtering of a 2-inch metal target (MaTeck Germany, 99.9% purity) in a $\text{Ar}/\text{H}_2/\text{O}_2$ (5N purity) atmosphere. The deposition chamber was kept at a base pressure below 1×10^{-4} Pa. During deposition three independent mass flow controllers were used to define the composition of the gas mixture while the total deposition pressure (p_{dep}) was varied by means of a butterfly reducing valve mounted at the inlet of the pumping stage. A constant Ar flow of 35 sccm was used in combination with different H_2 and O_2 flows to synthesize samples of different chemical composition. A total power of 175 W supplied as pulsed direct current (50 kHz, 90% duty cycle) was used to sustain the plasma excitation while avoiding arcing. All samples were grown on unheated UV-grade fused silica (f-SiO_2) and polished glassy carbon substrates.

Table 3.1 summarizes the different binary and ternary Gd-based thin films studied in this work as well as the corresponding deposition conditions together with the key material properties. While Gd dihydride is identified by its characteristic optical transmittance window,^[3,18] the oxyhydride is the only sample that shows photochromic behaviour (Fig. 3.1).^[4]

A Gd dihydride reference sample (hereafter labeled as *ex-situ*) was prepared by hydrogenation of a Pd-capped (20 nm) metal layer in a pressure cell at 1 bar of H_2 at room temperature. Employing the hydrogenography method,^[19] the change in optical transmittance was used to verify that the film was loaded to a H:Gd ratio above the dihydride

Sample	H ₂ /O ₂ flow (sccm)	P _{dep} (Pa)	Cap (20 nm)	Composition	Phase
Gd Metal	0/0	0.3	Pd	-	<i>P6₃/mmc</i>
Dihydride* (ex-situ)	0/0	0.3	Pd	GdH _{1.8}	<i>Fm$\bar{3}$m</i>
Dihydride	5/0	0.3	Al	-	<i>Fm$\bar{3}$m</i>
Oxyhydride	5/0	0.7	-	GdO _{0.8} H _{1.4} **	<i>Fm$\bar{3}$m</i>
Oxide	0/1	0.3	-	Gd ₂ O ₃	<i>Ia$\bar{3}$</i>
Hydroxide	5/0.4	0.3	-	GdO _{2.2} H _{1.2}	<i>amorph.</i>

Table 3.1: Summary of the Gd–O–H compounds studied in this work, corresponding deposition conditions and key material properties. *Deposition conditions refer to the pure Gd layer which is later hydrogenated in a pressure cell (1 bar of H₂ at room temperature) employing the hydrogenography method. [19] **Composition estimated from the EXAFS coordination numbers.

to trihydride phase transition, followed by unloading to dihydride in air after opening of the pressure cell.

The metallic materials (Gd and its dihydrides) were capped by a Pd or Al overlayer, that was deposited without breaking the vacuum, to protect them against oxygen contamination. No protection layer was applied to the oxygen containing semiconductors.

The photochromic oxyhydride is a transparent semiconductor which forms by air-oxidation at ambient conditions from the as-sputtered metallic dihydride state. Hence, air-oxidation is an important step of oxyhydride synthesis, which depends on the film porosity and was shown to occur above a certain critical deposition pressure. [3] In the case of Gd, we find that air oxidation sets in above a value of $p_{dep} = 0.7$ Pa. All other films were sputtered at $p_{dep} = 0.3$ Pa. In contrast to the oxyhydride, the oxide as well as the hydroxide samples are already transparent upon deposition inside the vacuum chamber, suggesting that all the oxygen is incorporated in-situ via the reactive O₂/H₂ atmosphere.

SAMPLE CHARACTERIZATION

Optical properties. The optical transmittance, $T(\lambda)$, of the wide band gap oxide and hydroxide samples was measured with a Perkin-Elmer Lambda 900 UV-VIS-NIR spectrometer with a wavelength range of 200-2500 nm. The remaining samples were investigated using a custom-built optical fiber based setup equipped with a white source (DH-2000BAL, Ocean Optics) and a Si-based energy dispersive spectrometer (HR4000, Ocean Optics). The transmittance of the dihydride film was measured prior to the deposition of the Al capping layer inside an oxygen free (<0.1 ppm) glove-box directly connected to the deposition chamber.

The optical bandgap, E_g , was determined using the Tauc plot method with an estimated error of about $\Delta E_g = 0.1$ eV. [20, 21]

The photo-darkening of the oxyhydride was initiated by a low pressure Hg UV-lamp (Herolab GmbH) with an emission range of 245-400 nm and an integrated irradiance of 5000 $\mu W cm^{-2}$, which is comparable to that of the sun (4610 $\mu W cm^{-2}$) in the same spectral range. [22]

Chemical composition. The absolute composition of the samples was determined by a combination of Rutherford backscattering (RBS) and Elastic recoil detection (ERD) ion beam techniques with an estimated accuracy of 1 at%. The reader is referred to Chapter 2 for further details. Note that ion beam analysis was crucial to clearly distinguish the Gd oxide, oxyhydride and hydroxide samples.

X-ray diffraction. Parallel-beam X-ray diffraction (XRD) data were recorded on a Bruker D8 Discover diffractometer equipped with a Cu tube ($\lambda = 1.5406 \text{ \AA}$) combined with a 40 mm Goebel mirror as well as a 0.2° equatorial Soller slit mounted to a LynxEye XE energy dispersive linear detector.

All samples were initially measured in symmetric geometry (2:1), where the incidence angle equals half of the scattering angle ($w = 2\Theta/2$). The presence of preferential orientation was assessed by rocking curves around the main peaks (scanning w at fixed 2Θ). For those samples showing no or minimal texture we report grazing incidence scans (incidence angle fixed at $w = 2^\circ$) to enhance the signal of the thin films.

Lattice constants were determined from the peak positions obtained by fitting a constrained double Pseudo-Voigt function (to account for the Cu-K $_{\alpha 1/2}$ doublet) to the experimental data. The resulting values were also corrected for instrumental deviations in scattering angle, 2Θ , by measuring a NIST certified powder standard (SRM-1976b corundum Al $_2$ O $_3$) in the same geometry. Given the large FWHM values observed for the sputtered polycrystalline films of this work, the uncertainty of the lattice constants is estimated to be $\pm 0.01 \text{ \AA}$.

X-ray absorption spectroscopy. Gd-L3 X-ray absorption spectra were collected on the EXAFS stations (Bending-Magnets n.26 and n.14) of the Dutch-Belgian beamline (DUBBLE) at the European Synchrotron Radiation Facility (ESRF, Grenoble France). The energy, E , of the X-ray beam was controlled by a Si(111) double crystal monochromator with a resolution of $\Delta E/E \sim 1 \times 10^{-4}$. Across the whole measurement range, from 7043 eV (200 eV before the Gd-L3 edge) to 7820 eV (just before the Gd-L2 edge), the accuracy of the energy calibration was confirmed to be within 0.25 eV by measuring the K-edge of Co (7112 eV), Fe (7708.9 eV) and Ni (8332.8 eV) reference foils. The thin films were measured in fluorescence geometry at an incidence angle of $\sim 35^\circ$ and an exit angle of $\sim 60^\circ$, defined by the orientation of the sample and the position of the ORTEC IGLET 9-element Ge detector respectively.

The metallic samples and the photochromic oxyhydride were measured at 80 K in a liquid nitrogen cryostat. In contrast, given the dominant site disorder, oxide and hydroxide samples were measured at room temperature (RT) in air.

Taking into consideration the Gd absorption cross section, the thickness of the films and their density, we estimate negligible effects of self-absorption (Sec. 3.B.2); therefore no correction is performed during data treatment. [23] After background subtraction of the raw data, EXAFS oscillations, $\chi(E)$, have been expressed in terms of the photoelectron wavenumber ($k = \sqrt{2m_e E}/\hbar$), $\chi(k)$, and Fourier Transformed (FT) to the direct space, $\chi(r)$, for a more intuitive interpretation. To compensate for the diminishing amplitude at high- k , a weighting factor of k^2 is adopted prior to the FT. In the framework of the single scattering (SS) and multiple-scattering (MS) path expansion, the weighted Fourier

transformed data, $FT[k^2 \times \chi(k)]$, is finally fitted according to the EXAFS equation (Sec. 3.B.1):

$$\chi(k) = S_0^2 \sum_j \frac{N_j}{kr_j^2} f_j(k, r_j) e^{-2\sigma_j^2 k^2} e^{-2r_j/\lambda_j(k)} \sin(2kr_j + \delta_j(k)) \quad (3.1)$$

For each j^{th} -shell the amplitude, $f_j(k, r_j)$, phase shift, δ , and photoelectron mean free path, $\lambda_j(k)$, are calculated ab-initio with the FEFF9 code. [24, 25] The coordination number, N_j , the effective distance, r_j , and the Debye Waller factor, σ_j , are taken instead as fitting parameters (sometimes constrained). A fourth variable, the energy shift, $e_{0,j}$, is added to account for experimental energy offsets and for the possible mismatch with the ab-initio calculation. Due to the absence of references, the amplitude reduction factor, S_0 , is taken as equal to 1, possibly leading to a systematic, small underestimation of the coordination numbers. [26, 27]

Data processing including averaging of scans, background subtraction, forward Fourier Transform of the k^2 -weighted data, and fitting was performed using the Viper software. [28] The errors have been estimated by the correlation map between parameters and reflect a confidence interval of $2\sigma = 68\%$.

MADELUNG ENERGY CALCULATION

The Madelung energies of Gd–O–H structures have been calculated using MADEL, an applet called in by VESTA. [29] The code employs the Fourier method, for which the radius of an ionic sphere was chosen to be slightly smaller than the shortest interatomic distance while the reciprocal space range was set to 6 \AA^{-1} . The convergence of the Madelung energy upon variation of both parameters was verified.

3.3. RESULTS

3.3.1. OPTICAL PROPERTIES AND PHOTOCROMISM

Due to the mixed H_2/O_2 reactive atmosphere and possible air-oxidation, a wide range of binary and ternary Gd–O–H compounds may result from reactive magnetron sputter deposition. [3, 4] Optical transmittance spectra were used to verify the electronic state of each of the Gd–O–H thin films (Fig. 3.1).

Gd dihydride films appear as optically thick metals with the exception of a region of weak transmittance in the red part of the visible spectrum. This transmittance window is a characteristic property of the RE dihydrides [3, 30] and is known to arise due to a combination of a weak inter-band and free electron absorption close to the plasma frequency. [18] Gd oxide and hydroxide are both wide bandgap semiconductors with indirect optical bandgaps of 5.1 eV and 5.3 eV respectively. Finally, the oxyhydride is the photochromic semiconductor that, after exposure to UV light for three hours, shows an average contrast (ΔT) of 31.5% in the 450 – 1000 nm wavelength range. By comparison to the trend in band gap variation with respect to $\text{REO}_x\text{H}_{3x-2}$ oxyhydride composition (Fig. 2.4), the measured band gap value (2.3 eV) suggests that the oxyhydride studied in this work belongs to the oxygen poor region ($0.5 < x < 1$) of the composition range. [4]

Additional information about the semiconducting samples can be inferred from the typical thin film interference patterns in the long wavelength part of the transmittance spectra. [31] The fact that the interference maxima reach the transmittance of the bare

f-SiO₂ substrate implies that the sub band gap absorption, i.e. due to optically active defects, is negligible. Moreover, the value of the interference minima is linked to the difference in refractive index between film and substrate. The data in Fig. 3.1 suggests that the refractive index decreases with increasing oxygen content, x , i.e. from oxyhydroxide to oxide to hydroxide, which is in good agreement with our earlier work [4] and a recent study by You et al. [7]

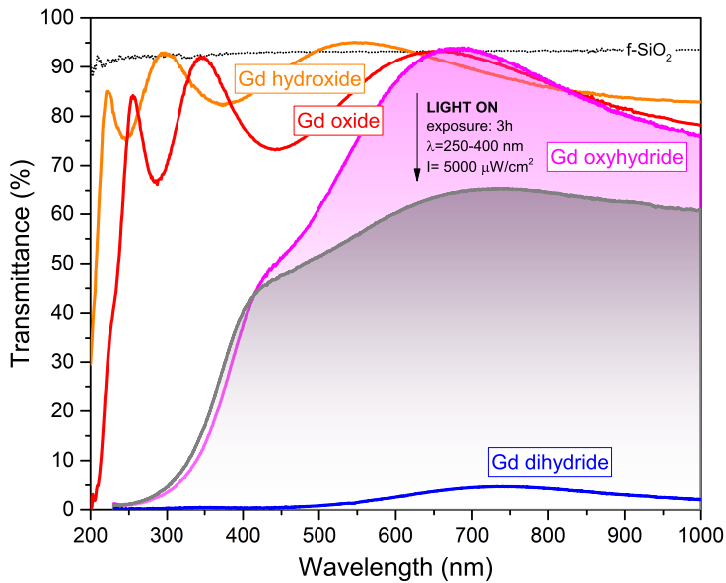


Figure 3.1: Transmittance of sputtered Gd–O–H thin films. Gd dihydride (blue) is a reflective metal with a transmittance window centered at ~ 750 nm. Gd oxide (red) and Gd hydroxide (orange) are wide bandgap semiconductors. Gd oxyhydroxide (magenta) is a semiconductor with characteristic photochromic behaviour i.e. transmittance decreases by $\sim 30\%$ after 3h of UV exposure (grey). The black dotted line is the transmittance of the bare f-SiO₂ substrate.

3.3.2. XRD: FCC CATION LATTICE

XRD is employed to probe the long range crystal structure and to determine the lattice constants of the Gd–O–H thin films, as shown in Fig. 3.2.

The phase of each compounds was identified by comparison to the ICDD-PDF patterns reported in Table 3.2. The Gd metal is the only film showing hexagonal structure and its two main peaks at 28.8° and 30.6° match with the (100) and (002) crystal planes of the hcp- $P6_3/mmc$ pattern (#00-02-0864).

In agreement with our previous studies, the diffraction patterns of the remaining films show fcc symmetry, best matched by the $Fm\bar{3}m$ pattern of GdH₂ (#00-50-1107). [3, 4] Due to the limited number of reflections and their large FWHM it is not possible to exclude the small degree of tetragonal distortion which was reported for the similar anion-ordered LnOH ($c/\sqrt{2}a = 0.997$) and LnO_{0.5}H₂ ($c/\sqrt{2}a = 0.999$) oxyhydroxides. [10, 32]

The rocking curve FWHM is a relative measure of the degree of out-of-plane preferen-

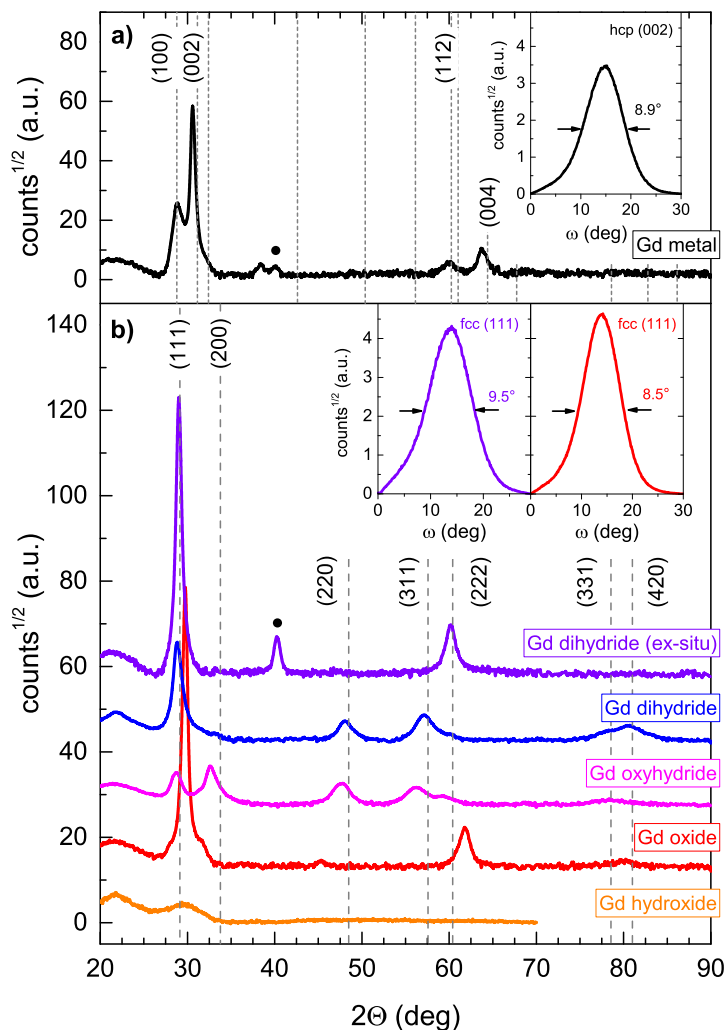


Figure 3.2: XRD patterns of the polycrystalline Gd–O–H thin films. *a*) Gd metal is ascribed to the hexagonal $P6_3/mmc$ pattern #00-02-0864 (dotted vertical lines). *b*) Gd dihydride, oxyhydride and oxide have cubic symmetry and are shown versus the $Fm\bar{3}m$ pattern #00-50-1107 of the GdH_2 (dashed vertical lines). The lattice constants of all compounds are reported and compared to the respective ICDD-PDF reference patterns in Table 3.2. The peak indexed with a dot is due to the Pd capping, while the broad feature centred at $2\theta \sim 22^\circ$ is due to scattering by the $f\text{-SiO}_2$ substrate. The inserts show the rocking curves of the prominent peaks of the textured samples.

tial orientation of thin films. According to the rocking curves shown in the inserts of Fig. 3.2 we find that the Gd metal film has a preferential out-of-plane orientation along the hcp c -axis. This texture is maintained during ex-situ hydrogenation of Gd to GdH₂, i.e. the phase transition occurs in such way that the hcp c -axis (002) is parallel to fcc space diagonal (111). This structure evolution is in agreement with the well documented case of hydrogenation of Y to YH₂. [4, 33] In contrast, the (in-situ) reactively sputtered GdH₂ film has no significant (111) texture, which is also indicated by the absence of the (222) peak. Similarly, the photochromic Gd oxyhydride is not textured either.

In case of Gd oxide, we would expect thermodynamically stable cubic bixbyite structure ($Ia\bar{3}$, #00-12-0797), which is essentially a distorted fcc structure with ordered oxygen vacancies. [34, 35] In the XRD pattern, this results in the appearance of (weak) superstructure peaks in addition to the main fcc peaks, as we have reported recently for the cases of reactively sputtered Y₂O₃ and Sc₂O₃ films. [4] Here, these superstructure peaks are absent in the Gd oxide XRD pattern (Fig. 3.2), which is probably a consequence of the substantial (111) texture of this sample that suppresses the signal from other crystal planes. Therefore, we identify the structure of the Gd₂O₃ as bixbyite despite the missing superstructure peaks.

Table 3.2 reports the determined lattice constants (d) and their variation with respect to the reference patterns. While the oxide appears compressed along the (111) direction, all the other samples show a slight expansion, which is typical for sputtered thin films. [3] Notably, the lattice constants of the hydrogenated ex-situ dihydride (5.33 Å), sputtered dihydride (5.36 Å) and oxyhydride (5.41 Å) present the increasing trend already reported for Gd, Dy, Y and Er based RE–O–H compounds. [3]

Sample	ICDD-PDF	Phase	d (Å)	$\Delta d/d_0$ (%)
Gd metal	#00-02-0864	$P6_3/mmc$	5.84	+1.4
Gd dihydride* (ex-situ)	#00-50-1107	$Fm\bar{3}m$	5.33	+0.5
Gd dihydride	#00-50-1107	$Fm\bar{3}m$	5.36	+1.0
Gd oxyhydride	#00-50-1107	$Fm\bar{3}m$	5.41	+1.9
Gd oxide	#00-12-0797	$Ia\bar{3}$	10.41	-3.9
Gd hydroxide		X-ray amorphous		

Table 3.2: Gd–O–H The experimental lattice constant (d) - as derived by XRD peak fitting - and ($\Delta d/d_0$) is its relative variation with respect to the reference ICDD-PDF pattern for the Gd–O–H compounds studied in this work.

3.3.3. EXAFS: TETRAHEDRAL OXYGEN LOCATION

EXAFS was used to investigate the Gd local environment and therefore understand the location of oxygen in the Gd–O–H structures. In Fig. 3.3 we show the Gd-L3 EXAFS data and their best fit up to the 2nd shell. The corresponding fitting parameters and their uncertainty are reported in Table 3.3.

All the polycrystalline thin films were fitted with models constructed from the insight inferred from XRD. To fit the EXAFS signal of the X-ray amorphous hydroxide, we tested all the relevant space groups of the ICDD-PDF database (Table 3.C.1), finding however

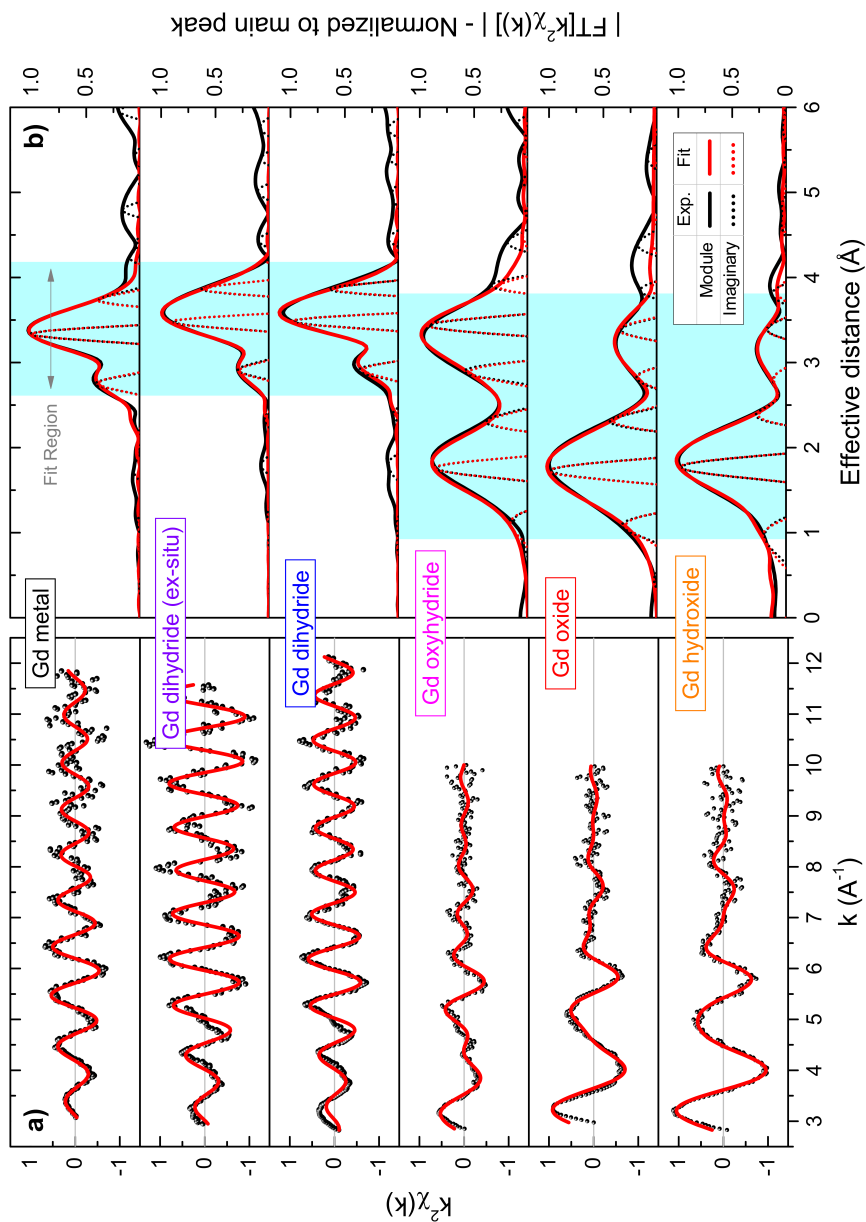


Figure 3.3: k^2 -weighted EXAFS data (a) and corresponding Fourier Transform (b) of the reactively sputtered Gd–O–H thin films. The red curves correspond to the best fits as done in real space for the shells indicated by the light blue background.

Path	N (Atoms)	r (Å)	σ (10^{-3} \AA^2)	e_0 (eV)
Gd metal (80K)			R=3.0%	$\nu = 2$
Gd-Gd #1	5.2(5)	3.55(1)	5.2(4)	2.8(8)
Gd-Gd #2	4.9(5)	3.67(1)	6.6(4)	"
Gd dihydride (ex-situ) (80K)			R=3.9%	$\nu = 7$
Gd-Gd #1	11.9(4)	3.737(2)	5.2(1)	3.0(1)
Gd dihydride (80K)			R=6.0%	$\nu = 6$
Gd-Gd #1	10.3(1)	3.745(1)	7.4(1)	3.5(3)
Gd oxyhydride (80K)			R=5.8%	$\nu = 6$
Gd-O #1	2.5(2)	2.305(6)	13(3)	4.4(3)
Gd-Gd #1	9.3(5)	3.677(6)	18(1)	"
Gd oxide (RT)			R=5.0%	$\nu = 5$
Gd-O #1	5.3(4)	2.27(1)	14(1)	3.2(9)
Gd-Gd #1	5.7(9)	3.63(2)	13(4)	"
Gd hydroxide (RT)			R=4.4%	$\nu = 6$
Gd-O #1	6.4(6)	2.34(1)	14(1)	1.8(5)
Gd-Gd #1	4.1(7)	3.65(2)	13(3)	"

Table 3.3: Results obtained from the EXAFS fitting of the Gd–O–H thin films. For each sample, R is the final value of the minimized function while ν is the difference between the number of independent data points and free variables. The error on the last significant figure is reported in round brackets after each number.

that the best fit parameters were always equal within error. In Table 3.3 we report those corresponding to the monoclinic $P2_1/m$ ($a = 4.39 \text{ \AA}$, $b = 3.75 \text{ \AA}$, $c = 6.13 \text{ \AA}$) oxyhydroxide $\text{GdO}(\text{OH})$, which is the hydroxide-like compound whose formula unit best matches the experimental composition of the sputtered film. The contribution of the H was always neglected because insignificant compared to that of the oxygen atoms, as it is visually evident comparing the spectra of the metallic samples to those of the oxygen containing semiconductors.

The fitting results show that in all cases the oxygen gives rise to a coordination shell at a distance of $\sim 2.3 \text{ \AA}$, which corresponds to a path of single scattering between the Gd atoms and the oxygen located in the tetrahedral sites of the Gd lattice. In contrast, the occupation of octahedral sites would appear at $\sim 2.7 \text{ \AA}$. While such distance matches the expectation for oxide and hydroxide, the case of the photochromic sample is less trivial: given the stoichiometry of a H-rich oxyhydride ($\text{REO}_x\text{H}_{3-2x}$ with $0.5 \leq x < 1$), it follows that in each unit cell there are more anions than available tetrahedral sites. The fact that the first coordination shell occurs at $2.305(6) \text{ \AA}$ implies that the oxygen incorporated upon air exposure enters the structure into the tetrahedral sites, displacing a fraction of H^-

anions to a different location. Constraining the distance of the O shell according to an ideal fcc unit led to a poor fit, suggesting that in the oxyhydride the O^{2-} anions are slightly displaced from the exact center of the interstitial sites. Besides this distortion, which is small ($\sim 13\%$) compared to the Gd–O bond length, all distances are consistent with the symmetry of the space group of each sample.

The Gd–O #1 coordination numbers of the semiconductors follow the trend of increasing oxygen concentration from oxyhydride (2.5) to oxide (5.3) to hydroxide (6.4), as qualitatively shown by the peak ratios of Fig. 3.3b. All the coordination numbers indicate a minor under-coordination with respect to the ideal bulk compounds, following from the assumption on S_0^2 and possibly reflecting the defective structure of reactively sputtered films and their finite grain size. 36 Based on the coordination of the oxyhydride, $N_{Gd-O\#1} = 2.7(2)$ and $N_{Gd-Gd\#2} = 9.9(8)$, we estimate an oxygen fraction of $x = 0.8(1)$ and therefore the chemical formula $GdO_{0.8}H_{1.4}$ (Supplementary, section II.D), which corresponds - as expected from the low E_g - to the H-rich end of the photochromic oxyhydride composition range.

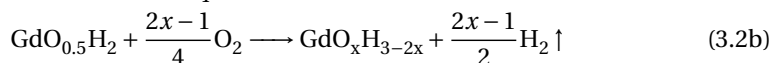
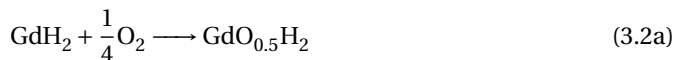
From the Debye Waller factors we conclude that the sputtered dihydride is more disordered than the ex-situ hydrogenated one while the oxyhydride is the most disordered structure of all, most likely because of the higher deposition pressure together with the large site disorder and strain induced by post deposition air-oxidation.

As an additional sign of consistency, we note that the Gd-L3 edge progressively shifts towards higher energies reflecting the increasing oxidation state of the Gd ions from metal to dihydride (Gd^{2+}) to oxide (Gd^{3+}) and hydroxide (Gd^{3+}) (Fig. 3.A.3).

3.4. DISCUSSION

3.4.1. LATTICE ENERGY AND AIR OXIDATION

The recently established RE–O–H phase diagram suggests that the formation of GdO_xH_{3-2x} oxyhydrides via air oxidation formally follows a two-step reaction path (visualized by the arrows in Fig. 3.4): 4



The EXAFS radial distribution of the oxyhydride reveals that the oxygen sits at $2.305(6)$ Å from the Gd atoms, therefore occupying the tetrahedral sites of the cation lattice. Such coordination appears counter-intuitive for two reasons. First, the oxygen enters into a structure where the tetrahedral sites are already filled by H^- ions, which therefore need to be displaced. Second, even though O^{2-} and H^- ions have fairly similar radii ($R_{O^{2-}} \sim 140$ pm, $R_{H^-} \sim 120 - 150$ pm), the first is far less polarizable than the second. 11 It follows that the oxygen insertion is accompanied by mechanical stress, as confirmed by the expanded lattice of the oxyhydrides compared to the dihydrides. 3

The tetrahedral sites of the fcc structure are smaller than the octahedral ones, therefore it is not a principle of size exclusion that guides the oxygen incorporation. On the contrary, given the largely ionic nature of the compound, the driving force behind the

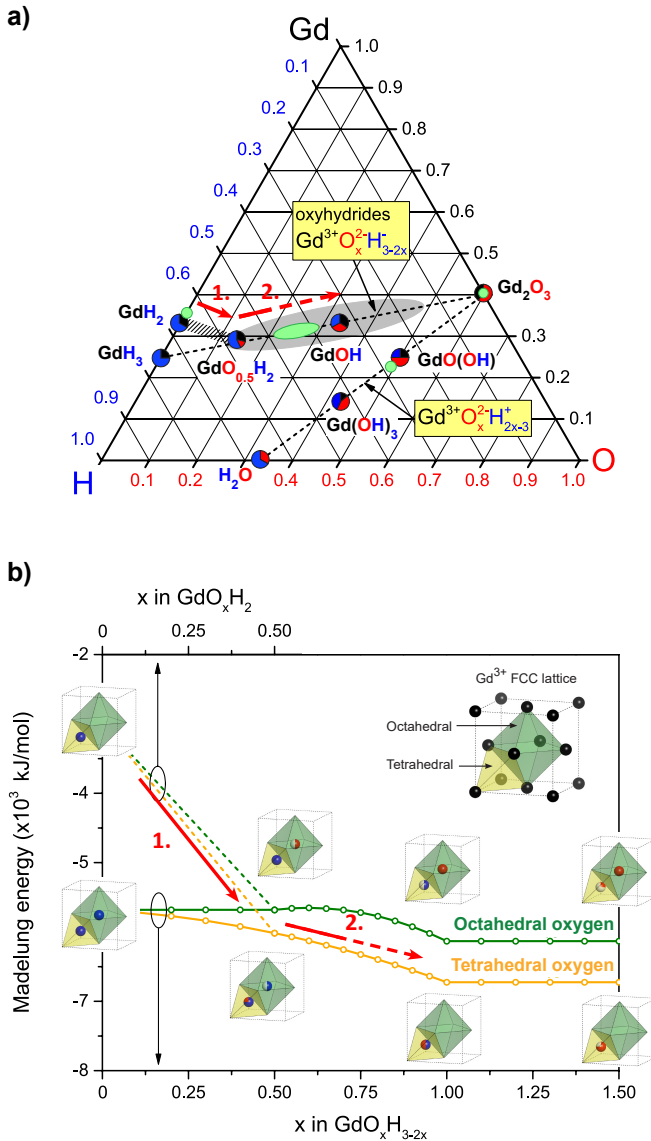


Figure 3.4: *a)* Ternary Gd–O–H chemical composition diagram. The dashed lines indicate compositions where elements are in the same charge state: M^{3+} , O^{2-} , H^- for the oxyhydride and M^{3+} , O^{2-} , H^+ for the hydroxide-like compounds. The bigger and labeled circles mark the ideal stoichiometric compounds and are coloured according to the fraction of Gd (black), O (red) and H (blue). The absolute chemical composition of the thin films studied in this work is indicated in green, where the circles are obtained from ion beam analysis while the larger ellipse is estimated from the EXAFS coordination numbers of the oxyhydride sample. *b)* Madelung energy evaluated along the oxyhydride composition line assuming oxygen incorporation into the tetrahedral (O_{tet} , yellow line) and octahedral (O_{oct} , green line) sites respectively. The inserts show the site occupation in the two cases for selected structures (GdH_3 , $\text{GdO}_{0.5}\text{H}_2$, GdOH and Gd_2O_3). In both panels the red arrows denote the hypothesised two-step pathway of air-mediated oxidation that leads to the formation of the oxyhydride from the in-situ sputtered dihydride (eq. 3.2a and 3.2b).

oxidation process is most likely of electrostatic nature. In this framework, the preferred occupation of the tetrahedral sites by the oxide ions can be explained by a difference in lattice enthalpy, i.e. the energy released when ions are brought together and spatially combined to form the compound.

Neglecting any covalency to the bonding and the finite size of the atoms, the lattice enthalpy rewrites as (minus) the coulomb energy (Madelung energy, E_M). Values of E_M for compounds that belong to the GdO_xH_2 and $\text{GdO}_x\text{H}_{3-2x}$ composition lines are shown in Fig. 3.4b. The first (dashed) line spans from GdH_2 to $\text{GdO}_{0.5}\text{H}_2$ and refers to the absolute composition of the compound as Gd is progressively oxidized and the metal to insulator transition occurs near $x = 0.5$ (eq. 3.2a). The second (full) line connects GdH_3 to Gd_2O_3 and includes the region of photochromism: $0.5 < x < 1.5$ (eq. 3.2b).

The evaluation of E_M was repeated for two cases, hereafter referred to as *octahedral oxygen* (O_{oct}) and *tetrahedral oxygen* (O_{tet}) respectively. In the O_{oct} case, the O^{2-} anions are assumed to reside in the bigger octahedral sites, while in the O_{tet} case they are placed in the tetrahedral sites and an equal number of H^- ions are displaced to octahedral positions. To focus on the contribution of the anions positioning only, the fcc lattice of the cations was kept constant and approximated for all structures to the one of the oxyhydride ($Fm\bar{3}m$, $a = 5.41\text{\AA}$).

In its simplicity, this model provides a qualitative explanation of the main driving force behind the dihydride oxidation and the preference of oxygen for the smaller tetrahedral sites. Indeed, there is not a single composition for which octahedral oxygen would lead to an energy gain with respect to a tetrahedral occupancy. This is also predicted by the so called *radius-ratio* rule, which is a direct consequence of the lattice energy and can be summarized as follows: if the radii allow, the most favourable structure for an ionic compound is the one that maximizes the coordination of the most charged constituents. 37 In our case, the Gd^{3+} is 8-fold coordinated by tetrahedral sites and only 6-fold coordinated by the octahedral ones, which moreover are further apart in space.

To understand the trends shown in Fig. 3.4b, one should consider that the Madelung energy is an infinite (but convergent) summation which runs over all the ions that make the crystal. In practice, to account for partial occupancies and for the mixed anion sublattice, it is convenient to define the average charge for each equivalent crystallographic site (tetrahedral, octahedral, etc.) and to sum over all the crystal site positions. When the anion substitution is not accompanied by a variation of the average charge in any of the crystallographic sites, E_M does not change ($x \leq 0.5$ for O_{oct} case and $x \geq 1$ for both cases). In the O_{tet} case, from $x = 0$ to $x = 1$, the absolute value of the Madelung energy increases as the charge is effectively displaced from the octahedral to the more advantageous tetrahedral sites. In contrast, for the O_{oct} case the energy gain due to a reduced anion-anion repulsion is counterbalanced by the charge displacement towards the less advantageous octahedral sites: from these two opposing contributions E_M shows a weak peak in the region $0.5 \leq x \leq 1.5$.

We stress that the results of our calculation, after correction with the repulsive (constant) term of the Born-Landé equation, match the experimental lattice energy of REH_2 (fcc) and RE_2O_3 (bixbyite) reference compounds (with $\text{RE} = \text{Y}, \text{Gd}$) within 10% of error. However, due to the challenges that thin films pose to the measurement of thermodynamic quantities, the ionic character of sputtered RE oxyhydrides has never been verified

via the Born-Haber cycle. Nevertheless, the electronegativities of the constituting atoms (Gd= 1.2, O=3.44, H= 2.20 in Pauling scale) and the insulating gap along the whole composition range point towards bound electronic states. Similar arguments have been originally raised to justify a local description in binary LaH_3 and YH_3 tri-hydrides and an extension to the ternary $\text{REO}_x\text{H}_{3-2x}$ appears well-founded. [38, 39] On this basis, the ionic picture seems to be a qualitatively valid approximation for the RE oxyhydrides. In addition, we notice that these considerations are not new in the context of mixed-anion compounds and it has already been shown that the Madelung energy is able to capture the essential features of the valence band structure of complex bismuth oxyhalide layered perovskites. [40]

3.4.2. GENERALIZED ANION-DISORDERED MODEL

The EXAFS data and the lattice energy minimization arguments of this work verify the preference of the anions for the tetrahedral sites, therefore substantiating the generalized structural model reported in Fig. 3.5. Here, the structural evolution along the GdO_xH_2 and $\text{GdO}_x\text{H}_{3-2x}$ composition lines is described in terms of an anion-disordered unit based on the fluorite fcc structure with variable lattice constant.

In this framework, air-oxidation of the as-deposited REH_2 films to the $\text{REO}_{0.5}\text{H}_2$ involves displacement of hydride ions from tetrahedral to octahedral sites as the O^{2-} ions take their place and the RE cation is oxidized from RE^{2+} to RE^{3+} (eq. 3.2a). This step also results in a well documented lattice expansion with respect to the initial dihydride. [3] Further oxygen inclusion is not accompanied by a change in oxidation states but rather requires the release of hydrogen to maintain charge neutrality (eq. 3.2b).

We notice that several groups reported ordering of the anion sub-lattice in RE oxyhydrides (RE = Y, Ln, Cr, Pr, Nd) prepared via high temperature/pressure chemical routes. [10, 41, 42] In addition, a variety of anion-ordered $\text{YO}_x\text{H}_{3-2x}$ polymorphs with different O:H ratios were hypothesized by density functional theory. [43] However, the air mediated post-oxidation of the reactively sputtered REH_2 does not proceed under thermodynamic control: as a result, oxyhydride films produced in this way (with RE= Sc, Y, Gd, Dy, Er) do not show any obvious structural variation from the cubic $Fm\bar{3}m$ symmetry. [3, 4, 44] This suggests a substantial absence of anion ordering in consequence of the initial structure of the dihydride layer as well as the insufficient energy for structural re-arrangement (via diffusion) at room temperature. Nevertheless, we cannot exclude a certain degree of anion-ordering and tetragonality. The small displacement of the oxygen ions from the exact center of the tetrahedral sites, similarly observed in the anion-ordered $\text{LaO}_x\text{H}_{3-2x}$ powders, [10] might indeed be an indication of the onset of anion ordering in the Gd oxyhydride film investigated in this work.

In any case, our simplified description provides an insightful framework whose added value is the ability to estimate the fraction of empty interstitial sites as a function of the H:O ratio along the $\text{REO}_x\text{H}_{3-2x}$ oxyhydride composition line. In the region of H-rich compounds ($0 < x \leq 1$), the occupancy, g , of the octahedrals diminishes linearly from $g_{oct} = 1$ in the REH_3 to $g_{oct} = 0$ in the REOH . For O-rich compositions ($1 \leq x \leq 1.5$), the tetrahedrals get linearly depleted from $g_{tet} = 1$ in the REOH to $g_{tet} = 0.75$ in the oxide RE_2O_3 .

Taking into account that the fraction and the kind of free sites strongly influence the

ionic/electronic conductivity, and most likely the photochromic effect as well, we believe that such insight will act as a guideline for designing RE oxyhydrides with optimally tuned functional properties.

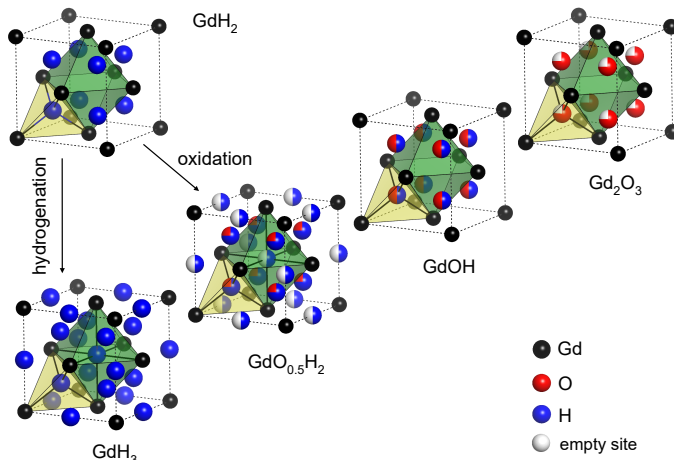


Figure 3.5: Generalized crystal structure evolution of rare-earth oxyhydrides with different H^-/RE and O^{2-}/RE ratios based on the fcc-fluorite ($Fm\bar{3}m$) structure motif. Anion sublattice disorder is visualized by multicolored spheres in terms of partial occupancy of tetrahedral (yellow polygon) and octahedral (green polygon) sites. The arrows indicate metal-insulator transitions. Figure adapted from *Cornelius et al., JPCL, (2019)*.^[4]

3.5. CONCLUSIONS

Multianion compounds are a largely unexplored class of widely tunable functional materials. In this context, RE based oxyhydrides stand out because of their unique photochromic properties and the possibility of synthesizing them via air-oxidation of reactively sputtered RE dihydride thin films.

In this work we investigated the local structure of various Gd–O–H compounds, whose increasing oxygen content is reflected by consistent trends of decreasing refractive index and increasing energy gap, Gd–O EXAFS coordination number and XANES edge position.

The EXAFS analysis presented here shows that the oxygen substitutes for hydrogen at the tetrahedral interstitial sites of the fcc Gd lattice.

Calculation of the Madelung Energy suggests that the preference of the oxide ions for the tetrahedral sites is related to a favourable electrostatics as compared to the octahedral occupancy. Furthermore, we identify in the lattice energy the main driving force for the oxyhydride formation by air-oxidation of dihydride films.

Still, much remains unknown about the degree of anion ordering, the hypothesized H^- conductivity, and the physical mechanism behind the photochromic effect of the RE oxyhydrides. The structural insight provided here may serve as valuable starting point for further experimental and computational work.

REFERENCES

- [1] H. Kageyama, K. Hayashi, K. Maeda, J. P. Attfield, Z. Hiroi, J. M. Rondinelli, and K. R. Poeppelmeier, *Expanding frontiers in materials chemistry and physics with multiple anions*, [*Nat. Commun.* **9**, 772 \(2018\)](#).
- [2] Y. Kobayashi, O. Hernandez, C. Tassel, and H. Kageyama, *New chemistry of transition metal oxyhydrides*, [*Sci. Technol. Adv. Mater.* **18**, 905 \(2017\)](#).
- [3] F. Nafezarefi, H. Schreuders, B. Dam, and S. Cornelius, *Photochromism of rare-earth metal-oxy-hydrides*, [*Appl. Phys. Lett.* **111**, 103903 \(2017\)](#).
- [4] S. Cornelius, G. Colombi, F. Nafezarefi, H. Schreuders, R. Heller, F. Munnik, and B. Dam, *Oxyhydride nature of rare-earth-based photochromic thin films*, [*The Journal of Physical Chemistry Letters* **10**, 1342 \(2019\)](#).
- [5] T. Mongstad, C. Platzter-Björkman, J. P. Maehlen, L. P. Mooij, Y. Pivak, B. Dam, E. S. Marstein, B. C. Hauback, and S. Z. Karazhanov, *A new thin film photochromic material: Oxygen-containing yttrium hydride*, [*Sol. Energy Mater. Sol. Cells* **95**, 3596 \(2011\)](#).
- [6] C. C. You, T. Mongstad, J. P. Maehlen, and S. Karazhanov, *Engineering of the band gap and optical properties of thin films of yttrium hydride*, [*Appl. Phys. Lett.* **105**, 031910 \(2014\)](#).
- [7] C. C. You, T. Mongstad, E. S. Marstein, and S. Z. Karazhanov, *The dependence of structural, electrical and optical properties on the composition of photochromic yttrium oxyhydride thin films*, [*Materialia* **6**, 100307 \(2019\)](#).
- [8] J. Montero, F. Martinsen, M. Lelis, S. Karazhanov, B. Hauback, and E. Marstein, *Preparation of yttrium hydride-based photochromic films by reactive magnetron sputtering*, [*Sol. Energy Mater. Sol. Cells* **177**, 106 \(2018\)](#).
- [9] F. Nafezarefi, S. Cornelius, J. Nijskens, H. Schreuders, and B. Dam, *Effect of the addition of zirconium on the photochromic properties of yttrium oxy-hydride*, [*Sol. Energy Mater. Sol. Cells* **200**, 109923 \(2019\)](#).
- [10] K. Fukui, S. Iimura, T. Tada, S. Fujitsu, M. Sasase, H. Tamatsukuri, T. Honda, K. Ikeda, T. Otomo, and H. Hosono, *Characteristic fast H^- ion conduction in oxygen-substituted lanthanum hydride*, [*Nat. Commun.* **10**, 2578 \(2019\)](#).
- [11] G. Kobayashi, Y. Hinuma, S. Matsuoka, A. Watanabe, M. Iqbal, M. Hirayama, M. Yonemura, T. Kamiyama, I. Tanaka, and R. Kanno, *Pure H^- conduction in oxyhydrides*, [*Science* **351**, 1314 \(2016\)](#).
- [12] A. Watanabe, G. Kobayashi, N. Matsui, M. Yonemura, A. Kubota, K. Suzuki, M. Hirayama, and R. Kanno, *Ambient pressure synthesis and H^- conductivity of $LaSrLiH_2O_2$* , [*Electrochemistry* **85**, 88 \(2017\)](#).

- [13] N. Matsui, G. Kobayashi, K. Suzuki, A. Watanabe, A. Kubota, Y. Iwasaki, M. Yonemura, M. Hirayama, and R. Kanno, *Ambient pressure synthesis of La_2LiHO_3 as a solid electrolyte for a hydrogen electrochemical cell*, [*Journal of the American Ceramic Society* **102**, 3228 \(2019\)](#).
- [14] Y. Iwasaki, N. Matsui, K. Suzuki, Y. Hinuma, M. Yonemura, G. Kobayashi, M. Hirayama, I. Tanaka, and R. Kanno, *Synthesis, crystal structure, and ionic conductivity of hydride ion-conducting Ln_2LiHO_3 ($\text{Ln} = \text{La}, \text{Pr}, \text{Nd}$) oxyhydrides*, [*J. Mater. Chem. A* **6**, 23457 \(2018\)](#).
- [15] J. Montero and S. Z. Karazhanov, *Spectroscopic ellipsometry and microstructure characterization of photochromic oxygen-containing yttrium hydride thin films*, [*Phys Status Solidi A* **215**, 1701039 \(2018\)](#).
- [16] J. Montero, F. A. Martinsen, M. García-Tecedor, S. Z. Karazhanov, D. Maestre, B. Hauback, and E. S. Marstein, *Photochromic mechanism in oxygen-containing yttrium hydride thin films: An optical perspective*, [*Phys. Rev. B* **95**, 201301 \(2017\)](#).
- [17] C. V. Chandran, H. Schreuders, B. Dam, J. W. G. Janssen, J. Bart, A. P. M. Kentgens, and P. J. M. van Bentum, *Solid state nmr studies of the photochromic effects of thin films of oxygen containing yttrium hydride*, [*J. Phys. Chem. C* **118**, 22935 \(2014\)](#).
- [18] A. T. M. van Gogh, D. G. Nagengast, E. S. Kooij, N. J. Koeman, J. H. Rector, R. Griessen, C. F. J. Flipse, and R. J. J. G. A. M. Smeets, *Structural, electrical, and optical properties of $\text{La}_{1-z}\text{Y}_z\text{H}_x$ switchable mirrors*, [*Phys. Rev. B* **63**, 195105 \(2001\)](#).
- [19] R. Gremaud, M. Slaman, H. Schreuders, B. Dam, and R. Griessen, *An optical method to determine the thermodynamics of hydrogen absorption and desorption in metals*, [*Appl. Phys. Lett.* **91**, 231916 \(2007\)](#).
- [20] J. Tauc, R. Grigorovici, and A. Vancu, *Optical properties and electronic structure of amorphous germanium*, [*physica status solidi \(b\)* **15**, 627 \(1966\)](#).
- [21] M. Cesaria, A. P. Caricato, and M. Martino, *Realistic absorption coefficient of ultrathin films*, [*J. Opt.* **14**, 105701 \(2012\)](#).
- [22] American Society for Testing and Materials (ASTM), [*Terrestrial reference spectra for photovoltaic performance evaluation, astm g173-03, global tilt*](#), Online; accessed 02-Jan-2022.
- [23] C. H. Booth and F. Bridges, *Improved Self-Absorption Correction for Fluorescence Measurements of Extended X-Ray Absorption Fine-Structure*, [*Phys. Scr.* **115**, 202 \(2005\)](#).
- [24] J. J. Rehr, J. J. Kas, M. P. Prange, A. P. Sorini, Y. Takimoto, and F. D. Vila, *Ab initio theory and calculations of x-ray spectra*, [*C. R. Phys.* **10**, 548 \(2009\)](#).
- [25] J. J. Rehr, J. J. Kas, F. D. Vila, M. P. Prange, and K. Jorissen, *Parameter-free calculations of x-ray spectra with FEFF9*, [*Phys. Chem. Chem. Phys.* **12**, 5503 \(2010\)](#).

- [26] D. E. Sayers, E. A. Stern, and F. W. Lytle, *New technique for investigating noncrystalline structures: Fourier analysis of the extended x-ray-absorption fine structure*, *Phys. Rev Lett.* **27**, 1204 (1971).
- [27] E. A. Stern, D. E. Sayers, and F. W. Lytle, *Extended x-ray-absorption fine-structure technique. III. determination of physical parameters*, *Phys. Rev. B* **11**, 4836 (1975).
- [28] K. V. Klementev, *K. V. Klementiev, VIPER, freeware*, *J. Phys. D Appl. Phys.* **34**, 209 (2001).
- [29] K. Momma and F. Izumi, *VESTA 3 for three-dimensional visualization of crystal, volumetric and morphology data*, *J. Appl. Crystallogr.* **44**, 1272 (2011).
- [30] M. Sakai, T. Kontani, O. Nakamura, K. Takeyama, Y. Uwatoko, Y. Obi, and K. Takanashi, *Electrical transport and optical properties of hydrogen-deficient YH_2 films*, *Jpn. J. Appl. Phys.* **43**, 681 (2004).
- [31] O. Stenzel, *The Physics of Thin Film Optical Spectra* (Springer, 2005) pp. 107–124.
- [32] T. Broux, H. Ubukata, C. J. Pickard, F. Takeiri, G. Kobayashi, S. Kawaguchi, M. Yone-mura, Y. Goto, C. Tassel, and H. Kageyama, *High-Pressure Polymorphs of LaHO with Anion Coordination*, *J. Am. Chem. Soc.* **141**, 8717 (2019).
- [33] D. G. Nagengast, J. W. J. Kerssemakers, A. T. M. van Gogh, B. Dam, and R. Griessen, *Epitaxial switchable yttrium-hydride mirrors*, *Appl. Phys. Lett.* **75**, 1724 (1999).
- [34] Adachi, Gin-ya, and N. Imanaka, *The binary rare earth oxides*, *Chem. Rev.* **98**, 1479 (1998).
- [35] M. Zinkevich, *Thermodynamics of rare earth sesquioxides*, *Progress in Materials Science* **52**, 597 (2007).
- [36] M. Borowski, *Size determination of small Cu-clusters by EXAFS*, *J. Phys. IV France* **7**, 259 (1997).
- [37] A. Michmerhuizen, K. Rose, W. Annankra, V. Griend, and D. A. *Radius Ratio Rule Rescue*, *J. Chem. Educ.* **94** (2017), <https://doi.org/10.1021/acs.jchemed.6b00970>.
- [38] R. Eder, H. F. Pen, and G. A. Sawatzky, *Kondo-lattice-like effects of hydrogen in transition metals*, *Phys. Rev. B* **56**, 10115 (1997).
- [39] K. K. Ng, F. C. Zhang, V. I. Anisimov, and T. M. Rice, *Theory for metal hydrides with switchable optical properties*, *Phys. Rev. B* **59**, 5398 (1999).
- [40] D. Kato, K. Hongo, R. Maezono, M. Higashi, H. Kunioku, M. Yabuuchi, H. Suzuki, H. Okajima, C. Zhong, K. Nakano, R. Abe, and H. Kageyama, *Valence band engineering of layered bismuth oxyhalides toward stable visible-light water splitting: Madelung site potential analysis*, *J. Am. Chem. Soc.* **139**, 18725 (2017).
- [41] N. Zapp, H. Auer, and H. Kohlmann, *YHO, an air-stable ionic hydride*, *Inorganic Chemistry* **58**, 14635 (2019).

- [42] H. Ubukata, T. Broux, F. Takeiri, K. Shitara, H. Yamashita, A. Kuwabara, G. Kobayashi, and H. Kageyama, *Hydride conductivity in an anion-ordered fluorite structure LnHO with an enlarged bottleneck*, *Chem. Mater.* **31**, 7360 (2019).
- [43] A. Pishtshev, E. Strugovshchikov, and S. Karazhanov, *Conceptual design of yttrium oxyhydrides: Phase diagram, structure, and properties*, *Crystal Growth and Design* **19**, 2574 (2019).
- [44] J. P. Maehlen, T. T. Mongstad, C. C. You, and S. Karazhanov, *Lattice contraction in photochromic yttrium hydride*, *J. Alloys Compd.* **580**, S119 (2013).

APPENDIX

3.A. XANES AND EDGE POSITION

Figure 3.A.1 reports the background subtracted and normalized XAS data. An enlargement over the XANES region is given in Figure 3.A.2. Notably, the edge position shifts towards higher energies upon progressive oxidation of the Gd atoms; i.e. from Gd metal to dihydride to oxide to hydroxide (Figure 3.A.3). Gd metal, dihydrides, oxyhydride and hydroxide samples have been measured on the EXAFS line bending-magnet (BM) n.26 while the Gd oxide sample was measured on the line BM n.14.

3

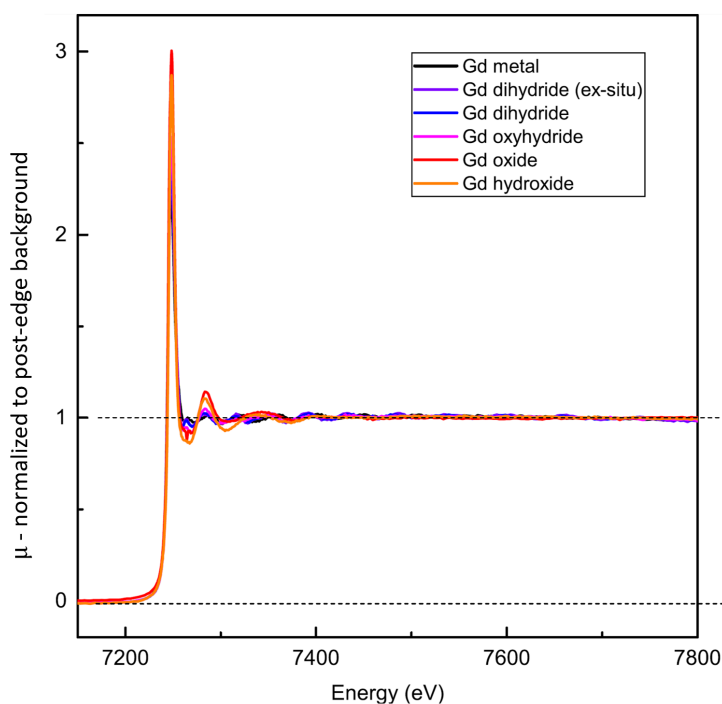


Figure 3.A.1: XAS data of Gd–O–H compounds studied in this work after pre-edge background subtraction and normalization to the post-edge background.

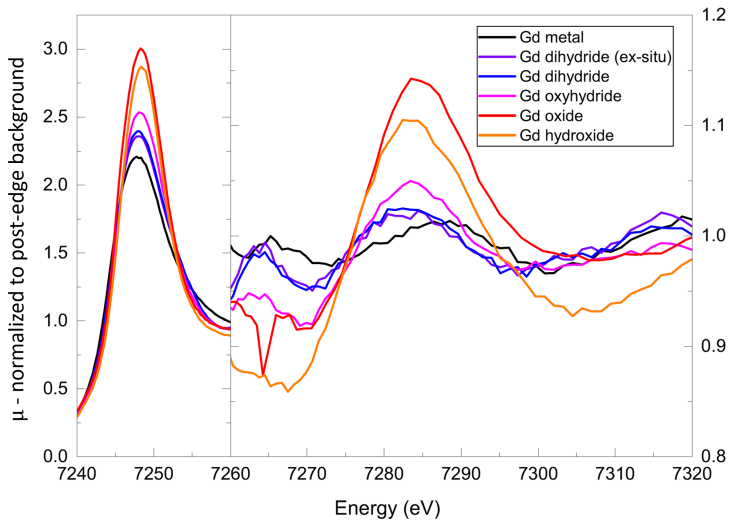


Figure 3.A.2: Zoom of Fig. 3.A.1 showing the white line and first post-edge oscillation.

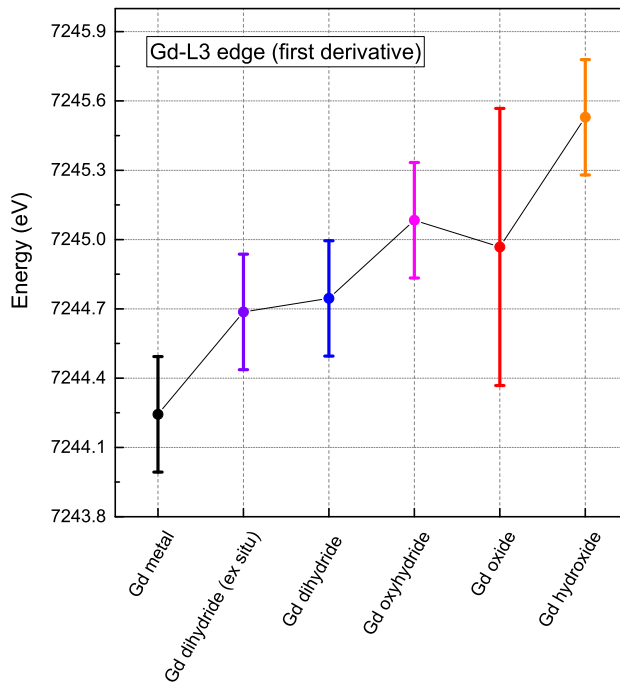


Figure 3.A.3: XANES edge position of Gd-O-H compounds determined using the first derivative method.

3.B. EXAFS

3.B.1. EXAFS THEORY

$$\chi(k) = S_0^2 \sum_j \frac{N_j}{kr_j^2} f_j(k, r_j) e^{-2\sigma_j^2 k^2} e^{-2r_j/\lambda_j(k)} \sin(2kr_j + \delta_j(k)) \quad (3.3)$$

In the EXAFS equation (eq. 3.3), the coordination environment of the central atom(s) is described as the summation of j scattering paths, where all equal atoms (i.e. same atomic number and same distance from the central absorber) are grouped into a single shell.

Upon X-ray absorption, a photoelectron is emitted from a resonant atom and scatters with the local environment of the central absorber, giving rise to interference oscillations in the absorption spectra. The sinusoidal term $\sin(2kr_j + \delta_j(k))$ provides a direct connection between their frequency in k -space and the absorber-backscatterer distance, r_j . As intuition would suggest, the strength of the EXAFS signal of each shell scales linearly with the corresponding number of atoms, N_j . Similarly, it is easily understood that a disordered environment and the inability of the photoelectron to probe long distances lead to a reduction of the signal, as reflected by the two damping exponentials. The first one depends on the EXAFS Debye-Waller factor, σ_j , which represents the variance of the distance for the given j shell and is therefore a measure of the local disorder at the given temperature. The second exponential scales with the photoelectron mean free path, $\lambda_j(k)$, therefore accounting for the losses arising from extrinsic inelastic effects during the propagation of the photoelectron. In contrast, intrinsic inelastic effects such as the excitation of the passive electrons (shake-up and shake-off processes) are included through the multiplying factor $S_0 \leq 1$, which effectively describes a reduction in the coherent signal. Finally, the scattering amplitude function, $f_j(k, r_j)$, and the phase shift, δ , are complex functions whose origin lies in the propagation in space of the photoelectron and its interaction with the local environment.

Notably, $f_j(k, r_j)$, δ and $\lambda_j(k)$ strongly depend on the composition and symmetry of the material but are only weakly influenced by the exact coordination and distances; therefore they are calculated ab-initio starting by ideal structure models as described in section III.C.

3.B.2. EXAFS SELF ABSORPTION

Eq. 3.3 is derived under the assumption that the emitted photoelectron is only scattered by the local environment and does not undergo any further processes of absorption while propagating through the material. This is not always true and, as a result, the fluorescence intensity emitted within the solid angle of the detector, Ω , is not simply proportional to the absorption cross section, $\mu(E)$ but is also modulated by $g(E)$, a second function of the photoelectron energy, E . [1, 2]

$$I_F \propto \mu(E) g(E) \quad (3.4)$$

$$g(E) \propto \int_{\Omega} \text{csc}(\alpha) \left(\frac{1 - \exp(-f(\alpha, \beta, E, E_F)t)}{f(\alpha, \beta, E, E_F)} \right) d\Omega \quad (3.5)$$

The function $g(E)$ depends in turn on the thickness of the sample, t , and on the function

$$f(\alpha, \beta, E, E_F) = \text{csc}(\alpha)\mu(E) + \text{csc}(\beta)\mu(E_F) \quad (3.6)$$

whose value reflects the probability of absorbing the X-ray beam entering into the material at angle α and the fluorescence photons (of energy E_F) emitted at angle β towards the detector.

Notably, eq. 3.5 simplifies under two sets of specific conditions often referred as dilute-thick regime ($ft \gg 1$) and dense-thin regime ($ft \ll 1$) respectively. In the latter case, the first order expansion of the exponential shows how $g(E)$ reduces to an energy-independent scale factor. Figure 3.B.1 shows a map versus entry and exit angles of ft . In the calculation, an average film thickness of 150 nm is used and the Gd cross section from NIST, μ_{Gd} , is evaluated for an incoming energy ($E = 7250$ eV) just after the L3-edge and for an emitted fluorescence corresponding to the $Gd - L_{\alpha}$ ($E_F = 6050$ eV).

Given the geometrical configuration adopted in this work ($\alpha \sim 35^\circ$ and $\beta \sim 60^\circ$), we estimate to be in the dense-thin limit, therefore the measured fluorescence is linearly dependent on the absorption cross section and no further correction is made during data analysis.

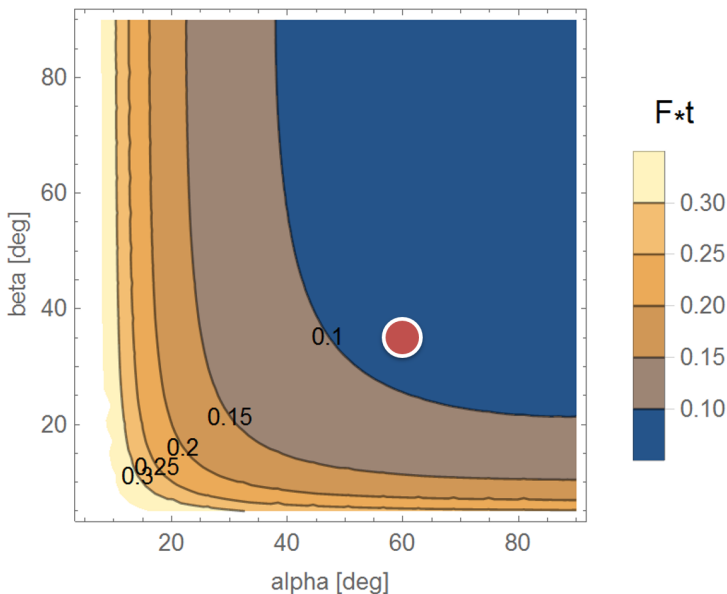


Figure 3.B.1: Estimated value of the function $f(\alpha, \beta, E, E_F)t = (\csc(\alpha)\mu_{Gd}(E) + \csc(\beta)\mu_{Gd}(E_F))t$ mapped versus entry, α , and exit, β , angles. A film thickness of 150 nm is used and the Gd cross section from NIST, μ_{Gd} , is evaluated for an incoming energy ($E = 7250$ eV) just after the L3-edge and for an emitted fluorescence corresponding to the $Gd - L_{\alpha}$ ($E_F = 6050$ eV). The red circle represents the geometrical configuration adopted in this work.

3.B.3. ADDITIONAL DETAILS ON EXAFS DATA ANALYSIS

In case of the metallic samples (Gd metal and dihydrides), low noise EXAFS data were collected until 12 \AA^{-1} . The EXAFS data of the semiconducting thin films (Gd oxyhydride, hydroxide and oxide) were limited to 10 \AA^{-1} due to the reduced signal to noise ratio. The fitting was done up to the 2^{nd} shell and the contribution of H was neglected because

insignificant compared to that of the O atoms.

A positive value of ν is essential for a stable fitting and said guideline was employed when choosing the number of paths included in the model. For the same reason, the number of free variables was reduced constraining the energy shift to a unique value for each spectra.

The FEFF9 code has been used to calculate the functions $f_j(k, r_j)$, δ and $\lambda_j(k)$ on the basis of the phase and lattice parameters inferred from XRD (Table I).

3

Gd oxyhydride

Constraining the distances according to fcc symmetry led to poor fitting of the experimental data. Most likely, a certain degree of distortion is present in analogy to the bixbyte oxide and to the anion-ordered oxyhydride powders.^{[3][4]} Possibly, such distortion is also responsible for the fact that the Gd–Gd shell appears slightly contracted with respect to the distance of the bulk dihydride, even though the XRD shows an overall expansion of the unit cell. However, we point out that the tail of the Gd–Gd shell partially overlaps with several paths of MS not accounted in the fitting model, therefore the distance derived by EXAFS might be affected by a significant systematic error.

Gd oxide and hydroxide

These two compounds have been measured at room temperature. Nevertheless, we do not expect that a measure at low temperature would significantly improve the quality of the EXAFS data because it is the site disorder, and not the active phonon modes, the main source of signal dumping. As a matter of fact, the low-symmetry structures of bixbyte oxide and monoclinic oxyhydroxide are characterized by a spread in the Gd–O bond distances of 0.1 Å and 0.3 Å respectively.

3.B.4. GD OXYHYDRIDE COMPOSITION FROM EXAFS COORDINATION NUMBERS

The composition of the oxyhydride is estimated from the EXAFS coordination numbers with the following reasoning:

1. The oxyhydride has composition described by the general formula $\text{GdO}_x\text{H}_{3-2x}$.^[5]
2. The value of x can be inferred from the coordination number of the oxygen shell. In each unit cell there are 4 Gd atoms and 8 tetrahedral interstitial. The number of tetrahedral oxygen per unit cell corresponds to the EXAFS oxygen coordination number ($N_{\text{Gd-O}\#1} = 2.5(2)$). This is visually shown in Figure [3.B.2](#).

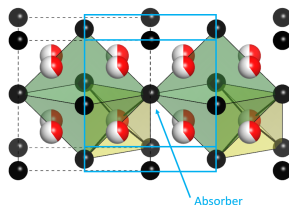


Figure 3.B.2: fcc unit cell centered on a Gd absorber.

Therefore: $x = \frac{2.5}{4} = 0.63 \rightarrow \text{GdO}_{0.63}\text{H}_{1.74}$

3. In truth, the EXAFS coordination of the Gd-Gd shell ($N_{\text{Gd-Gd}\#1} = 9.3(5)$ instead of 12) implies that some Gd is missing in the highly defective structure of the sputtered film. On average, each unit cell contains therefore only $4 * (9.3/12)$ Gd atoms.

Therefore: $x = \frac{2.5}{4 * (9.3/12)} = 0.77 \rightarrow \text{GdO}_{0.77}\text{H}_{1.46}$

4. The uncertainty on x is estimated from the error of the EXAFS coordination numbers ($\delta N_{\text{Gd-O}\#1} = 0.2$ and $\delta N_{\text{Gd-Gd}\#2} = 0.5$) using the two extreme cases (x_- and x_+):

$$x_- = \frac{2.5-0.2}{4 * ((9.3+0.5)/12)} = 0.72 \quad x_+ = \frac{2.5+0.2}{4 * ((9.3-0.5)/12)} = 0.93$$

5. Therefore we propose $x = (0.8 \pm 0.1) \rightarrow \text{GdO}_{0.8}\text{H}_{1.4}$

3.C. X-RAY DIFFRACTION REFERENCE PATTERNS

Phase	ICDD-PDF n.	unit cell
<i>hcp-Gd</i> ($P6_3/mmc$)	#00-02-0864	$a = 3.629\text{\AA}$ $c = 5.760\text{\AA}$
<i>fcc-GdH₂</i> ($Fm\bar{3}m$)	#00-50-1107	$a = 5.303\text{\AA}$
<i>bixbyite-Gd₂O₃</i> ($Ia\bar{3}$)	#00-12-0797	$a = 10.831\text{\AA}$
<i>monocl.-Gd₂O₃</i> ($C2/2$)	#00-42-1465	$a = 14.095\text{\AA}$ $b = 3.5765\text{\AA}$ $c = 8.7692\text{\AA}$ $\beta = 100.08^\circ$
<i>hcp-Gd(OH)₃</i> ($P6_3/m$)	#00-83-2037	$a = 6.329\text{\AA}$ $c = 3.631\text{\AA}$
<i>monocl.-GdO(OH)</i> ($P2_1/m$)	mp-625147*	$a = 4.391\text{\AA}$ $b = 3.746\text{\AA}$ $c = 6.132\text{\AA}$ $\beta = 109.28^\circ$

Table 3.C.1: Reference patterns and associated lattice constants, as taken by the ICDD-PDF database, used to identify the phase of the sputtered Gd-O-H thin films. *Data from Materials-Project. [6](#) On the ICDD-PDF database no monoclinic GdO(OH) is reported. However most of the lanthanide elements form monoclinic oxyhydroxide (e.g. Ln #00-19-0656, Er #00-18-0510, Tb #00-70-2040).

REFERENCES

- [1] C. H. Booth and F. Bridges, *Improved Self-Absorption Correction for Fluorescence Measurements of Extended X-Ray Absorption Fine-Structure*, [Phys. Scr. **115**, 202 \(2005\)](#).
- [2] G. Bunker, *Introduction to XAFS: A Practical Guide to X-ray Absorption* (Cambridge University Press, 2010).
- [3] K. Fukui, S. Iimura, T. Tada, S. Fujitsu, M. Sasase, H. Tamatsukuri, T. Honda, K. Ikeda, T. Otomo, and H. Hosono, *Characteristic fast H⁻ ion conduction in oxygen-substituted lanthanum hydride*, [Nat. Commun. **10**, 2578 \(2019\)](#).
- [4] T. Broux, H. Ubukata, C. J. Pickard, F. Takeiri, G. Kobayashi, S. Kawaguchi, M. Yone-mura, Y. Goto, C. Tassel, and H. Kageyama, *High-Pressure Polymorphs of LaHO with Anion Coordination*, [J. Am. Chem. Soc. **141**, 8717 \(2019\)](#).
- [5] S. Cornelius, G. Colombi, F. Nafezarefi, H. Schreuders, R. Heller, F. Munnik, and B. Dam, *Oxyhydride nature of rare-earth-based photochromic thin films*, [The Journal of Physical Chemistry Letters **10**, 1342 \(2019\)](#).
- [6] A. Jain, S. P. Ong, G. Hautier, W. Chen, W. D. Richards, S. Dacek, S. Cholia, D. Gunter, D. Skinner, G. Ceder, and K. a. Persson, *The Materials Project: A materials genome approach to accelerating materials innovation*, [APL Materials **1**, 011002 \(2013\)](#).

4

MODELLING ANION-DISORDER: ENERGY, METASTABILITY AND OPTICAL PROPERTIES OF $\text{REO}_x\text{H}_{3-2x}$ OXYHYDRIDES

*No man was ever yet a great poet, without
being at the same time a profound philosopher.*

Samuel Taylor Coleridge, Biographia Literaria (1817)

Here a set of special quasirandom structures (SQS) is introduced to model the influence of the O:H ratio on the energy, metastability, and optical properties of Y and La anion-disordered $\text{REO}_x\text{H}_{3-2x}$ oxyhydrides. A comparison with anion-ordered polymorphs of the same composition shows the comparable energy of the anion-disordered phase, although its metastability rather depends on the cation size, which determines the maximum H content above which the CaF_2 -type structure itself becomes unstable. To overcome the accuracy limitations of classical DFT, the modified Becke-Johnson (mBJ) scheme is employed in the study of the electronic properties. We show that major differences occur between H-rich and O-rich RE oxyhydrides, as the octahedral H^- present for $x < 1$ form electronic states at the top of the valence band, which reduce the energy bandgap and dominate the electronic transitions at lower energies, thus increasing the refractive index of the material in the VIS-nIR spectral range. Comparing the DFT results to experimental data on photochromic Y oxyhydride films, reinforces the hypothesis of anion-disorder in the H-rich films ($x < 1$), while it hints towards some degree of anion ordering in the O-rich ones ($x > 1$).

This chapter is an adaptation of:

G. Colombi, R. Stigter, D. Chaykina, S. Banerjee, S. W. H. Eijt, B. Dam, and G. A. de Wijs, *Energy, metastability, and optical properties of anion-disordered $\text{REO}_x\text{H}_{3-2x}$ ($\text{RE}=\text{Y},\text{La}$) oxyhydrides: A computational study*, Phys. Rev. B **105**, 5 (2022).

4.1. INTRODUCTION

Rare-earth (RE) oxyhydrides, $\text{REO}_x\text{H}_{3-2x}$, are gaining attention in view of their fast hydride ion conductivity,^[1] and peculiar optoelectronic behaviour (i.e., large reversible photo-conductivity and photochromism),^[2-4] properties that hold promises for electrochemical devices, such as solid-state batteries and fuel cells,^[5] as well as smart coatings for windows and sensors.

RE oxyhydrides are *mixed-anion* compounds, a class of inorganic materials which offers unprecedented degrees of freedom in the design of functional properties thanks to the broad spectrum of different anion characteristics (e.g., electronegativity, polarizability, ionic radii) and the possibility to tune the anion-ratio within a wide compositional interval.^[6,7] From a structural perspective, this large compositional flexibility is reflected in a variety of stable and metastable phases. In addition, given the comparable ionic radii of O^{2-} (140 pm) and H^- (120-150 pm),^[6] in RE oxyhydrides the anions can either order periodically (anion-order), or randomly share the same anion-sites available within the RE cation lattice (anion-disorder).^[8,9]

While many anion-ordered polymorphs were reported for stoichiometric REOH ($x = 1$),^[1,9-11] it is thought that anion-disorder is energetically favourable in the case of smaller cations,^[8,12] and outside this 1:1:1 composition.^[9]

The anion-disordered phase resembles the structure of CaF_2 , with a face-centred cubic^[3,12] or tetragonal^[9] cation lattice and distinct tetrahedral and additional (less stable) octahedral anion-sites. As visualized in Fig. 4.1, the occupation of the anion-sites depends on the composition: for $x \geq 1$, there are enough tetrahedral sites to host all anions, while for $x < 1$ the tetrahedral sites are completely occupied with O^{2-} and H^- and the remaining fraction of H^- sits in the octahedral sites.^[13] Notably, high hydride conductivities are observed in H-rich ($x < 1$) $\text{LaO}_x\text{H}_{3-2x}$ with anion-disordered structure,^[1] an aspect clarified by the same authors in a second publication.^[9] Similarly, Sc, Y, and Gd oxyhydride thin films show stronger photochromism for Y:O:H ratios far from the 1:1:1 composition.^[4] The anion-disordered phase in the H-rich range of compositions is therefore of primary importance for applications in electrochemical devices and optics.

From the point of view of anion dynamics, the link between functional properties and the underlying composition/structure has been subject of speculation. It is thought that the energy landscape for H^- site hopping influences the kinetics of hydride conduction,^[12] as well as the speed of the photochromic effect.^[4] Direct information concerning trajectories and rates of H^- hopping are however difficult to obtain; insight is scattered, and only based on 1:1:1 REOH. For this composition, Ubukata et al.^[12] proposed that H^- migrates preferentially *via* the so-called indirect route (i.e., from tetrahedral to octahedral site) passing through a triangular bottleneck whose size defines the activation energy of the hop. This barrier is typically found on the order of 1-1.3 eV for $P4/nmm$ LaOH and NdOH anion-ordered oxyhydrides.^[1,12,14] Conversely, anion-disorder was shown to suppress H^- mobility in REOH.^[12] The apparent contradiction with the high H^- conductivity of anion-disordered H-rich La oxyhydrides indicates that the properties of the 1:1:1 REOH case do not necessarily reflect those of $\text{REO}_x\text{H}_{3-2x}$ with varying O:H composition. For example, one might expect different migration pathways for H-rich oxyhydrides, such as the direct octahedral to octahedral route.

From a computational perspective, anion-disorder introduces an additional level

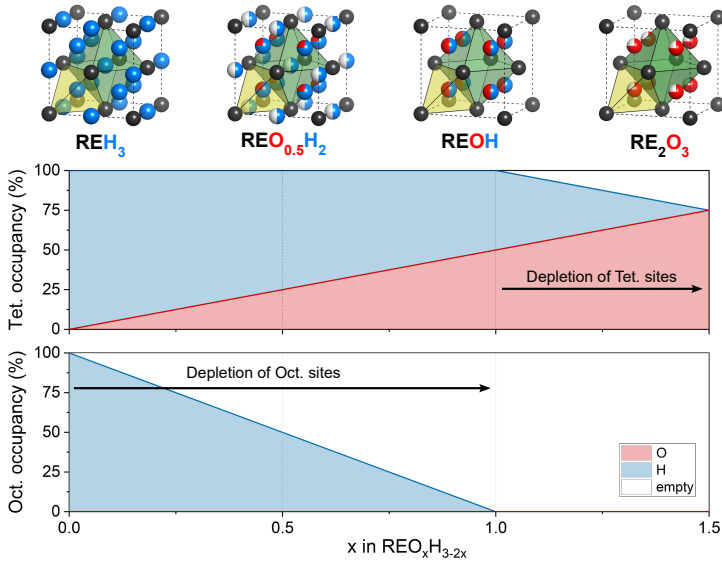


Figure 4.1: Trend upon O:H ratio of the occupation of tetrahedral (yellow polygon) and octahedral (green polygon) anion-sites in anion-disordered REO_xH_{3-2x} oxyhydrides with CaF_2 -type structure. [13] Colour scheme: RE, black; O, red; H, blue.

of complexity. A quantitative evaluation of the energy landscape for H^- hopping in anion-disordered RE oxyhydrides is still missing, as well as for the formation energy of the vacancies that might assist its diffusion. Additionally, it remains largely unclear how material properties, such as energy, phase-stability, band structure and optical absorption/refraction, depend on the O:H ratio.

To address this knowledge gap, we introduce here a set of special quasi-random structures (SQS) that, while maintaining a computationally affordable size, are able to model the disordered anion sub-lattice along the entire $REH_3-RE_2O_3$ composition line. We assess the predictive ability of the SQS approach, and discuss how the O:H ratio defines the total energy, metastability, and optical properties of Y and La anion-disordered oxyhydrides. We chose Y and La as case-studies because their (ionic) radii lie at different ends of the Lanthanoid series, and their 1:1:1 oxyhydrides have been reported as anion-disordered ion insulators (Y) and anion-ordered ion conductors (La), respectively. [8, 12]

Finally, we compare the results of this computational study to (i) the experimental phase diagrams recently proposed for Y and La oxyhydrides, [9] and (ii) to the optical data available for reactively-sputtered Y oxyhydride thin films. [3, 15, 16] In this latter case, where there is no direct information concerning the anion-sub-lattice of the material, our work reinforces the hypothesis of anion-disorder in H-rich YO_xH_{3-2x} thin films ($x < 1$), while, at the same time, it hints towards some degree of anion ordering in the O-rich ones ($x > 1$).

In Sec. 4.2 the structural model considered in this work are introduced, and the computational details explained. In sec. 4.3.1 the lattice energy of all the structures is

discussed, showing the relative stability of the anion-disordered phase in comparison to other ordered polymorphs. In Sec. 4.3.2 we address the compositional limits, in terms of O:H ratios, in which the anion-disordered phase is metastable against spontaneous rearrangement of the anion sub-lattice. In Sec. 4.3.3 we discuss the influence of the O:H ratio on the opto-electronic properties of anion-disordered Y and La oxyhydrides. Finally, In Sec. 4.4 we compare our computational results to our own experimental work on reactively sputtered thin films, and to the experimental work of Fukui *et al.* [9] on oxyhydride powders produced *via* conventional high temperature solid-state reaction.

4.2. COMPUTATIONAL DETAILS

4

Structural models While our focus is specifically on the anion-disordered oxyhydrides, in this work we compare three different sets of structures to provide a broader overview and consistently compare anion-disordered and anion-ordered structures.

The first set (Fig. 4.2a) includes anion-ordered structures experimentally reported, such as the binary REH_3 tri-hydrides ($P6_3/mmc$, $Fm\bar{3}m$) and RE_2O_3 sesquioxides ($P\bar{3}m1$, $I\bar{3}a$), and the three space groups observed for 1:1:1 Y and La oxyhydrides ($P4nmm$, $P2_1/m$, $Pnma$ [10]).

The second set (Fig. 4.2b, Fig. 4.A.1), is a group of hypothetical structures that we investigate to supplement the lack of information on anion ordering outside the stoichiometric REOH compound and the binary extremes of the $\text{REO}_x\text{H}_{3-2x}$ line. For $x \neq 0, 1, 1.5$ it is unclear *how* the anions might order inside the tetrahedral and octahedral interstitial sites available within the CaF_2 -type cation lattice. Therefore we built all schemes of anion ordering that are possible within one fcc unit cell (4 RE atoms, 8 tetrahedral anion-sites, 4 octahedral anion-site). Since we showed in our previous study that the tetrahedral sites are energetically favoured compared to the octahedral ones, and that the O^{2-} anions occupy exclusively the tetrahedral sites even in H-rich compositions, [13] these constraints were taken into account. The resulting anion-ordered structures are not yet comprehensive, as they do not survey ordering schemes extending beyond one fcc unit cell.

Finally, in the third set (Fig. 4.2c, Fig. 4.A.2-4.A.3) we model anion-disordered oxyhydrides as special quasi-random structures (SQS), i.e., relatively small supercells that mimic the most relevant radial correlations, and thus properties, of oxyhydrides with a perfectly random anion-sub-lattice. [17] The mcsqs code, [18] as implemented in the Alloy Theoretic Automated Toolkit, [19] was used to generate SQS for several O:H anion ratios ($x = 0.25, 0.50, 0.75, 0.875, 1, 1.25, 1.375, \text{ and } 1.5$) covering the entire $\text{REO}_x\text{H}_{3-2x}$ composition line, from REH_3 to RE_2O_3 . The same constraints as mentioned above were forced during the generation of SQS. Quantitatively, one estimates the goodness of an SQS via the so-called objective function (Table 4.A.1), which measures how well the radial correlations of the SQS match those of the ideal disordered structure. However, different physical properties converge at a different speed against the goodness of the SQS, and a qualitative discussion is better done in hindsight. In this work, we considered 3 different SQS for each O:H ratio (2 in case of $x = 0.75, 1, 1.375$) so to quantify the uncertainty ($(\text{max} - \text{min})/2$) of each of the physical quantities here reported. Hereafter, we refer to the SQS as disordered structures.

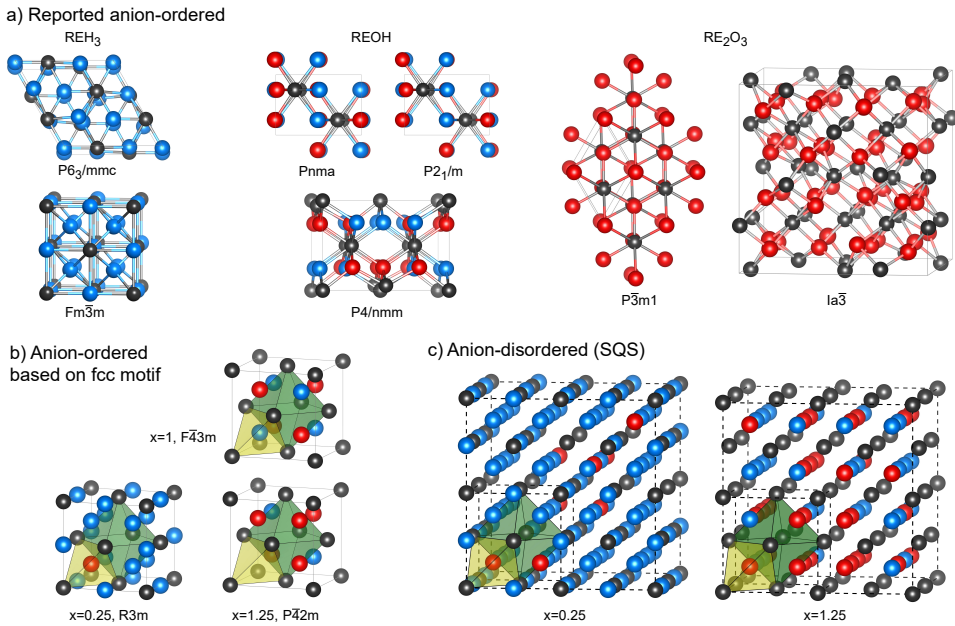


Figure 4.2: Selected examples of the structures considered in this work. Colour scheme: RE, black; O, red; H, blue. *a*) Previously reported anion-ordered compounds. This includes the binary REH₃ tri-hydride (*P6₃/mmc*, *Fm3m*) and RE₂O₃ sesquioxide (*P3m1*, *I3a*), and the 1:1:1 REOH oxyhydride (*P4/nmm*, *Pnma*, and *P2₁/m*). The structural difference between *Pnma* and *P2₁/m* is minimal, and in the figure it appears as a minor translation of the anions relative to each other. *b*) Examples of anion-ordered oxyhydrides based on the CaF₂ motif. Here, the anions preferentially occupy the tetrahedral sites (yellow polygons), while the octahedral ones (green polygons) only host the excess hydrogen for $x < 1$. In this work we considered all schemes of anion ordering that are possible within one fcc unit cell. The three structures here reported are the only ones that resulted in an energy stabilization compared to the anion-disordered lattice, in view of their particular symmetry that mitigates Coulomb repulsion between neighbouring O²⁻ anions. In *R3m*-REO_{0.25}H_{2.5} the only octahedral empty site is adjacent to the only oxygen atom; in *F43m*-REOH the anions alternate throughout the tetrahedral sites; and in *P42m*-REO_{1.25}H_{0.5} all the next-nearest neighbours of the empty tetrahedral site are oxygen anions. *c*) Examples of special-quasirandom-structures to model anion-disordered REO_xH_{3-2x} oxyhydrides.

Structural optimization and energy First-principle density functional theory (DFT) calculations are carried out with the Vienna *Ab-initio* Simulation Package (VASP).^[20, 21] Within the scheme of the projector augmented wave (PAW) method,^[22, 23] a plane-wave basis set is used and periodic boundary conditions are applied. Standard frozen core PAW potentials are used, and the H 1s, O 2s2p, Y 4s4p4d5s, and La 5p5d6s are treated as valence shells. For self consistent electronic calculations, as well as ionic relaxation runs, we employ the PBE generalized gradient approximation for the exchange-correlation functional.^[24, 25] Integrations over the Brillouin zone are performed on a Γ -centred K-mesh ($8 \times 8 \times 8$ for smaller cells and $3 \times 3 \times 3$ for SQS supercells) using a Gaussian smearing of 0.05 eV. For each structure, all cell parameters and atomic position are simultaneously optimized, reaching convergence ($\delta E < 0.1$ meV) with an overkill kinetic energy cut-off of 850 eV.

To avoid ill-defined values of absolute energy, only energy differences are considered

in this work. According to Hess's law, the formation energy (ΔH_f) is quantified by subtracting the energy of the isolated elements in their standard state ($P6_3/mmc$ -RE, O_2 , H_2), and the binding energy (ΔH_b) is quantified by subtracting the energy of the isolated atoms. Exploiting the Born-Haber cycle, the lattice energy (ΔH_L) is finally estimated as the sum of binding energy, experimental RE ionization energies,^[26] and experimental O and H electron affinities^[27] (more details in Sec. 4.B).

The Lattice energy extracted by DFT is then compared to the one predicted by the Born-Landé equation (eq. 4.2, see text). The first term of this equation, the Madelung energy, is here calculated using MADEL,^[28] an application implemented in VESTA.^[29] The code employs an Ewald summation^[30] in the Fourier space, for which the radius of the ionic sphere was chosen to be slightly smaller than the shortest interatomic distance, and the reciprocal space range was set to 6 \AA^{-1} . The convergence of the Madelung energy upon variation of both parameters was verified.

4

Optical properties To overcome the limits of GGA-DFT, modified Becke-Johnson (mBJ) exchange potentials in combination with L(S)DA-correlation have been used to compute the electronic properties of the structures previously relaxed using PBE.^[31, 32] The mBJ approach has been chosen because it yields a description of the electronic states of comparable accuracy^[32] to GW methods,^[33-36] while being computationally far less expensive and, thus, employable also for the larger SQS structures. A validation of mBJ results against G_0W_0 was carried for several anion-ordered Y oxyhydrides, confirming a good agreement along the whole YH_3 - Y_2O_3 composition line. (Fig. 4.C.1). To extract the partial electron Density-of-States (pDOS) and direct/indirect bandgaps, the same kinetic energy cut-off (850 eV) and integration parameters used for PBE-DFT were maintained during the mBJ runs.

The calculation of the complex inter-band dielectric function, $\varepsilon(\omega) = \varepsilon_1(\omega) + i\varepsilon_2(\omega)$, is performed in the independent particle approximation, neglecting local fields and accounting only for direct transitions ($|\mathbf{q}| \rightarrow 0$). In this limit, which largely represents the dielectric properties probed at room temperature by optical spectroscopy, the imaginary part $\varepsilon_2(\omega)$ reads:^[37]

$$\varepsilon_2(\omega, \hat{\mathbf{q}}) = \frac{8\pi e^2}{V} \lim_{|\mathbf{q}| \rightarrow 0} \frac{1}{|\mathbf{q}|^2} \sum_{\nu\mathbf{k}} |\langle \psi_{c,\mathbf{k}+\mathbf{q}} | \psi_{\nu,\mathbf{k}} \rangle|^2 \times \delta(E_{c,\mathbf{k}+\mathbf{q}} - E_{\nu,\mathbf{k}} - \hbar\omega) \quad (4.1)$$

where V is the volume of the unit cell, $\hat{\mathbf{q}}$ the direction of the momentum transfer, (ν, \mathbf{k}) and $(c, \mathbf{k} + \mathbf{q})$ indicate occupied (valence) and unoccupied (conduction) single-particle states, E their energy, and ψ the cell-periodic part of their wavefunctions. The real part of the dielectric function is found by Kramers-Kronig transformation of the imaginary part. To maintain analogy with the experimental data based on polycrystalline samples, in this work we report directionally-averaged (i.e., over $\hat{\mathbf{q}}$) dielectric functions $\varepsilon(\omega)$. The convergence of $\varepsilon(\omega)$ was checked with respect to energy cut-off, K-mesh, and number of computed unoccupied states. We find an optimum trade-off between accuracy (i.e., invisible differences in the scale of the figures of this paper) and computational expense for a kinetic energy cut-off of 400 eV and a total of 2000 bands. K-mesh and Gaussian smearing are maintained equal to the structural optimization runs.

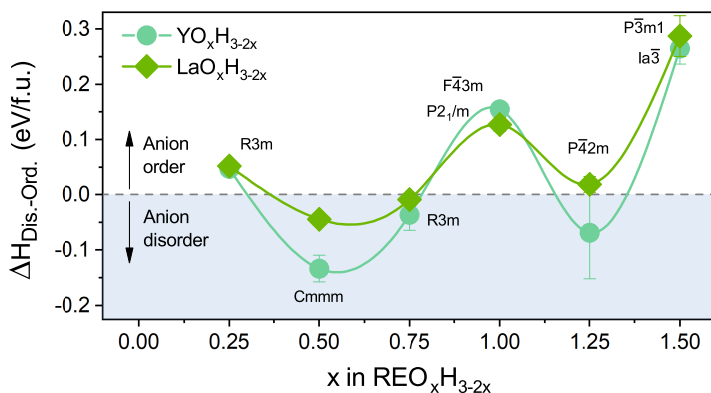


Figure 4.3: Energy difference along the $\text{REO}_x\text{H}_{3-2x}$ ($\text{RE}=\text{Y,La}$) composition line between the anion-disordered and the most stable anion-ordered structure simulated in this work. For each composition, the space group of the most stable anion-ordered structure is indicated next to the point.

4.3. RESULTS

4.3.1. ENERGY: RELATIVE STABILITY OF ANION-DISORDER

In this section we discuss the energy $\Delta H_{\text{Dis.-Ord.}}$ after relaxation, of all structures considered in this work. First, we show that anion-disorder does not lead to a large energy penalty compared to the anion-ordered polymorphs, but, in fact, within the group of structures considered in this work, is even favourable for $0.25 < x < 1$. Second, we discuss the progressive stabilization (i.e., decrease of energy) upon increasing O:H content, rationalizing this trend in terms of lattice energy. Finally, we discuss the energy of all 1:1:1 REOH structures, and compare the computational results of this study to the many YOH and LaOH polymorphs reported in the literature.

Fukui et al. [9] have proposed that RE oxyhydrides are stable in an anion-ordered structure only within a limited compositional interval around the 1:1:1 REOH composition. The results in Fig. 4.3 support this proposition, showing the energy difference between the anion-disordered structures and the most stable anion-ordered ones of same composition. At the 1:1:1 composition, we find an energy penalty for disorder of 0.16 eV/f.u. for YOH and 0.14 eV/f.u. for LaOH. In the H rich region, the trend inverts, and – among the structures considered in this work – the anion-disordered ones present the lowest energy for compositions $x = 0.5$ and $x = 0.75$. For Y oxyhydrides, that is the case also in the O-rich region, around $x = 1.25$.

Fig. 4.4a sketches the Born-Haber cycle of the oxyhydride, showing all contributions to its formation energy. The dependency of the formation energy upon the O:H ratio is shown for all structures in Figs. 4.4b (Y) and 4.4c (La). Here, the (negative) formation energy increases in magnitude upon increasing oxygen content, and – reflecting the ionic character of the oxyhydrides – it follows a trend that is almost identical for the two cations.

In an ionic compound, the lattice energy is in fact dominated by the crystal structure

¹As temperature is not included in our simulations, energy is here to be interpreted as enthalpy at 0 K.

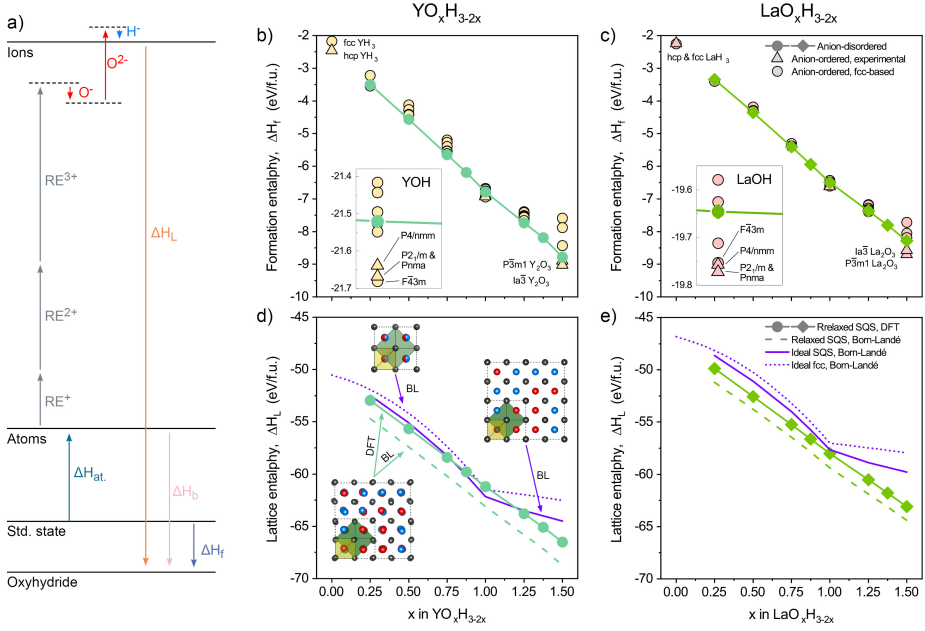


Figure 4.4: *a)* Born-Haber cycle of RE oxyhydride. The arrows are at scale for the 1:1:1 composition and indicate: atomization energy (ΔH_{at}), RE ionization energies, O and H electron affinities, oxyhydride lattice energy (ΔH_L), binding energy (ΔH_b) and formation energy (ΔH_f). *b)* and *c)* Influence of O:H ratio on the formation energy of Y and La oxyhydrides, respectively. The insets focus on the stoichiometric 1:1:1 composition. *d)* and *e)* Influence of O:H ratio on the lattice energy of Y and La anion-disordered oxyhydrides, respectively. For $x \leq 1$, the (negative) lattice energy increases mainly due to a shift of charge from the less-stable octahedral to the more-stable tetrahedral anion-sites. For $x > 1$, further stabilization results from a larger freedom for structural distortion related to the presence of empty tetrahedral sites. For comparison, the lattice energy evaluated with the Born-Landé equation is also reported for three different structural models of increasing resemblance to the real material: (i) idealized anion-disordered model based on $Fm\bar{3}m$ symmetry (dotted lines), (ii) non-relaxed SQS structures (solid lines), and (iii) relaxed SQS structures (dashed lines).

and by the oxidation state of the constituting ions, while their identity has a marginal influence. This is formalized in the Born-Landé equation: [27]

$$\Delta H_L = \frac{e^2}{4\pi\epsilon_0} \sum_{i \neq j} \frac{z_i z_j}{|r_i - r_j|} \left(1 - \frac{1}{n}\right) \quad (4.2)$$

where the i, j ions of oxidation state z are initially treated as point charges, and the resulting electrostatic energy (i.e., the Madelung energy) is subsequently corrected to account for an additional repulsion due to the finite atomic size. The identity of the ions therefore only enters in the mean Born-Landé exponent (n), which for the oxyhydrides we estimate as the weighted average of generalized Pauling's values ($n_Y \sim n_{Kr} = 10$, $n_{La} \sim n_{Xe} = 10$, $n_O \sim n_{Ne} = 7$, $n_H \sim n_{He} = 5$): [27]

$$n = \frac{n_{RE} + xn_O + (3 - 2x)n_H}{1 + x + (3 - 2x)}. \quad (4.3)$$

The lattice energy extracted from DFT of the anion-disordered Y and La oxyhydrides is reported as solid points in Fig. 4.4d and 4.4e, respectively. This energy decreases upon increasing O:H ratio, with a slope that is very similar for both Y and La oxyhydrides due to the dominance of the Madelung term over the Born-Landé correction (Fig. 4.D.1). The absolute values, instead, differ because of the different lattice parameters of Y and La oxyhydrides. Indeed, along the whole $\text{REO}_x\text{H}_{3-2x}$ composition line, we find a constant ratio $\Delta H_Y/\Delta H_{La} \sim 1.07(1)$ from DFT, in excellent agreement with the inverse ratio between lattice constants $a_{La}/a_Y \sim 1.07(1)$, and therefore in line with the $\Delta H_L \propto 1/r$ dependency expected from the Born-Landé equation.

To understand the origin of the progressive energy decrease upon increasing O:H ratio, an analysis of the Madelung energy is needed. A simplified discussion on the trend of Madelung energy along the $\text{REO}_x\text{H}_{3-2x}$ oxyhydride line can be found in our previous work. [13] There, two compositional intervals of different behaviour are identified under the approximation of an invariant fcc cation lattice and the assumption of idealized anion-sites of average valence (e.g., in REOH, all tetrahedral anion-sites are equivalently occupied by a point charge of $-1.5e$). In the first interval ($x \leq 1$), the Madelung energy decreases monotonously due to an effective displacement of charge from the octahedral anion-sites towards the more stable tetrahedral sites, leading on average to a shorter distance between positive and negative charges. In the second interval ($x > 1$), no charge displacement occurs and the Madelung energy levels off. This model, after correction with the Born-Landé factor (purple dotted lines in Fig. 4.4d and 4.4e), matches well the lattice energies extracted from DFT in the interval $x \leq 1$. It does not account, however, for the further decrease in lattice energy that occurs in the second interval ($x > 1$). We exclude that the plateau at $x > 1$ is an artefact due to the assumption of an average valency of the anion-sites, because a comparable plateau is found evaluating the lattice energy of ideal (i.e., non-relaxed) SQS structures with the Born-Landé equation (purple solid lines). In contrast, when the Born-Landé equation is used for the relaxed SQS structures, we find an excellent agreement with the slope of the lattice energy as obtained by DFT. This again verifies the ionic character of the oxyhydrides, and shows that the further energy decrease that occurs for $x > 1$ is the result of structural distortions - prominent in the O-rich interval - that lead to more stable atomic configurations.

Clearly, the freedom for structural distortions correlates with the presence of empty tetrahedral sites, which are fully occupied for $x \leq 1$, but progressively deplete for $x > 1$. It is therefore not surprising that the Y_2O_3 oxide crystallizes in the $I\bar{3}a$ -bixbyite structure, as this is a cubic superstructure where the tetrahedral empty sites order to maximize(minimize) distortion(repulsion). [38] We find the bixbyite structure to be in fact ~ 0.3 eV/f.u. lower in energy compared to the disordered counterpart. In analogy, it is expected that at 0 K other anion-ordered oxyhydride structures of low energy could be found considering ordering schemes that extend beyond the first coordination shell. In analogy, it is expected that at 0 K other anion-ordered oxyhydride structures of lower energy could be found considering ordering schemes that extend beyond the first coordination shell. However, with increasing temperature, the additional effect of configurational entropy will further stabilize the disordered limit. At the time of writing, it remains unclear if it is configurational entropy, rather than kinetic limitations during the material synthesis, the

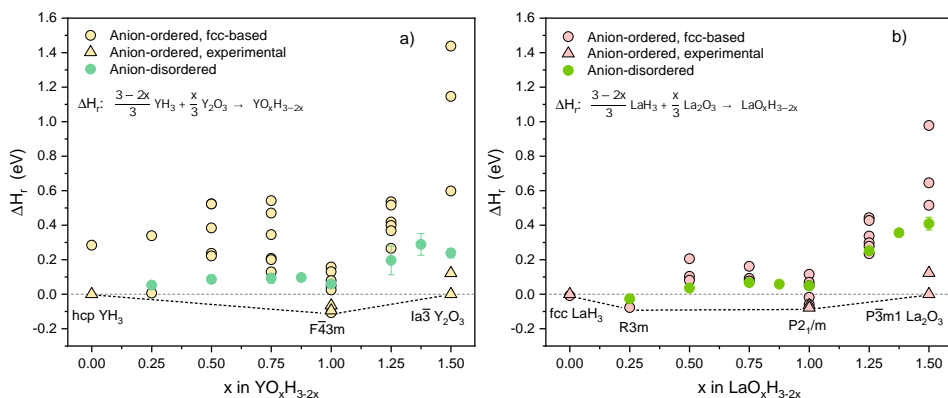


Figure 4.5: Reaction energy for the formation of (a) Y-based and (b) La-based $\text{REO}_x\text{H}_{3-2x}$ oxyhydrides starting from the REH_3 and RE_2O_3 binary precursors. The convex hull formed by the compounds of lowest energy is indicated with a dashed black line.

reason why no anion-ordered polymorphs have been experimentally reported outside the 1:1:1 REOH composition and the binary REH_3 and RE_2O_3 extremes.

In the previous paragraphs, we (i) compared the relative stability of the anion-ordered and the anion-disordered structures at parity of composition, and (ii) discussed the progressive energy decrease upon increasing O:H ratio. In the following we briefly address the question of thermodynamic stability. In general, a ternary compound is stable if its energy is lower than any stoichiometric combination of competing ternary, binary and/or elemental constituents. [39] On a plot of formation energy vs composition, this requirement geometrically manifests as a convex hull connecting all the compounds with lowest energy. For the other compound with energy above the convex hull, decomposition is energetically favourable, and they can exist at most as a metastable phase. Exploring the energetics of the entire RE–O–H ternary diagram is beyond the scope of this work, however, here we apply the reasoning of the convex hull specifically to the $\text{REO}_x\text{H}_{3-2x}$ composition line. In Fig. 4.5 the reaction energy for the formation of an oxyhydride starting from the REH_3 and RE_2O_3 binary precursors is shown. In the case of Y, the convex hull is formed by $P6_3/mmc$ - YH_3 , $Fm\bar{3}m$ - YOH , and $I\bar{3}a$ - Y_2O_3 . These three compounds might be thermodynamically stable at 0 K, depending on the energetics of the other non-assessed compounds in the RE–O–H ternary diagram. All of the Y oxyhydrides outside the 1:1:1 stoichiometry are instead metastable at best, with a propensity for the H-rich Y oxyhydrides to decompose towards a YH_3 – YOH phase mixture, and for the O-rich oxyhydrides to decompose towards a YOH – Y_2O_3 phase mixture. In the case of La, the convex hull is formed by $Fm\bar{3}m$ - YH_3 , $R3m$ - $\text{YO}_{0.25}\text{H}_{2.5}$, $P2_1/m$ - YOH , and $P\bar{3}m1$ - Y_2O_3 . The stability of the points at $x = 0.25$ (the anion-ordered $R3m$ - $\text{LaO}_{0.25}\text{H}_{2.5}$ might be thermodynamically stable, and the anion-disordered is only 0.03 eV above the hull line) is particularly interesting in view of the reported high ionic conductivity. The other La oxyhydrides considered in this work are instead metastable at best, with the H-rich ones having a propensity to decompose towards a $\text{LaO}_{0.25}\text{H}_{2.5}$ – LaOH phase mixture, and

the O-rich ones towards a LaOH–La₂O₃ phase mixture. Finally, we note that the energy above the hull line tends to be higher in the O-rich interval, possibly reflecting the lack of success in producing O-rich oxyhydrides via thermodynamically controlled methods. [9]

In terms of relative stability, clear differences between Y and La compounds are found at the binary extremes, which are well known to form different thermodynamically stable phases (namely $P6_3/mmc$ -YH₃ vs $Fm\bar{3}m$ -LaH₃, and $I\bar{3}a$ -Y₂O₃ vs $P\bar{3}m1$ -La₂O₃), [38] and at the 1:1:1 composition (Fig. 4.4b and 4.4c, insets). In the case of the 1:1:1 composition, the energy difference between the three known anion-ordered structures ($P4/nmm$, $Pnma$, and $P2_1/m$) is relatively small, explaining why different polymorphs have been reported on different occasions. This includes $Pnma$ [10] and $P2_1/m$ [9] for YOH, and $P4/nmm$ [1, 12, 40] and $P2_1/m$ [9] for LaOH. Notably, the $F43m$ phase has never been reported for YOH, which is particularly surprising as we predict it to be the energetically most favourable structure. This result is in agreement with a previous study, where, in addition to an identical theoretical conclusion for Y, it was experimentally shown that other small REs (Dy, Ho, Er) do form $F43m$ -REOH. [41] Since the anions alternate within its lattice, the $F43m$ phase is the one that effectively maximizes the distance between O²⁻ ions, and consequently minimizes the overall electrostatic repulsion in the anion sublattice; therefore, one intuitively expects it to be particularly favourable for the smaller REs. Despite the higher energy, anion-disordered REOH have been reported in a multitude of cases for the smaller RE cations, [8, 9, 12, 40] as well as for LaOH synthesized at high pressure. [9] Since the synthesis of oxyhydride powders relies on a high-temperature solid state reaction between REH₃ and RE₂O₃, we suppose that kinetic limitations, together with configurational entropy, play in favour of the resulting anion-disordered phase. We stress, however, that XRD alone is not sufficient to discriminate between the anion-disordered phase and the anion-ordered $F43m$ polymorph, and care should be taken in the absence of neutron diffraction data, as is the case for Refs. [9, 40]

4.3.2. STRUCTURES: COMPOSITIONAL LIMIT OF ANION-DISORDER

Relaxing the generated SQS gives an indication of their metastability²; if the atoms change site or restructure beyond small distortions, it indicates that the hypothesised structure was not metastable. We exploit this fact to computationally verify the results of Fukui et al., [9] who recently proposed that the compositional interval in which the anion-disordered phase is stable depends on the size of the cation, with La and Y being two extremes. It is worth mentioning that structural relaxation does not sample the whole space of parameters, but rather finds a local minimum not too far from the starting positions. This approach is, thus, incapable of predicting long-range anion reordering or phase segregations, but is nevertheless suitable to discuss the maximum range of O:H ratios in which the anion-disordered CaF₂-type phase is metastable.

The radial pair distribution function (PDF) and its cumulative value (CPDF) are the most transparent indicators to assess the type and the extent of the structural rearrangement that the disordered structures undergo during relaxation. Irrespective of the com-

²Here we use the term metastability because this approach verifies the presence/absence of a local energy minimum associated with the anion-disordered phase. The *most* stable, or *thermodynamically* stable phase for a given composition is to be inferred by different energy consideration, such as in Fig. 4.3 and Fig. 4.5

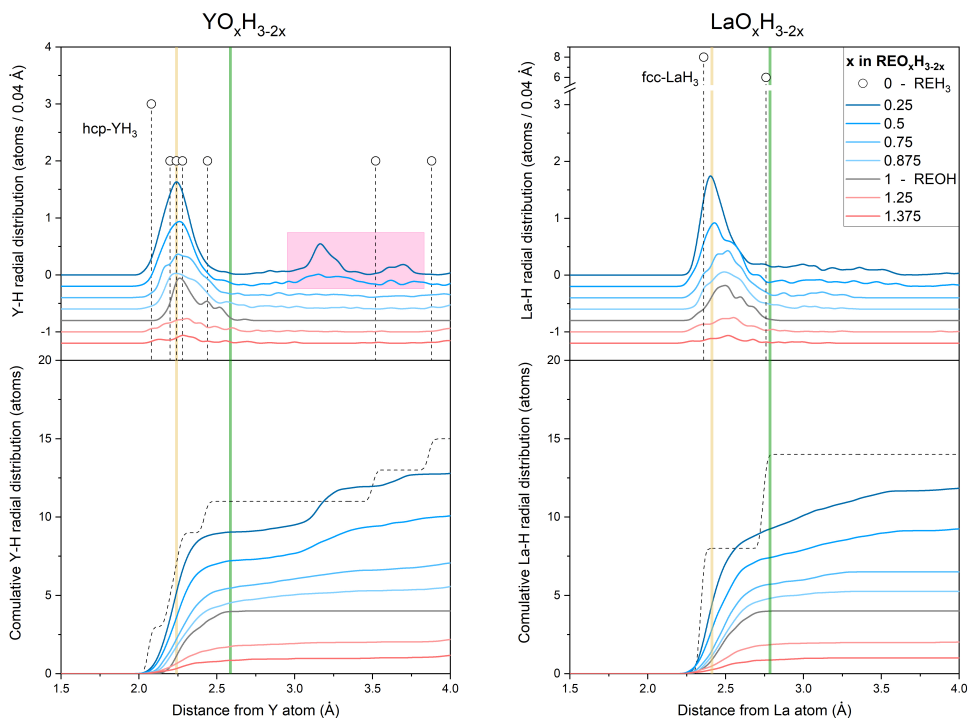


Figure 4.6: RE–H Radial pair distribution functions (*top panels*) and their cumulative values (*bottom panels*) for the relaxed SQS of Y and La anion-disordered oxyhydrides. The dashed vertical lines refer to the thermodynamically stable $P6_3/mmc$ - YH_3 and $Fm\bar{3}m$ - LaH_3 hydrides. Yellow and green vertical lines mark the position of tetrahedral and octahedral interstitial sites for an ideal fcc structure with lattice constant tuned to match the $\text{REO}_{0.25}\text{H}_{2.5}$ composition. The pink region highlights peaks that do not match the CaF_2 -type structure. To help visualization, lines in the top panels are shifted downward by a constant value of -0.2 .

position, we find that the RE^{3+} and O^{2-} ions do not move significantly from their original site (Fig. 4.E.1–4.E.2). For the H sub-lattice the case is different, and a change in symmetry occurs depending on the cation and on the O:H ratio (Fig. 4.6 and Fig. 4.E.3). In the following, we first discuss the O-rich compositional interval, and then the H-rich one.

In the O-rich interval ($x > 1$), both O^{2-} and H^- anions occupy exclusively the tetrahedral sites of the cation lattice, which are the energetically most stable anion-sites in this compositional range. [13] As such, there is no driving force to induce local rearrangements beyond small distortions. In Fig. 4.6 one observes one broad peak corresponding to the tetrahedral H^- , whose spread is due to small distortions and whose overlaying features are the result of the finite number of possible local environments.

In the H-rich compositional range ($x < 1$), where all tetrahedral sites and part of the octahedral ones are occupied, the electrostatic repulsion between neighbouring anions becomes more determining. [9] The associated electrostatic energy scales as $1/r$, and is thus stronger for smaller lattice constants. The H-sub-lattice of the most H-rich Y oxyhydrides ($x \leq 0.5$) appears in fact destabilized, as indicated in Fig. 4.6 by the appearance of

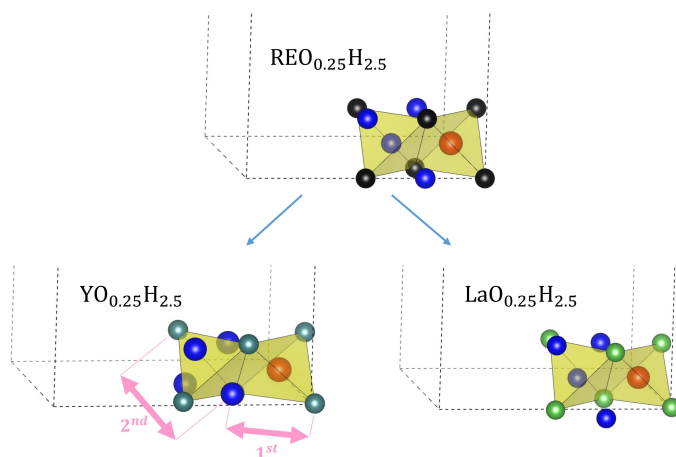


Figure 4.7: Example of the effect of structural relaxation on the anion-disordered structure of $\text{YO}_{0.25}\text{H}_{2.5}$ and $\text{LaO}_{0.25}\text{H}_{2.5}$ oxyhydrides. The yellow polygons indicate the tetrahedral anion-sites. Irrespective of the composition, the displacement of RE^{3+} and O^{2-} is minimal. However, a shift of the tetrahedral H^- to the empty octahedral sites is observable in the case of Y (see text). The pink arrows indicate the interatomic distances that correspond to the two additional peaks in the PDF (Fig. 4.6). In the case of La, no major reorganization happens and the ions only relax within the space of their initial site.

two new coordination shells at $\sim 3.2 \text{ \AA}$ and $\sim 3.7 \text{ \AA}$. These features do not match the initial symmetry, but rather correspond to the second and third coordination shells that result from a single highly distorted octahedral H^- site. Conversely, the bigger La oxyhydrides maintain the CaF_2 -type structure throughout the whole compositional interval, although with a significant degree of distortion. The anion repulsion close by an O^{2-} ion, in particular, leads to the displacement of the neighbouring octahedral H^- and therefore to the broadening of the corresponding peak(step) in the PDF(CPDF). The different behaviour between Y and La oxyhydrides aligns with the different thermodynamically stable phases of the Y and La tri-hydrides, which is hexagonal for YH_3 and cubic for LaH_3 .

Fig. 4.7 gives a visual impression of the structural rearrangements that occur upon relaxation of an anion-disordered H-rich ($x=0.25$) oxyhydride. In the case of Y, the proximity of a tetrahedral H^- to several octahedral H^- is energetically unfavourable, therefore it is advantageous for the tetrahedral H^- to shift towards an empty octahedral position. After that, all the octahedral H^- relax towards the empty tetrahedral site. An approximated description in terms of tetrahedral and octahedral anion-sites is no longer valid as all H^- ions now sit in comparable intermediate positions. This reorganization reflects the propensity to deform towards an hexagonal YH_3 -like structure, a tendency likely present also for higher oxygen contents but that becomes evident in the PDF(CPDF) only for $x \leq 0.5$. In the case of La, no major reorganization happens and the ions only relax within the space of their initial site.

In view of the symmetry change of the H sub-lattice, we conclude that the interval of metastability of anion-disordered Y oxyhydrides based on the CaF_2 -type structure is limited to $x > 0.5$. On the contrary, anion-disordered La oxyhydrides appear metastable along the whole $\text{REH}_3 - \text{RE}_2\text{O}_3$ composition line.

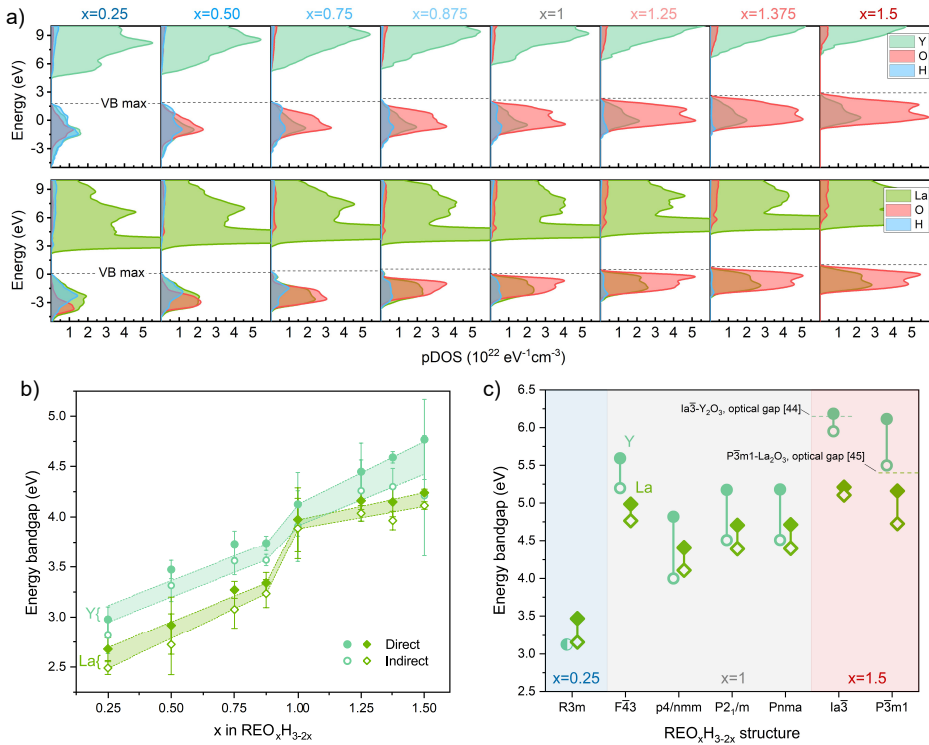


Figure 4.8: *a*) Projected mBJ density of states around the Fermi level for Y and La anion-disordered $\text{REO}_x\text{H}_{3-2x}$ oxyhydrides. The valence band has hybrid character, with the extend of the hybridization depending on the lattice dimension and on the rearrangements of the H-sub-lattice involving tetrahedral and octahedral sites (see text). A Gaussian smearing of 0.2 eV has been used in the figure to aid visualization. *b*) Dependency of the direct and indirect energy bandgaps upon the O:H ratio in Y and La anion-disordered $\text{REO}_x\text{H}_{3-2x}$ oxyhydrides. The energy bandgap widens upon increasing O:H content, with a bigger jump at $x \geq 1$, where the octahedral anion-sites are all empty. Lines are a guide for the eyes. *c*) Direct/Indirect bandgaps (filled/open points) of the Y and La anion-ordered oxyhydrides of lower energy compared to the anion-disordered phase. Reference values for the optical gap of RE_2O_3 oxides (corresponding to $x = 1.5$) are also reported, showing the excellent predictive ability of the mBJ scheme ($\delta E_g < 10\%$).

The fact that (i) different SQS of same composition relax towards comparable pair radial distributions, and (ii) that the different behaviour shown by Y and La compounds is in excellent agreement with the experimental work of Fukui et al.,^[9] indicates that the finite size of the SQS does not introduce artefacts that overrule the structural behaviour of the two different materials.

4.3.3. OPTICAL PROPERTIES

Following from the valence implied by the oxyhydride composition ($\text{RE}^{3+}\text{O}_x^2-\text{H}_{3-2x}^-$), and the large difference in Pauling electronegativity between cations ($Y = 1.22$, $La = 1.1$) and anions ($O = 3.44$, $H = 2.20$), all compounds simulated in this work show a sizeable energy bandgap (E_g) between the valence band (VB), dominated by occupied anion states, and

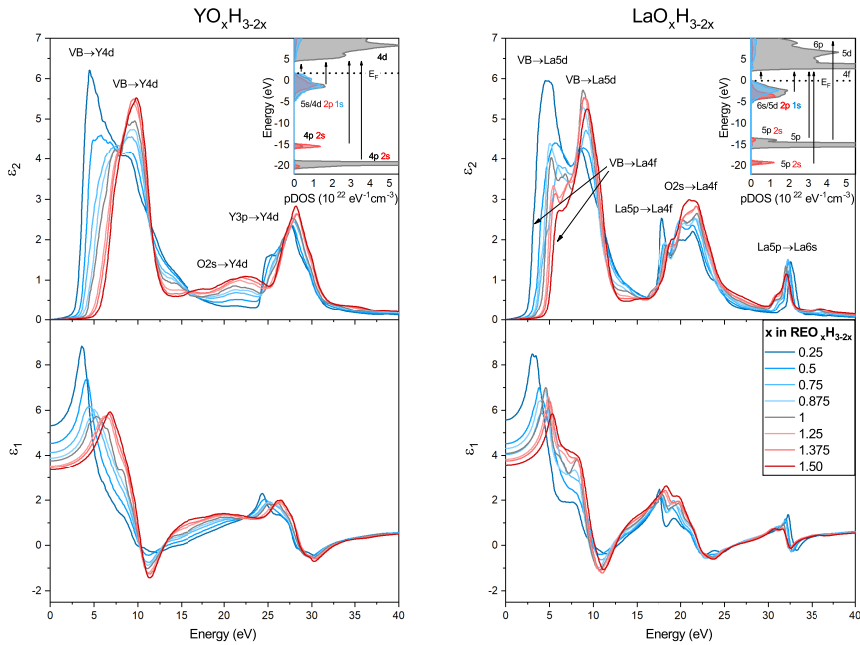


Figure 4.9: Imaginary and Real mBJ dielectric functions of Y and La anion-ordered $\text{REO}_x\text{H}_{3-2x}$ oxyhydrides upon increasing O:H content. The electronic transitions responsible for the main features are indicated in the insets, which report the pDOS of $\text{YO}_{0.25}\text{H}_{2.5}$ and $\text{LaO}_{0.25}\text{H}_{2.5}$, respectively.

the conduction band (CB), largely made of empty cation states.

Fig. 4.8a reports the pDOS of Y and La anion-disordered oxyhydrides around the Fermi level. Most interestingly, across the whole $\text{REO}_x\text{H}_{3-2x}$ composition line, the valence band retains a hybrid character, which originates from the overlap of Y(La) 5s4d(6s5d), O 2p, and H 1s atomic orbitals. In the H-rich range ($x < 1$), however, the extent of the hybridization between O 2p and H 1s orbitals is different among Y and La compounds: in Y oxyhydrides, O and H states overlap thoroughly, while for La oxyhydrides the top of the valence band is largely dominated by H states. Likely, the rearrangement of the H-sub-lattice that occurs in Y oxyhydrides for $x \leq 0.5$ contributes to the strong hybridization observed here, since there is no more distinction between tetrahedral and octahedral H. Conversely, in La oxyhydrides, the distinct tetrahedral and octahedral hydride ions contribute differently to the DOS, with the less-stable octahedral H^- resulting in states of higher energy, that in fact disappear at higher O:H ratios. Additionally, the larger interatomic distances in La oxyhydrides imply a reduced overlap between H and O atomic orbitals, leading to a weaker hybridization and, in general, to narrower energy bands compared to Y oxyhydrides of the same O:H ratio.

For both Y and La anion-disordered oxyhydrides, the resulting energy bandgaps are reported in Fig. 4.8b. Here, direct and indirect bandgaps are shown, their difference is rather small in view of the limited periodicity of the disordered anion sub-lattice. For both cations, the bandgap widens upon increasing the O:H ratio, with a bigger step at

$x = 1$ that further confirms how the octahedral H is largely responsible for the topmost part of the VB. For all O/H ratios, we find that the bandgap of La oxyhydrides is smaller than that of Y oxyhydrides, a consequence of the additional La 4f unoccupied states that form the the bottom of the CB. A similar trend of bandgap expansions, and smaller energy bandgaps for La compared to Y, is generally observed for the anion-ordered polymorphs as well (Fig. 4.8c).

Experimental optical gaps are available only for the ordered, binary extremes of the $\text{REH}_3\text{-RE}_2\text{O}_3$ composition line, which are here used to further validate the accuracy of the mBJ scheme. The REH_3 tri-hydrides pose a notorious challenge to most flavours of DFT, with LDA/GGA approximations erroneously predicting semi-metallic character and self-consistent *GW* calculations returning a severely underestimated bandgap. [42] While an exact description of the REH_3 is beyond the scope of this work, in Fig. 4.C.1 we show that the mBJ scheme successfully predicts the semiconducting character of YH_3 (optical gap 2.5 eV) [43] with a quantitative estimation (~ 1 eV) in line with previous *YH*₃ studies. [42] Concerning the RE_2O_3 oxides, we find an excellent match within 0.1 eV and 0.3 eV between the direct bandgaps computed with the mBJ scheme and the experimental optical gaps of $Ia\bar{3}\text{-Y}_2\text{O}_3$ (6.15 eV) [44] and $P\bar{3}m1\text{-La}_2\text{O}_3$ (5.5 eV) [45], respectively.

The prominent role of octahedral H in determining the $\text{REO}_x\text{H}_{3-2x}$ optical behaviour is even clearer from the evolution of the dielectric function upon increasing O:H ratio (Fig. 4.9). The imaginary part (ϵ_2), reported in the top panels, shows a main feature between 3 eV and 10 eV. This corresponds to the electronic transitions from VB to CB, with an onset closely matching the direct bandgap of the compounds, and two peaks which can be connected to the octahedral and tetrahedral anions. In fact, the first(second) peak decreases(increases) upon increasing O:H ratio, with $x=1$ marking, again, a transition point for properties dependent on the anion composition. Here, the ratio between the two peaks inverts. The first peak disappears completely in the case of Y, whose oxyhydrides have a smoother dielectric function because fewer electronic transitions are possible, and their energy bands are wider and more spaced compared to the case of La. In the case of La, the sharp 4f-band at the CB bottom contributes to the persistence of a two-peak structure.

A related trend upon O:H content can be seen in the real part of the dielectric function. The refractive behaviour at UV-VIS-NIR frequencies is defined by the first ~ 5 eV, where $\text{REO}_x\text{H}_{3-2x}$ oxyhydrides of higher H content show significantly higher ϵ_1 .

4.4. DISCUSSION

4.4.1. COMPARISON TO PHOTOCHROMIC THIN FILMS

At the time of writing, there are no experimental data on the optical properties of either anion-ordered or anion-disordered $\text{REO}_x\text{H}_{3-2x}$ produced *via* the conventional solid-state reaction between REH_3 and RE_2O_3 precursors. However, the optical properties of RE oxyhydride films produced *via* post-oxidation of reactively sputtered REH_2 films have been studied extensively, with a particular focus on their reversible photochromism. Such photochromic effect has been so far reported for a variety of RE cations (Sc, Y, Nd, Gd, Dy, Er), [3, 46-48] and in a range of O:H ratios as big as $0.5 < x < 1.3$. [3]

While the composition of the oxyhydride and the deposition conditions influence the

extent and the speed of photochromism,^[4] the general presence of the phenomenon indicates that its origin is intrinsic to the RE oxyhydride thin film material. Currently, there is not yet conclusive agreement concerning (i) the nature of the absorbing species responsible for the photo-darkening, (ii) the mechanism of their formation under illumination and subsequent disappearance during bleaching in the dark, and (iii) the driving forces behind these processes. While the photo-darkening is initiated by an inter-band electronic transition, most research converges towards the idea that structural rearrangements enabled by the high H (local) mobility are at the heart of the photochromism. In this sense, it was hinted that the photodarkening depends on the segregation of an absorbing phase,^[15, 16] a process accompanied by reversible contraction of the crystal lattice,^[49] and quenching of the NMR signal of the most mobile H fraction (~ 3%).^[50] A reversible change in the H-sub-lattice upon illumination was recently suggested as well via muon spin rotation spectroscopy (μ SR).^[51] Finally, the bleaching was shown to be a thermally activated process.^[52]

In this context, a deeper understanding of the crystal structure and anion-sub-lattice of the sputtered $\text{REO}_x\text{H}_{3-2x}$ is important to further explore the photo-induced process, as well as to assess the actual similarity to the well-characterized oxyhydride powders. Since neutron diffraction is not a viable option for thin films, as per today there is no experimental information on their anion sub-lattice other than the already discussed preference for the tetrahedral sites.^[13] Considering that the oxidation of the parent REH_2 occurs at room temperature and rapidly, thus likely missing the narrow energetic minima expected for anion-ordered structures, a model based on anion-disorder was heuristically proposed for the photochromic $\text{REO}_x\text{H}_{3-2x}$ thin films.^[3, 13] In fact, independently from cation and O:H ratio, the fcc symmetry was generally reported for the cation sub-lattice, with XRD patterns lacking any additional superstructure-peaks typical of anion ordering (e.g., due to periodicity in the small distortion as in the $Ia\bar{3}$ oxide).^[3, 13, 48] The hypothesis of an anion-disordered structure can now be investigated by comparing the optical properties computed in this work with the experimental ones of $\text{YO}_x\text{H}_{3-2x}$ thin films.

Fig. 4.10 shows the comparison between computed energy bandgaps and the indirect optical gap from Cornelius et al..^[3] The anion-disordered model captures a trend of increasing gap for increasing O:H ratio, however, up to $x \leq 1$, the computed bandgaps systematically overestimate the experimental ones by 0.5-1 eV. This is a significant difference even considering that excitonic effects were neglected. Comparison to the reference compounds REH_3 and RE_2O_3 suggests the absence of systematic overestimations of the bandgaps in our simulations; REH_3 tri-hydrides are in fact known to present the opposite challenge to any flavour of DFT (including mBJ - Fig. 4.E.1),^[42] while the optical gaps of the RE_2O_3 match our results within 0.3 eV.

It is worth noting that all anion-ordered structures return even higher bandgaps and do not show a monotonously increasing trend with O:H ratio (Fig. 4.8c and Fig. 4.F1), therefore, despite the disagreement we observe with the experiment, anion-disorder remains the best candidate for the anion sub-lattice of the H-rich (i.e., $x \leq 1$) Y oxyhydride thin films. Two aspects not included in the model might be responsible for the mismatch with the experimental optical gaps, namely: (i) unaccounted defects that might give in-gap states and, (ii) the substrate-induced stress and the limited freedom for distortion of the grains in the polycrystalline films. In addition, (iii) it is possible that compositional

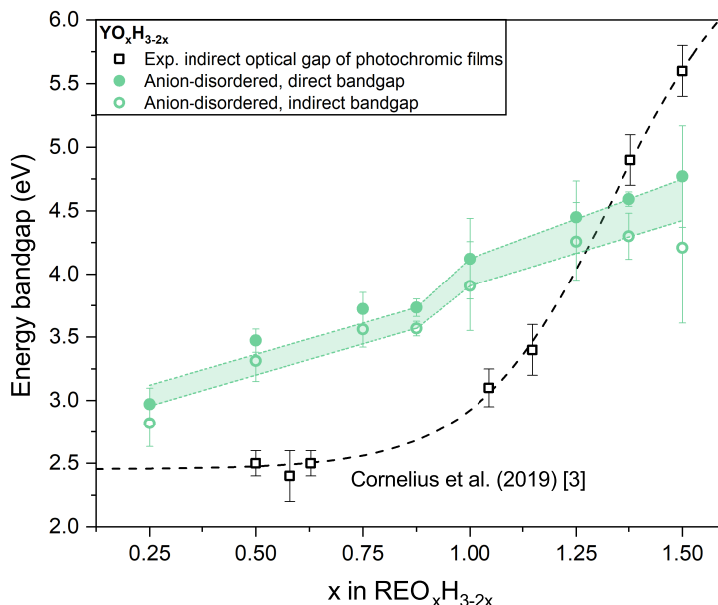


Figure 4.10: Comparison between the experimental optical gap of photochromic Y oxyhydride thin films [3] and the direct/indirect energy bandgaps computed for anion-disordered $\text{YO}_x\text{H}_{3-2x}$. Lines are a guide for the eyes.

inhomogeneity within the sputtered films results in band extrema that do not reflect the average $\text{REO}_x\text{H}_{3-2x}$ composition, but rather some local deviations, e.g., a very H-rich region more similar to YH_3 ($E_g \sim 2.6$ eV).

Being less sensitive to defects and local inhomogeneity (at least in the absence of absorption, for $E \ll E_g$), the refractive index ($\tilde{n} = n + ik = \epsilon^{1/2}$) would be a better property to compare. However, in the limit of $E \ll E_g$, it is the composition and not the crystal structure that dominates its value (Fig. 4.G.1). Focusing on the energies relevant to UV-VIS-nIR spectroscopy, Fig. 4.11 shows the good agreement between the computed refractive index of anion-disordered $\text{YO}_x\text{H}_{3-2x}$ and reported experimental values, [15, 16] further proving that the oxyhydride $\text{REO}_x\text{H}_{3-2x}$ composition well describes the photochromic thin films. Unfortunately the exact O:H ratio of the films measured in Refs. [15, 16] was not known. However their refractive indexes match the values computed for the interval $x : [0.75, 1.25]$, which - considering the challenges of predicting optical properties *ab-initio* - is largely compatible with the composition range of $x : [0.5, 1]$ that is expected for air-oxidized thin films. [4]

We conclude, that an anion-disordered sub-lattice is the most likely configuration for H-rich photochromic thin films ($x < 1$). The situation appears different for O-rich compositions ($x > 1$), where the experimental optical gaps show a steep increase which is not present in the trend computed for the anion-disordered oxyhydrides. This suggests that a certain degree of anion ordering must be present in O-rich oxyhydrides films, intuitively facilitated by the presence of empty tetrahedral sites. Notably, reactively sputtered Y_2O_3 films assume the bixbyite $Ia\bar{3}$ phase, and their experimental optical gap of 5.7 eV

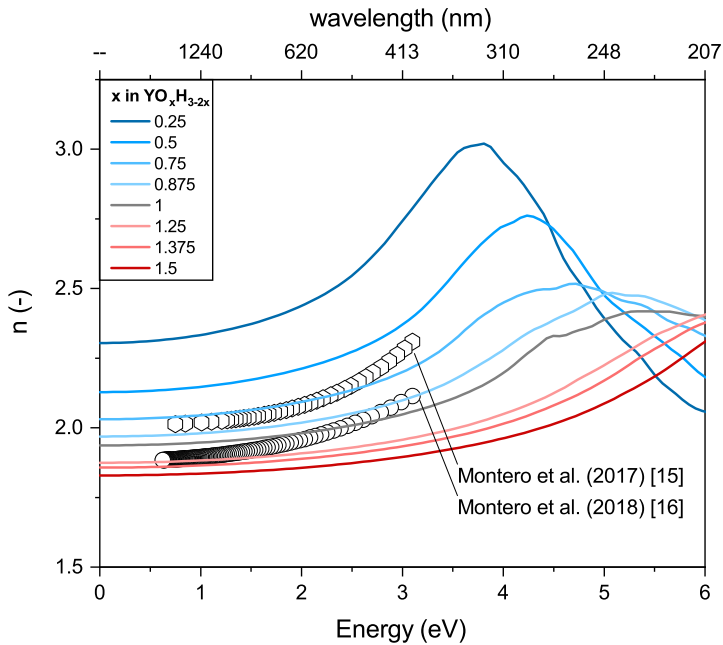


Figure 4.11: Comparison between the experimental refractive index of photochromic Y oxyhydride thin films [15] [16] and the ones computed for anion-disordered $\text{YO}_x\text{H}_{3-2x}$.

matches well both reference and computed values. A somewhat gradual transition from anion-disorder to anion-order is thus expected for $x > 1$.

4.4.2. COMPARISON TO EXPERIMENTALLY REPORTED OXYHYDRIDES

Our DFT calculation suggest that the anion-disordered phase can potentially be metastable in a wide range of O:H ratios. In this section we discuss our predicted rage of metastability, for both Y and La oxyhydrides, in comparison to (i) the experimental works of Fukui *et al.* [9] on conventionally synthesized powders and (ii) our own experimental work (see Chapter 2) on reactively sputtered thin films. [3] Given the high temperature and long time of the solid-state powder synthesis, this route of synthesis is likely to occur under thermodynamic control. Conversely, the outcome of reactive sputtering followed by post-oxidation is undoubtedly dependent on the kinetic limitations of the process. Fig. 4.12 gives an overview of the crystal phase(s) reported in these different studies at given O:H ratio.

In the O-rich interval ($x > 1$), no Y or La anion-disordered O-rich oxyhydride was reported experimentally. With a conventional powder synthesis, Fukui *et. al* report segregation of an oxide phase; while from reactive sputtering we produced thin films whose large E_g suggests a degree of anion ordering. Nevertheless, DFT predicts the anion-disordered phase to be metastable against spontaneous rearrangement of the lattice. Therefore we do not exclude that O-rich Y and La oxyhydrides could in principle be synthesised *via* kinetically-controlled routes.

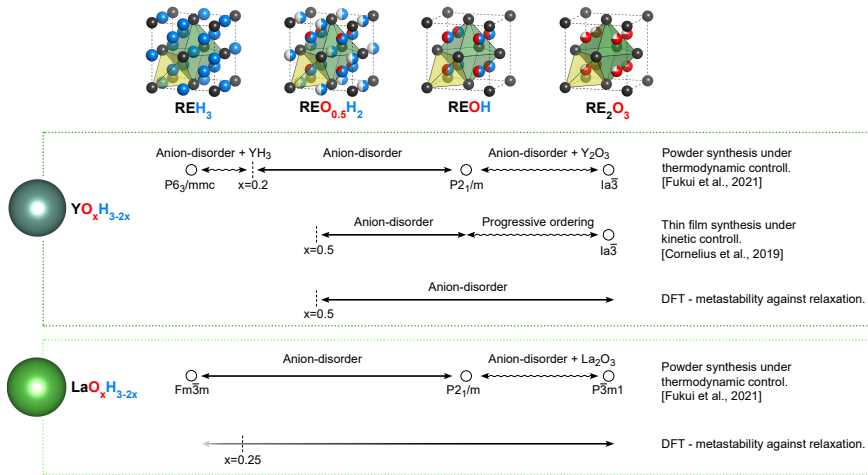


Figure 4.12: Compositional ranges of metastability of anion-disordered Y and La oxyhydrides as reported in different studies.

In the H-rich interval ($x < 1$), we have already discussed that the metastability of Y and La oxyhydrides is different. While the DFT results, in the case of La, well align to the experimental work of Fukui et. al., the case of Y is less straightforward. Our DFT results suggest show that the H-sublattice of Y oxyhydrides undergoes major rearrangements for $x \leq 0.5$. This threshold roughly corresponds to the most H-rich oxyhydride thin films that we have produced, however this is due to the experimental route of synthesis (see Chapter 2 and 3) for which compositions below $x = 0.5$ are not accessible, and therefore it does not necessarily reflect an intrinsic instability of the experimental thin films for $x < 0.5$. Conversely, for powder synthesis the whole compositional range is, in principle, accessible. In their pressure-composition phase diagram, Fukui et al. have shown that when the synthesis is carried under a modest pressure, the anion-disordered phase is stable only for $0.8 < x < 1$, while an hexagonal phase (probably YH_3) segregates for higher H contents. However, carrying the synthesis under an high pressure, in the order of *few* GPa, widens this compositional range, with the most H-rich anion-disordered Y oxyhydride reported at $x \sim 0.25$. Notably, this corresponds to an H content which is higher than the limit of metastability predicted by DFT. We hope that future studies of neutron diffraction will shed light on the H-sublattice in this particularly H-rich Y oxyhydride.

4.5. CONCLUSIONS

In this work, we have introduced a set of special quasirandom structures (SQS) to model the anion-disordered lattice of $\text{REO}_x\text{H}_{3-2x}$ oxyhydrides along the entire REH_3 – RE_2O_3 composition line. This allowed us to investigate *ab-initio* the influence of the O:H ratio of the energy, metastability, and optical properties of Y and La oxyhydrides.

In agreement with the experimental result of Fukui et al.,^[9] anion-ordered polymorphs ($P4/nmm$, $Pnma$, and $P2_1/m$) are energetically favoured for the REOH 1:1:1 stoichiometric oxyhydrides. Notably, we find that the energetically most stable YO_H has

$F\bar{4}3m$ symmetry, a so-far experimentally unreported structure where the Y^{3+} cations assume fcc lattice and the H^- and O^{2-} anions alternate in its tetrahedral interstitial sites. Comparing to the most stable anion-ordered polymorphs among those considered in this work, anion-disorder leads to an energy penalty of 0.16 eV/f.u. and 0.14 eV/f.u. for YO₃ and LaOH₃, respectively. Moving away from the 1:1:1 composition, the energy penalty becomes lower, and the anion-disordered phase even presents the lowest energy in the H-rich composition interval for both Y and La oxyhydrides.

Upon increasing oxygen content, anion-disordered REO_xH_{3-2x} show a progressive stabilization, which we rationalize in terms of increasing (negative) lattice energy. For $x \leq 1$, this is due to a shift of charge from the octahedral to the more-stable tetrahedral anion-sites. For $x > 1$, further stabilization results from a larger freedom for structural distortion related to the presence of empty tetrahedral sites.

We find that the cation size (and thus the lattice constant) determines the compositional interval in which the CaF₂-type anion-disordered phase is metastable against spontaneous structural rearrangement of the anion-sub-lattice. In particular, the bigger cell of La oxyhydride can accommodate any O:H ratios, while the most H-rich ($x \leq 0.5$) anion-disordered Y oxyhydrides proved unstable.

Finally, the influence of the O:H ratio on the electronic bandgap, DOS, and dielectric function of anion-disordered oxyhydrides was discussed. To do so, in our simulation we employed - and validated - the mBJ scheme, achieving an accuracy comparable to far more expensive *GW* methods. Our results show major differences between H-rich and O-rich regimes. For $x < 1$, we find that the octahedral H^- anions play a decisive role: they form electronic states at the top of the valence band, which reduce the energy bandgap and dominate the electronic transitions at lower energies, thus increasing the refractive index of the material in the VIS-nIR spectral range.

A comparison of these results to the experimental data available for photochromic Y oxyhydride thin films reinforces the hypothesis of anion-disorder for H-rich oxyhydrides ($x < 1$), while it hints towards some degree of anion ordering for the O-rich ones ($x > 1$).

In prospective, we believe that the SQS structures introduced here will also open the possibility of studying the H^- dynamics of anion-disordered oxyhydrides of any O:H ratio.

REFERENCES

- [1] K. Fukui, S. Iimura, T. Tada, S. Fujitsu, M. Sasase, H. Tamatsukuri, T. Honda, K. Ikeda, T. Otomo, and H. Hosono, *Characteristic fast H^- ion conduction in oxygen-substituted lanthanum hydride*, [Nat. Commun.](#) **10**, 2578 (2019).
- [2] T. Mongstad, C. Platzer-Björkman, J. P. Maehlen, L. P. Mooij, Y. Pivak, B. Dam, E. S. Marstein, B. C. Hauback, and S. Z. Karazhanov, *A new thin film photochromic material: Oxygen-containing yttrium hydride*, [Sol. Energy Mater. Sol. Cells](#) **95**, 3596 (2011).
- [3] S. Cornelius, G. Colombi, F. Nafezarefi, H. Schreuders, R. Heller, F. Munnik, and B. Dam, *Oxyhydride nature of rare-earth-based photochromic thin films*, [The Journal of Physical Chemistry Letters](#) **10**, 1342 (2019).
- [4] G. Colombi, T. De Krom, D. Chaykina, S. Cornelius, S. W. H. Eijt, and B. Dam, *Influence of cation ($RE = Sc, Y, Gd$) and O/H anion ratio on the photochromic properties of REO_xH_{3-2x} thin films*, [ACS Photonics](#) **8**, 709 (2021).
- [5] G. Kobayashi, Y. Hinuma, S. Matsuoka, A. Watanabe, M. Iqbal, M. Hirayama, M. Yone-mura, T. Kamiyama, I. Tanaka, and R. Kanno, *Pure H^- conduction in oxyhydrides*, [Science](#) **351**, 1314 (2016).
- [6] H. Kageyama, K. Hayashi, K. Maeda, J. P. Attfield, Z. Hiroi, J. M. Rondinelli, and K. R. Poeppelmeier, *Expanding frontiers in materials chemistry and physics with multiple anions*, [Nat. Commun.](#) **9**, 772 (2018).
- [7] Y. Kobayashi, O. Hernandez, C. Tassel, and H. Kageyama, *New chemistry of transition metal oxyhydrides*, [Sci. Technol. Adv. Mater.](#) **18**, 905 (2017).
- [8] T. Broux, H. Ubukata, C. J. Pickard, F. Takeiri, G. Kobayashi, S. Kawaguchi, M. Yone-mura, Y. Goto, C. Tassel, and H. Kageyama, *High-Pressure Polymorphs of LaHO with Anion Coordination*, [J. Am. Chem. Soc.](#) **141**, 8717 (2019).
- [9] K. Fukui, S. Iimura, J. Wang, T. Tada, T. Honda, K. Ikeda, T. Otomo, and H. Hosono, *Stabilization factor of anion-excess fluorite phase for fast anion conduction*, [Chemistry of Materials](#) **33**, 1867 (2021).
- [10] N. Zapp, H. Auer, and H. Kohlmann, *YHO, an air-stable ionic hydride*, [Inorganic Chemistry](#) **58**, 14635 (2019).
- [11] N. Zapp, D. Sheptyakov, A. Franz, and H. Kohlmann, *HoHO: A paramagnetic air-resistant ionic hydride with ordered anions*, [Inorganic Chemistry](#) **60**, 3972 (2021).
- [12] H. Ubukata, T. Broux, F. Takeiri, K. Shitara, H. Yamashita, A. Kuwabara, G. Kobayashi, and H. Kageyama, *Hydride conductivity in an anion-ordered fluorite structure LnHO with an enlarged bottleneck*, [Chem. Mater.](#) **31**, 7360 (2019).
- [13] G. Colombi, S. Cornelius, A. Longo, and B. Dam, *Structure model for anion-disordered photochromic gadolinium oxyhydride thin films*, [J. Phys. Chem. C](#) **124**, 13541 (2020).

- [14] K. Ooya, J. Li, K. Fukui, S. Iimura, T. Nakao, K. Ogasawara, M. Sasase, H. Abe, Y. Niwa, M. Kitano, and H. Hosono, *Ruthenium catalysts promoted by lanthanide oxyhydrides with high hydride-ion mobility for low-temperature ammonia synthesis*, *Advanced Energy Materials* **11**, 2003723 (2021).
- [15] J. Montero, F. A. Martinsen, M. García-Tecedor, S. Z. Karazhanov, D. Maestre, B. Hauback, and E. S. Marstein, *Photochromic mechanism in oxygen-containing yttrium hydride thin films: An optical perspective*, *Phys. Rev. B* **95**, 201301 (2017).
- [16] J. Montero and S. Z. Karazhanov, *Spectroscopic ellipsometry and microstructure characterization of photochromic oxygen-containing yttrium hydride thin films*, *Phys. Status Solidi A* **215**, 1701039 (2018).
- [17] A. Zunger, S.-H. Wei, L. G. Ferreira, and J. E. Bernard, *Special quasirandom structures*, *Phys. Rev. Lett.* **65**, 353 (1990).
- [18] A. van de Walle, P. Tiwary, M. M. de Jong, D. L. Olmsted, M. D. Asta, A. Dick, D. Shin, Y. Wang, L.-Q. Chen, and Z.-K. Liu, *Efficient stochastic generation of special quasirandom structures*, *Calphad* **42**, 13 (2013).
- [19] A. van de Walle, M. D. Asta, and G. Ceder, *The Alloy Theoretic Automated Toolkit: A user guide*, *Calphad* **26**, 539 (2002).
- [20] G. Kresse and J. Furthmüller, *Efficient iterative schemes for ab initio total-energy calculations using a plane-wave basis set*, *Phys. Rev. B* **54**, 11169 (1996).
- [21] G. Kresse and J. Furthmüller, *Efficiency of ab-initio total energy calculations for metals and semiconductors using a plane-wave basis set*, *Computational Materials Science* **6**, 15 (1996).
- [22] P. E. Blöchl, *Projector augmented-wave method*, *Phys. Rev. B* **50**, 17953 (1994).
- [23] G. Kresse and D. Joubert, *From ultrasoft pseudopotentials to the projector augmented-wave method*, *Phys. Rev. B* **59**, 1758 (1999).
- [24] J. P. Perdew, K. Burke, and M. Ernzerhof, *Generalized gradient approximation made simple*, *Phys. Rev. Lett.* **77**, 3865 (1996).
- [25] J. P. Perdew, K. Burke, and M. Ernzerhof, *Generalized gradient approximation made simple [phys. rev. lett. 77, 3865 (1996)]*, *Phys. Rev. Lett.* **78**, 1396 (1997).
- [26] A. Kramida, Yu. Ralchenko, J. Reader, and NIST ASD Team, NIST Atomic Spectra Database (ver. 5.9), [Online]. Available: <https://physics.nist.gov/asd> [2021, November 1]. National Institute of Standards and Technology, Gaithersburg, MD. (2021).
- [27] J. E. Huheey, E. A. Keiter, R. L. Keiter, and O. K. Medhi, *Inorganic Chemistry: Principles of Structure and Reactivity* (Springer, 2006) pp. 99–104.
- [28] K. Kato and F. Izumi, *Unpublished work*, (2008).

- [29] K. Momma and F. Izumi, *VESTA 3 for three-dimensional visualization of crystal, volumetric and morphology data*, *J. Appl. Crystallogr.* **44**, 1272 (2011).
- [30] P. P. Ewald, *Die berechnung optischer und elektrostatischer gitterpotentiale*, *Annalen der Physik* **369**, 253 (1921).
- [31] A. D. Becke and E. R. Johnson, *A simple effective potential for exchange*, *The Journal of Chemical Physics* **124**, 221101 (2006).
- [32] F. Tran and P. Blaha, *Accurate band gaps of semiconductors and insulators with a semilocal exchange-correlation potential*, *Phys. Rev. Lett.* **102**, 226401 (2009).
- [33] M. Shishkin and G. Kresse, *Implementation and performance of the frequency-dependent GW method within the PAW framework*, *Phys. Rev. B* **74**, 035101 (2006).
- [34] M. Shishkin and G. Kresse, *Self-consistent gw calculations for semiconductors and insulators*, *Phys. Rev. B* **75**, 235102 (2007).
- [35] M. Shishkin, M. Marsman, and G. Kresse, *Accurate quasiparticle spectra from self-consistent gw calculations with vertex corrections*, *Phys. Rev. Lett.* **99**, 246403 (2007).
- [36] F. Fuchs, J. Furthmüller, F. Bechstedt, M. Shishkin, and G. Kresse, *Quasiparticle band structure based on a generalized Kohn-Sham scheme*, *Phys. Rev. B* **76**, 115109 (2007).
- [37] M. Gajdoš, K. Hummer, G. Kresse, J. Furthmüller, and F. Bechstedt, *Linear optical properties in the projector-augmented wave methodology*, *Phys. Rev. B* **73**, 045112 (2006).
- [38] M. Zinkevich, *Thermodynamics of rare earth sesquioxides*, *Progress in Materials Science* **52**, 597 (2007).
- [39] W. Sun, C. J. Bartel, E. Arca, S. R. Bauers, B. Matthews, B. Orvananos, B.-R. Chen, M. F. Toney, L. T. Schelhas, W. Tumas, J. Tate, A. Zakutayev, S. Lany, A. M. Holder, and G. Ceder, *A map of the inorganic ternary metal nitrides*, *Nature Materials* **18**, 732 (2019).
- [40] H. Yamashita, T. Broux, Y. Kobayashi, F. Takeiri, H. Ubukata, T. Zhu, M. A. Hayward, K. Fujii, M. Yashima, K. Shitara, A. Kuwabara, T. Murakami, and H. Kageyama, *Chemical pressure-induced anion order-disorder transition in LnHO enabled by hydride size flexibility*, *Journal of the American Chemical Society* **140**, 11170 (2018).
- [41] N. Zapp, D. Sheptyakov, and H. Kohlmann, *Computational chemistry-guided syntheses and crystal structures of the heavier lanthanide hydride oxides DyHO, ErHO, and LuHO*, *Crystals* **11** (2021), <https://doi.org/10.3390/cryst11070750>.
- [42] P. v. Gelderen, P. A. Bobbert, P. J. Kelly, G. Brocks, and R. Tolboom, *Parameter-free calculation of single-particle electronic excitations in YH₃*, *Phys. Rev. B* **66**, 075104 (2002).

- [43] A. T. M. van Gogh, D. G. Nagengast, E. S. Kooij, N. J. Koeman, J. H. Rector, R. Griessen, C. F. J. Flipse, and R. J. J. G. A. M. Smeets, *Structural, electrical, and optical properties of $La_{1-z}Y_zH_x$ switchable mirrors*, [Phys. Rev. B **63**, 195105 \(2001\)](#).
- [44] V. Mudavakkat, V. Atuchin, V. Kruchinin, A. Kayani, and C. Ramana, *Structure, morphology and optical properties of nanocrystalline yttrium oxide (Y_2O_3) thin films*, [Optical Materials **34**, 893 \(2012\)](#).
- [45] A. Prokofiev, A. Shelykh, and B. Melekh, *Periodicity in the band gap variation of Ln_2X_3 ($X = O, S, Se$) in the lanthanide series*, [Journal of Alloys and Compounds **242**, 41 \(1996\)](#).
- [46] F. Nafezarefi, H. Schreuders, B. Dam, and S. Cornelius, *Photochromism of rare-earth metal-oxy-hydrides*, [Appl. Phys. Lett. **111**, 103903 \(2017\)](#).
- [47] S. Adalsteinsson, M. Moro, D. Moldarev, S. Droulias, M. Wolff, and D. Primetzhofer, *Correlating chemical composition and optical properties of photochromic rare-earth oxyhydrides using ion beam analysis*, [Nuclear Instruments and Methods in Physics Research Section B: Beam Interactions with Materials and Atoms **485**, 36 \(2020\)](#).
- [48] D. Chaykina, F. Nafezarefi, G. Colombi, S. Cornelius, L. J. Bannenberg, H. Schreuders, and B. Dam, *Influence of crystal structure, encapsulation, and annealing on photochromism in nd oxyhydride thin films*, [The Journal of Physical Chemistry C **126**, 2276 \(2022\)](#).
- [49] J. P. Maehlen, T. T. Mongstad, C. C. You, and S. Karazhanov, *Lattice contraction in photochromic yttrium hydride*, [J. Alloys Compd. **580**, S119 \(2013\)](#).
- [50] C. V. Chandran, H. Schreuders, B. Dam, J. W. G. Janssen, J. Bart, A. P. M. Kentgens, and P. J. M. van Bentum, *Solid state nmr studies of the photochromic effects of thin films of oxygen containing yttrium hydride*, [J. Phys. Chem. C **118**, 22935 \(2014\)](#).
- [51] D. Chaykina, T. de Krom, G. Colombi, H. Schreuders, A. Suter, T. Prokscha, B. Dam, and S. Eijt, *Structural properties and anion dynamics of yttrium dihydride and photochromic oxyhydride thin films examined by in situ μ^+ SR*, [Phys. Rev. B **103**, 224106 \(2021\)](#).
- [52] E. M. Baba, P. M. Weiser, E. z. Zayim, and S. Karazhanov, *Temperature-dependent photochromic performance of yttrium oxyhydride thin films*, [physica status solidi \(RRL\) – Rapid Research Letters **15**, 2000459 \(2021\)](#).

APPENDIX

4.A. STRUCTURAL MODELS

4.A.1. ANION-ORDERED RE OXYHYDRIDES BASED ON CaF_2 -TYPE LATTICE

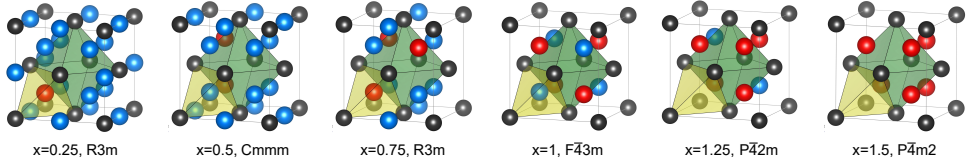


Figure 4.A.1: Anion-ordered structures based on the CaF_2 -type lattice which, after relaxation, showed the lowest energy among all of the ordering schemes possible within one unit cell.

4

4.A.2. ANION-DISORDERED SQS

x in $\text{REO}_x\text{H}_{3-2x}$	Objective Function	$\text{YO}_x\text{H}_{3-2x}$			
		ΔH_F [eV/f.u.]	Volume [\AA^3 /f.u.]	E_g ind. [eV]	E_g dir. [eV]
0.25	-4.602(1)	-3.50(1)	36.9(2)	2.8(2)	3.0(1)
0.5	-5.5(3)	-4.56(2)	37.6(1)	3.3(2)	3.47(9)
0.75	-4.5(2)	-5.65(3)	38.14(6)	3.6(1)	3.7(1)
0.875	-2.295(1)	-6.192(8)	38.53(9)	3.57(6)	3.73(7)
1	*	-6.776(6)	38.565(3)	3.9(4)	4.1(3)
1.25	-4.552(2)	-7.73(8)	39.1(4)	4.3(3)	4.5(3)
1.375	-1.995(1)	-8.19(6)	39.4(1)	4.3(2)	4.59(6)
1.5	-5.8(8)	-8.79(3)	38.89(5)	4.2(6)	4.8(4)

x in $\text{REO}_x\text{H}_{3-2x}$	Objective Function	$\text{LaO}_x\text{H}_{3-2x}$			
		ΔH_F [eV/f.u.]	Volume [\AA^3 /f.u.]	E_g ind. [eV]	E_g dir. [eV]
0.25	-4.602(1)	-3.344(4)	45.7(1)	2.49(6)	2.6(1)
0.5	-5.5(3)	-4.358(9)	47.0(2)	2.7(3)	2.9(3)
0.75	-4.5(2)	-5.403(8)	47.76(1)	3.1(2)	3.27(9)
0.875	-2.295(1)	-5.949(4)	48.04(9)	3.2(1)	3.3(1)
1	*	-6.50(1)	48.02(4)	3.9(3)	4.0(3)
1.25	-4.552(2)	-7.37(2)	48.6(2)	4.03(9)	4.16(9)
1.375	-1.995(1)	-7.80(1)	49.00(7)	3.96(9)	4.2(2)
1.5	-5.8(8)	-8.29(4)	48.5(5)	4.11(4)	4.24(4)

Table 4.A.1: Average objective function for the SQS generated in this work. Since different physical properties converge at a different rate, evaluation of the errors is better done in hindsight. For this purpose, the average formation energy (ΔH_F), volume, indirect E_g , and direct E_g are also reported for both Y and La oxyhydrides. The number between brackets is the error on the last significant figure, estimated from the results of the different SQS as $\delta = (\max - \min)/2$. *SQS taken from Jiang *et al.* [\[1\]](#)

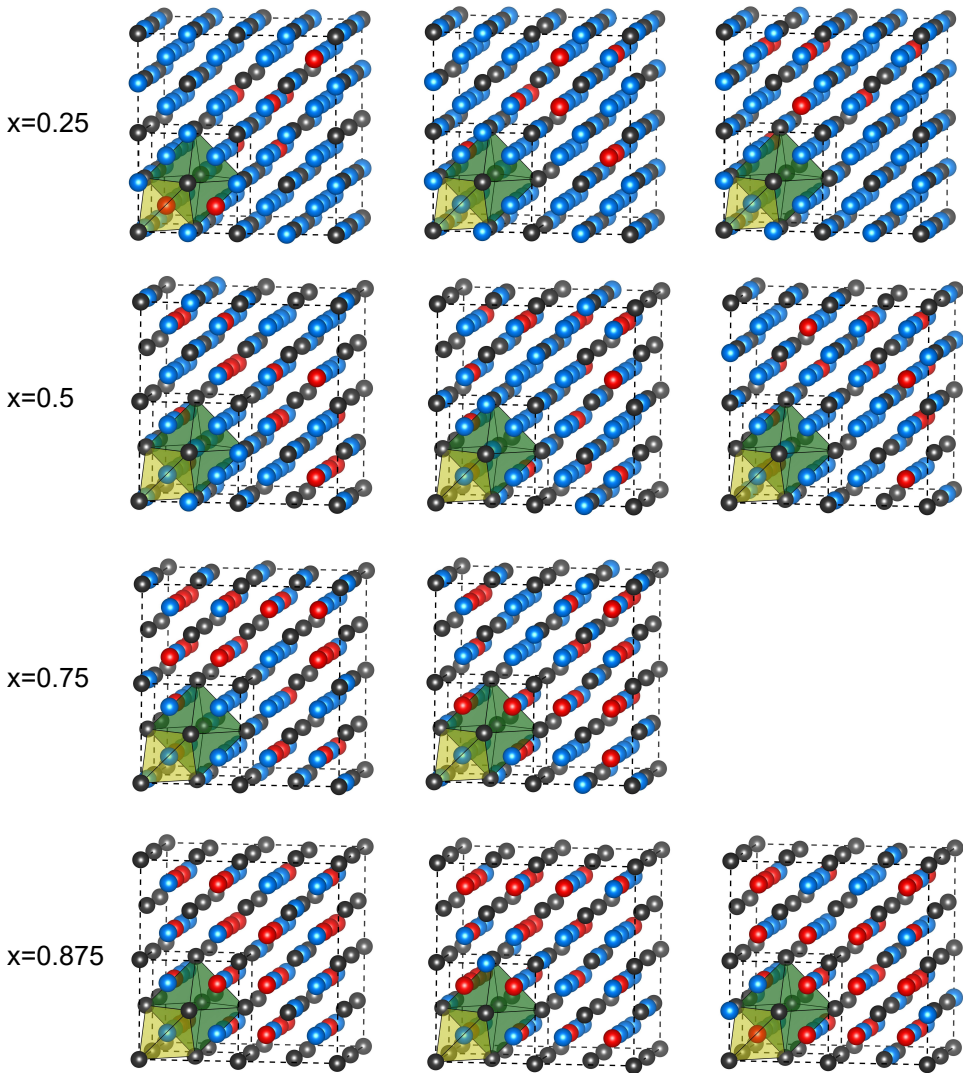


Figure 4.A.2: SQS used to model the anion-disordered RE oxyhydride of composition $x < 1$.

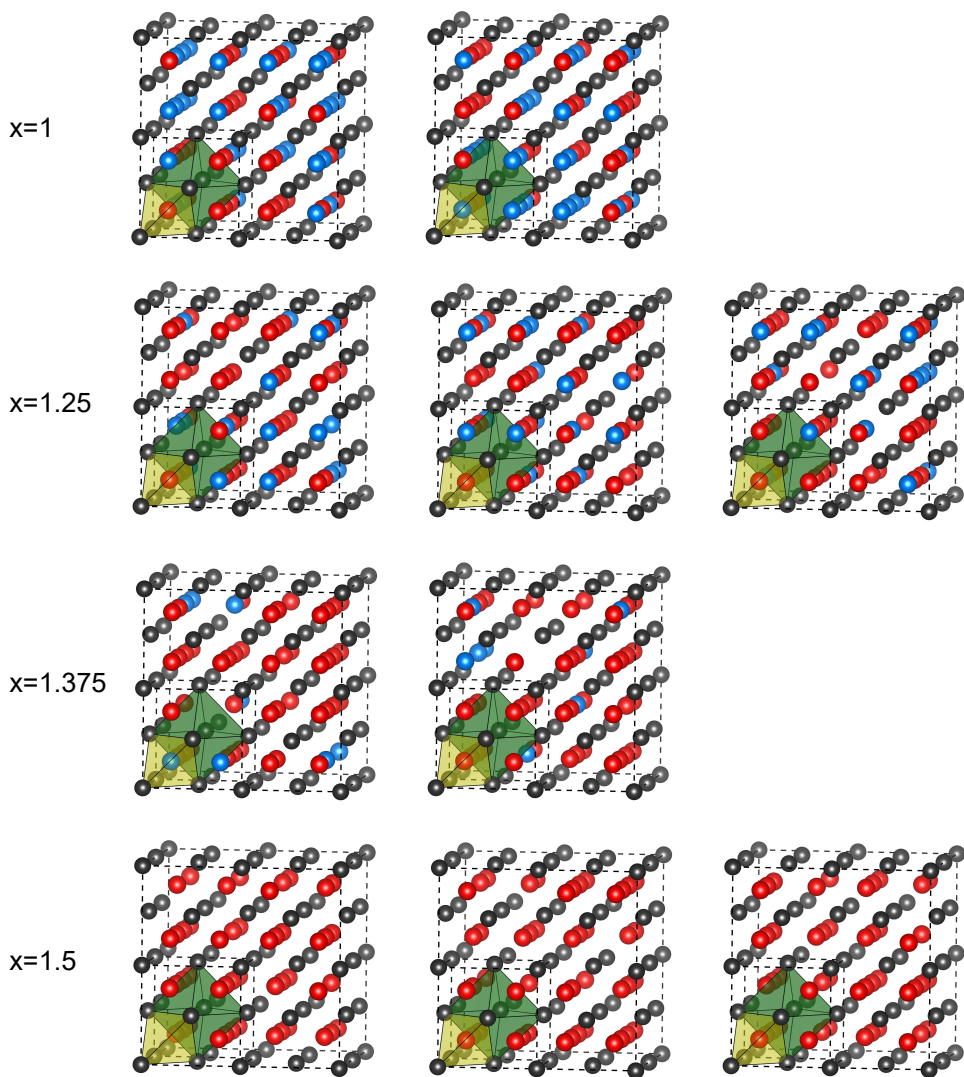
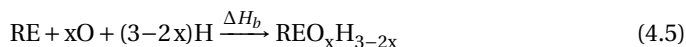


Figure 4.A.3: SQS used to model the anion-disordered RE oxyhydride of composition $x \geq 1$.

4.B. DFT BINDING, FORMATION AND LATTICE ENERGY

To avoid ill-defined absolute values of energy, in this work we always refer to energy differences between the absolute energy of the final compound and the absolute energy of its constituents (i) in their standard state, resulting in the formation energy (ΔH_f), (ii) in their atomized state, resulting in the binding energy (ΔH_b), and (iii) in their ionized state, resulting in the lattice energy (ΔH_L). Eq. 4.4, 4.5, and 4.6 report the corresponding reactions, which are also visualized in the Born-Haber cycle in Fig. 4.4.



This approach requires to calculate the energy of isolated molecules, spin-polarized atoms and ions. This was trivial from the neutral species but proved impossible for the highly charged O^{2-} , because a negative ion in a box with compensating background charge tends to lose electrons to the vacuum levels - a well known artefact of all semi-local DFT functionals (textbook wisdom).

Exploiting the Born-Haber cycle and the Hess's laws, we therefore calculate ΔH_L as the sum of binding energy, RE ionization energies, and O and H electron affinities (eq. 4.7). Here the binding energy is extracted from DFT (eq. 4.5), while ionization energies and electron affinities are taken from tabulated experimental data.

$$\Delta H_L = \Delta H_b + IE_{\text{RE} \rightarrow \text{RE}^{3+}} + xEA_{\text{O} \rightarrow \text{O}^{2-}} + (3-2x)EA_{\text{H} \rightarrow \text{H}^-} \quad (4.7)$$

4.C. COMPARISON BETWEEN MBJ AND G_0W_0

To verify the quality of the mBJ scheme in the prediction of electronic states, we show here the indirect E_g of some small Y-O-H compounds calculated with PBE, mBJ and G_0W_0 approximations (Fig. 4.C.1). For PBE and mBJ functionals, computational details are reported in the main text. Single-shot G_0W_0 calculations (i.e., no iteration of either G and W) are performed on the structures previously relaxed with PBE. We employed the dedicated pseudo-potentials provided in the VASP library, treating H 1s, O 2s2p, and Y 4s4p4d5s as valence orbitals. In comparison to mBJ and PBE, due to the higher computational cost of G_0W_0 , integration over the Brillouin zone are performed on a Γ -centred K-mesh of reduced density ($4 \times 4 \times 4$) and with a higher Gaussian smearing of 0.2 eV. Electronic transitions within the first 2000 bands are considered. With some exceptions (marked in fig. 4.C.1), we find that the indirect bandgap to be converged within $\delta E_g < 0.2$ eV.

4

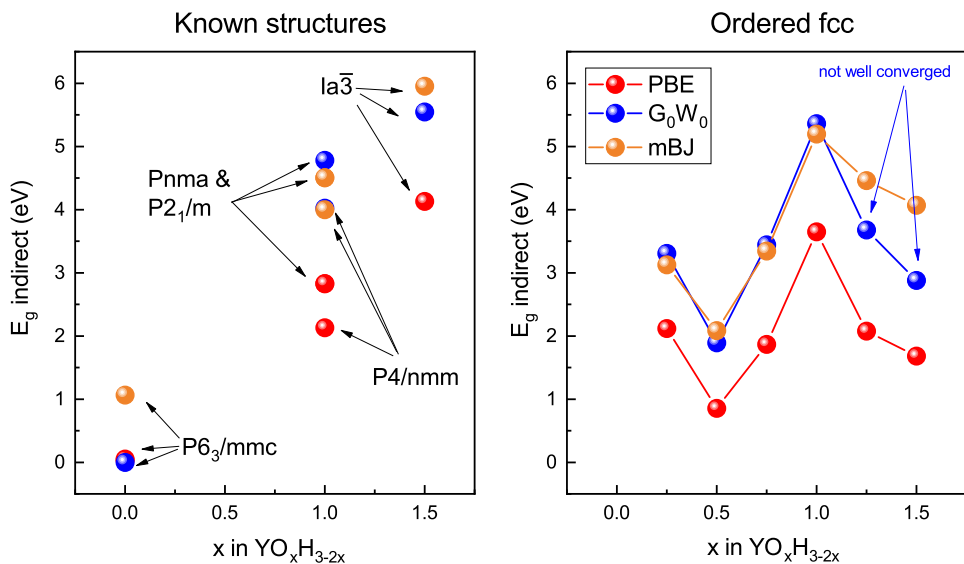


Figure 4.C.1: Comparison between the indirect bandgap of some small Y-O-H compounds calculated with PBE (red), mBJ (orange), and G_0W_0 (blue) approximations. Left panel: selection of some known anion-ordered structures. Right panel: anion-ordered schemes of lowest energy based on the CaF_2 motif.

4.D. MADELUNG ENERGY AND BORN-LANDÉ CORRECTION

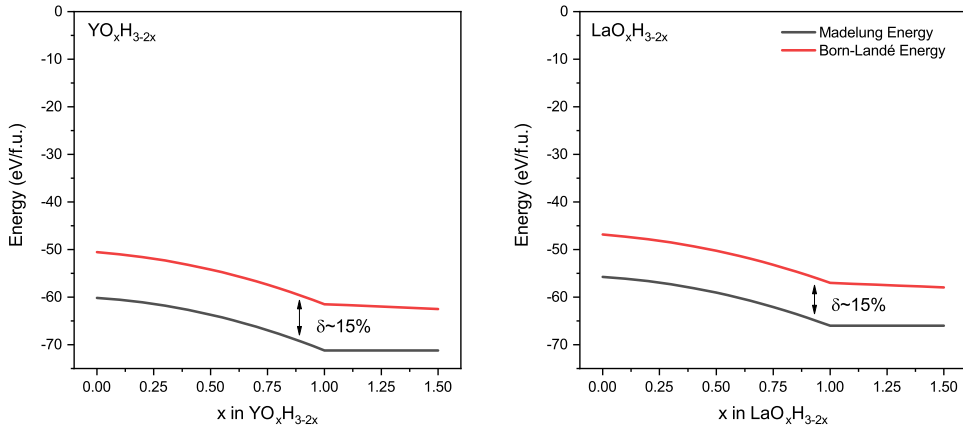


Figure 4.D.1: comparison between the Madelung Energy and the Born-Landé energy of anion-disordered Y and La oxyhydrides idealized according to the idealized model based on the CaF_2 motif. The Born-Landé correction reflects the repulsion due to the finite size of the atoms and thus predicts a lower stability for the compound. For Y and La oxyhydrides, we find a difference of $\sim 15\%$ between Madelung energy and Born-Landé energy.

4.E. RE-RE, RE-O, AND RE-H RADIAL DISTRIBUTION FUNCTION

4

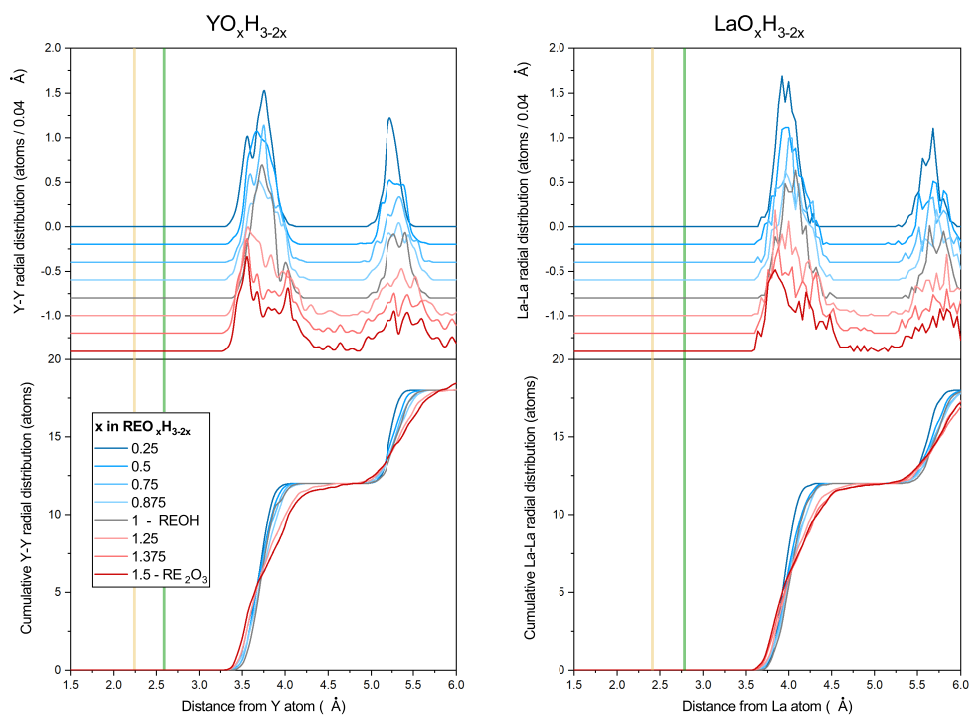


Figure 4.E.1: RE-RE Radial distribution functions (*top panels*) and their cumulative values (*bottom panels*) for the relaxed SQS of Y and La anion-disordered oxyhydrides. Yellow and green vertical lines mark the position of tetrahedral and octahedral interstitial anion-sites. To help visualization, lines in the top panels are shifted downward by a constant value of -0.2.

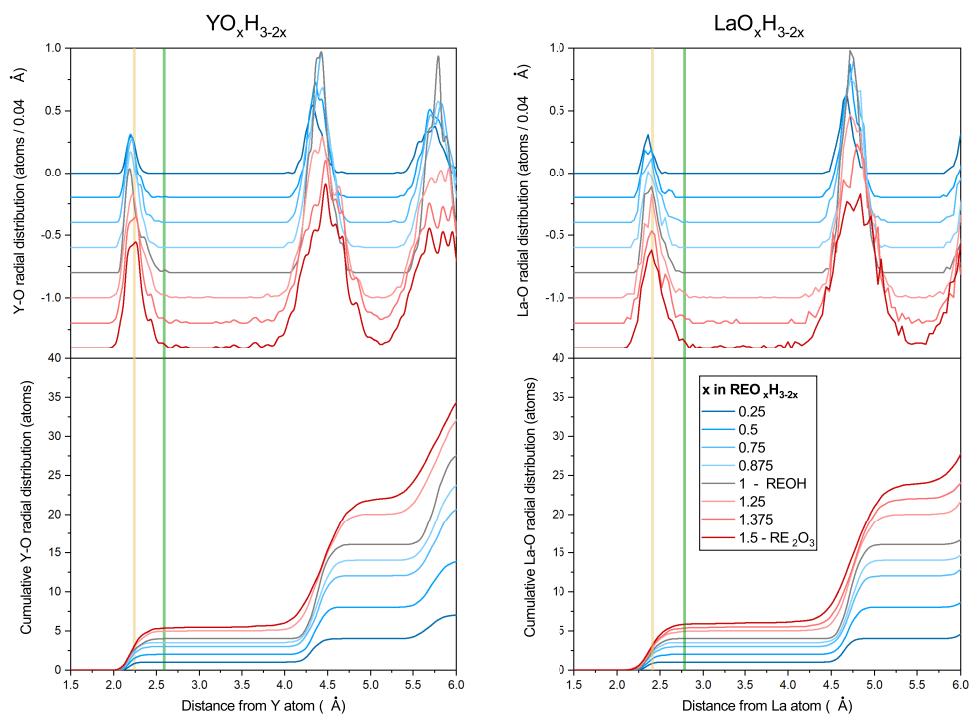


Figure 4.E.2: RE–O Radial distribution functions (*top panels*) and their cumulative values (*bottom panels*) for the relaxed SQS of Y and La anion-disordered oxyhydrides. Yellow and green vertical lines mark the position of tetrahedral and octahedral interstitial anion-sites. To help visualization, lines in the top panels are shifted downward by a constant value of -0.2.

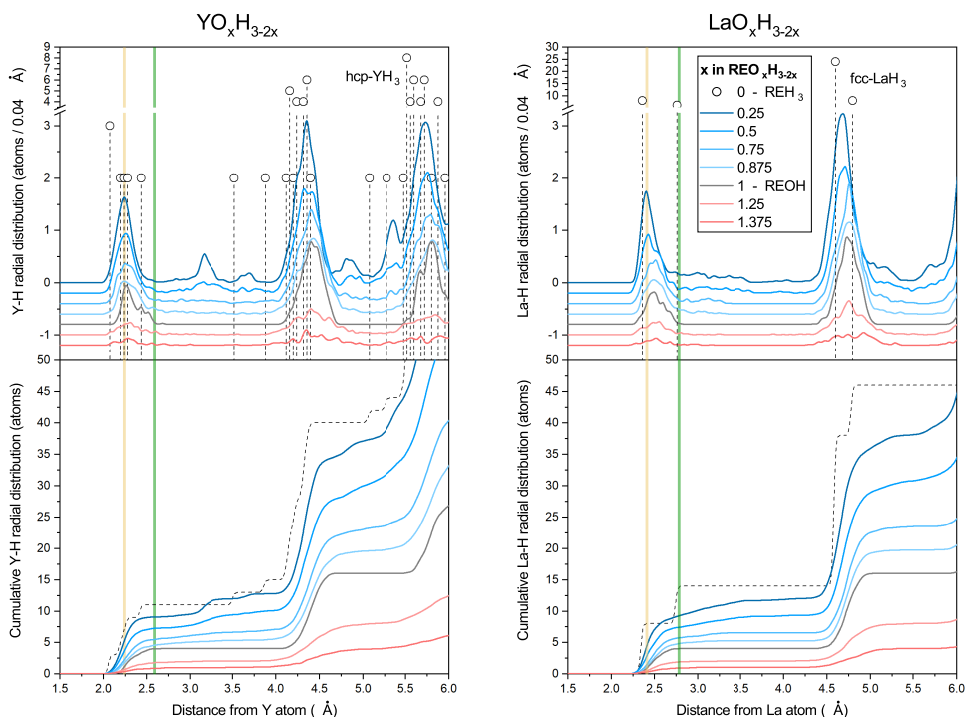


Figure 4.E.3: RE–H Radial distribution functions (*top panels*) and their cumulative values (*bottom panels*) for the relaxed SQS of Y and La anion-disordered oxyhydrides. The Dashed lines refer to the thermodynamically stable $P63/mmc$ - YH_3 and $Fm\bar{3}m$ - LaH_3 hydrides. Yellow and green vertical lines mark the position of tetrahedral and octahedral interstitial sites for an ideal fcc structure with lattice constant tuned to match the $\text{REO}_{0.25}\text{H}_{2.5}$ composition. The pink region highlights peaks that do not match the CaF_2 -type structure. To help visualization, lines in the top panels are shifted downward by a constant value of -0.2.

4.F. BANDGAP COMPARISON

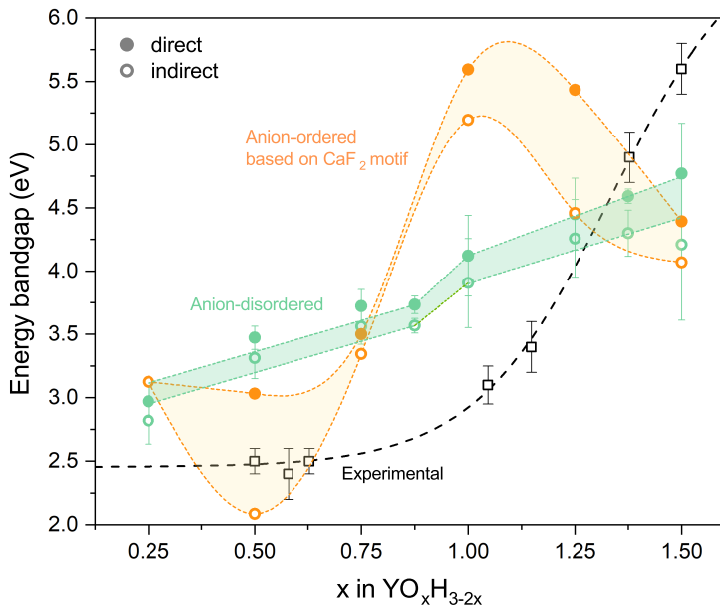


Figure 4.F1: Comparison between (i) the experimental optical gap of photochromic Y oxyhydride thin films (open squares), (ii) the direct/indirect energy bandgaps computed for anion-disordered structures and (green circles), (iii) the direct/indirect energy bandgaps computed for the anion-ordered structures of lowest energy among those possible in one CaF_2 -type unit cell (orange circles). Lines are a guide for the eyes.

4.G. REFRACTIVE INDEX COMPARISON

4

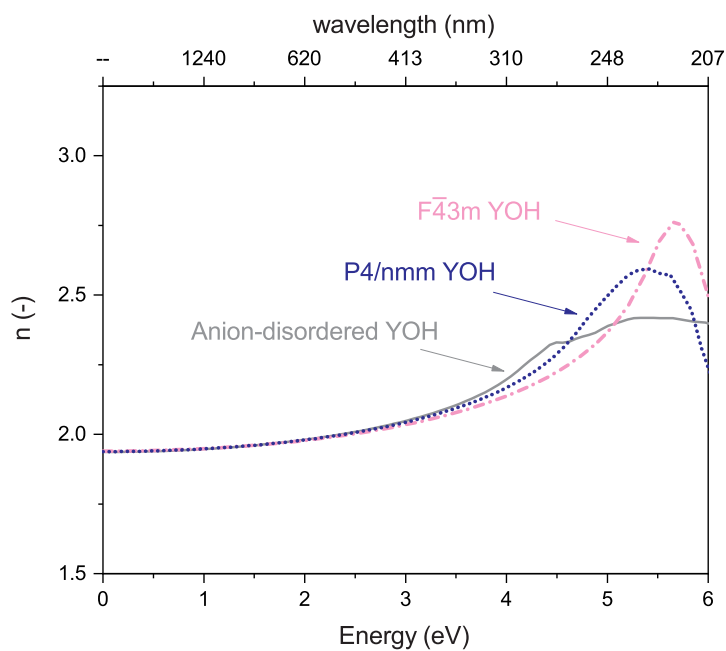


Figure 4.G.1: Comparison between the real refractive index of anion-disordered, $P4/nmm$, and $F\bar{4}3m$ YOH. At low energies, far from the absorption edge, the refractive index is completely dominated by the composition and not by the crystal structure.

REFERENCES

- [1] Z. Jiang, Y. Nahas, B. Xu, S. Prosandeev, D. Wang, and L. Bellaiche, *Special quasirandom structures for perovskite solid solutions*, IOP Publishing **28**, 475901 (2016).

5

INFLUENCE OF CATION (Sc, Y, Gd) AND O:H ANION RATIO ON THE PHOTOCHROMISM OF REO_xH_{3-2x} THIN FILMS

*We were the Leopards, the Lions;
those who'll take our place will be little jackals, hyenas;
and the whole lot of us, Leopards, jackals, and sheep,
we'll all go on thinking ourselves the salt of the earth.*

Giuseppe Tomasi di Lampedusa, *Il Gattopardo* (1958)

Rare-earth oxyhydride REO_xH_{3-2x} thin films prepared by air-oxidation of reactively sputtered REH_2 dihydrides show a color-neutral, reversible photochromic effect at ambient conditions. In this chapter, we show that the O:H anion ratio, as well as the choice of the cation, allow to largely tune the extent of the optical change and its speed. The bleaching time in particular can be reduced by an order of magnitude by increasing the O:H ratio, indirectly defined by the deposition pressure of the parent REH_2 . The influence of the cation ($RE=Sc, Y, Gd$) under comparable deposition conditions is discussed. Our data suggest that REs of larger ionic radius form oxyhydrides with larger optical contrast and faster bleaching speed, hinting to a dependency of the photochromic mechanism on the anion site-hopping.

This chapter is an adaptation of:

G. Colombi, T. De Krom, D. Chaykina, S. Cornelius, S. W.H. Eijt, and B. Dam, *Influence of cation ($RE=Sc, Y, Gd$) and O:H anion ratio on the photochromic properties of REO_xH_{3-2x} thin films*, ACS Photonics **8**, 709 (2021).

5.1. INTRODUCTION

While the properties of *single-anion* compounds, like the metal oxides, are to a large extent dictated by their cation chemistry, *multi-anion* compounds offer unprecedented degrees of freedom in the design of functional materials thanks to the broad spectrum of different anion characteristics, such as electronegativity, polarizability, and ionic radii. [1, 2] Within this class of materials, rare earth (RE) oxyhydride $\text{REO}_x\text{H}_{3-2x}$ compounds stand out not only for their exceptional H^- conductivity, [3, 4] but also for the possibility of preparing them via post-oxidation of reactively sputtered REH_2 thin films: a route of synthesis which allows indirect control over the resulting microstructure and O:H ratio. [5]

Since the first report in 2011, [6] $\text{REO}_x\text{H}_{3-2x}$ oxyhydride thin films prepared in this way (with $\text{RE}=\text{Sc}, \text{Y}, \text{Gd}, \text{Dy},$ and Er and $0.5 \leq x < 1.5$) have gathered increasing attention in view of their color-neutral reversible photochromic effect and photo-conductivity at ambient conditions, making them promising candidates for smart windows and sensors. [5, 7, 8]

While such optical behaviour is shared by many REs, it remains unexplored what is the root of such generality and the influence of the cation. In addition, the physical mechanism behind the photochromic effect is unclear, as well as its limits in terms of optical contrast and speed.

The present work exemplifies the tunability of the RE multi-anion compounds and contributes to the understanding of these materials by surveying the effect of both the cation and the O:H ratio on the photochromic contrast and speed of RE oxyhydrides thin films.

First, we show that the deposition pressure of the parent (i.e., as-grown) REH_2 indirectly defines the anion ratio of the final oxyhydride, as well as its porosity and lattice constant. Consequently, optical properties such as the refractive index, optical band gap, and photochromic behaviour can be tuned. We report that the bleaching time constant in particular can be reduced by an order of magnitude to below 10 min by an optimal choice of the deposition pressure.

Second, by having mapped the effect of the deposition pressure on the photochromic properties of Sc, Y, and Gd oxyhydrides, we address the influence of the cation under comparable deposition conditions. Our data suggest that REs of higher atomic number and larger ionic radius form oxyhydrides with *better* photochromic properties - i.e., larger optical contrast and faster bleaching speed.

To maintain connection with the bigger picture, the influence of the deposition pressure on the material properties is here discussed adopting a bird-eye perspective. Relevant supporting information are reported in the appendix.

5.2. EXPERIMENTAL

Sample preparation Sc, Y, and Gd based REH_2 thin films (thickness ~ 150 nm) were prepared by reactive magnetron sputtering of a 2-inch metal target (MaTeck Germany, 99.9% purity) in a Ar/H_2 (5N purity) atmosphere. The deposition chamber was kept at a base pressure below 1×10^{-6} Pa. During deposition the total gas flow was fixed at 40 sccm with an Ar/H_2 gas ratio of 7:1, while the total deposition pressure (p_{dep}) was varied by

means of a butterfly reducing valve mounted at the inlet of the pumping stage. The DC power supplied to the Sc, Y, and Gd targets was set at 200 W, 200 W, and 165 W respectively, corresponding to metal deposition rates of 1.2 \AA/s , 3.0 \AA/s and 3.0 \AA/s . All samples were grown on unheated UV-grade fused silica (f-SiO₂) and polished glassy carbon substrates.

The as-deposited REH₂ thin films were then oxidized in ambient conditions by exposure to air. Being the oxidation a self-limiting process, after a few days in air the samples reach a (meta)stable state (Fig. 5.A.1). All material characterization presented in this work was done only after such a stable condition was reached.

Sample characterization Structural and optical properties were studied by a combination of X-ray diffraction (XRD, Bruker D8 Discovery) and photospectrometry. A custom-built optical-fiber based *in-situ* spectrometer (range: 230-1150 nm) with a time resolution of ~ 1 s was employed to test the photochromic effect as triggered by a narrow-band LED ($\lambda = 385 \text{ nm}$, $I = 75 \text{ mW/cm}^2$). Throughout this work, all values of average transmittance, $\langle T \rangle$, refer to the interval $\lambda : [450, 1000] \text{ nm}$. The REO_xH_y chemical composition was studied by combination of Rutherford backscattering spectrometry (RBS) and elastic recoil detection (ERD) at the 2 MV Van-de-Graaff accelerator at Helmholtz-Zentrum Dresden-Rossendorf (Dresden, Germany).^[5] A series of thicker ($\sim 450 \text{ nm}$), Al-capped ($\sim 20 \text{ nm}$) Y oxyhydrides produced in the same way was studied by Doppler Broadening positron annihilation spectroscopy (DB-PAS) at the Variable Energy Positron (VEP) facility located at the Reactor Institute Delft (Netherlands). The aforementioned 385 nm LED was used for *in-situ* illumination (2.5 h), although with a reduced irradiance ($I = 30 \text{ mW/cm}^2$) due to the larger distance between light source and sample.

5.3. RESULTS

5.3.1. INFLUENCE OF DEPOSITION PRESSURE

Fig. 3.1 shows the impact of the deposition pressure of the parent REH₂ dihydride on the key material properties of the resulting REO_xH_{3-2x} after exposure to air. We observe similar trends in Sc, Y, and Gd oxyhydrides, whose cations respectively belong to the 4th, 5th, and 6th period of the periodic table and, albeit maintaining a similar chemistry and valence electron configuration, represent a wide range of ionic radii within the group of REs (Fig. 3.1a). Sc is the smallest extreme, while Gd is a good proxy for the largest lanthanides. Therefore we suppose that these trends are general to virtually any RE that forms a stable oxyhydride.

In Fig. 3.1b we distinguish three regions, reflecting the onset of the oxidation and the metal REH₂ dihydride to semiconducting REO_xH_{3-2x} oxyhydride transition. Nafezarefi et al.^[7] reported that oxygen incorporates only in RE dihydride thin films sputtered at a sufficiently high deposition pressure, above a threshold value (critical pressure, p^*) that depends on the RE and on the specificities of the sputtering chamber. Above this pressure, the metal-to-insulator transition takes place when exposing the thin film to air: an optical bandgap opens and the transmittance maxima at $E < E_g$ approach the value of the bare substrate, implying the absence of a second absorbing/scattering phase and a negligible concentration of deep, optically active defects.^[7] We recognize this behaviour

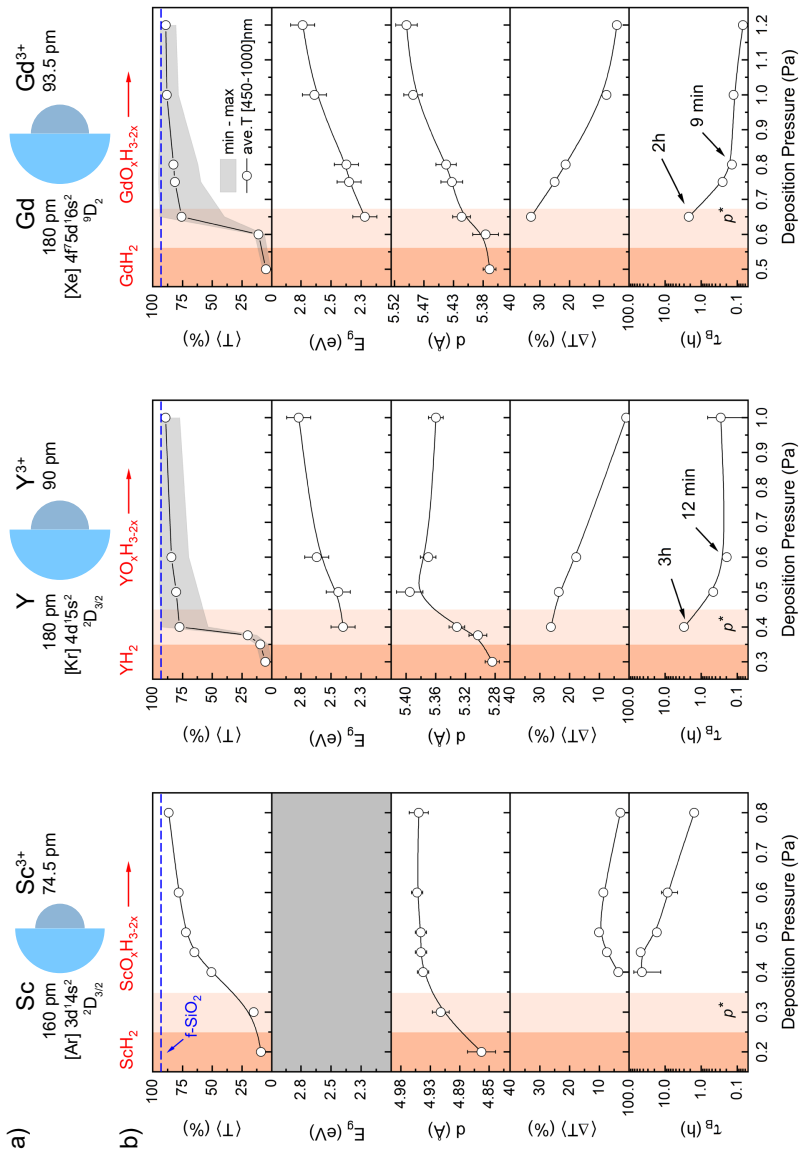
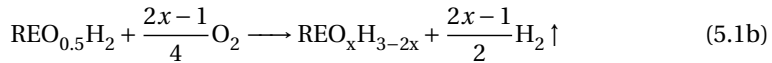


Figure 5.1: a) Radius, g ground state electron configuration, and term symbol for Sc, Y, and Gd atoms. The Shannon effective radii of their trivalent ions are also given. r_{Sh} b) Effect of deposition pressure of the parent REH_2 dihydride (RE=Sc, Y, Gd) on the key material properties of the resulting $\text{REO}_x\text{H}_{3-2x}$ after exposure to air - From top to bottom: min, max and average optical transmittance ($\langle T \rangle$), optical band gap (E_g), lattice constant (d), photochromic contrast ($\langle \Delta T \rangle$), and photochromic bleaching time (τ_B). A higher deposition pressure results in a higher porosity and, consequently, higher oxygen content. Samples sputtered at pressures below the critical pressure p^* (dark orange background) do not incorporate oxygen upon air exposure and remain optically thick REH_2 metal hydrides. Around p^* (light orange background) the metal to semi-conducting $\text{REO}_x\text{H}_{3-2x}$ transition sets in. Films sputtered at $p \sim p^*$ show composition gradients, with higher oxygen concentration at the film surface (Fig. S3). Only at higher deposition pressures ($p > p^*$), single-phase homogeneous photochromic oxyhydrides are obtained. Further increase in deposition pressure leads to increasing O:H ratio (Fig. S3), decreasing photochromic contrast and faster bleaching.

in Y and Gd oxyhydrides (Fig. 3.1b, top panel) while the absorption spectra of Sc-based compounds show a prominent absorption tail (Fig. 5.B.1) which extends to the whole measured spectral range and impedes the evaluation of the optical bandgap from the transmittance spectra.

RBS/ERD data show that the Sc, Y, and Gd oxyhydride thin films sputtered at pressures near p^* (0.3 Pa, 0.375 Pa, and 0.6 Pa respectively) present a composition gradient throughout their thickness, resembling the diffusion profile of oxygen starting from the film surface. Only at higher deposition pressures homogeneous photochromic oxyhydrides are obtained (Fig. 5.C.1). RBS/ERD data additionally verify that a higher deposition pressure results in a higher O:H ratio, in qualitative agreement with the progressive decrease of refractive index - as implied by the decreasing amplitude of the thin-film interference oscillations (Fig. S2; Fig. 3.1b, top panel) - and with previous studies on both Y and Gd oxyhydride thin films. [8] [11] [12] We argued recently that the reaction from metallic REH_2 dihydride to photochromic $\text{REO}_x\text{H}_{3-2x}$ oxyhydride happens in two steps: [5] [13] first, a net oxygen incorporation (Eq. 5.1a); second, a continuous oxygen-for-hydrogen (1:2) exchange (Eq. 5.1b). [13]



These reactions are driven by a large gain in lattice energy and occur spontaneously even at ambient conditions when the kinetic barriers of oxygen diffusion are not prohibitive. [13] In this context, porosity is an enabling factor for the formation of RE-oxyhydrides via post oxidation of sputtered REH_2 thin films. As depicted in the well-known sputtering zone diagram, [14] a higher deposition pressure translates to a higher porosity because of the increased probability of collisions of the sputtered atoms in the gas phase, and therefore a reduced kinetic energy once they reach the substrate. Thus, higher deposition pressures lead to higher O:H ratios due to the increased porosity of the films.

Though we can tune the O:H ratio by the deposition pressure, we find that this is limited to the H-rich range ($0.5 < x < 1$) of the $\text{REO}_x\text{H}_{3-2x}$ composition line. Indeed, the optical band gap gradually increases from 2.3(1) eV to 2.8(1) eV (Fig. 3.1b, second panel) and, by comparison to the phenomenological relation that links E_g and composition, [5] shows that all the oxyhydrides investigated here belong to the H-rich region. Hence, in agreement with our previous ion-beam analysis, [5] it appears that O-rich oxyhydrides ($x > 1$) with $E_g \geq 3$ eV do not form via air exposure of highly porous REH_2 films at room temperature. This might relate to the limited driving force for further oxygen inclusion at $x > 1$, [13] as well as to the substrate-induced strain that hinders the further lattice expansion and distortion that is expected for compositions that approach the bixbyite oxide.

While no obvious structural phase change is observed from the $\text{fcc-}Fm\bar{3}m$ structure motif of the parent dihydride (Fig. 5.D.1), we note, in agreement with previous works, [5] [7] that the oxidation to the oxyhydride state is accompanied by a lattice expansion (Fig. 3.1b, third panel). Our data show that reaction 5.1a, which coincides with the oxidation of

the cation from RE^{2+} to RE^{3+} and with the metal to semiconductor transition, is always accompanied by a lattice expansion, intuitively needed to accommodate the additional O^{2-} anions. The volume changes corresponding to reaction 5.1b appear instead to be different from cation to cation, with Sc plateauing, Y showing a weak maximum, and Gd expanding monotonously for increasing deposition pressures.

The lower two panels in Fig. 3.1b show the dependence of the photochromic properties of Sc, Y, and Gd oxyhydrides on the deposition pressure. While the full cycles of photo-darkening (30 min) and bleaching are reported in Fig. 5.E.1, we introduce here two figures of merit to quantitatively express the photochromic behaviour in terms of the application-limiting aspects, namely the magnitude of the optical change and its speed. First, we define the absolute contrast, $\langle \Delta T \rangle$, as the difference between the initial average transmittance, $\langle T_0 \rangle$, and that at the end of the darkening, $\langle T_{\text{dark}} \rangle$:

$$\langle \Delta T \rangle = \langle T_0 \rangle - \langle T_{\text{dark}} \rangle. \quad (5.2)$$

Second, we address the bleaching speed via a characteristic time constant, τ_B , which reflects the time required for the material to revert to its initial transmittance after the illumination is ceased. Under the only hypothesis that all absorbing species formed during illumination disappear following reaction kinetics of equal order, τ_B is equal to the inverse of the weighted-average rate at which the photo-generated absorbing species disappear. Assuming a first order bleaching kinetics, Eq. 5.3 is employed in Fig. 5.E.1 to derive the bleaching time constant from the time evolution of the average optical transmittance $\langle T(t) \rangle$: 115

$$\ln \left(-\ln \frac{\langle T(t) \rangle}{\langle T_0 \rangle} \right) = -\frac{1}{\tau_B} t - \ln \langle T_{\text{dark}} \rangle. \quad (5.3)$$

A higher deposition pressure leads to photochromic Sc, Y, and Gd oxyhydrides of lower absolute contrast and significantly shorter bleaching time. The latter in particular is reduced by an order of magnitude, from *tens* of hours to *some* hours for Sc-based oxyhydrides and from *few* hours to *few* minutes for Y and Gd based oxyhydrides. It appears that the atomic number of the cation, and even more its size, correlates with overall *better* photochromic properties - i.e., larger contrast and faster kinetics. The ~ 150 nm Gd oxyhydride films produced at higher pressures, with a bleaching time constant below 10 min, present the *best* bleaching kinetics among the RE oxyhydrides thin films studied here. At the time of writing, quantitative analysis of the bleaching kinetics can be found only in ref. [8] and [13]; where time constants in the order of several hours are reported for bare and Zr-doped Y oxyhydride films. Similarly long bleaching times can be qualitatively observed also elsewhere. 116

5.3.2. IRREVERSIBLE LIGHT-INDUCED VACANCY FORMATION

While the relation between deposition pressure (i.e., composition), optical band gap, and lattice constant is fairly well understood, the mechanism behind the photochromic effect remains unclear. The bandgap excitation points to an electronic origin; yet, at present it is not known if other electronic processes follow the inter-band absorption. In any case, the

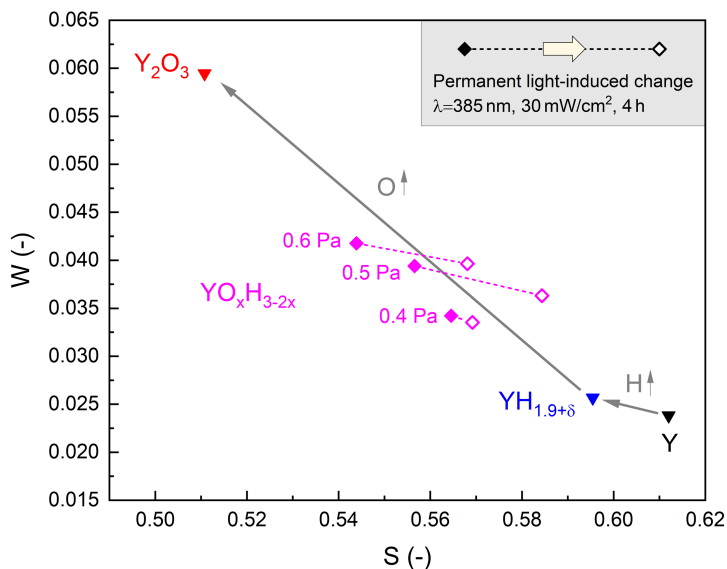


Figure 5.2: DB-PAS S:W diagram of the Y to YH_2 to Y_2O_3 composition range, including $\text{YO}_x\text{H}_{3-2x}$ oxyhydrides sputtered at different deposition pressures in their virgin state (full points). The arrows indicate the general trends in S:W for the transition from metallic Y to metallic YH_2 (hydrogenation) to insulating Y_2O_3 (oxidation). The open points show the permanent light-induced change in the S:W of the oxyhydrides after a full cycle of photo-darkening (4h) and bleaching in the dark (72h).

large time constants involved in the photochromism suggest that structural rearrangement might play a dominant role. In this sense, it was hinted that the photo-darkening depends on the segregation of an absorbing phase, [17, 18] a process accompanied by reversible contraction of the crystal lattice [16, 19] and quenching of the NMR signal of the most mobile H fraction ($\sim 3\%$). [20] Hence, in the following we consider the influence of the deposition pressure on both electronic and structural properties, and support our discussion with the insight from DB-PAS on Y-based thin films.

In Fig. 5.2 reference materials and photochromic oxyhydrides sputtered at different deposition pressures are mapped versus the so-called line shape DB-PAS parameters W and S, which indicate the probability of positron annihilation with electrons of high momentum (e.g., (semi-)core states), and low momentum (e.g., semiconductor valence states), respectively. We have already mentioned that the deposition pressure influences the final composition and hence the optical bandgap. Accordingly, DB-PAS shows a trend of increasing W and reduced S parameter upon increased O:H ratio, indicating a broadening of the electron momentum distribution as the valence band gains a progressively larger O(2p) character. This supports the hypothesis, originally advanced by Cornelius et al. [5] in analogy to other multi anion compounds, that the valence band of RE oxyhydrides is a mixture of occupied H(1s) and O(2p) states, and that it shifts towards lower energies with increasing O:H ratio because of the higher electronegativity of oxygen ($\chi_{\text{O}} = 3.44$) compared to hydrogen ($\chi_{\text{H}} = 2.20$).

After a full cycle of photo-darkening and bleaching, we observe irreversible changes in the S:W parameters of all samples, evidence that permanent light-induced structural modifications occur in Y oxyhydrides sputtered at any deposition pressure. In particular, we find the same trend originally reported by Plokker et al., [21] where upon *in-situ* illumination S increases and W decreases, suggesting a permanent formation of positron trapping sites that might include negatively charged cation monovacancies (V_Y) or neutrally charged vacancy clusters (e.g. V_Y-V_H , V_H-V_H , V_O-V_H). [21] [22] Visually, we note that the direction of the change in the S:W plot is similar for all samples. This is quantified by the so-called R parameter ($R = \Delta S/\Delta W$), a defect-specific value which is independent of the concentration of defects and on the positron trapping efficiency. [23] For $\text{YO}_x\text{H}_{3-2x}$ sputtered at 0.4, 0.5, and 0.6 Pa we find respectively $R = -7(5)$, $R = -9(1)$, and $R = -11(3)$. While further studies are needed to exactly identify the vacancies that irreversibly form upon photo-darkening, the fact that all samples show a similar R parameter suggests that the deposition pressure does not influence the type of formed negative and/or neutral vacancies seen by DB-PAS. This vacancy formation under modest illumination conditions indicates local mobility/displacement of ions in the RE oxyhydrides induced by photo-excitation. However, we exclude that the involvement of these vacancies is a necessary condition for the bleaching to occur, since no reversibility over time is observed in the oxyhydrides deposited at 0.5 Pa and 0.6 Pa (Fig. 5.F1 Fig. 5.F2 Fig. 5.F3).

5

5.4. DISCUSSION

Let us now look at the implications of a change in O:H ratio in more detail. Recently we verified that for any oxyhydride composition ($\text{REO}_x\text{H}_{3-2x}$ with $0.5 \leq x \leq 1.5$) the O^{2-} anions are located in the tetrahedral interstitial sites defined by the cation lattice. [13] On that basis, we proposed an idealized structure model which serves as a guideline to estimate the fraction and type of free interstitial sites depending on the anion ratio. Fig. 5.3 shows the correlation between this structural model and the trend observed in this work of decreasing photochromic contrast and increasing bleaching speed upon O:H ratio.

We suppose that RE oxyhydride thin films share the exceptional H^- conductivity of the bulk RE oxyhydrides, [3] [4] and that the mobility of the hydride ions is an enabling factor for the photo-darkening. While there is yet no data available for either local or long-range hydrogen motion in $\text{REO}_x\text{H}_{3-2x}$ thin films, $\text{LaO}_x\text{H}_{3-2x}$ powders show higher H^- ionic conduction at lower O:H anion ratio (i.e., lower x). [3] Comparing to the trend of photochromic contrast in the compositional interval $0.5 < x < 1$, the bulk diffusion of H^- ions might then influence the overall extent of the photochromic process: the increase in contrast would then be related to an increase in the H^- diffusion coefficients. In this range of compositions, we suggest that H^- ions move either via *direct* hopping between neighbouring octahedral sites or via the *indirect* hopping mediated by tetrahedral vacancies, in analogy to what is proposed for other fluorite-type anion conductors, such as LnOH (with $\text{Ln}=\text{La, Nd}$), [4] $\beta\text{-PbF}_2$, [24] and $\beta\text{-PbSnF}_4$. [25] Conversely, we expect *direct* tetrahedral-based mobility to be severely inhibited by the lack of free tetrahedral sites and by the high activation energy. [4] In this sense, we point out that the Y and Gd oxyhydrides

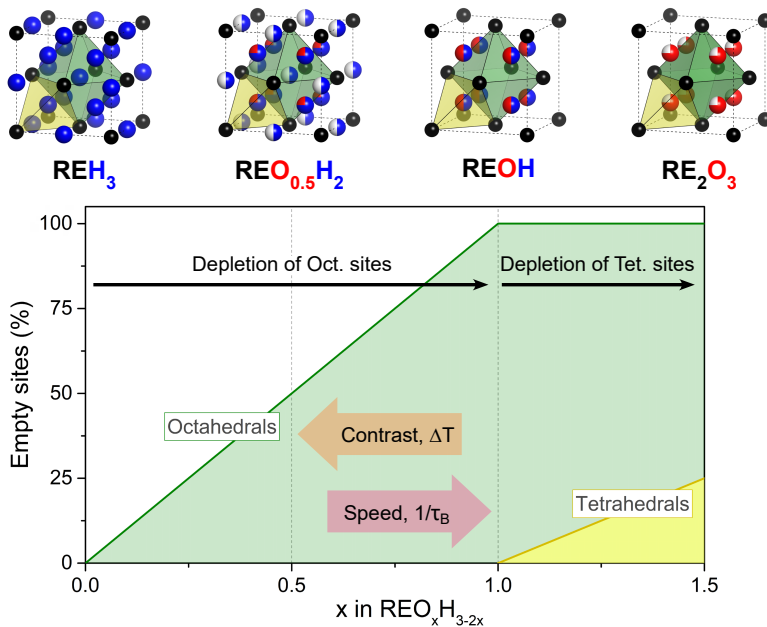


Figure 5.3: Fraction of empty octahedral (green polygons) and tetrahedral (yellow polygons) interstitial sites upon increasing O:H ratio in fcc, anion-disordered $\text{REO}_x\text{H}_{3-2x}$ oxyhydrides. The arrows indicate the correlation with the photochromic contrast and bleaching time constant.

produced respectively at 1.0 Pa and 1.2 Pa are only weakly photochromic ($\langle \Delta T \rangle < 4\%$) and their $E_g = 2.8(1)$ eV suggests a composition that approaches the stoichiometric REOH. [5](#) Possibly the photochromic properties of oxyhydrides of composition close to $x = 1$ are suppressed due to their specific interstitial-site occupation (tetrahedrals all occupied and octahedrals all empty) which hinders the aforementioned diffusion pathways and therefore reduces the attempt frequency for site hopping and the anion mobility altogether. [3](#) Finally, it cannot be excluded that also the diffusion of oxygen plays a role, as suggested by Baba et al. [16](#) When compared to the rate of hydrogen hopping, however, the oxide sublattice of bulk oxyhydrides is found essentially stationary by computational [3, 4, 26-28](#) and experimental [29, 30](#) works alike. Intuitively, the reason lies in the lower polarizability and double charge of the O^{2-} oxide ions compared to H^- hydride ions. [11](#)

The fact that we could rationalize (i) composition, (ii) optical transmittance, (iii) optical bandgap, (iv) lattice constant, and (v) trends in photochromic properties within the framework of a single-phase line-compound strongly indicates that the photochromism is an intrinsic property of the $\text{REO}_x\text{H}_{3-2x}$ oxyhydride phase. We note that the alternative hypothesis of Hans et al., [31](#) who recently proposed the co-existence of an oxide and a dihydride phase, is not compatible with the well-established optical bandgaps and complete transmittance for $E < E_g$ of $\text{REO}_x\text{H}_{3-2x}$ thin films. Conversely, our careful study of the oxidation behaviour and its dependency on the deposition pressure can explain the specific composition reported by Hans et al. as that of a partially oxidized REH_2 , a non-general case that we obtain only around p^* . However, we do not exclude the

possibility of domains with slightly reduced/increased oxygen or hydrogen content - i.e., small local variations of x within the $\text{REO}_x\text{H}_{3-2x}$ phase. In analogy to what observed in mixed halide perovskites, as recently reviewed by Brennan et al.,^[32] local compositional inhomogeneity of this type might facilitate structural rearrangements upon illumination.

5.5. CONCLUSION

In summary, we have systematically shown that the photochromic properties of $\text{REO}_x\text{H}_{3-2x}$ oxyhydrides thin films, namely the photochromic contrast and the bleaching kinetics, can be largely tuned controlling the deposition pressure of the parent REH_2 . We suppose that the root of this tunability lies in the different O:H anion ratio and, consequently, in the different number and energetics of the empty sites which enable anion hopping and therefore facilitate the structural rearrangements thought to occur during the photochromic process. DB-PAS shows vacancy formation during photo-darkening, indicating local mobility of ions as a consequence of photo-excitation of charge carriers. However, the observed vacancy formation is irreversible and does not play an essential role in the bleaching process. The photochromic properties of oxyhydrides of different REs are compared in a comprehensive way, showing a trend of increasing contrast and bleaching speed from Sc to Y to Gd based oxyhydrides. While a conclusive answer on the role of the cation is still missing, we note that these trends and their correlation to the cation size hint once again to a process limited by diffusion. As a matter of fact, the cation size translates to a larger lattice constant, 4.94(4) Å for Sc, 5.36(4) Å for Y, and 5.45(6) Å for Gd oxyhydrides, reducing the activation barriers for site hopping.^[4] However we do not exclude that other factors indirectly influenced by the deposition pressure might play a role in the photochromic process - e.g. porosity, grain size, defects, texture, stress, and degree of anion ordering.

The fact that we could produce photochromic films that bleach in less than 10 minutes brings the RE oxyhydrides one step closer to applications as smart coatings for sensors and windows.

REFERENCES

- [1] H. Kageyama, K. Hayashi, K. Maeda, J. P. Attfield, Z. Hiroi, J. M. Rondinelli, and K. R. Poeppelmeier, *Expanding frontiers in materials chemistry and physics with multiple anions*, [Nat. Commun. **9**, 772 \(2018\)](#).
- [2] Y. Kobayashi, O. Hernandez, C. Tassel, and H. Kageyama, *New chemistry of transition metal oxyhydrides*, [Sci. Technol. Adv. Mater. **18**, 905 \(2017\)](#).
- [3] K. Fukui, S. Iimura, T. Tada, S. Fujitsu, M. Sasase, H. Tamatsukuri, T. Honda, K. Ikeda, T. Otomo, and H. Hosono, *Characteristic fast H^- ion conduction in oxygen-substituted lanthanum hydride*, [Nat. Commun. **10**, 2578 \(2019\)](#).
- [4] H. Ubukata, T. Broux, F. Takeiri, K. Shitara, H. Yamashita, A. Kuwabara, G. Kobayashi, and H. Kageyama, *Hydride conductivity in an anion-ordered fluorite structure $LnHO$ with an enlarged bottleneck*, [Chem. Mater. **31**, 7360 \(2019\)](#).
- [5] S. Cornelius, G. Colombi, F. Nafezarefi, H. Schreuders, R. Heller, F. Munnik, and B. Dam, *Oxyhydride nature of rare-earth-based photochromic thin films*, [The Journal of Physical Chemistry Letters **10**, 1342 \(2019\)](#).
- [6] T. Mongstad, C. Platzer-Björkman, J. P. Maehlen, L. P. Mooij, Y. Pivak, B. Dam, E. S. Marstein, B. C. Hauback, and S. Z. Karazhanov, *A new thin film photochromic material: Oxygen-containing yttrium hydride*, [Sol. Energy Mater. Sol. Cells **95**, 3596 \(2011\)](#).
- [7] F. Nafezarefi, H. Schreuders, B. Dam, and S. Cornelius, *Photochromism of rare-earth metal-oxy-hydrides*, [Appl. Phys. Lett. **111**, 103903 \(2017\)](#).
- [8] C. C. You, T. Mongstad, E. S. Marstein, and S. Z. Karazhanov, *The dependence of structural, electrical and optical properties on the composition of photochromic yttrium oxyhydride thin films*, [Materialia **6**, 100307 \(2019\)](#).
- [9] J. C. Slater, *Atomic radii in crystals*, [J. Chem. Phys. **41**, 3199 \(1964\)](#).
- [10] R. D. Shannon, *Revised effective ionic radii and systematic studies of interatomic distances in halides and chalcogenides*, [Acta Crystallogr., Sect. A: Found. Adv. **32**, 751 \(1976\)](#).
- [11] C. C. You, T. Mongstad, J. P. Maehlen, and S. Karazhanov, *Engineering of the band gap and optical properties of thin films of yttrium hydride*, [Appl. Phys. Lett. **105**, 031910 \(2014\)](#).
- [12] E. M. Baba, J. Montero, D. Moldarev, M. V. Moro, M. Wolff, D. Primetzhofer, S. Sartori, E. Zayim, and S. Karazhanov, *Preferential orientation of photochromic gadolinium oxyhydride films*, [Molecules **25**, 3181 \(2020\)](#).
- [13] G. Colombi, S. Cornelius, A. Longo, and B. Dam, *Structure model for anion-disordered photochromic gadolinium oxyhydride thin films*, [J. Phys. Chem. C **124**, 13541 \(2020\)](#).

- [14] A. Anders, *A structure zone diagram including plasma-based deposition and ion etching*, [Thin Solid Films **518**, 4087 \(2010\)](#).
- [15] F. Nafezarefi, S. Cornelius, J. Nijskens, H. Schreuders, and B. Dam, *Effect of the addition of zirconium on the photochromic properties of yttrium oxy-hydride*, [Sol Energy Mater. Sol. Cells **200**, 109923 \(2019\)](#).
- [16] E. M. Baba, J. Montero, E. Strugovshchikov, E. O. Zayim, and S. Karazhanov, *Light-induced breathing in photochromic yttrium oxyhydrides*, [Phys. Rev. Mater. **4**, 025201 \(2020\)](#).
- [17] J. Montero, F. A. Martinsen, M. García-Tecedor, S. Z. Karazhanov, D. Maestre, B. Hauback, and E. S. Marstein, *Photochromic mechanism in oxygen-containing yttrium hydride thin films: An optical perspective*, [Phys. Rev. B **95**, 201301 \(2017\)](#).
- [18] J. Montero and S. Z. Karazhanov, *Spectroscopic ellipsometry and microstructure characterization of photochromic oxygen-containing yttrium hydride thin films*, [Phys Status Solidi A **215**, 1701039 \(2018\)](#).
- [19] J. P. Maehlen, T. T. Mongstad, C. C. You, and S. Karazhanov, *Lattice contraction in photochromic yttrium hydride*, [J. Alloys Compd. **580**, S119 \(2013\)](#).
- [20] C. V. Chandran, H. Schreuders, B. Dam, J. W. G. Janssen, J. Bart, A. P. M. Kentgens, and P. J. M. van Bentum, *Solid state nmr studies of the photochromic effects of thin films of oxygen containing yttrium hydride*, [J. Phys. Chem. C **118**, 22935 \(2014\)](#).
- [21] M. Plokker, S. Eijt, F. Naziris, H. Schut, F. Nafezarefi, H. Schreuders, S. Cornelius, and B. Dam, *Electronic structure and vacancy formation in photochromic yttrium oxy-hydride thin films studied by positron annihilation*, [Sol. Energy Mater. Sol. Cells **177**, 97 \(2018\)](#).
- [22] S. W. H. Eijt, T. W. H. de Krom, D. Chaykina, H. Schut, G. Colombi, S. Cornelius, W. Egger, M. Dickmann, C. Hugenschmidt, and B. Dam, *Photochromic YO_xH_y thin films examined by in situ positron annihilation spectroscopy*, [Acta Phys. Pol., A **137**, 2041 \(2020\)](#).
- [23] R. Krause-Rehberg and H. S. Leipner, *Positron Annihilation in Semiconductors: Defect Studies* (Springer Verlag, Berlin, 1999) p. 93.
- [24] K. Koto, H. Schulz, and R. A. Huggins, *Anion disorder and ionic motion in lead fluoride (β - PbF_2)*, [Solid State Ionics **1**, 355 \(1980\)](#).
- [25] P. Hagenmuller, J.-M. Réau, C. Lucat, S. Matar, and G. Villeneuve, *Ionic conductivity of fluorite-type fluorides*, [Solid State Ionics **3-4**, 341 \(1981\)](#).
- [26] Q. Bai, X. He, Y. Zhu, and Y. Mo, *First-principles study of oxyhydride H^- ion conductors: toward facile anion conduction in oxide-based materials*, [ACS Appl. Energy Mater. **1**, 1626 \(2018\)](#).

- [27] X. Liu, T. S. Bjørheim, and R. Haugrud, *Formation of defects and their effects on hydride ion transport properties in a series of K_2NiF_4 -type oxyhydrides*, *J. Mater. Chem A* **6**, 1454 (2018).
- [28] X. Liu, T. S. Bjørheim, L. Vines, Ø. S. Fjellvåg, C. Granerød, Ø. Prytz, T. Yamamoto, H. Kageyama, T. Norby, and R. Haugrud, *Highly correlated hydride ion tracer diffusion in $SrTiO_{3-x}H_x$ oxyhydrides*, *J. Am. Chem. Soc.* **141**, 4653 (2019).
- [29] T. Yajima, F. Takeiri, K. Aidzu, H. Akamatsu, K. Fujita, W. Yoshimune, M. Ohkura, S. Lei, V. Gopalan, K. Tanaka, C. M. Brown, M. A. Green, T. Yamamoto, Y. Kobayashi, and H. Kageyama, *A labile hydride strategy for the synthesis of heavily nitridized $BaTiO_3$* , *Nat. Chem.* **7**, 1017 (2015).
- [30] Y. Tang, Y. Kobayashi, K. Shitara, A. Konishi, A. Kuwabara, T. Nakashima, C. Tassel, T. Yamamoto, and H. Kageyama, *On hydride diffusion in transition metal perovskite oxyhydrides investigated via deuterium exchange*, *Chem. Mater.* **29**, 8187 (2017).
- [31] M. Hans, T. T. Tran, S. M. Aðalsteinsson, D. Moldarev, M. V. Moro, M. Wolff, and D. Primetzhofer, *Photochromic mechanism and dual-phase formation in oxygen-containing rare-earth hydride thin films*, *Adv. Opt. Mater.* **8**, 2070078 (2020).
- [32] M. C. Brennan, A. Ruth, P. V. Kamat, and M. Kuno, *Photoinduced anion segregation in mixed halide perovskites*, *Trends Chem.* **2**, 282 (2020).

APPENDIX

5.A. AIR OXIDATION

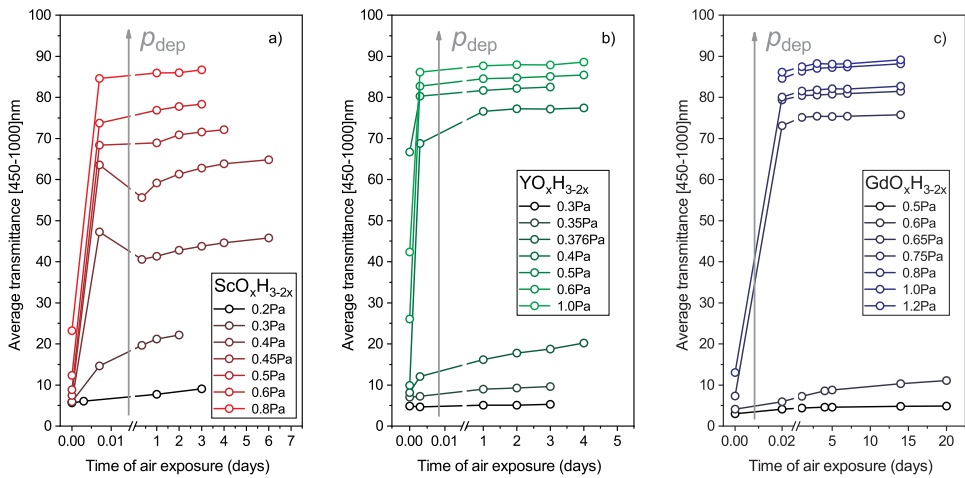


Figure 5.A.1: Evolution of the average transmission during air oxidation at ambient conditions of (a) ScO_xH_{3-2x} , (b) YO_xH_{3-2x} , and (c) GdO_xH_{3-2x} oxyhydroxides sputtered at different deposition pressures. Grey arrows indicate the trend with the deposition pressure.

5.B. TRANSMISSION SPECTRA AND ENERGY BANDGAP

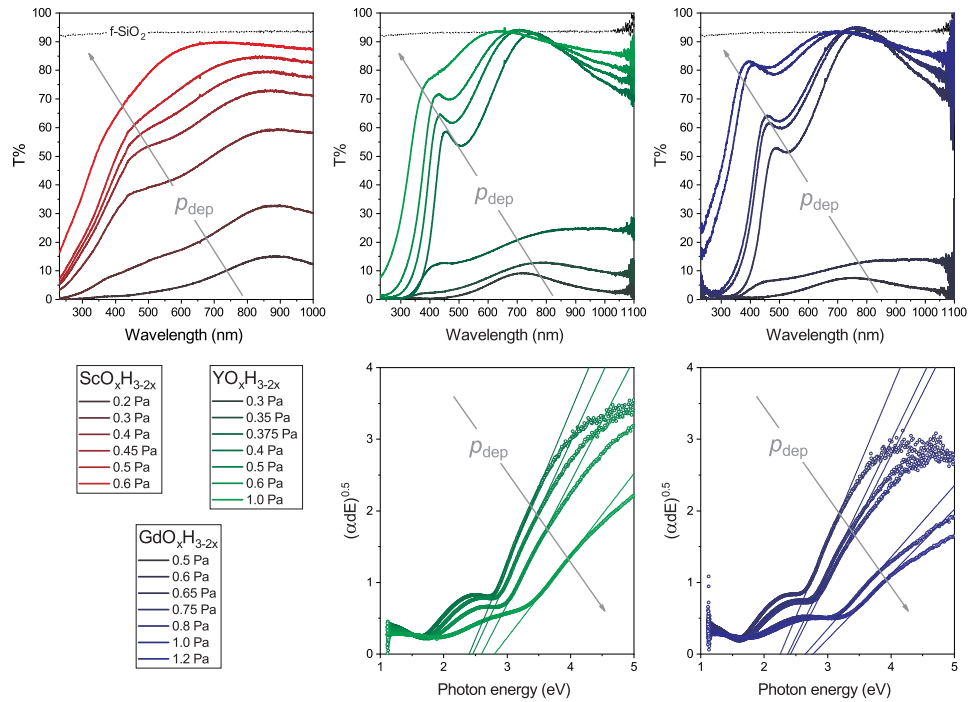


Figure 5.B.1: *Top*: Transmission spectra of ScO_xH_{3-2x}, YO_xH_{3-2x}, and GdO_xH_{3-2x} oxyhydrides after oxidation in air. *Bottom*: Corresponding Tauc plots for the extraction of the indirect energy gap. Grey arrows indicate the trend with the deposition pressure.

5.C. ION-BEAM COMPOSITION ANALYSIS

RBS (ERD) measurements were performed with a 1.7 MeV 4He^+ beam at 0° (70°) incidence and 160° (30°) scattering angle using energy dispersive detectors with an energy resolution of ~ 17 keV. The ERD detector was covered by a $6.6\ \mu\text{m}$ Al stopper foil to discriminate recoiled H from forward scattered He. While we could not quantify the exact composition due to a poor estimation of the solid angle of the ERD detector, the fact that all samples were exposed to the same total beam charge ($30\ \mu\text{C}$) allows for qualitative comparisons.

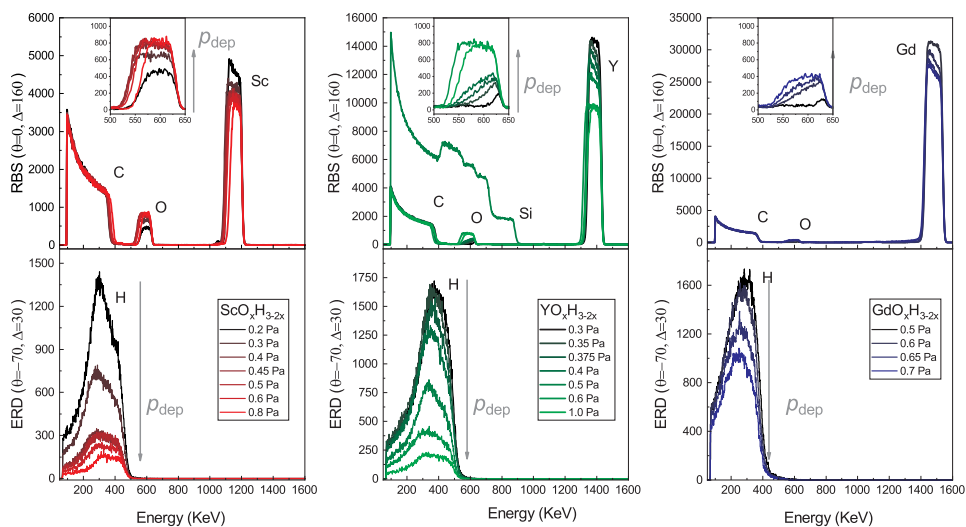


Figure 5.C.1: RBS and ERD spectra for $\text{ScO}_x\text{H}_{3-2x}$, $\text{YO}_x\text{H}_{3-2x}$, and $\text{GdO}_x\text{H}_{3-2x}$ sputtered at different deposition pressures. The insets show a zoom of the oxygen RBS signal. While we could not quantify the exact composition due to the lack of proper standards, it can be qualitatively observed that the amount of oxygen (hydrogen) increases (decreases) with the deposition pressure (grey arrows). Notice that some thin films produced on the carbon substrate peeled off before we could analyse them: this is the case of the Gd oxyhydrides sputtered at pressures above 0.7 Pa and the Y oxyhydride sputtered at 0.5 Pa, for which we measured a twin produced on a SiO_2/Si substrate

5.D. XRD PATTERNS

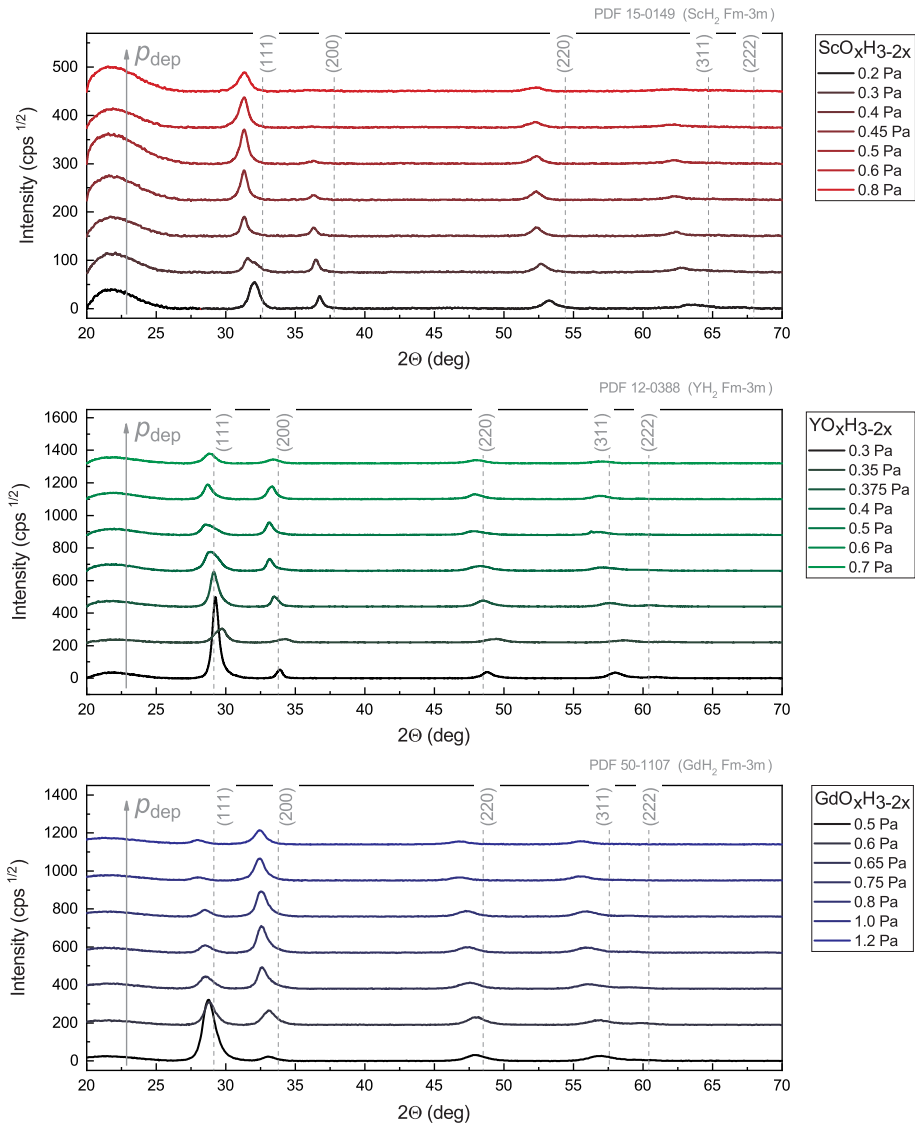


Figure 5.D.1: XRD patterns of the polycrystalline $\text{ScO}_x\text{H}_{3-2x}$, $\text{YO}_x\text{H}_{3-2x}$ and $\text{GdO}_x\text{H}_{3-2x}$ sputtered at different deposition pressures. Each series of data is compared to the reference pattern of the corresponding RE-dihydride. Upon increasing deposition pressure, the peaks shift towards lower angles reflecting a progressive expansion of the lattice. In addition, the change in peak ratio reflects a progressive change in preferential orientation, as also observed by Baba et al. [11] for Gd oxyhydrides. The broad feature centred at $2\theta \sim 22^\circ$ is due to scattering by the f-SiO₂ substrate. Grey arrows indicate the trend with the deposition pressure.

5.E. PHOTOCROMIC EFFECT

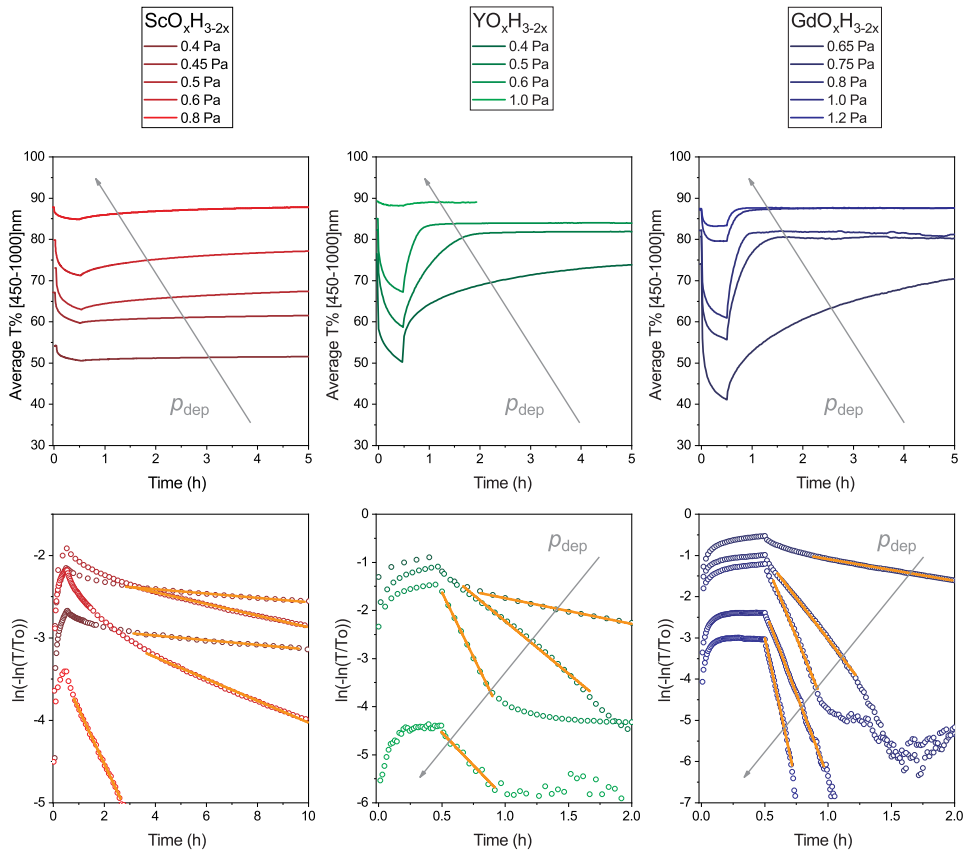


Figure 5.E.1: Photochromic behaviour of $\text{ScO}_x\text{H}_{3-2x}$, $\text{YO}_x\text{H}_{3-2x}$ and $\text{GdO}_x\text{H}_{3-2x}$ sputtered at different deposition pressures. *Top*: Evolution of the average optical transmission upon 30 min of photodarkening and subsequent bleaching in the dark. *Bottom*: Linearisation of the bleaching data according to equation [3] and corresponding best fit. Grey arrows indicate the trend with the deposition pressure.

5.F. DETAILS ON DB-PAS ANALYSIS ON $\text{YO}_x\text{H}_{3-2x}$

For each Y oxyhydride film a DB-PAS depth profile was measured in the virgin state, meaning that the films were not exposed to UV-light during and before these measurements, and 3 days after a fullcycle of photodarkening and bleaching. Given the much faster kinetics of the optical changes, it is safe to assume that after 3 days the bleaching of the samples to their initial color was complete. Therefore, comparing this measure to the one made in the virgin state, we consider any change in the S:W parameter as *permanent*, meaning that it does not revert with a kinetics comparable to the one of the photochromic effect. The use of a narrow-band LED placed outside the vacuum chamber guarantees minimal heating of the samples, with a temperature increase upon illumination below 2 °C.

The cycle of *in-situ* photo-darkening and bleaching was monitored in a time-resolved manner by measuring S and W at a single implantation energy of 6.4 keV, corresponding to a mean probe depth approximately in the center of the film. The samples were illuminated for 2.5h from the side of the substrate and the S:W parameters monitored for at least 30 more hours after the illumination was ceased.

A four-layer model was used in VEPFIT to fit S and W depth profiles of the three oxyhydrides; with the first layer being the Al capping, second and third layers combined the oxyhydride film, and fourth (semi-infinite) layer the f-SiO₂ substrate. Independent DB-PAS depth profiles of the bare substrate and of a thick Al film (sputtered in the same manner of the Al capping layers), were used to fix the fitting parameters of first layer and substrate. The choice of modelling the oxyhydride film by two layers was dictated by the need to account for the interface with the Al capping layer (i.e., the valley(peak) in the S(W) at ~3 keV) and for the fact that during illumination the light intensity is progressively attenuated throughout the material, leading to a less pronounced darkening as the distance from the point of first exposure (i.e., the interface with the substrate) increases. Two layers are the minimal model sufficient to describe the experimental depth profiles. The average of the fitted values of S and W for the top and bottom oxyhydride layer, weighted by the layer thickness, are reported in Fig. 2 of the main text and are used to derive the R-parameter of each sample.

5.F.1. AL-CAPPED $\text{YO}_x\text{H}_{3-2x}$ SPUTTERED AT 0.4 PA

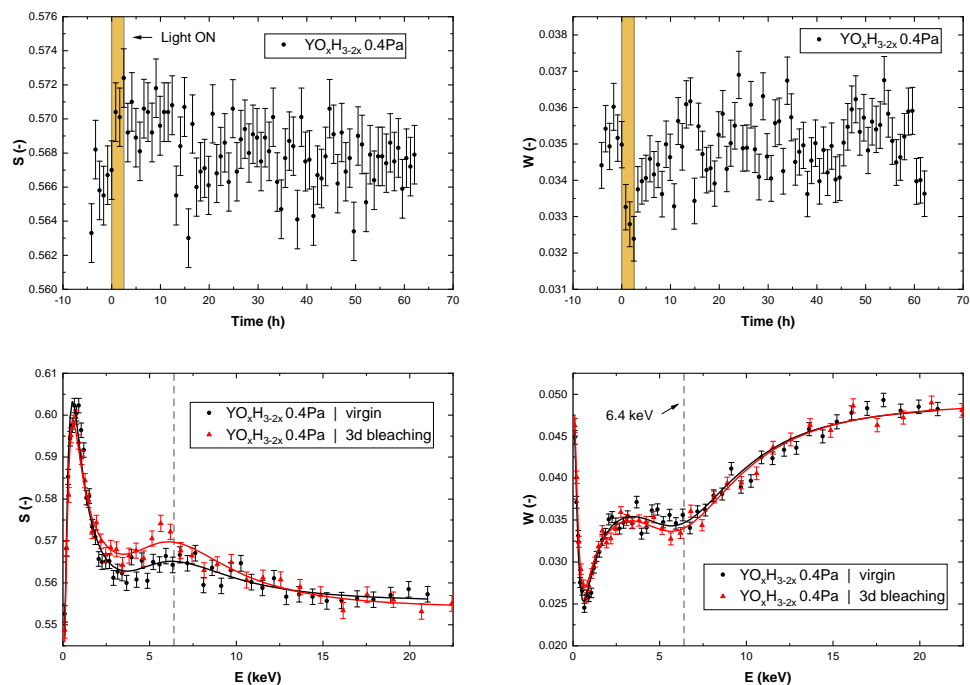


Figure 5.F.1: DB-PAS analysis of Al-capped $\text{YO}_x\text{H}_{3-2x}$ sputtered at 0.4 Pa. *Top*: Time evolution of the S and W parameters probed at $E_{imp} = 6.4 \text{ keV}$ during 2.5 h of photo-darkening ($\lambda = 385 \text{ nm}$, $I = 30 \text{ mW/cm}^2$) and 40 h of bleaching in the dark. *Bottom*: S:W depth profiles and best fits for the sample in its virgin state and 3 days after the cycle of in-situ illumination and bleaching.

$\text{YO}_x\text{H}_{3-2x}$ 0.4 Pa	S_1 (-)	W_1 (-)	S_2 (-)	W_2 (-)	$d_{fit,1/2}$ (nm)
Virgin	0.5600(6)	0.0363(2)	0.569(1)	0.0322(4)	115/188
3d Bleaching	0.5643(7)	0.0357(3)	0.574(1)	0.0314(5)	

Table 5.F.1: Best fit parameters for the DB-PAS depth profiles of Al-capped $\text{YO}_x\text{H}_{3-2x}$ sputtered at 0.4 Pa before and after the full photochromic cycle.

$\text{YO}_x\text{H}_{3-2x}$ 0.4 Pa	S (-)	W (-)	
Virgin	0.5646(8)	0.0342(3)	
3d bleaching	0.5692(9)	0.0335(4)	
	ΔS (-)	ΔW (-)	R (-)
	0.005(1)	-0.0007(5)	-7(5)
	ΔS (%)	ΔW (%)	R (%)
	0.8(2)	-2(1)	-0.4(3)

Table 5.F.2: Weighted-average S:W parameters for the DB-PAS depth profiles of Al-capped $\text{YO}_x\text{H}_{3-2x}$ sputtered at 0.4 Pa. Absolute and relative changes, as well as the absolute and relative R value are additionally reported.

5.F.2. AL-CAPPED $\text{YO}_x\text{H}_{3-2x}$ SPUTTERED AT 0.5 PA

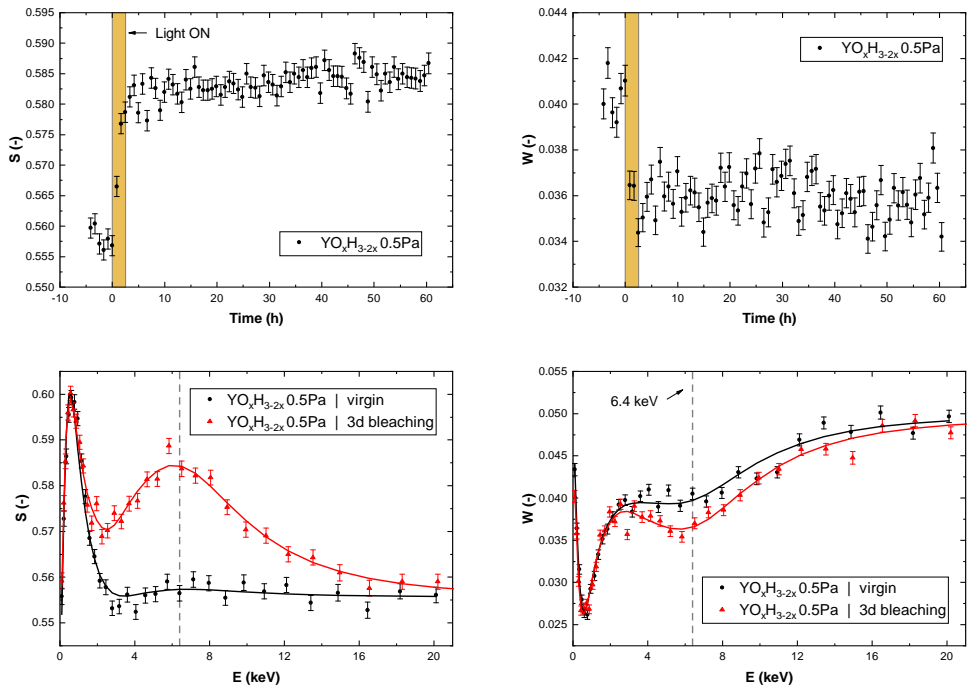


Figure 5.F.2: DB-PAS analysis of Al-capped $\text{YO}_x\text{H}_{3-2x}$ sputtered at 0.5 Pa. *Top*: Time evolution of the S and W parameters probed at $E_{imp} = 6.4 \text{ keV}$ during 2.5 h of photo-darkening ($\lambda = 385 \text{ nm}$, $I = 30 \text{ mW/cm}^2$) and 60 h of bleaching in the dark. *Bottom*: S:W depth profiles and best fits for the sample in its virgin state and 3 days after the cycle of in-situ illumination and bleaching.

$\text{YO}_x\text{H}_{3-2x}$ 0.5 Pa	S_1 (-)	W_1 (-)	S_2 (-)	W_2 (-)	$d_{fit,1/2}$ (nm)
Virgin	0.5506(9)	0.0410(3)	0.5581(9)	0.0390(3)	65/256
3d Bleaching	0.5642(9)	0.0407(3)	0.5895(9)	0.0352(3)	

Table 5.E3: Best fit parameters for the DB-PAS depth profiles of Al-capped $\text{YO}_x\text{H}_{3-2x}$ sputtered at 0.5 Pa before and after the full photochromic cycle.

$\text{YO}_x\text{H}_{3-2x}$ 0.5 Pa	S (-)	W (-)	
Virgin	0.5567(9)	0.0394(3)	
3d bleaching	0.5844(9)	0.0363(3)	
	ΔS (-)	ΔW (-)	R (-)
	0.028(1)	-0.0031(4)	-9(1)
	ΔS (%)	ΔW (%)	R (%)
	5.0(2)	-8(1)	-0.64(9)

Table 5.E4: Weighted-average S:W parameters for the DB-PAS depth profiles of Al-capped $\text{YO}_x\text{H}_{3-2x}$ sputtered at 0.5 Pa. Absolute and relative changes, as well as the absolute and relative R value are additionally reported.

5.F.3. AL-CAPPED $\text{YO}_x\text{H}_{3-2x}$ SPUTTERED AT 0.6 PA

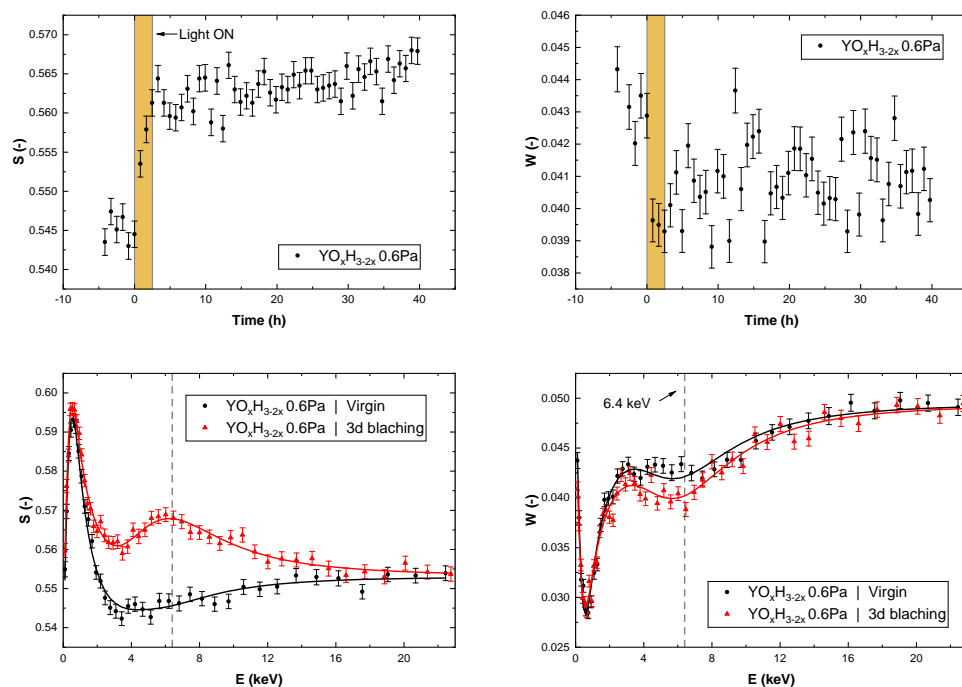


Figure 5.F.3: DB-PAS analysis of Al-capped $\text{YO}_x\text{H}_{3-2x}$ sputtered at 0.6 Pa. *Top*: Time evolution of the S and W parameters probed at $E_{imp} = 6.4 \text{ keV}$ during 2.5 h of photo-darkening ($\lambda = 385 \text{ nm}$, $I = 30 \text{ mW/cm}^2$) and 40 h of bleaching in the dark. *Bottom*: S:W depth profiles and best fits for the sample in its virgin state and 3 days after the cycle of in-situ illumination and bleaching.

$\text{YO}_x\text{H}_{3-2x}$ 0.6 Pa	S_1 (-)	W_1 (-)	S_2 (-)	W_2 (-)	$d_{fit,1/2}$ (nm)
Virgin	0.5419(7)	0.0443(3)	0.545(1)	0.0404(5)	65/256
3d Bleaching	0.5571(7)	0.0425(3)	0.574(1)	0.0381(4)	

Table 5.F5: Best fit parameters for the DB-PAS depth profiles of Al-capped $\text{YO}_x\text{H}_{3-2x}$ sputtered at 0.6 Pa before and after the full photochromic cycle.

$\text{YO}_x\text{H}_{3-2x}$ 0.6 Pa	S (-)	W (-)	
Virgin	0.5439(3)	0.0418(4)	
3d bleaching	0.5681(3)	0.0396(4)	
	ΔS (-)	ΔW (-)	R (-)
	0.0242(4)	-0.0021(6)	-11(3)
	ΔS (%)	ΔW (%)	R (%)
	4.45(8)	-5(1)	-0.9(2)

Table 5.F6: Weighted-average S:W parameters for the DB-PAS depth profiles of Al-capped $\text{YO}_x\text{H}_{3-2x}$ sputtered at 0.6 Pa. Absolute and relative changes, as well as the absolute and relative R value are additionally reported.

REFERENCES

- [1] E. M. Baba, J. Montero, , D. Moldarev, M. V. Moro, M. Wolff, D. Primetzhofer, S. Sartori, E. Zayim, and S. Karazhanov, *Preferential orientation of photochromic gadolinium oxyhydride films*, [Molecules](#) **25**, 3181 (2020).

6

PHOTOCHROMISM AND PHOTOCONDUCTIVITY IN $\text{REO}_x\text{H}_{3-2x}$

*[..] a land yet without history
but only chronicles of hunt and tales of adventure
that with time transformed in myths and legends.*

Walter Bonatti, Klondike (1965)

While the optical photochromism of RE oxyhydride thin films has been extensively studied, their large persistent photo-conductivity have been somewhat neglected. Here we present an extensive characterization and demonstrate that photochromism and photo-conductivity originate from the same process, as indicated by a comparable time and temperature dependence, and by a unique exponential relation linking material conductivity and optical absorption. While a definitive understanding of the mechanism behind the process is still missing, we use this new insight to discuss if, and under which conditions, the mechanisms proposed for the photochromism can also account for the photo-conductivity. We rule out that purely electronic processes are sufficient, and suggest that light exposure either leads to (i) the formation of an ensemble of in-gap defects capable of trapping electrons and holes alike, or (ii) to the segregation of a percolating network of metallic domains.

Based on this chapter, we are preparing the following paper:

G. Colombi, B. Boshuizen, D. Chaykina, H. Schreuders, T. J. Savenije, and B. Dam, *Relation between photochromism and photoconductivity in $\text{REO}_x\text{H}_{3-2x}$ thin films*, In preparation (2022).

6.1. INTRODUCTION

Photochromism and photo-conductivity of Y oxyhydrides thin films were first reported by Mongstad *et al.* [1] in 2011 – a time when composition and structure of this material were unknown, as well as its relation to the bulk $\text{REO}_x\text{H}_{3-2x}$, which only two years later will be found exceptional H^- ionic conductors. [2] Since the original work of Mongstad, several other rare-earths (RE=Sc,Y,Nd,Gd,Dy,Er), [3-6] were reported to form photochromic oxyhydride thin films as well. In 2019 we established that all these photochromic films have $\text{REO}_x\text{H}_{3-2x}$ oxyhydride composition, and proposed a structural model based on the CaF_2 -type lattice where the anion preferentially occupy the tetrahedral interstitial sites of the cation lattice. [4, 7] The composition of the oxyhydride and the deposition conditions were found to influence the extent and the speed of photochromism, [8-10] however the general presence of the phenomenon indicates that its origin is intrinsic to the RE oxyhydride thin film material. While there is no conclusive agreement on the photochromic mechanism, most research converges towards the idea that structural rearrangements enabled by the high H^- (local) mobility are at the heart of the photochromism. In this sense, it was hinted that the photodarkening depends on the segregation of an absorbing phase, [11, 12] a process accompanied by reversible contraction of the crystal lattice, [13] and quenching of the NMR signal of the most mobile H fraction (~3%). [14] A reversible change in the H-sub-lattice upon illumination was indirectly observed as well via muon spin rotation spectroscopy (μSR). [15] Finally, the bleaching was shown to be a thermally activated process, while the photo-darkening could be induced even at a temperature of 4 K. [16]

Despite the interest in this class of materials, on their photochromic properties, and later on on their ionic conduction, very little research has been spent towards the study of their photo-conductivity – whose measurement is inherently much more challenging, as explained throughout this chapter. In fact, at the time of writing, no other study managed to reproduce the results originally presented by Mongstad *et al.* [1], namely a *tenfold* reduction of the material resistance upon illumination, followed by a partial, slow reversibility in the dark. In his Ph.D. thesis, Mongstad himself mentions the many (and unquantified) sources of error in the measurement, warning the reader against quantification of the material resistivity (in contrast to the system resistance), and against over-interpretation of the resistance time-dependence.

Nonetheless, reliable information on the conductivity and photo-conductivity of these thin films are (i) a potential source of insight on the photochromic mechanism, (ii) essential to evaluate their employability as solid state ionic conductors in any electrochemical devices, (iii) a necessary prerequisite for any further tuning of their ionic/electronic transport properties, and (iv) a potential probe for the type and concentration of defects inside the material. From a more fundamental perspective, a better understanding on the conduction of the RE oxyhydrides might help to understand at which extent their properties resemble or depart from those of the related REH_x hydride systems, which have been extensively investigated in view of the metal-to-insulator transition that occurs with a change of the H content. [17-20] In this chapter, we address this knowledge gap, presenting for the first time high-quality, time-dependent, measurements of optical and transport properties, including Hall-Effect (HE). [21] While the limited range of sensitivity of our current(voltage) source(reader) forced us to work with the most conductive Gd-

based oxyhydrides (optical gap 2.5(1) eV), we expect that the conclusions drawn here hold for the other RE oxyhydride photochromic thin films as well.

6.2. EXPERIMENTAL

Sample preparation Gd based REH_2 thin films (thickness ~ 1500 nm) were prepared by reactive magnetron sputtering of a 2-inch Gd target (MaTeck Germany, 99.9% purity) in a Ar/H_2 (5N purity) atmosphere. The deposition chamber was kept at a base pressure below 1×10^{-6} Pa. During deposition the total gas flow was fixed at 40 sccm with an Ar/H_2 gas ratio of 7:1, while the total deposition pressure (p_{dep}) was set to 0.75 Pa by means of a butterfly reducing valve mounted at the inlet of the pumping stage. A total power of 175 W supplied direct current was used to sustain the plasma excitation. Ten *twin* samples were grown on unheated UV-grade fused silica (f-SiO₂) in a single deposition, so to guarantee a high homogeneity between them. The as-deposited REH_2 thin films were then oxidized in ambient conditions by exposure to air. Having previously shown that the oxidation is a self-limiting process,^[8] a rest time of 7 – 14 days was allowed to the samples before any further characterization.

Contact deposition To guarantee Ohmic metal-semiconductor junctions (and minimize contact resistances) during transport measurements, we find the deposition of additional contact layers to be needed. Being an high-effort and low-reward activity, with a large space of parameters to consider, it is said that making contacts is an *art*, rather than a systematic science. This work makes no exception to such empirical approach, and we find the following multilayer (in order, from the sample surface) to be optimal: ~ 100 nm YH_2 , ~ 100 nm Cr, ~ 100 nm Au. The heuristic reasoning behind this choice is discussed in the following.

1. Among pure metals, Y has one of the lowest workfunctions, thus, in the absence of other information, is always a good candidate for an Ohmic metal-semiconductor interface. However, (i) the hcp lattice of Y poses an additional strain at the interface with the fcc oxyhydride, and (ii) the large affinity that Y has for H induces a fraction of the H to diffuse from the oxyhydride to the contact. Notably, during our pilot experiments, we observed that such H exchange was further encouraged by UV exposure, leading to a non-reversibility of both photochromism and photo-conductivity. This effects are vastly mitigated by using an fcc- YH_2 layer.
2. Cr acts as an adhesion layer between YH_2 and Au. Additionally, Cr is one of the pure metals that least suffers from hydrogen embrittlement,^[22] therefore, we think it might further help to prevent H diffusion from the bottom layers to the Au top contact.
3. The top-most Au layer acts as a barrier for oxidation, something that Cr, and YH_2 even more, are particularity sensitive to.

Finally, to further minimize the contact-oxyhydride interaction and the systematic errors during transport measurements,^[23] the contacts were deposited at the corners of a 7×7 mm square and their size was kept to a minimum of around 0.5 mm^2 .

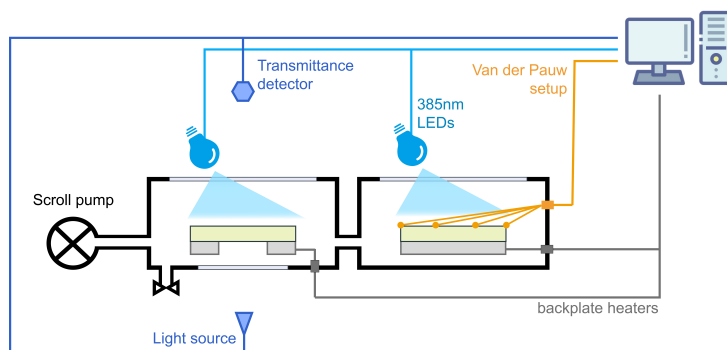


Figure 6.1: Schematics of the experimental setup used in this work. Optical transmittance and transport properties can be measured in sync under very comparable illumination, temperature, and vacuum conditions.

6

Sample characterization Fig. 6.1 shows a schematic of the experimental setup used to simultaneously measure optical transmittance and transport properties under very comparable temperature, vacuum, and illumination conditions. To achieve that, two samples are placed in connected vacuum chambers (pressure $\sim 10^{-1}$ mbar) and kept at the same temperature by independent backplate heaters with a PID control loop. Specialized setups are then used to measure their properties.

The optical transmittance is measured with a custom-built fiber based spectrometer equipped with a white source (DH-2000BAL, Ocean Optics) and a Si-based energy dispersive spectrometer (HR4000, Ocean Optics). The wavelength range is approximately 230-1150 nm, and the time resolution of ~ 1 s.

Resistance and Hall-effect are measured in a squared Van der Pauw^[23] geometry using a H50 Hall-effect current(voltage) source(meter), a commercial system from *MMR Technologies* that operates in a nominal resistance range of $10^2 - 10^{10} \Omega$, and with a time resolution of approximately 3 min. A permanent magnet of ~ 850 G is used in the Hall-effect measurements.

Photochromism and photo-conductivity are triggered by two narrow-band LED calibrated to deliver the same intensity at the sample surface ($\lambda = 385$ nm, $I = 75$ mW/cm²). Note that while light intensity does not need to be particularly homogeneous for the transmittance, which is probed in a central spot of ~ 2 mm², that is not the case for the transport measurements, which probe the entire sample 7×7 mm². To guarantee an homogeneous light intensity over the whole sample surface, a set of optical elements is installed in front of both LEDs following the principle of Köhler illumination.

Knowing that regions of RE oxyhydrides films that were previously exposed to light suffer from a so-called "memory effect",^[1] namely a slower bleaching speed compared to a non-illuminated area, all the measurements presented here correspond to the first cycle of virgin (i.e., as-deposited) samples.

6.3. RESULTS

In the following, we first look at some basic transport properties of the Gd oxyhydride, and then we discuss the photo-induced effects, which are the focus of this work.

6.3.1. GD OXYHYDRIDE TEMPERATURE STABILITY

It is well known that the temperature dependence of the material resistivity is an insightful indication of the electronic state of the material and of the underlying mechanism of charge transport. However, due to the high concentration of defects and of the tendency to oxidise, the range of temperatures in which our RE oxyhydride thin films are stable is relatively narrow. This interval of temperatures is here discussed, using the material resistivity as a probe.

Fig. 6.2 shows how the material resistivity changes over time during a temperature ramp that goes from 300 K to 400 K, in steps of 5 K. Up to ~340 K, the material shows the expected semiconductor behaviour, with the resistivity decreasing monotonously for increasing temperature. No metal-like temperature dependence ($d\rho/dT > 0$) is observed, which is no surprise given the optical bandgap and ionic character of the RE oxyhydride bond. In this low-temperature interval, at any given temperature, the resistivity does not change in time. Starting at ~350 K, we observe instead an increase of resistivity while the film soaks at fixed temperature. This is most likely due to a progressive increase of the oxygen content in the thin film, a process that is thermodynamically favoured (see chapter 4). Such increase of resistivity is observed up to ~390 K, where a second process becomes dominant and the material resistivity starts to decrease over time. An exact understanding of the behaviour in this high temperature regime is beyond the scope of this work, however, we suppose that some hydrogen release – and consequent reduction of some metal cations – might be happening. This hypothesis seems validated by the slight darkening of the material as observed by eye. After the material is cooled down back to the initial temperature, a permanent increase of resistivity confirms the occurrence of irreversible structural processes (most likely oxidation). On the basis of these data, we limit any further measurements to a moderately low temperature range of 300 – 350 K.

To further verify the hypothesis of oxidation during the measurement, a second sample deposited around the critical deposition pressure ($p_{dep} = 0.65$ Pa) – therefore resulting in a dark-looking partially oxidized $\text{GdO}_x\text{H}_{3-2x} // \text{GdH}_x$ phase mixture (see chapter 5) – was tested following the same routine (Fig. 6.3). The resistivity of this sample is initially found to be around $10^{-2} \Omega\text{cm}$, which is ~ 100 times lower than the pure Gd oxyhydride phase and yet quite higher than the typical values of metallic compounds ($10^{-5} - 10^{-6} - \Omega\text{cm}$). Notably, at low temperatures the resistivity of this sample decreases for increasing temperature, indicating that the semiconducting phase dominates its behaviour. All of this suggests that this sample contains only a minor fraction of metallic domains in an otherwise semiconducting, oxyhydride matrix. Heating this mixed-phase sample at temperatures above ~310 K results in a continuous increase of resistivity over time. This result is analogous to what was observed for the oxyhydride, although with an earlier temperature onset that can be understood considering the higher driving force for the dihydride oxidation (see section 3.4.1). After the annealing treatment, when the temperature of 300 K is restored, the sample is largely transparent and its conductivity is one order of magnitude higher than the initial one. All together, these observation

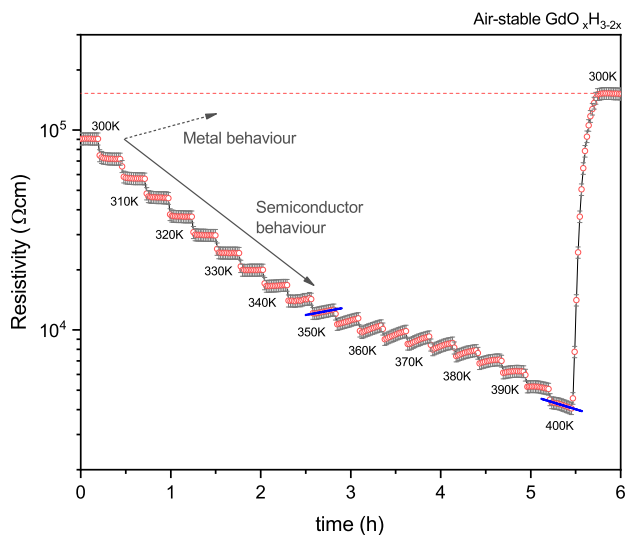


Figure 6.2: Resistivity of Gd oxyhydride during a temperature ramp that goes from 300 K to 400 K, in steps of 5 K. While the material appears stable up to ~ 340 K, the resistivity starts to drift at higher temperatures, indicating permanent compositional and/or structural changes.

6

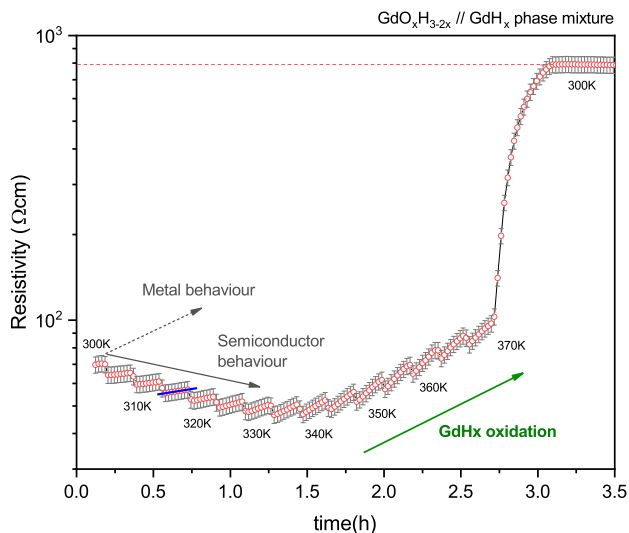


Figure 6.3: Resistivity of a $\text{GdO}_x\text{H}_{3-2x} // \text{GdH}_x$ phase mixture during a temperature ramp that goes from 300 K to 370 K, in steps of 5 K. As the temperature rises above ~ 3100 K, the resistivity start to increase. The major permanent change (and color changes) observed at the end of the treatment indicate the oxidation of the GdH_x phase.

strongly indicate that, despite the rough vacuum ($\sim 10^{-1}$ mbar) achieved in the set-up, our thin films are still prone to oxidation.

6.3.2. GD OXYHYDRIDE TRANSPORT PROPERTIES

Hall-effect (HE) measurements are arguably one of the most insightful tools to investigate the transport properties of a semiconductor, as they permit to identify the dominant carrier type (i.e., electron or holes), and allow to quantify carrier density ($n_{e/h}$) and carrier drift mobility ($\mu_{e/h}$). Strictly speaking, however, the Hall-mobility μ_H well approximates the actual drift mobility of the charge carriers only if they freely move within a band that is much wider than $k_B T$. [24] This type of electronic transport is often referred as *coherent*, and envisions the carrier motion to be free and only occasionally disrupted by scattering events. Coherent transport is characteristic of most conventional semiconductors and typically involves a mobility that decreases with increasing temperature; typical values greatly exceed $1 \text{ cm}^2 \text{ s}^{-1} \text{ V}^{-1}$. In contrast, *incoherent* transport envisions the carrier to only make occasional jumps between localized regions in the material. In this case the mobility reflects the activation energy needed for the jump and rises with increasing temperature; typical values are well below $1 \text{ cm}^2 \text{ s}^{-1} \text{ V}^{-1}$. [24]

At present, what type of electronic transport better describes the RE oxyhydride material remains unclear, therefore in the following we first discuss our measurements in the framework of a free-carrier model, and then we briefly consider the alternative option of a polaron conduction.

FREE CARRIERS HYPOTHESIS

In framework of a free-carrier model, here we first discuss the Gd oxyhydride carrier density/mobility in comparison to other semiconductors, and later show their temperature dependence. The reader is, however, warned to be cautious with these results because they are extracted under assumption of a perfectly homogeneous film, and a single carrier type (i.e., $n_e \mu_e / n_h \mu_h \gg 10$ or $n_e \mu_e / n_h \mu_h \ll 0.1$). However, the homogeneity of the sample was indirectly assessed (see section 6.A), and the assumption of a dominant carrier is most often verified in defect-rich semiconductors.

In all our measurements, we find the Hall voltage (V_H) to have a positive sign, indicating that holes are the dominant charge carrier in this set of Gd oxyhydride thin films. Since the hole effective mass is typically much smaller than the one of the electrons, this would be rather surprising in a defect free semiconductor. In the case of our highly defective thin films it might, however, indicate a net dominance of in-gap electron traps and/or shallow electron acceptor states. Fig. 6.4 shows a map of carrier density and mobility where the properties of the Gd oxyhydride are compared to a selection of reference values. While the carrier density of the Gd oxyhydride ($n_h \sim 10^{11} - 10^{12} \text{ cm}^{-3}$) is in line with that of common intrinsic semiconductors, the hole mobility is found to be exceptionally high ($\mu_h \sim 10^3 - 10^4 \text{ cm}^2 \text{ V}^{-1} \text{ s}^{-1}$). [25-29] Unfortunately, while the conductivity of many REH_x hydrides was extensively characterized, [17, 18, 30-34] we could not find any reference value for the carrier mobility to make a comparison.

It is important to note here that if the assumption of a single carrier were not verified, that would lead to under-estimation of the carrier mobility (Fig. 6.A.5). Similarly, an over-estimated material resistivity (for example due to contact resistances) would lead to an under-estimation of the carrier mobility. Therefore, the exceptional high mobility of the Gd oxyhydrides cannot be traced back to any obvious experimental artefact.

Fig. 6.5 shows the temperature dependence of the Gd oxyhydride conductivity, hole

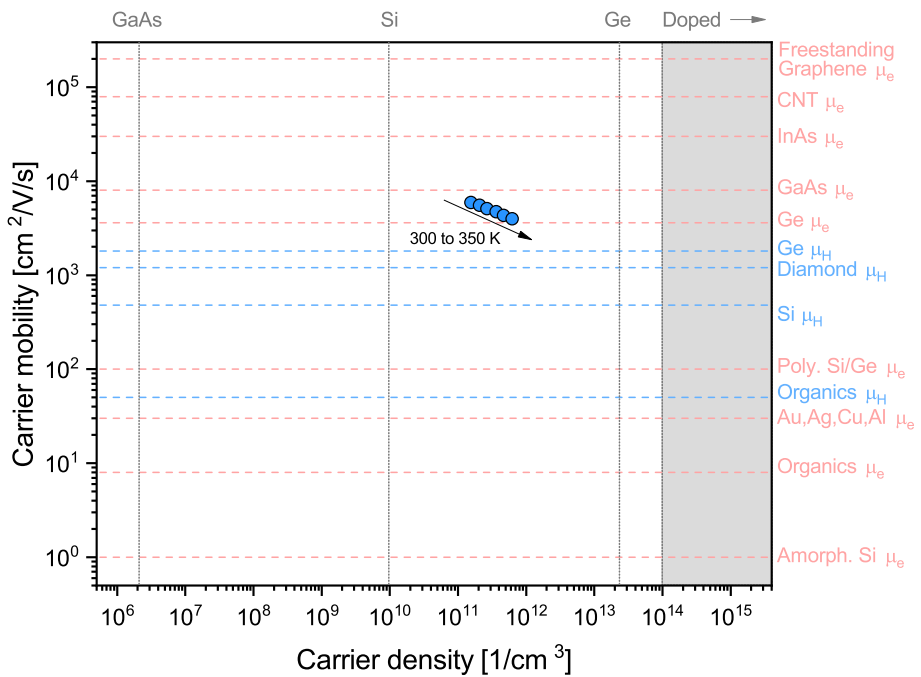


Figure 6.4: Hole carrier density and mobility of reactively sputtered Gd oxyhydride thin films. Measure uncertainty is estimated to be smaller than the point size. The experimental values are compared to the carrier density (vertical dotted lines) and the carrier mobility (dashed horizontal lines; pink: electron mobility, blue: hole mobility) of other materials at room temperature (280 – 300 K). [25-29](#)

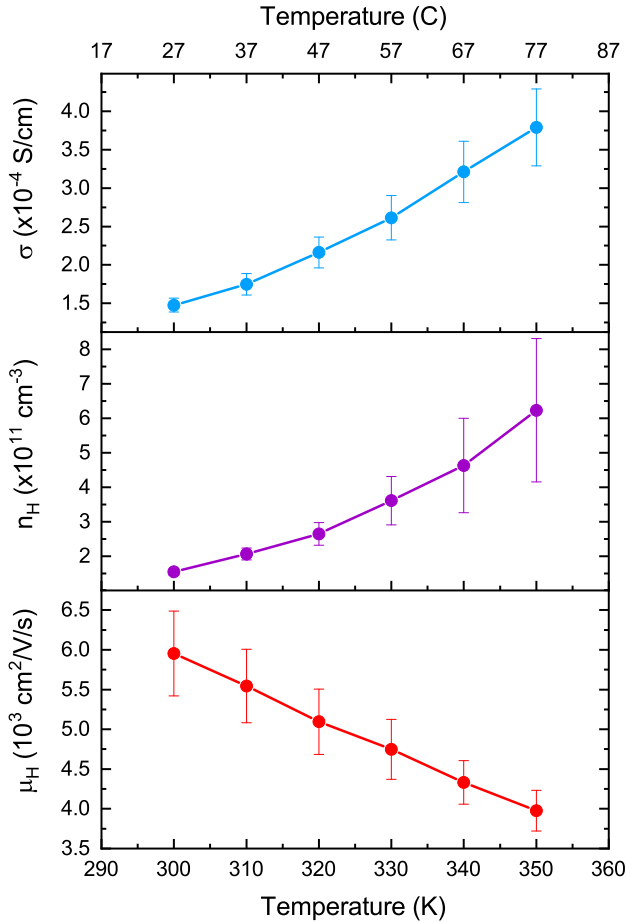


Figure 6.5: Temperature dependence of conductivity, carrier density, and mobility as probed by Van der Pauw and Hall-effect measurements of the Gd oxyhydride thin films studied in this work.

density, and hole mobility. As the temperature increases, the total conductivity increases as well due to a net increase of carrier density. Conversely, the carrier mobility decreases. Unfortunately, the limited temperature interval makes it difficult to quantitatively discuss any material-specific temperature dependence, thus, we limit our discussion to the ideal, approximated $n \propto \text{Exp}(-\Delta E/2k_B T)$ relation that follows from a Fermi-Dirac distribution of the occupied/unoccupied states. [25] For an intrinsic semiconductor ΔE corresponds to the E_g , while for an extrinsic semiconductor ΔE corresponds to energy distance of the main donor(acceptor) level from the conduction(valence) band. [25] From the fit of the experimental data, we find $\Delta E \sim 0.9$ e.V.(Fig. 6.6), which is clearly much smaller than the optical gap and indicates the presence of deep states that, in view of the positive Hall potential, must act as electron acceptors (i.e., hole donors). Finally, the decrease of mobility with increasing temperature is typical of a coherent electron transport and can

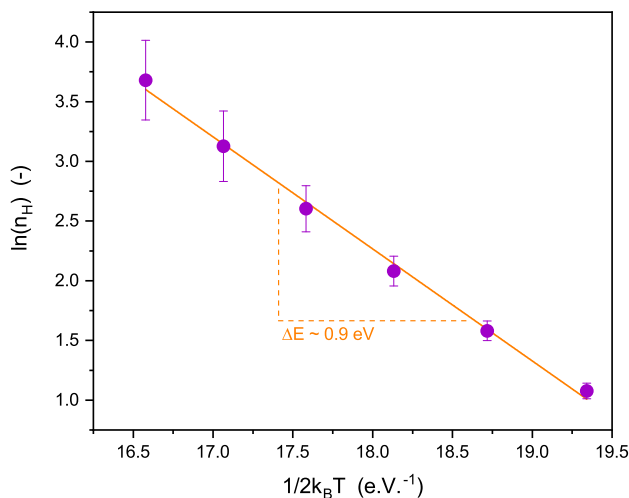


Figure 6.6: Fit of temperature-dependent carrier (holes) density of the Gd oxyhydride thin films studied in this work according to the ideal relation $n \propto \text{Exp}(-\Delta E/2k_B T)$.

6

be rationalized in terms of increasing phonon-scattering. We rule out any significant ionic contribution to the total conductivity measured here, as the ionic H^- conductivity that was reported in $\text{LaO}_x\text{H}_{3-2x}$ powders is (i) orders of magnitude smaller ($< 10^{-6} \text{ S/cm}$), and (ii) a temperature activated process, thus at odds with the decrease of mobility measured for increasing temperature. [2] The picture of a p-type semiconductor seems, therefore, sufficient to describe the electronic transport behaviour in the Gd oxyhydride thin films studied in this work. The exceptionally high mobility, however, warrants further verification and might be a symptom of skewed Hall effect results due to polaronic conduction.

POLARONS HYPOTHESIS

In view of the ionic character of the compound (see chapter [4]), one might expect the free charges to experience some coupling with the crystal lattice, potentially leading to polaron formation. [35] In this case, being the polaron motion qualitatively different from that of free carriers, the analysis of the Hall-effect becomes far from simple and dependent on the specific material and the specific type of polaron. As a result, the magnitude, temperature dependence, and even the sign of the Hall voltage extracted under the assumption of free-carriers might be incorrect. [24] In this regard, we note that such an erroneous analysis of the Hall-effect was reported to overestimate the mobility of small polarons by a factor of $10^2 - 10^3$ in Fe_2O_3 -based epitaxial films and BiVO_4 -based single crystals alike. [36] Since in the previous section we derived an exceptionally high mobility that seem at odds with the high density of defects expected in a porous, air-oxidized, reactively-sputtered thin film, we consider likely the eventuality of a systematic overestimation due to polaron conduction.

6.3.3. RELATION BETWEEN PHOTOCONDUCTIVITY AND PHOTOCROMISM

Mongstad *et al.* [1], and later You *et al.* [10], have undoubtedly shown that photochromism in RE oxyhydride thin films is accompanied by a photo-induced change of conductivity. Neither of the two studies, however, presented a sufficiently accurate time-dependent measurement of the conductivity to discuss the connection between the two photo-induced phenomena. The reasons behind this knowledge gap are essentially of experimental nature, namely: (i) the challenges of contact optimization, and sample homogeneity in general; (ii) the extremely high resistance of a ~ 1000 nm RE oxyhydride thin film, which requires a current source and a voltage reader capable of working in the range of pA and V , respectively; (iii) the rather low resistance of the films under illumination, which requires the current source and the voltage reader to work now in a opposite regime of mA and mV , respectively; and (iv) the need for an homogeneous illumination.

Having addressed all these experimental challenges, Fig. 6.7 gives a visual overview of the photo-induced effect on optical absorption and electronic conduction. Here, the two phenomena follow a very comparable time and temperature dependence, strongly pointing towards a common origin.

Looking at the material conductivity, with 30 min of illumination we find an enormous, reversible increase from $\sim 10^{-5}$ S/cm to $\sim 10^{-1}$ S/cm . This is 3 orders of magnitude higher than the increase measured in the original work of Mongstad *et al.* [1], although a direct comparison is difficult because of the different wavelength and intensity of the LEDs used for illumination. Additionally, differently from Mongstad *et al.* [1], our results do not show signs of large irreversibility. Indeed, allowing enough bleaching time in the dark (e.g., 10 h at 303 K), we find that the conductivity of all samples returns to the initial value. We suspect that the irreversibility observed in the earlier studies is due to a loss of hydrogen from the RE oxyhydride towards the measuring probes, similar to what we have observed for non-optimized contacts.

Unfortunately accurate measures of the Hall-effect cannot be combined with illumination, as the permanent magnet would cover the light path. We could, however, measure the sample immediately after the 30 min of UV exposure, finding a remarkable switch of the polarity of the Hall voltage that implies a change from p-type to n-type conductivity. A quantitative evaluation of the carrier density and mobility is not reliable because of the change that the sample undergoes during the ~ 5 min necessary for the measurement. However, considering the relation $\sigma \propto n/\mu$ and the fact that the carrier mobility cannot change by orders of magnitude, it must follow that the increase of conductivity is due to a comparable increase of carrier density.

Comparing the trend of optical transmittance and material conductivity gives a strong indication that the changes that occur under illumination have a common origin. Using the data at 303 K as an example (Fig. 6.8a), the relation between conductivity and relative optical transmittance is visualized in Fig. 6.8b, where these two properties are plotted one against the other. When the material is in its optically transparent state, either before illumination or at the end of the bleaching process, the relative optical transmittance and conductivity do not follow any obvious relation. However, during illumination and during most of the bleaching, there is a linear relation between σ and $-\ln(T/T_0)$. Neglecting the reflectivity of the sample, in first approximation, it holds that $-\ln(T/T_0) \sim \Delta\alpha d$, where d is the thickness of the thin film, and $\Delta\alpha$ is the absorption coefficient of the optically

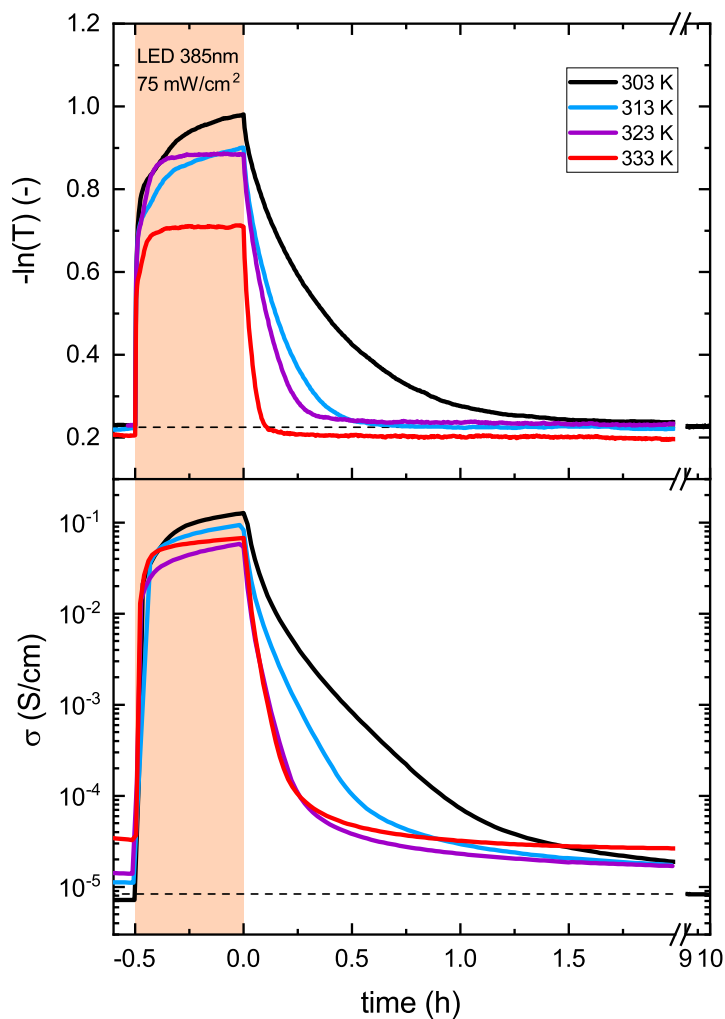


Figure 6.7: Photo-induced effects on optical transmittance (top) and material conductivity (bottom) of Gd oxyhydride as measured at different temperatures. To avoid artefacts due to the memory effect, \square all measurements correspond to the first illumination cycle of a virgin sample.

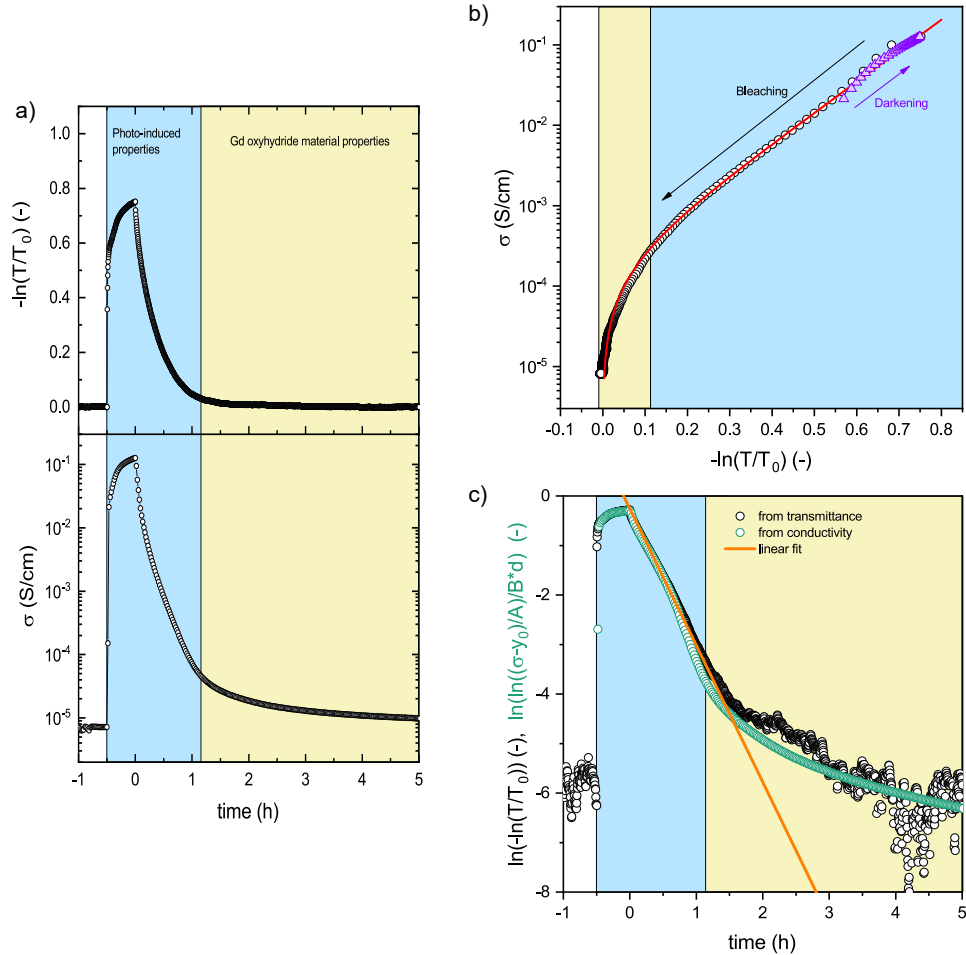


Figure 6.8: *a*) Photo-induced effects on relative optical transmittance (top) and material conductivity (bottom) of Gd oxyhydride measured at 303 K. *b*) Relation between the increase of optical absorption ($-\ln(T/T_0) \sim \Delta \alpha d$) and conductivity. The black points refer to the bleaching, while the purple ones to the darkening process. A fit based on eq. 6.1 is shown in red. *c*) Time dependence of optical transmission and conductivity linearised according to the assumption that all optically-absorbing species disappear following a first order bleaching kinetics. 6.7 A fit based on eq. 6.4 is shown in orange. In all panels, the background colors are used to highlight the regimes in which optical absorption and conductivity are dominated by the photo-induced effects (blue), in contrast to the material properties of the Gd oxyhydride as largely recovered at the end of the bleaching (yellow).

absorbing species formed by light exposure. [3] The negative Hall voltage and the proportionality between σ and $\Delta\alpha$ suggests that these two photo-induced properties either originate (i) from the same absorbing and electron-conductive species that is formed upon illumination, and/or (ii) from a single process leading to the formation of absorbing species and to an increase of mobile electrons in the material.

We propose eq. [6.1] as an empirical relation between conductivity and $\Delta\alpha$ in the Gd oxyhydride, which in the limit of $\Delta\alpha \rightarrow 0$ describes the conductivity of the material in its transparent state (σ_0) as a constant (eq. [6.2]), and by subtraction, the photo-induced conductivity (σ_{ph}) as a shifted exponential (eq. [6.3]):

$$\sigma(\Delta\alpha) = y_0 + Ae^{\Delta\alpha B} \quad (6.1)$$

$$\sigma_0 = \lim_{\Delta\alpha \rightarrow 0} \sigma(\Delta\alpha) = y_0 + A \quad (6.2)$$

$$\sigma_{ph} = \sigma(\Delta\alpha) - \sigma_0 = A(e^{\Delta\alpha B} - 1). \quad (6.3)$$

The ability of eq. [6.1] to fit the experimental data, especially in the region where the photo-conductivity dominates, is shown in Fig. [6.8b].

While the physical reason behind the exponential relation of σ_{ph} and $\Delta\alpha$ remains unclear, as well as the physical meaning of the fitting parameters, we note that B is largely unaffected by temperature and memory effect (Fig. [6.B.1]), again reinforcing the idea that photo-conductivity and photochromism have a single origin.

As a double check, Fig. [6.8c] confirms that by applying eq. [6.1] to the conductivity data one recovers the same time dependence that is well-known to describe the optical-bleaching kinetics: [8, 37]

$$\ln\left(\frac{d}{B} \ln \frac{\sigma(t) - y_0}{A}\right) \sim \ln\left(-\ln \frac{\langle T(t) \rangle}{\langle T_0 \rangle}\right) = -\frac{1}{\tau_B} t - \ln\langle T_{dark} \rangle. \quad (6.4)$$

The unusual time dependence of the photo-conductivity, notably, implies that the the rate determining step of the bleaching is not a purely independent electronic process. The decay of the photo-generated charge carriers must therefore depend on some type of structural rearrangement, or reaction, in the solid state.

6.4. DISCUSSION

Since the discovery of the photochromism in $\text{REO}_x\text{H}_{3-2x}$ thin films, several ideas have been proposed to describe such behaviour, as recently reviewed by Chaykina *et al.* [15] The first step of the process involves the formation of an electron-hole pair *via* inter-band ($h\nu \geq E_g$) photo-excitation. The subsequent formation of optical absorbing species and their identity remains a topic of debate. At the time of writing, two groups of mechanisms are under consideration, namely (i) the formation of small defects within the $\text{REO}_x\text{H}_{3-2x}$ phase, and (ii) the phase segregation of a secondary absorbing/conductive phase. A third group of mechanisms involving the exchange of matters with the environment, such as in Baba *et al.* [38], was essentially ruled out from the observation of reversible photochromism in ALD-capped films [6, 39] and in an ultra high vacuum environment. [15, 40] While interaction with the environment can likely influence the rates of photo-darkening

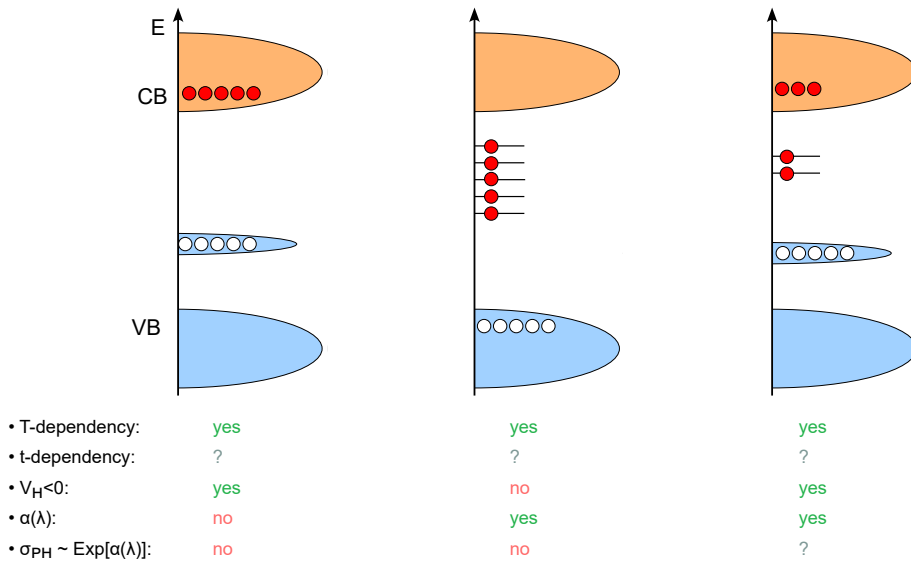


Figure 6.9: The formation of small, long-living defects is considered a possibility to describe the optical and electronic changes observed upon illumination of RE oxyhydride thin films. Such defects might act as a trap for holes, electrons, or both. A visual overview of these three possibilities is given here, together with their ability/limits of describing the experimental findings, namely (i) temperature dependence, (ii) time dependence, (iii) negative Hall voltage, (iv) spectral shape of the absorption coefficient, and (v) exponential relation between photo-conductivity and absorption coefficient (see text).

and bleaching,^[40] that does not seem to be a necessary condition for the reversible photochromism to occur. In the following we discuss the remaining two groups of mechanisms with the added insight of the transport measurements presented here. In doing so, we try to assess if the species responsible for the optical absorption can also be responsible for the increase in conductivity.

6.4.1. HYPOTHESIS OF LONG LIVING SMALL DEFECTS

In this hypothesis, light exposure induces the formation of long-living small defects which trap either the electron, the hole, or both. Fig. 6.9 gives a schematic overview of these three possibilities, their merits, and their pitfalls.

Trapped hole, free electron. So far, two type of defects have been proposed to act as hole-traps in RE oxyhydrides, namely molecular H_2 and hydroxide diatomic anions (OH^-). However, we do not exclude that other hole-trapping defects might be possible.

Formation of molecular H_2 was suggested in a computational study,^[41] where two H^- in adjacent octahedral sites were seen to bond creating a shallow donor level close to the conduction band edge. Interestingly, the activation energy for the formation and dissolution of the H_2 molecule was seen to depend on the O:H anion-ratio, possibly ex-

plaining the compositional dependence of the bleaching kinetics. [8] This computational study was, however, conducted on $\text{YO}_x\text{H}_{3-2x}$ of extremely high H-content ($x < 0.25$), a compositional range that is far from the experimental one ($x > 0.5$) and that we have already discussed as inherently unstable and, thus, not necessarily representative (see chapter 4).

Formation of hydroxide diatomic anions $(\text{OH})^-$ was suggested in analogy with mayenite ($12\text{CaO}_3 \cdot 7\text{Al}_2\text{O}_3$). [42-45] Here, light converts a fraction of the H^- ions into hydroxides, releasing electrons and, thus, improving conductivity and optical absorption of the originally insulating oxide. Similarly to the case of our photochromic thin films, this reaction is reversible and influenced by temperature.

The implication with this class of defects, is that the free electrons released in the conduction band are responsible for both the optical absorption and conduction. This hypothesis is in line with many experimental aspects, including (i) the negative Hall potential, (ii) the comparable kinetics and temperature dependence of photochromism and photo-conduction, and (iii) the fact that no major structural rearrangement and/or long-distance atomic diffusion is needed.

There are, however, two unresolved shortcomings, as this hypothesis does not explain (i) the exponential relation between σ and α , which would both be linearly proportional to the fraction of free electrons and therefore to each other, and (ii) the experimental dependence of the absorption coefficient on the wavelength. In this sense, Nafezarefi *et al.* [3] reported that the absorption coefficient of $\text{REO}_x\text{H}_{3-2x}$ thin films decreases with the wavelength, showing a trend that is opposite to the normal free carrier absorption in semiconductors ($\alpha(\lambda) \propto \lambda^p$, with $p > 0$). [46, 47]

Trapped electrons, free holes. Often considered in the past was the possibility that the electron of the photo-generated electron-hole pair could be trapped in a anion vacancy, forming a colour center responsible for the optical absorption of the photo-darkened material. Such colour centres have been observed before in rare-earth compounds, [48, 49] and recognized as the cause of photochromism in other inorganic materials. [50, 51]

The implication, in this case, is that the free holes are responsible for the photo-conductivity of the material. Being this in direct contrast with the negative Hall potential measured for the photo-darkened material, we exclude this to be a viable explanation. Additionally, similar to the previous case, the optical absorption and photo-conductivity would both be linearly proportional to the fraction of trapped electrons, thus, resulting in a linear relation between σ and α .

Some trapped electrons, trapped holes. As a final possibility we consider a combination of the first two cases, where the holes are trapped in small defects that impede the recombination of the carriers, and a fraction of the electrons is trapped as well in the form of colour centres. In this case the free electrons would be dominantly responsible for the photo-conductivity, while the trapped electrons would be dominantly responsible for the optical absorption. Compared to the first case, this hypothesis has the merit of solving the λ dependence of the absorption coefficient. However, the relation between σ and α becomes non-trivial and its relation to the experiment cannot be assessed.

6.4.2. HYPOTHESIS OF METALLIC PHASE SEGREGATION

The second hypothesis to describe photo-darkening and photo-conductivity of the RE oxyhydride thin films is the segregation of a second phase with metallic properties. In this case, the optical absorption would result from the plasmonic resonance localized at the surface of small metallic domains within the dielectric RE oxyhydride matrix.

The hypothesis of metallic phase segregation was first advanced in analogy to the Cu-doped Ag-halide glasses, whose reversible photochromism is well known to depend on the segregation of plasmonic Ag particles. [50, 52-55]. Later, the ellipsometry study of Montero *et al.* [11] reinforced this hypothesis, showing that the dielectric function of the darkened state could result from a small volume fraction ($v_{\%} = 1 - 10\%$) of metallic inclusions (most likely RE di-hydride) within the transparent matrix.

In qualitative terms, the merits of this hypothesis are several. The slow [3, 8] temperature activated [16] kinetics and the volume contraction [13] would, in fact, be a natural consequence of the structural rearrangement necessary for the segregation (dissolution) of the metallic phase during photo-darkening (bleaching). From an optical perspective, the extremely broad absorption of the darkened films ($\lambda \sim 400 - 2500$ nm) and its spectral shape [3] can result from an ensemble of metallic domains with different shapes and different concentrations of free carriers and/or different effective masses. From an electronic perspective, the conductivity would effectively increase upon illumination due to the formation of metallic domains within the thin film. In line with this idea, we note that during illumination the Gd oxyhydride films reach a conductivity ($\sim 10^{-1}$ S/cm) which is not too distant from that ($\sim 10^{-2}$ S/cm) of the $\text{GdO}_x\text{H}_{3-2x}/\text{GdH}_x$ mixed-phase sample of Fig. 6.3. Finally, the time-dependence of the bleaching (Fig. 6.8c) can be directly connected to the average rate of dissolution of the metallic domains.

Having a measurement of the film electronic properties under illumination, we probe the hypothesis of metallic domains in Fig. 6.10. Here, the Maxwell-Garnett [56] and Bruggeman [57] effective medium approximations (EMAs) [58] are used to estimate the volume fraction of the metallic phase (here assumed GdH_2 , $\sigma_{\text{GdH}_2} = 1.7 \times 10^3$ S/cm [34]) that would correspond to the experimental photo-induced conductivity. While the two models are equivalent in the limit of small volume fractions, it is well known that only the Bruggeman EMA is qualitatively capable of describing the behaviour of a composite where the two phases are in comparable amounts. In any case, both models show a plateau during darkening and during most of the bleaching (Maxwell-Garnett: $v_{\%} \sim 1$, Bruggeman: $v_{\%} \sim 0.33$), indicating that the hypothesis of segregation of metallic domains can account for the experimental photo-conductivity only if such domains form percolation channels throughout the whole sample.

While the Bruggeman EMA qualitatively predicts an abrupt shift in conductivity when percolation is reached (at $v_{\%} \sim 0.33$), a quantitative analysis cannot be done without knowledge of the three-dimensional topology of the conductive network within the insulating matrix. Intuitively, at parity of volume fraction, a fiber-like arrangement of the metallic domains results in a higher conductivity compared to dense and more isolated clusters. Given the lack of direct information on the RE oxyhydride system, here we further estimate which range of volume fractions potentially describes the experimental photo-conductivity using the relatively generic model of Cai *et al.* [59]. This model is a modification of the Bruggeman EMA, where the conductivity in the percolation regime is

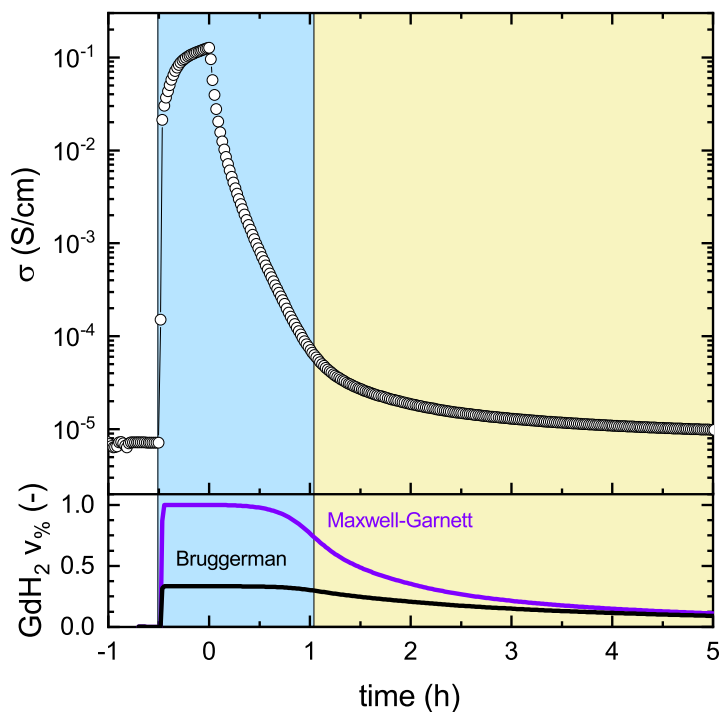


Figure 6.10: Time-dependence of the conductivity of Gd oxyhydride thin film during a cycle of darkening and bleaching at 303 K. Under the hypothesis that illumination induces the segregation of GdH_2 metallic domains, the bottom panel shows their volume fraction as estimated with Maxwell-Garnett and Bruggeman effective medium approximations. In both cases, the plateau indicates that percolation of the metallic domains is needed to account for the experimental photo-conductivity. The background colors are used to highlight the regimes in which optical absorption and conductivity are dominated by the photo-induced effects and show exponential relation (blue), in contrast to the material properties of the Gd oxyhydride as largely recovered at the end of the bleaching (yellow).

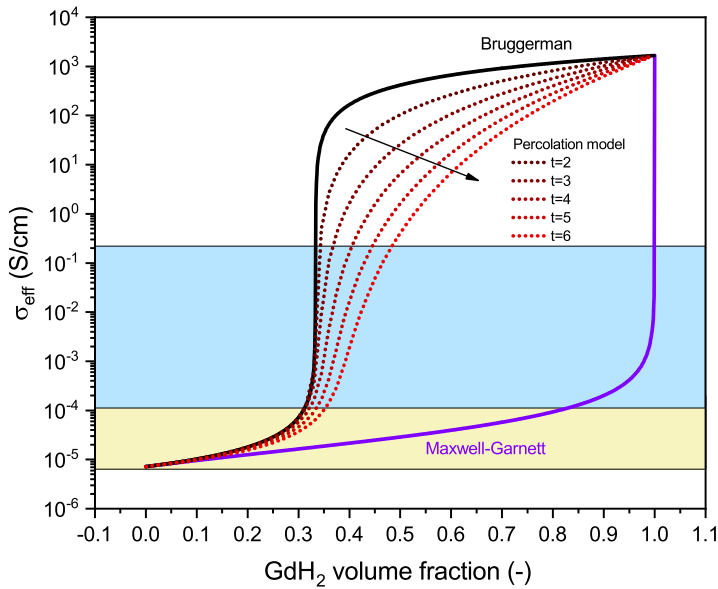


Figure 6.11: Effective conductivity for the $\text{GdO}_x\text{H}_{3-2x}/\text{GdH}_2$ composite material for any volume fraction of GdH_2 . The estimation is shown for the Maxwell-Garnett and Bruggeman effective medium approximations, as well as for the model of Cai *et al.* [59], which in the percolation regime corrects the Bruggeman theory with a semi-empirical parameter (t), whose effect is also shown. The background colors are used to highlight the regimes in which optical absorption and conductivity are dominated by the photo-induced effects and show exponential relation (blue), in contrast to the material properties of the Gd oxyhydride as largely recovered at the end of the bleaching (yellow).

essentially rescaled with a single semi-empirical parameter ($2 \leq t < 6$) that depends on the type of network, and is often found in the range of $t \sim 2$. [59] The effect of this correction is reported in Fig. 6.11 which shows how 30 – 50% of the RE oxyhydride material would need to convert into a conductive GdH_2 -like phase.

To do the above estimation, the conductivity of the metallic domains was assumed to be equal to that reported for a GdH_2 thin film, [34] however, the lower boundary of $v_{\%} \sim 30\%$ would remain even if the metallic domains were to present an arbitrarily higher conductivity. A minimum metallic volume fraction of $\sim 30\%$ is significantly higher than the value reported by Montero *et al.* [11], even considering that in this work we used a much higher light intensity, and that the Gd oxyhydride films present a higher photochromic contrast than the Y-based ones. [8]. A possibility to consider, however, is that the metallic domains do not disperse throughout the whole material, but rather nucleate and grow in favourable regions, such as at grain boundaries, around the columns of the film, or at the substrate/air interfaces. This would effectively greatly reduce the volume fraction required to have percolation of the segregated phase.

Finally, we note that the hypothesis of metallic phase segregation, like the hypothesis of small defects, does not provide a clear explanation for the exponential relation between σ and α . In this sense, approximating the absorption coefficient as $\alpha \sim c\sigma_{abs}$, where c is the concentration of metallic domains and σ_{abs} their average absorption cross section,

one might consider two limit cases. Firstly, let's suppose that the UV exposure induces the nucleation of small metallic particles with similar size, and that such particles do not grow further. In this case, the absorption coefficient would linearly scale with the metallic volume fraction, as that would reflect the number of metallic particles. Fig. 6.11 clearly shows that no EMA expression presents an exponential relation between conductivity and volume fraction. Second, let's suppose that the UV exposure initially nucleates a fixed number of metallic particles, and that these particles grow upon further illumination. In this case, the particle concentration would remain constant, while their σ_{abs} would scale with the cube of their volume, as predicted by the Mie theory in the sub-wavelength limit. [60-62] Once again, no EMA theory predict an exponential relation between conductivity and $\nu_{\%}^3$.

While the two limit cases here discussed contradict the exponential relation between σ and α , the general case (particle of different size/shape, nucleation and growth happening at the same time) presents too many variables to be assessed.

6.5. CONCLUSION

In conclusion, in this chapter we have presented an extensive characterization of the transport properties of photochromic and photo-conductive $\text{GdO}_x\text{H}_{3-2x}$ thin films, including the effects induced by light exposure. Analysing the Hall-effect data in the framework of a free-carriers transport, we find the reactively sputtered Gd oxyhydride thin films to be p-type semiconductors characterized by a low concentration of charge carriers ($n \sim 10^{11} - 10^{12} \text{ cm}^{-3}$) with exceptionally high mobility ($\mu \sim 10^3 - 10^4 \text{ cm}^2 \text{ V}^{-1} \text{ s}^{-1}$). Such high mobility evidently warrens further verification and is likely to be an overestimation due to "misinterpreted" polaronic conduction.

We find photochromism and photo-conductivity (in the darkened state electrons are the main carriers) to be connected properties, as indicated by a comparable time and temperature dependence, and by a unique exponential relation between material conductivity and the optical absorption. All these facts indicate, beyond reasonable doubt, that photochromism and photo-conductivity originate either (i) from the same absorbing and electron-conductive species formed upon illumination, or (ii) from a single light-induced structural process which leads to the formation of absorbing species and to the increase of mobile electrons in the material. The hypothesis of a completely electronic process is ruled out.

Finally, we have used this new insight to discuss the two mechanisms proposed for the photochromic effect, namely the formation of small defects and the phase segregation of metallic domains, with the intention of assessing if the optically absorbing species can also be responsible of the photo-induced conductivity. While a definitive understanding of the mechanism behind the process is still missing, our data help to narrow the picture. For the hypothesis of small defects, we rule out that having only hole-traps or electron-traps is sufficient, showing that both type of traps would be needed. For the hypothesis of metallic phase segregation, a *semi-quantitative* discussion of the photo-conductivity shows that a minor fraction of isolated and dispersed metallic domains would not suffice to describe the experimental data. Upon illumination the conductivity increases by an impressive factor of $\sim 10^4$, something that metallic domains can account for only if they form a network that percolates throughout the whole film.

It seems that neither of the two mechanism provides a simple compelling explanation of both photochromism and photo-conductivity, if not under stringent conditions that are at odds with previous works. Therefore, in future research, we think that the hypotheses of metallic phase segregation (explaining the optical absorption) and defect formation in the RE oxyhydride matrix (explaining the increase of negative charge carriers) should be considered – together and simultaneously – in the framework of a single process initiated by the electron-hole formation.

REFERENCES

- [1] T. Mongstad, C. Platzer-Björkman, J. P. Maehlen, L. P. Mooij, Y. Pivak, B. Dam, E. S. Marstein, B. C. Hauback, and S. Z. Karazhanov, *A new thin film photochromic material: Oxygen-containing yttrium hydride*, *Sol. Energy Mater. Sol. Cells* **95**, 3596 (2011).
- [2] K. Fukui, S. Iimura, T. Tada, S. Fujitsu, M. Sasase, H. Tamatsukuri, T. Honda, K. Ikeda, T. Otomo, and H. Hosono, *Characteristic fast H^- ion conduction in oxygen-substituted lanthanum hydride*, *Nat. Commun.* **10**, 2578 (2019).
- [3] F. Nafezarefi, H. Schreuders, B. Dam, and S. Cornelius, *Photochromism of rare-earth metal-oxy-hydrides*, *Appl. Phys. Lett.* **111**, 103903 (2017).
- [4] S. Cornelius, G. Colombi, F. Nafezarefi, H. Schreuders, R. Heller, F. Munnik, and B. Dam, *Oxyhydride nature of rare-earth-based photochromic thin films*, *The Journal of Physical Chemistry Letters* **10**, 1342 (2019).
- [5] S. Adalsteinsson, M. Moro, D. Moldarev, S. Droulias, M. Wolff, and D. Primetzhofer, *Correlating chemical composition and optical properties of photochromic rare-earth oxyhydrides using ion beam analysis*, *Nuclear Instruments and Methods in Physics Research Section B: Beam Interactions with Materials and Atoms* **485**, 36 (2020).
- [6] D. Chaykina, F. Nafezarefi, G. Colombi, S. Cornelius, L. J. Bannenberg, H. Schreuders, and B. Dam, *Influence of crystal structure, encapsulation, and annealing on photochromism in nd oxyhydride thin films*, *The Journal of Physical Chemistry C* **126**, 2276 (2022).
- [7] G. Colombi, S. Cornelius, A. Longo, and B. Dam, *Structure model for anion-disordered photochromic gadolinium oxyhydride thin films*, *J. Phys. Chem. C* **124**, 13541 (2020).
- [8] G. Colombi, T. De Krom, D. Chaykina, S. Cornelius, S. W. H. Eijt, and B. Dam, *Influence of cation ($RE = Sc, Y, Gd$) and O/H anion ratio on the photochromic properties of REO_xH_{3-2x} thin films*, *ACS Photonics* **8**, 709 (2021).
- [9] C. C. You, T. Mongstad, J. P. Maehlen, and S. Karazhanov, *Engineering of the band gap and optical properties of thin films of yttrium hydride*, *Appl. Phys. Lett.* **105**, 031910 (2014).
- [10] C. C. You, T. Mongstad, E. S. Marstein, and S. Z. Karazhanov, *The dependence of structural, electrical and optical properties on the composition of photochromic yttrium oxyhydride thin films*, *Materialia* **6**, 100307 (2019).
- [11] J. Montero, F. A. Martinsen, M. García-Tecedor, S. Z. Karazhanov, D. Maestre, B. Hauback, and E. S. Marstein, *Photochromic mechanism in oxygen-containing yttrium hydride thin films: An optical perspective*, *Phys. Rev. B* **95**, 201301 (2017).
- [12] J. Montero and S. Z. Karazhanov, *Spectroscopic ellipsometry and microstructure characterization of photochromic oxygen-containing yttrium hydride thin films*, *Phys Status Solidi A* **215**, 1701039 (2018).

- [13] J. P. Maehlen, T. T. Mongstad, C. C. You, and S. Karazhanov, *Lattice contraction in photochromic yttrium hydride*, *J. Alloys Compd.* **580**, S119 (2013).
- [14] C. V. Chandran, H. Schreuders, B. Dam, J. W. G. Janssen, J. Bart, A. P. M. Kentgens, and P. J. M. van Bentum, *Solid state nmr studies of the photochromic effects of thin films of oxygen containing yttrium hydride*, *J. Phys. Chem. C* **118**, 22935 (2014).
- [15] D. Chaykina, T. de Krom, G. Colombi, H. Schreuders, A. Suter, T. Prokscha, B. Dam, and S. Eijt, *Structural properties and anion dynamics of yttrium dihydride and photochromic oxyhydride thin films examined by in situ μ^+ SR*, *Phys. Rev. B* **103**, 224106 (2021).
- [16] E. M. Baba, P. M. Weiser, E. z. Zayim, and S. Karazhanov, *Temperature-dependent photochromic performance of yttrium oxyhydride thin films*, *physica status solidi (RRL) – Rapid Research Letters* **15**, 2000459 (2021).
- [17] E. S. Kooij, A. T. M. van Gogh, and R. Griessen, *In situ resistivity measurements and optical transmission and reflection spectroscopy of electrochemically loaded switchable YH_x films*, *J. Electrochem. Soc.* **146**, 2990 (1999).
- [18] A. F. T. Hoekstra, A. S. Roy, T. F. Rosenbaum, R. Griessen, R. J. Wijngaarden, and N. J. Koeman, *Light-induced metal-insulator transition in a switchable mirror*, *Phys. Rev. Lett.* **86**, 5349 (2001).
- [19] K. K. Ng, F. C. Zhang, V. I. Anisimov, and T. M. Rice, *Theory for metal hydrides with switchable optical properties*, *Phys. Rev. B* **59**, 5398 (1999).
- [20] A. T. M. van Gogh, D. G. Nagengast, E. S. Kooij, N. J. Koeman, J. H. Rector, R. Griessen, C. F. J. Flipse, and R. J. J. G. A. M. Smeets, *Structural, electrical, and optical properties of $La_{1-z}Y_zH_x$ switchable mirrors*, *Phys. Rev. B* **63**, 195105 (2001).
- [21] E. H. Hall, *On a new action of the magnet on electric currents*, *American Journal of Mathematics* **2**, 287 (1879).
- [22] National Research Council (U.S.). Committee on Coatings, *High-temperature Oxidation-resistant Coatings: Coatings for Protection from Oxidation of Superalloys, Refractory Metals, and Graphite* (National Academy of Sciences, 1970).
- [23] L. J. Van der Pauw, *A method of measuring specific resistivity and hall effect of*, *Philips Res. Rep.* **13**, 1 (1958).
- [24] D. Emin, *Polarons* (Cambridge University Press, 2012).
- [25] C. Kittel, *Introduction to Solid State Physics, 9th Ed.* (John Wiley and Sons, 2018).
- [26] K. Bolotin, K. Sikes, Z. Jiang, M. Klima, G. Fudenberg, J. Hone, P. Kim, and H. Stormer, *Ultra-high electron mobility in suspended graphene*, *Solid State Communications* **146**, 351 (2008).

- [27] Y. Yongbo, G. Gaurav, A. A. L., A. P. Zoombelt, S. C. B. Mannsfeld, C. Jihua, N. Dennis, T. M. F., Huang, Jinsong, and B. Zhenan, *Ultra-high mobility transparent organic thin film transistors grown by an off-centre spin-coating method*, [Nature Communications](#) **5**, 351 (2014).
- [28] P. Heremans, A. K. Tripathi, A. de Jamblinne de Meux, E. C. P. Smits, B. Hou, G. Pourtois, and G. H. Gelinck, *Mechanical and electronic properties of thin-film transistors on plastic, and their integration in flexible electronic applications*, [Advanced Materials](#) **28**, 4266 (2016).
- [29] D. Joshi and R. Srivastava, *Mobility and carrier concentration in polycrystalline silicon*, [Solar Cells](#) **12**, 337 (1984).
- [30] P. Vajda, *Chapter 137 hydrogen in rare-earth metals, including rh_{2+x} phases*, (Elsevier, 1995) pp. 207–291.
- [31] P. Vajda, *Hydrogen in rare earths: a wealth of structural and electronic phenomena*, [Solid State Ion.](#) **168**, 271 (2004).
- [32] M. Sakai, T. Kontani, O. Nakamura, K. Takeyama, Y. Uwatoko, Y. Obi, and K. Takashi, *Electrical transport and optical properties of hydrogen-deficient YH₂films*, [Japanese Journal of Applied Physics](#) **43**, 681 (2004).
- [33] R. C. Heckman, *Hall effect and conductivity in the neodymium–hydrogen system*, [The Journal of Chemical Physics](#) **48**, 5281 (1968).
- [34] A. Miniotas, B. Hjörvarsson, L. Douysset, and P. Nostell, *Gigantic resistivity and band gap changes in gdoyhx thin films*, [Applied Physics Letters](#) **76**, 2056 (2000).
- [35] C. Franchini, M. Reticcioli, M. Setvin, and U. Diebold, *Polarons in materials*, [Nature Reviews Materials](#) **6**, 560 (2021).
- [36] A. J. E. Rettie, W. D. Chemelewski, D. Emin, and C. B. Mullins, *Unravelling small-polaron transport in metal oxide photoelectrodes*, [The Journal of Physical Chemistry Letters](#) **7**, 471 (2016).
- [37] F. Nafezarefi, S. Cornelius, J. Nijskens, H. Schreuders, and B. Dam, *Effect of the addition of zirconium on the photochromic properties of yttrium oxy-hydride*, [Sol Energy Mater. Sol. Cells](#) **200**, 109923 (2019).
- [38] E. M. Baba, J. Montero, E. Strugovshchikov, E. O. Zayim, and S. Karazhanov, *Light-induced breathing in photochromic yttrium oxyhydrides*, [Phys. Rev. Mater.](#) **4**, 025201 (2020).
- [39] M. V. Moro, S. M. Aðalsteinsson, T. T. Tran, D. Moldarev, A. Samanta, M. Wolff, and D. Primetzhofer, *Photochromic response of encapsulated oxygen-containing yttrium hydride thin films*, [physica status solidi \(RRL\) – Rapid Research Letters](#) **15**, 2000608 (2021).

- [40] D. Moldarev, L. Stolz, M. V. Moro, S. M. Aðalsteinsson, I.-A. Chioar, S. Z. Karazhanov, D. Primetzhofer, and M. Wolff, *Environmental dependence of the photochromic effect of oxygen-containing rare-earth metal hydrides*, *Journal of Applied Physics* **129**, 153101 (2021).
- [41] J. Chai, Z. Shao, H. Wang, C. Ming, W. Oh, T. Ye, Y. Zhang, X. Cao, P. Jin, S. Zhang, and Y.-Y. Sun, *Ultrafast processes in photochromic material yhxoy studied by excited-state density functional theory simulation*, *Science China Materials* **63**, 1579 (2020).
- [42] K. Hayashi, S. Matsuishi, T. Kamiya, M. Hirano, and H. Hosono, *Light-induced conversion of an insulating refractory oxide into a persistent electronic conductor*, *Nature* **419**, 1476 (2002).
- [43] K. Hayashi, *Kinetics of electron decay in hydride ion-doped mayenite*, *The Journal of Physical Chemistry C* **115**, 11003 (2011).
- [44] K. Hayashi, P. V. Sushko, Y. Hashimoto, A. L. Shluger, and H. Hosono, *Hydride ions in oxide hosts hidden by hydroxide ions*, *Nature Communications* **5**, 2041 (2014).
- [45] K. Hayashi and H. Hosono, *Green apatites: hydride ions, electrons and their interconversion in the crystallographic channel*, *Phys. Chem. Chem. Phys.* **18**, 8186 (2016).
- [46] K. Seeger, *Semiconductor Physics: an introduction, 9th Ed.* (Springer, 2004).
- [47] R. M. Culpepper and J. R. Dixon, *Free-carrier adsorption in n-type indium arsenide*, *J. Opt. Soc. Am.* **58**, 2578 (1968).
- [48] D. L. Staebler and S. E. Schnatterly, *Optical studies of a photochromic color center in rare-earth-doped CaF_2* , *Phys. Rev. B* **3**, 516 (1971).
- [49] H. Bill and G. Calas, *Color centers, associated rare-earth ions and the origin of coloration in natural fluorites*, *Physics and Chemistry of Minerals* **3**, 117 (1978).
- [50] R. Araujo, *Inorganic photochromic systems*, *Molecular Crystals and Liquid Crystals Science and Technology. Section A. Molecular Crystals and Liquid Crystals* **297**, 1 (1997).
- [51] T. He and J. Yao, *Photochromism of molybdenum oxide*, *Journal of Photochemistry and Photobiology C: Photochemistry Reviews* **4**, 125 (2003).
- [52] R. J. Araujo, *Photochromism in glasses containing silver halides*, *Contemporary Physics* **21**, 77 (1980).
- [53] N. F. Borrelli, J. B. Chodak, and G. B. Hares, *Optically induced anisotropy in photochromic glasses*, *Journal of Applied Physics* **50**, 5978 (1979).
- [54] T. Seward, *Coloration and optical anisotropy in silver-containing glasses*, *Journal of Non-Crystalline Solids* **40**, 499 (1980), proceedings of the Fifth University Conference on Glass Science.

- [55] C. L. Marquardt, J. F. Giuliani, and R. T. Williams, *Darkening mechanisms in silver-halide photochromic glasses: Flash photolysis and esr studies*, *Journal of Applied Physics* **47**, 4915 (1976).
- [56] J. C. M. Garnett and J. Larmor, *Xii. colours in metal glasses and in metallic films*, *Philosophical Transactions of the Royal Society of London. Series A, Containing Papers of a Mathematical or Physical Character* **203**, 385 (1904).
- [57] D. A. G. Bruggeman, *Berechnung verschiedener physikalischer konstanten von heterogenen substanzen. i. dielektrizitätskonstanten und leitfähigkeiten der mischkörper aus isotropen substanzen*, *Ann. Phys.* **416**, 636 (1935).
- [58] O. Stenzel, *The Physics of Thin Film Optical Spectra* (Springer, 2005) pp. 107–124.
- [59] W.-Z. Cai, S.-T. Tu, and J.-M. Gong, *A physically based percolation model of the effective electrical conductivity of particle filled composites*, *Journal of Composite Materials* **40**, 2131 (2006).
- [60] G. Mie, *Beiträge zur optik trüber medien, speziell kolloidaler metallösungen*, *Annalen der Physik* **330**, 377 (1908).
- [61] S. A. Maier, *Plasmonics: fundamentals and applications* (Springer, 2007).
- [62] M. Pelton and B. Garnett, *Introduction to Metal-Nanoparticle Plasmonics* (Wiley, 2013).

APPENDIX

6.A. ADDITIONAL DETAILS ON TRANSPORT MEASUREMENTS

Measures of resistivity and Hall Effect are central to semiconductor science, yet, the classical Van der Pauw technique presents many practical challenges and remains prone to errors. Therefore we put special care in assessing the reliability of our data. In the following we briefly describe Van der Pauw and Hall-Effect measurement schemes, and then the quality-control checks that we implemented at different steps of the analysis. The theory summarized hereafter is all textbook wisdom.

Van der Pauw resistivity Fig. 6.A.1 shows the Van der Pauw geometry and the cyclic permutation of measurements that are used to extract the resistivity of a thin film. Four contacts are placed along the perimeter of the sample, and in each measure current is forced along one pair, while the voltage drop on the opposite pair is recorded. To increase the precision of the overall procedure, each of 4 measures depicted in the figure, is repeated inverting the direction of the current, resulting in a total of 8 acquisitions. The Van der Pauw geometri *de facto* implies that the resistance of the sample is probed along its horizontal (R_A , eq. 6.5) or vertical axis (R_B , eq. 6.6) depending on the cyclic permutation.

$$R_A = \left(\frac{V_{DC}}{I_{AB}} + \frac{V_{CD}}{I_{BA}} + \frac{V_{AB}}{I_{DC}} + \frac{V_{BA}}{I_{CD}} \right) / 4 \quad (6.5)$$

$$R_B = \left(\frac{V_{CD}}{I_{DA}} + \frac{V_{BC}}{I_{AD}} + \frac{V_{DA}}{I_{CB}} + \frac{V_{AD}}{I_{BC}} \right) / 4 \quad (6.6)$$

From that, the actual sheet resistance (R_s) can be calculated from the numerical solution of:

$$e^{(-\pi R_A / R_s)} + e^{(-\pi R_B / R_s)} = 1. \quad (6.7)$$

Provided that the contacts are at the perimeter of the sample, eq. 6.7 holds for samples of any arbitrary shape. However, having used a squared sample provides us with the opportunity of conducting a series of checks on the consistency of the acquired data.

1. An Ohmic behaviour of the metal-semiconductor junction is of paramount importance. Throughout the whole measure, the Ohmic behaviour is monitored looking at what happens when the polarity of the current source is switched (eg. from I_{AB} to I_{BA}). Fig. 6.A.2a confirms that, for each contact pair, the difference of voltage drop upon polarity switch is well below $\sim 10\%$.
2. An underlying assumption to any transport measurement is the homogeneity of the sample. In view of the symmetric squared shape of the sample, the degree of homogeneity can be probed comparing R_A and R_B . Fig. 6.A.2b confirms that the difference between these two is within $\sim 20\%$.
3. To further assess the influence of homogeneity on the extracted value of resistivity, we compare the value extracted from eq. 6.7, with the special solution $R_{s,ideal} = \pi R / \ln(2)$ that holds for $R_A = R_B = R$. Figure Fig. 6.A.2c confirms that the two approaches return almost identical result.

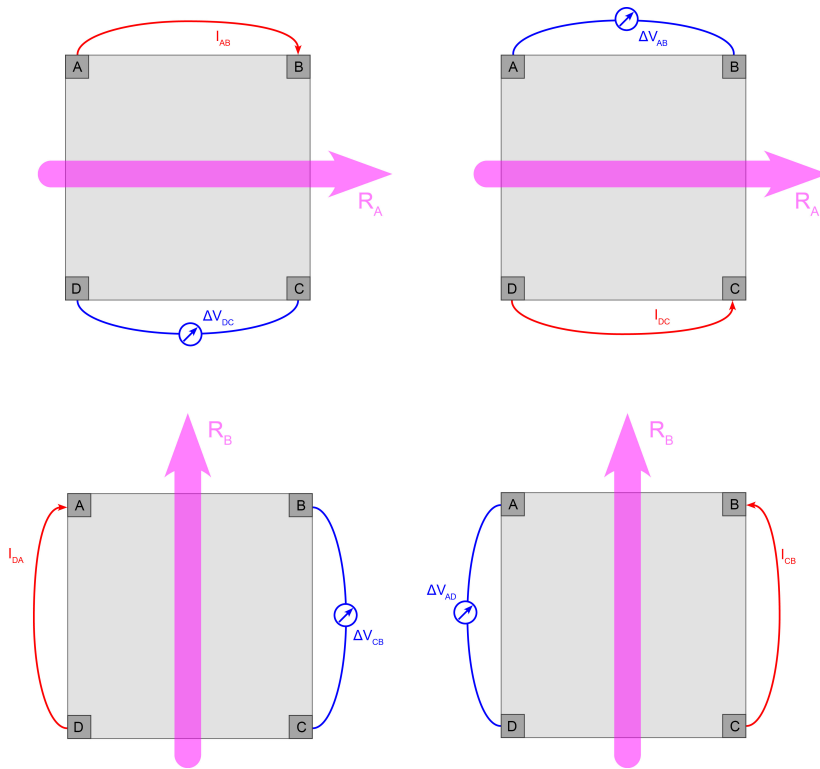


Figure 6.A.1: Cyclic permutation of measurements used to quantify the sheet resistance of a thin film according to the Van der Pauw method. Four contacts are placed along the perimeter of the sample, and in each measure current is forced along one edge of the sample, while the voltage drop on the opposite edge is recorded. Red and blue lines indicate the connections to the external current source and voltage meter, respectively. The purple arrows indicated the axis along which the resistance is probed.

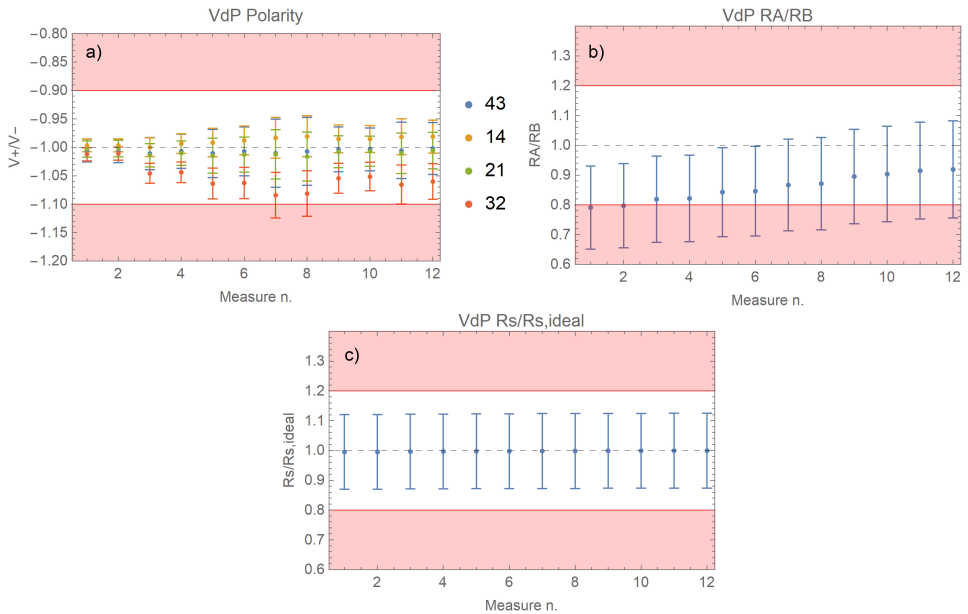


Figure 6.A.2: Consistency checks on the Van der Pauw measurements for the temperature-dependent conductivity reported in Fig. 6.5. Each panel reports 12 measures on the x-axis, which corresponding to the 6 studied temperatures, each of them repeated twice for statistics. Error bars reflect the propagation of the (over)estimated uncertainty for each current and voltage readout ($\delta I = 20\%I, \delta \Delta V = 3 \text{ mV}$). *a*) Ratio between the potential difference measured upon current reversal. The sign of the potential drop changes but its value remains equal within 10% error, verifying Ohmic behaviour in all measures. *b*) Ratio between the resistance probed along the horizontal (R_A) and vertical (R_B) axes of the sample. The difference between R_A and R_B is within 20%, verifying that the sample is largely homogeneous. *c*) Ratio between the sheet resistance evaluated with the general Van der Pauw equation and with its special, ideal solution that holds for $R_A = R_B$. The two results are almost identical, showing the resiliency of the method against small errors.

Hall Effect Fig. 6.A.3 shows the cyclic permutation of measurements and of current reversal that are used in an Hall Effect experiment. The Van der Pauw geometry is maintained, but this time current is forced across the diagonal of the squared samples. A stationary magnetic field (B) perpendicular to the sample surface effectively induces a bending of the current trajectory, which in turn gives a potential difference (Hall voltage, V_H) along the other diagonal of the sample. Under the assumption of a single type of charge carriers (i.e., only electrons, or only holes), it can be easily proved that the Hall Voltage reads:

$$V_H = \frac{q}{|q|} \frac{IB}{ned} \quad (6.8)$$

where d is the sample thickness, e the electron charge, q the charge of the carriers, and n the carrier density. In practice, V_H and I are estimated as the average values from the cyclic permutation of measurements, and then all experimentally accessible information are grouped in the so-called Hall coefficient (R_H):

$$R_H = \frac{V_H d}{BI}. \quad (6.9)$$

From eq. 6.9 and from the well known relation between conductivity and carrier mobility ($\sigma = e_0 n \mu$), follows that carrier density and mobility can be quantified as:

$$n = \frac{1}{e|R_H|} \quad (6.10)$$

$$\mu = \sigma|R_H|. \quad (6.11)$$

Similar to the case of Van der Pauw resistivity, and on top of the checks already done for it, the cyclic permutation of measurements gives us the opportunity to evaluate the consistency of the measured quantities in a series of checks:

1. Being the sample symmetric, one expects the Hall voltage to be similar for any considered pair of contacts. Fig. 6.A.4a compares each readout to the average value of all of them, showing that most of them are with a 30% of difference.
2. Reversing the polarity of current source, and changing the direction of the magnetic field at the same time, induces the current trajectory to bend towards the same direction. That is schematically shown along each row of Fig. 6.A.3. Since the same region of material is probed, the Hall potential should as well be comparable. Fig. 6.A.4b shows this to be the case at $T = 300$ K, while at higher temperatures there is a progressive decline in the quality of the measure.
3. Reversing only the magnetic field, induces the current trajectory to bend in the opposite direction. However, for a symmetrical and homogeneous sample one expects a comparable Hall voltage. That is confirmed in Fig. 6.A.4c.
4. Reversing only the polarity of the current source, induces the current trajectory to bend in the opposite direction. However, for a symmetrical and homogeneous sample one expects a comparable Hall voltage. Fig. 6.A.4d shows that this is the case at $T = 300$ K, while at higher temperatures there is a progressive decline in the quality of the measure.

In summary, we find the measure done at $T = 300$ K to pass all the quality-checks that we could conceive, with a spread of Hall voltages always well below 10%, as expected for a homogeneous film of symmetric geometry. This makes a strong case for the reliability of the estimated carrier density ($n \sim 10^{11} - 10^{12} \text{ cm}^{-3}$) and carrier mobility ($\mu \sim 10^3 - 10^4 \text{ cm}^2 \text{ V}^{-1} \text{ s}^{-1}$), at least the order of magnitude.

The measures done at higher temperature show instead some problems when the polarity of the current source is changed. This might point towards a loss of Ohmic behaviours, but no such thing was observed instead in the Van der Pauw measurements. It is here important to mention that Van der Pauw and Hall effect measurements were not done one after the other in two different moments, but they were alternated during a single temperature ramp. Since the Hall voltage can be very small, and since is heavily influenced by any residual polarization of contacts and interfaces, we suspect that upon polarity reversal not enough time was given to the sample to find a new equilibrium before. Why this happened at higher temperature is likely related to a worsening of the contact with the spring loaded tips of our probe station. In any case, the quality of the Hall effect measurements done at $T > 300$ K is more ambiguous to assess, because it is unclear how the increasing spread in Hall voltage affects the final estimation of the carrier density and mobility. Since (i) these material properties are extracted from the average value of Hall voltage, and (ii) in view of the physically reasonable trend observed in Fig. 6.5 and (iii) in analogy with the resiliency of the Van der Pauw method for resistivity, we suppose that the Hall effect analysis is relatively resilient as well.

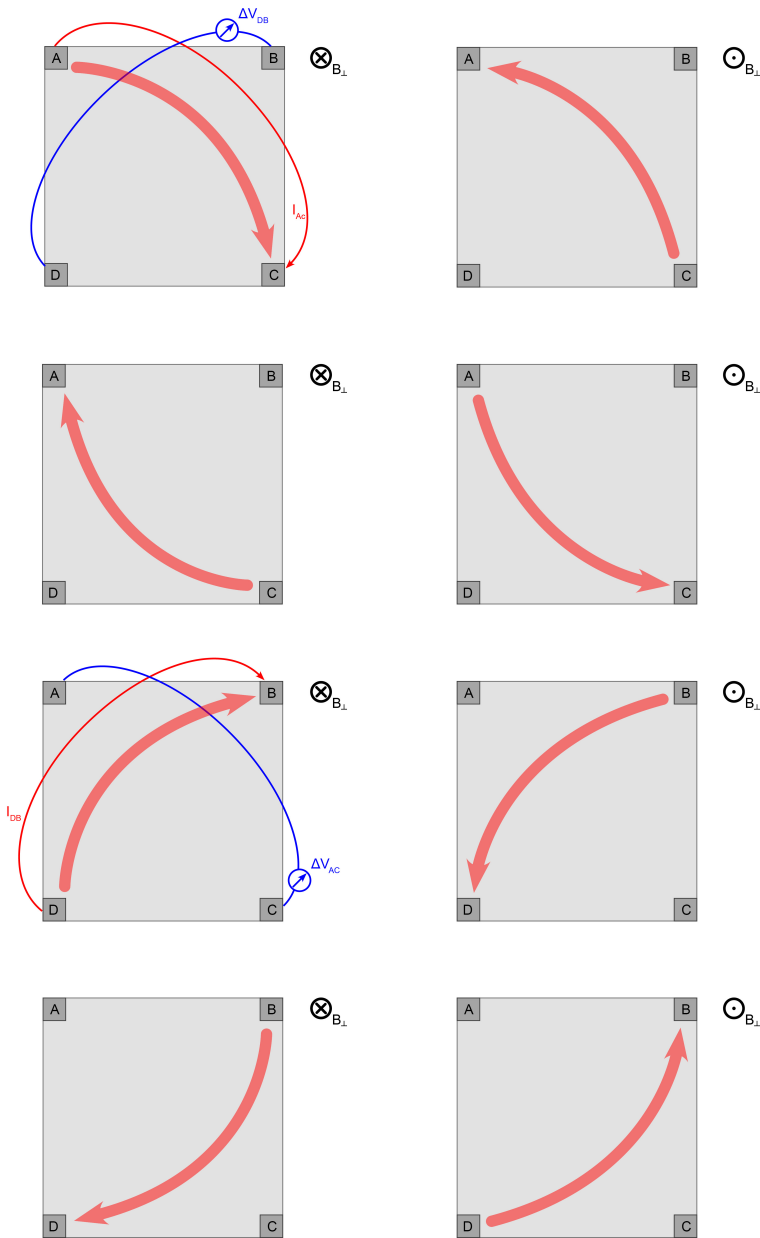


Figure 6.A.3: Cyclic permutation of the 8 measurements used that contribute to an Hall effect experiment and that are used to quantify carrier density and mobility. Four contacts are placed along the perimeter of the sample, and in each measure current is forced along one diagonal pair, while the Hall voltage on the opposite diagonal is recorded. This is done with the sample soaking in a stationary magnetic field perpendicular to its surface, which effectively results in a bending of the current trajectory (visualized by red arrows under the case of positive charge carriers). The connection to the external current source (red) and voltage reader (blue) remain identical for the first four cases, and for the last four cases, therefore they are drawn only once.

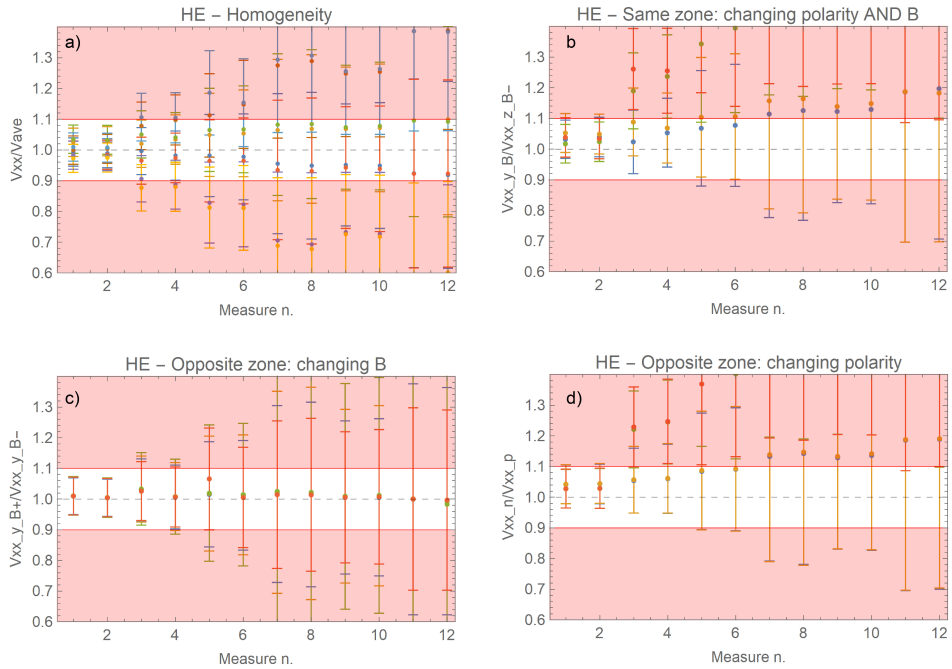


Figure 6.A.4: Consistency checks on the Hall effect measurements for the temperature-dependent carrier density and mobility of Fig. 6.5. Each panel reports 12 measures on the x-axis, which corresponding to the 6 studied temperatures, each of them repeated twice for statistics. Error bars reflect the propagation of the (over)estimated uncertainty for each current and voltage readout ($\delta I = 20\% I$, $\delta \Delta V = 3$ mV). *a)* Ratio between the Hall voltages measured upon current reversal. At least for the first two measures (done at $T = 300$ K) the value of Hall voltage remains equal within 10% error, verifying Ohmic behaviour. *b)* Ratio between the Hall voltage measured upon reversal of the direction of both current and magnetic field, implying that the current trajectory remains unchanged. In the first two measures (done at $T = 300$ K) the value of Hall voltage is equal within 10% error, but a progressive decline of quality is observed later on. *c)* Ratio between the Hall voltage measured upon reversal of the magnetic field, implying that the current trajectory bends in the opposite direction. All measures show that the Hall voltage remains within 10% of error. *d)* Ratio between the Hall voltage measured upon reversal of the source polarity, implying that the current trajectory bends in the opposite direction. In the first two measures (done at $T = 300$ K) the value of Hall voltage is equal within 10% error, but a progressive decline of quality is observed later on.

Finally, we take a closer look at what happens if the approximation of having carriers with only one polarity (i.e., only holes or only electrons) is used outside of its limits of validity in an *ambipolar* semiconductor. We do so because the rather low carrier density could indicate that the degree of doping is limited. The scope of this assessment is essentially to understand if the exceptionally high mobility that was found can be an artefact of the use of an improper theory.

In an ambipolar semiconductor, the equations that describe conductivity and Hall coefficient can be easily shown as:

$$\sigma = e_0(\mu_h n_h + \mu_e n_e) \quad (6.12)$$

$$R_H = \frac{1}{e_0} \frac{n_h \mu_h^2 - n_e \mu_e^2}{(n_h \mu_h + n_e \mu_e)^2}. \quad (6.13)$$

clearly, with two experimentally accessible quantities (σ, R_H) and four unknown variables in the form of mobility and density for both electrons and holes (μ_e, μ_h, n_e, n_h), the two equations above do not offer a unique solution for the quantities of interest.

A qualitative comparison of the general theory to the special case of one carrier type only can be done substituting the mass action law ($n_i^2 = n_h n_e$) in eq. 6.13, and rewriting the Hall coefficient in the variable $x = n_e/n_i$, i.e., the normalized electron concentration:

$$e_0 n_e R_H = \frac{\frac{1}{x} - x \left(\frac{\mu_e}{\mu_h} \right)^2}{\left(\frac{1}{x} + x \frac{\mu_e}{\mu_h} \right)^2}. \quad (6.14)$$

Fig. 6.A.5 shows how the general theory for ambipolar semiconductor compares to the approximation of only one carrier type. As expected, the models overlap in the limits $n_e \mu_e / n_h \mu_h \gg 10$ and $n_e \mu_e / n_h \mu_h \ll 0.1$. In the intermediate region, instead, the single carrier approximation always over-estimates the absolute value of the Hall coefficient. This implies that when the single carrier approximation is used outside of its limits of validity, eq. and eq. will respectively lead to an over-estimation of the carrier density, and an under-estimation of the carrier mobility. An immediate example is given by the special case $R_H = 0$ (e.g., for an ideal intrinsic semiconductor with $\mu_e = \mu_h$). The two equations give diverging carrier density and null carrier mobility.

We thus conclude that the exceptionally high carrier mobility that we have measured cannot be an artefact due to the single-carrier approximation.

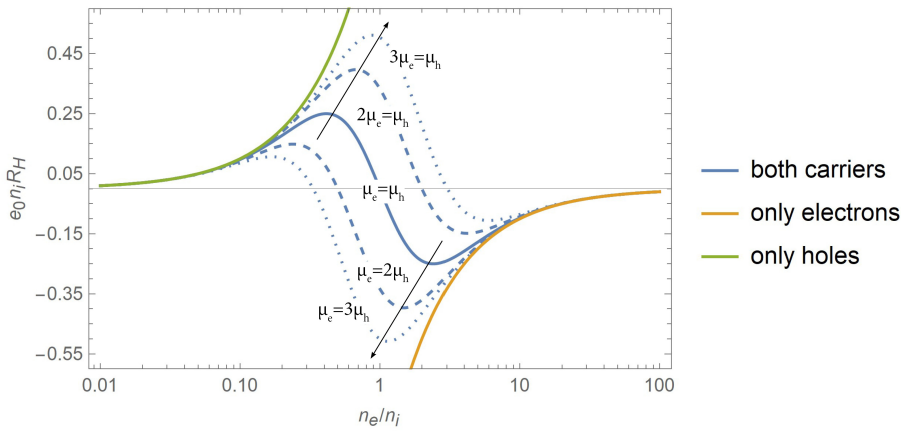


Figure 6.A.5: Hall coefficient as modelled with the general theory for an ambipolar semiconductor (eq. 6.14) and according to the approximation of a single carrier type. In the limits of high doping the two models overlap, while in the ambipolar region the single carrier approximation always over-estimates the magnitude of the Hall coefficient

6.B. PHOTOCROMISM AND PHOTO-CONDUCTIVITY

Fig. 6.B.1a shows that the parameter B in eq. 6.1, namely the slope between $\ln(\sigma)$ and $\Delta\alpha$, is largely uninfluenced by the temperature and by the illumination history of the sample. An example of three successive cycles of illumination and bleaching is given in Fig. 6.B.1b for $T = 323$ K.

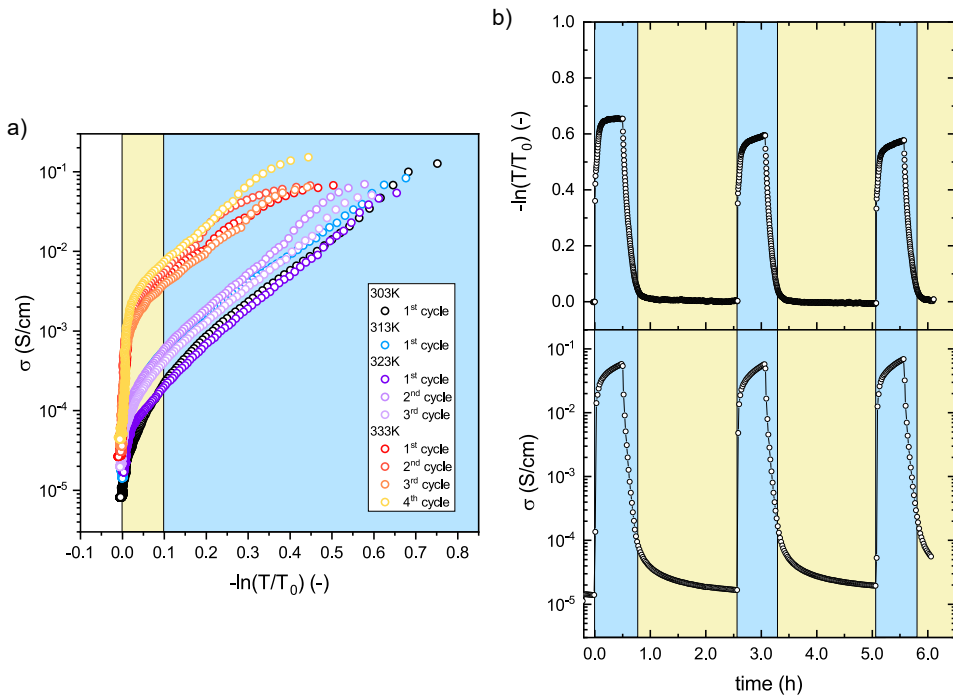


Figure 6.B.1: *a*) Relation between conductivity and the increase of optical absorption ($-\ln(T/T_0) \sim \Delta\alpha d$) for all the temperatures considered in this work. Repeated illumination cycles are also shown. *b*) Three successive cycles of illumination and bleaching showing the photo-induced effects on relative optical transmittance (top) and material conductivity (bottom) of Gd oxyhydride measured at 323 K. In all panels, the background colors are used to highlight the regimes in which optical absorption and conductivity are dominated by the photo-induced effects (blue), in contrast to the material properties of the Gd oxyhydride as largely recovered at the end of the bleaching (yellow).

7

REFLECTION & FUTURE OUTLOOK

The uncommon photochromism, photo-conductivity, and H-mobility of RE oxyhydride materials make them promising candidates for application in optics, opto-electronics and electrochemical devices alike. Additionally, their extreme compositional flexibility and the connected variety of possible (meta)stable phases make them an excellent case study to advance our understanding of the link between composition, structure, and properties in mixed-anion materials. Further, the possibility of producing RE oxyhydride not only under thermodynamic control (e.g., high temperature/pressure solid state reaction) but also under kinetic control (e.g., topochemical anion-exchange, or post-oxidation of reactively sputtered polycrystalline/epitaxial REH_x thin films) largely expands the possibility of tuning their properties influencing other aspects such as concentration of defect, material morphology, film texture, film stress, etc..

While this thesis started with the ambition of unrevealing the photochromic mechanism in RE oxyhydride thin films, science rarely - if ever - goes from A to B. In particular, at that time little other than the occurrence of the photochromism itself was known about these air-oxidized reactively sputtered thin films, and it became clear that investigating the solid-state photo-induced reaction, structural rearrangement, and atomic mobility could not prescind from a sound understanding of basic material properties. Having established the composition and a structural model for these thin films, as well as their correlation with the material properties and the photochromism, my hope is that this work might contribute to the transition from an exploratory, phenomenological, and inductive phase towards a more deductive approach in the study of the RE oxyhydrides properties.

Approaching the topic from bottom-up, we have surveyed the structure-properties relation and shown that controlling the deposition condition and thus the O:H anion-ratio allows to tune the photochromism at a large extent. However, we suppose that other aspects might play a role as well. We think that going beyond an idealized picture should be topic of further research, in particular on those aspects that might condition the metastability of the RE oxyhydride film (such as any residual stress) and/or facilitate

the separation of the electron-hole pair and any possible structural rearrangement (such as micro-structure, local inhomogeneity, and concentration of defects).

Approaching the topic from top-down, we have shown that the photochromism and the photo-conductivity do originate from a single process. However, the reported photo-conductivity does not find a simple explanation in the framework of the mechanisms proposed for the photochromism, if not under rather stringent conditions that are at odds with previous works. A better understanding of the transport property of the RE oxyhydrides, before and under illumination, seems therefore a promising direction to gain insight into the photochromism mechanism as well. Particularly, we think that the hypotheses of metallic phase segregation (explaining the optical absorption) and defect formation in the RE oxyhydride matrix (explaining the increase of negative charge carriers) should be considered – together and simultaneously – in the framework of a single process initiated by the electron-hole formation. Finally, we find that understanding the root/type of electronic transport in the RE oxyhydrides is an essential milestone to further research a strategy of suppression and achieve *pure* H^- conduction in RE oxyhydride materials.

Whatever RE oxyhydride films will ever be used as a smart coating on windows and sensors remains to be seen. Particularly, their memory effect remains a reason of major concern for applications with a long lifetime. We hope that a deeper understanding of the photochromic mechanism will shed some light on the origin of the memory effect and on possible prevention strategies. Once again, we think that the answer might lie beyond the idealized structure-properties relation.

7

In my eyes, the work covered by this thesis was dramatically necessary to the field of RE oxyhydride thin films, and, at the same time, dramatically unsatisfactory in its ability to provide a compelling understanding for phenomena that are likely assisted by defects. Such is the joy and sorrow of the structure-property relation.

SUMMARY

The uncommon photochromism, photo-conductivity, and H-mobility of RE oxyhydride materials make them promising candidates for application in optics, opto-electronics and electrochemical devices alike. Additionally, their extreme compositional flexibility and the connected variety of possible (meta)stable phases make them an excellent case study to advance our understanding of the link between composition, structure, and properties in mixed-anion materials. Further, the possibility of producing RE oxyhydride not only under thermodynamic control (e.g., high temperature/pressure solid state reaction) but also under kinetic control (e.g., topochemical anion-exchange, or post-oxidation of reactively sputtered polycrystalline/epitaxial REH_x thin films) largely expands the possibility of tuning their properties, influencing other aspects such as concentration of defect, material morphology, film texture, film stress, etc.

At time when this thesis started, in 2018, none of the above was clearly understood and this work was prompted by the technological interest in photochromic *oxygen containing* REH_2 thin films.

We clarify the nature of these films by RBS and ERD analysis, establishing a RE–O–H composition diagram which identifies the photochromic compounds as oxyhydrides with chemical formula $\text{REO}_x\text{H}_{3-2x}$ ($0.5 \leq x < 1.5$). Due to the high degree of anion sublattice disorder expected in these reactively-sputtered thin films, the structure models proposed for the related bulk oxyhydrides are, however, not directly applicable. Instead, we use a combination of XRD, EXAFS analysis, and lattice energy calculations to establish an anion-disordered CaF_2 -type structure which links the oxyhydrides to the related binary compounds. The oxide anions are found to occupy predominantly the tetrahedral sites in the fcc structure which is attributed to electrostatic lattice energy minimization.

The hypothetical anion-disordered oxyhydride phase is further investigated by *ab-initio* DFT, showing that the O:H ratio influences the formation and lattice energy, metastability, and optical properties. We do so by: (i) introducing a set of special quasirandom structures (SQS) to model anion-disorder along the whole $\text{REH}_3\text{--RE}_2\text{O}_3$ composition line, and (ii) by comparing the two limit cases of Y and La oxyhydrides, which greatly differ in lattice parameter and H^- ionic conductivity. A comparison with anion-ordered polymorphs of the same composition shows the similar energy of the anion-disordered phase, although its metastability rather depends on the cation size, which determines the maximum H content above which the CaF_2 -type structure itself becomes unstable. To overcome the accuracy limitations of classical DFT, the modified Becke-Johnson (mBJ) scheme is employed in the study of the electronic properties. Major differences occur between H-rich and O-rich RE oxyhydrides, as the octahedral H^- present for $x < 1$ form electronic states at the top of the valence band, which reduce the energy bandgap and

dominate the electronic transitions at lower energies, thus increasing the refractive index of the material in the VIS-nIR spectral range. Comparing the DFT results to experimental data on photochromic Y oxyhydride films reinforces the hypothesis of anion-disorder in the H-rich films ($x < 1$), while it hints towards some degree of anion-ordering in the O-rich ones ($x > 1$).

We survey the relation between RE oxyhydride composition and photochromism, demonstrating that the O:H anion ratio, as well as the choice of the cation, allow to largely tune the extent of the optical change and its speed. The bleaching time in particular can be reduced by an order of magnitude by increasing the O:H ratio, indirectly defined by the deposition pressure of the parent REH₂. The influence of the cation (RE=Sc, Y, Gd) under comparable deposition conditions is discussed. These facts suggest that REs of larger ionic radius form oxyhydrides with larger optical contrast and faster bleaching speed, hinting to a dependency of the photochromic mechanism on the anion site-hopping.

Finally, we show that photochromism and photo-conductivity originate from a single process, as indicated by a comparable time and temperature dependence, and by a unique exponential relation linking material conductivity and optical absorption. This relation rules out that purely electronic processes occur under illumination, and further narrows the hypothesis for the photochromic mechanism to (i) the formation of an ensemble of in-gap defects capable of trapping electrons and holes alike, or (ii) to the segregation of a percolating network of metallic domains. Individually, each of these hypotheses is at odds with previous works, and thus we think that metallic phase segregation (explaining the optical absorption) and defect formation in the RE oxyhydride matrix (explaining the increase of negative charge carriers) should be considered together and simultaneously in the framework of a single process initiated by the electron-hole formation.

SAMENVATTING

De ongebruikelijke fotochromische, foto-conductieve en H-mobiliteit eigenschappen van zeldzame aardmetaal (RE) oxyhydrides zorgt ervoor dat deze materialen veelbelovend zijn voor het gebruik in optische, opto-elektronische en elektrochemische toepassingen. De extreme flexibiliteit in compositie en de daarmee verbonden variëteit van mogelijke (meta)stabiele fases zorgt ervoor dat deze materialen perfect kunnen worden gebruikt in een case study om de link tussen de compositie, structuur en eigenschappen van gemixte-anion materialen beter te begrijpen. Verder maakt RE oxyhydriden produceren onder niet alleen thermodynamische controle (zoals hoge temperatuur en druk van de vaste fase reactie), maar ook onder kinetische controle (zoals topochemische anion-uitwisseling of post-oxidatie van reactief gesputterde polykristallijne/epitaxiale RE hydride (REH_x) thin films) het mogelijk een grote variatie aan eigenschappen te stemmen, waaronder de concentratie aan materiaal defecten, morfologie, thin film textuur, thin film spanning, etc.

Toen deze thesis was begonnen, in 2018, was er weinig bekend over de bovengenoemde onderwerpen en dit werk was begonnen vanuit de technologische interesse in fotochromische zuurstof bevattende REH_2 thin films.

We lichten het karakter van deze films nader toe met behulp van RBS en ERD analyse, en maken op basis hiervan een RE–O–H compositiediagram. Hiermee is geïdentificeerd dat de oxyhydriden verbindingen met fotochromisch karakter zich houden aan de chemische formule $\text{REO}_x\text{H}_{3-2x}$ ($0.5 \leq x < 1.5$). Vanwege de hoge graad aan wanorde in het anion subrooster die verwacht zijn in deze reactief gesputterde thin films, zijn de modellen die voorgesteld zijn voor gerelateerde bulk oxyhydriden niet direct toepasbaar. In plaats daarvan hebben wij een combinatie van XRD, EXAFS analyse en roosterenergie berekeningen gebruikt om een anion-verstoorde CaF_2 -type structuur tot stand te brengen die de oxyhydriden linkt aan de vergelijkbare binaire stoffen. Hieruit is gebleken dat de oxide anionen voornamelijk de tetraëdrische posities in de fcc-structuur bezetten, wat toegeschreven wordt aan de minimalisering van elektrostatistische rooster energie.

De hypothetische anion-verstoorde oxyhydride fase is verder onderzocht door middel van ab-initio DFT, waaruit is gebleken dat de O:H ratio invloed heeft op zowel de formatie- en roosterenergie als op de metastabiliteit en optische eigenschappen van het materiaal. Dit is gedaan door middel van (i) het introduceren van een set aan speciale quasi-willekeurige structuren (SQS) om anion-wanorde te modelleren voor composities langs de REH_3 – RE_2O_3 lijn en (ii) het vergelijken van de twee limiet casussen van Yttrium (Y) en Lanthanium (La) oxyhydriden, die beide erg verschillen in rooster parameters en ionische H^- conductiviteit. Een vergelijking tussen anion-geordeerde polymorphen met dezelfde samenstelling tonen vergelijkbare energieën voor de anion-verstoorde fase, ech-

ter is gevonden dat de metastabiliteit afhangt van de grootte van het kation, waarmee de maximale H concentratie is bepaald. Boven deze H concentratie is gevonden dat de CaF_2 -type structuur zelf onstabiel wordt. Om de gelimiteerde accuratie van klassieke DFT te omzeilen is er hier gebruik gemaakt van het gemodificeerde Becke-Johnson (mBJ) schema om de elektronische eigenschappen te bestuderen. Met deze methode worden er grote verschillen tussen de H-rijke en O-rijke oxyhydriden gevonden, omdat de octahedrische H^- die aanwezig zijn in $x < 1$ composities elektronische niveaus boven de valentieband vormen. Deze niveaus verkleinen de energie van de bandgap en domineren elektronische transitie bij lagere energieën en hiermee zorgen voor een vergrootte refractie index van het materiaal in het VIS-nIR spectrum. Wanneer we de DFT resultaten vergelijken met experimentele data voor fotochromische Y oxyhydride films, wat de hypothese versterkt dat H-rijke films ($x < 1$) anion-verstoord zijn, terwijl O-rijke films ($x > 1$) juist een sterkere graad van anion-coördinatie vertonen.

We bestuderen de relatie tussen RE oxyhydride composities en fotochromisme, waarmee we zien dat zowel de ratio van O:H anionen als de keuze van kation kunnen worden gebruikt om voor een groot deel de extensie van optische verandering en de snelheid van verkleuring kunnen worden aangepast. Voor de verblekingstijd specifiek geldt dat het verhogen van de O:H ratio kan leiden tot een orde-grootte verschil. Deze ratio kan indirect worden gecontroleerd door middel van de depositiedruk van het ouder REH_2 . De invloed van het kation ($\text{RE} = \text{Sc}, \text{Y}, \text{Gd}$) onder vergelijkbare depositiecondities. De data toont dat REs met grotere ionische radii leiden tot oxyhydriden met sterker optisch contrast en een snellere verbleking, wat hint naar dat het fotochromisch mechanisme afhankelijk is van anion site-hopping.

Ten slotte laten we zien dat het fotochromisch effect en de foto-conductiviteit ontstaan vanuit één proces, zoals kan worden afgeleid van de vergelijkbare tijd- en temperatuurafhankelijkheden en van de unieke exponentiele relatie tussen de conductiviteit en optische absorptie. Deze relatie sluit uit dat een puur elektronisch proces plaatsvindt onder belichting, en beperkt de hypothese voor fotochromisme verder tot (i) de formatie van een ensemble van in-gap defecten die elektronen en gaten beide kunnen opvangen, of (ii) de segregatie van een percolerend netwerk van metallische domeinen. Individueel zijn beide hypothesen tegenstrijdig met voorgaande werken, en daarom denken wij dat een metallische fase segregatie (wat de optische absorptie verklaart) en defectformatie in de RE oxyhydride matrix (wat de verhoogde concentratie van charge carriers verklaart) samen en tegelijk moeten worden bekeken als gevolg van een enkel proces dat geïnitieerd is door de elektron-gat formatie.

ACKNOWLEDGEMENTS

By accident or by design, by choice or by necessity, a PhD program is an immersive journey that simultaneously nurtures and devours your life and persona. Like a monster from the abyss, it swallows you up, and it spits you out different. Now, my feathers might be a little roughed up, and I might be covered in slime, but I would do it 100-times again. This, I completely owe to the people that I met in the belly of the beast. You made all the difference.

First of all, I want to thank who made this thesis not only possible, but meaningful. Prof. **Bernard Dam**, for all your guidance, patience and support, for immediately accommodating my working style, for believing in me. At a personal level, your empathy, patience, authenticity and fairness perfectly embody the qualities of the Dutch leader. At a scientific level you are living proof that a generalist with incredible intuition can do wonders. Today as well as tomorrow, I will keep your example as an reference for my own. Dr. **Steffen Cornelius**, whose contribution to this thesis, and to my personal and scientific development is enormous. I cherish the thought provoking conversation that you initiated with your words and your behaviour; which even today that still make me reflect. Your knowledge, of science and of the world, is rock-solid. I am grateful for every bit you shared with me. Dr. **Gilles de Wijs**, whose spirit of service is a continuous inspiration. You are an artist of DFT, and it was a pleasure to learn from you. Dr. **Alessandro Longo**, who understands life and sails through it like no one else. You never gave up on me, doesn't matter how many phone calls I would miss. Of all the people here mentioned, you alone told me "Not ok, you can do better". At that time, your words gave me the momentum that I needed. To all of you, my special thanks. And if I have used your title and full names, that is to acknowledge your contribution. To me, you are more than colleagues.

Further, this work was enabled by an unstoppable team of technicians. **Herman Schreuders**, throughout these years you have been fixing all real and perceived problems. With you, all question had a solutions. In fact, I am convinced that you know all the answers to the oxyhydride's photochromism, but let us enjoy the puzzle. Together, you and **Joost** are the heart of MECS, keep the boat afloat, and the crew happy. Thank you for everything! **Bart Boshuizen**, thank you for the extra spicy code of our LabVIEW software; THE PHOCS IS BACK. **Marcel**, thank you for the help with the AFM, and for always having a cool anecdotal story to share. **Ben** and **Xiaohui**, thank you for the help with the XRD.

My gratitude also goes to my co-promotor Dr. **Tom Savenije** and to the other colleagues of the Mat4Sus tribe: Dr. **Stephan Eijt**, **Shrestha Banerjee**, **Ziyang Wu**, and Prof. **Arno Kentgens**. A special thank to Dr. **Fahimeh Nafezarefi**. In this case, it is a pleasure to mention your title! You were my warm welcome in the photochromics group, and as a good older scientific sibling, you always looked out for me while being a good friend at the same

time. You are a kind spirit and that matters. A lot. Thank you! For a warm and friendly atmosphere during my initial year, my thanks also to the photochromics-students of the time **Lijie** (the first to ask for my educated guess), **Ankit**, **Joost**, and especially **Jelle** and **Eline**.

A shoutout also to all MSc and BSc students that I had the luck to supervise. By all means, you have been the highlight of my phd experience. **Kim**, you were my first student and I have learnt more from you than the other way around. Thank you! You went by as an unseen gem, and not insisting for an higher grade for you is one of the biggest regrets of my PhD. Keep being awesome! **Tom de Krom** and **Rens Stigter**, you have been giants in this research, and when it comes to positron annihilation and DFT, after so many years, we still live in your shadows. Supervising brilliant students is incredibly motivating, and it was a lot of fun to have you around. **Leyi** and **Matthijs**, aka my kids, your enthusiasm was a blessing during covid times! Finally, **Daan** and **Brenda**, you never gave up even when your plate was overflowing. Not that you need it, but to all of you, I wish wind on tail!

Despite an average of 10 summer days a year, and the constant deficiency of vitamin D, my life has never been so rich like here in the Netherlands. This, I owe to many old and new friends. It is said that we are the average of the people that we hang out with the most. I can only hope it is true.

First and foremost, I want to thank our little climbing community. We might seek the heights, but in fact you became my solid, safe ground when I first moved to the Netherlands. **Nienke**, of this community, you are the center and the glue. For me, a rare friend. **Nate**, the downhill butt-sliding under the stars of the snowy White Mountains was one of the coolest things that I have ever done, I thank you for that! On living life with a smile, you are second to none. Well... maybe except **Joram**! And then **Marijn**, In Kalimnos you taught me how to swim butterfly, and called me out when I acted selfish. Both lessons I proudly bring with me! Finally **Katie**, and **Peter**, who climb like lizards on horizontal ground, and walk in a permanent state of free-to-take optimism. To many more!

Now hold your breath, you folks, because what you witness is beyond the limits of mortal minds. The earth and the sky shatter, and a blood-thirsty madness slowly regurgitates from the cracks of your foolish definition of reality. Your fear is such that you cannot even shiver, and yet... you marvel at the unspeakable beauty of a world that is crumbling. Feeding the imagination is not an easy job, and for that and much more, I thank the cool kids club, aka Dorlamin's friends. **Dylan**, the forever borrel master, and **Peter**, apparently introvert but in fact an excellent storyteller and fight-picker, you brought a fresh vibe to our group and I look forward to more coffees with you! **Mark**, you are the kindest pirate out there, a story in the story, the stroop in the MECS waffle. To new adventures.! ...Roll a D100. Oeps..

Kailun and **Anirudh**, thank you for being the best office mates that one could ask for. You are two of most trustworthy people (and best chefs!) I ever met, and it is an honour to call you my friends. And then **Sanjana**, who in our office has not been much, but every

time brought a big smile and a light-hearted atmosphere. Thank you all! Kailun, I raise my cup to the day you kidnapped my computer to bring me into this office!

The thing is, that a part of me did not want to move out from my initial desk, because from that student room I met incredible people. **Tomasz** (a leader with the curious eyes of a child), **Qian** (always positive, always caring), **Serhii**, **Angie** (broken together is better than broken alone), **Elmira** (always ready to share her food, and a ping pong wizard), **Audrey**, **Hendrik**, and **Emma**, thank you for all the small things that we did together!

My thanks also to all other past and present MECStians. **Robin**, we started together, and these have been years full of changes. *Journey before destination*. **Martin**, I admire your confidence, courage and sarcasm. And let's not forget that I slept 3 night on your floor. **Recep**, from you I learnt to ask the difficult questions, and the value of males above 30 on the dating market. Much respect! **Davide**, my safe space for Italian nostalgia. And more again: **Erdem**, **Kai**, **Sid**, **Divya**, **Tom**, **Aaron**, **Andreas**, **Wim**, **Dowon**, **Hugo**, **Wilson**, **Hans**, **Mark W.**, **Bernhard**, **Pranav**, **Fokko**, **Maryam**, thank you for bringing all your knowledge and passion to group meetings and coffee breaks. **Heleen**, **Adinda**, **Rajshree**, **Roos**, I would have been lost countless times without your administrative support. **Lars**, **Georgy**, **Elena**, **Robbert**, **Valentina**, all my esteem. And of course the **PhD Council**, with you around, chemE is in good hands.

It would have not been possible for me to balance the stress of a PhD without a lot of biking and a few more hobbies. In rough seas, at least you can surf: **Jorgos**, **Nadine**, **Paulina**, good waves together! To my volleyball team, **Kalinko H6**, and to the **Wing Tsun** training group, thank you for the intense moments, for believing against all evidence that I will learn Dutch, for the hard lesson that actions speak louder than words, and in general, for a refreshing time outside the academic bubble.

Science comes with ups and downs, and all these emotions I shared with my flatmates, who have been a major support group and a reliable source of chaos and entertainment. **Fabian** (what an incredible friend!), **Logan** (A big man not afraid to do little things to make everyone happy. Thank you for the crash course into American culture), **Ekim**, **Nikita** and **Kristina**, you made that house warm with laughter.

And if with some people you share an apartment, some others are your home.

To my friends from Padova, a huge nostalgic thanks. **Bragone** (contagious and addictive in the best way), Master **Andrea** (fellow survivor of the BeNeLux life), **Miki** (we went through so much!), **Scapo** (our Italian anchor) and, **Gimã** (who is living his best northern life, but if needed would jump on the back of his reindeer in no time), we might all be far away, and yet feel so close. **Skatto** and **Fab** I look forward to meet again where the skies are blue and the grass is dry! And finally **Carlone**, a brother in arms in this Dutch life. With you around, any problem appears small!

And to my friends from Rome, **Giuliana**, **Viola**, and **Nur** another big hug filled with

anticipation, because I know that a lot more is to come! **Lorenzo**, you are thirsty of life and your energy, enthusiasm, and curiosity are uncontrollable. You could change the world. We have all been caught in your tornado, and don't want to leave. **Giacomo**, you are one of the most dependable people I ever met. A massive rock at sea, a freaking bright star: when disoriented, we look at you. For different reasons, here you both got stuck on my sofa, and for me those were great days. At this point, I have no doubts we will be friends for life.

Diana, I am afraid I won't find the words to thank you enough. This PhD thesis is as much yours as mine, but that is secondary, because *work is stupid* and you are so much more. Colleague, friend, sport and adventure buddy, my safe island, a constant inspiration, family... It defies reason how in my life you are everywhere and yet never enough: I can't wait for what the future brings! Your name could have appeared in almost all of the paragraphs above, but you know... we have to leave some space also for the others. Here I thank you for being unique, and being there.

Finally, I want to thank my Family. A **Nonna** e alla mia famiglia allargata, spero che con questa tesi vi abbia dato una piccola soddisfazione. A **Mamma, Papà e Daniele**, grazie per il vostro affetto incondizionato. Sapere che c'è un posto dove tornare, mi dà coraggio per andare lontano.

CURRICULUM VITAE

Giorgio Colombi was born on the 2nd of April 1993 in Rome, Italy. In 2012 he graduated from the scientific high school Istituto A. Righi, Rome. He continued his education at the University of Padua, Italy, where he received his bachelor (2015) and master (2017) degree in material science, both awarded *cum laude*. At the same time, between 2014 and 2016, he participated to the FSAE student engineering competition, working together with a team of 25+ students to design and produce the first 4WD electric race car of the University of Padua. In 2017 he spent 6 months at the Århus University, Denmark, as a visiting student in the *Nanobiointerfaces* group of prof. D. Sutherland. After that he came back to Padua to complete his master thesis on the luminescence enhancement of emitters coupled with plasmonic particles and nanostructured surfaces in the *Nanostructures* group of prof. G. Mattei. From January 2018 to January 2022 he has been a PhD student at the Delft University of Technology, in the *Materials for Energy Conversion and Storage (MECS)* group under the supervision of prof. B. Dam. Currently, he is a post-doctoral researcher in the same group. During his time in Delft he worked on rationalizing the photochromic properties of RE oxyhydride thin films in terms of their composition and local/electronic structure. The results of his doctoral research are presented in this thesis.

LIST OF PUBLICATIONS

11. **G. Colombi**, B. Boshuizen, D. Chaykina, H. Schreuders, T.J. Savenije, and B. Dam *Relation between photochromism and photoconductivity in REO_xH_{3-2x} thin films*, In preparation (2022).
10. S. Banerjee, D. Chaykina, R. Stigter, **G. Colombi**, B. Dam, G. de Wijs, and A. Kentgens, *Solid state NMR studies on yttrium oxyhydrides: exploring multi-anion chemistry*, In preparation (2022).
9. D. Chaykina, I. Usman, **G. Colombi**, B. Tyburska-Pueschel, L. J. Bannenberg, Z. Wu, H. Schreuders, and B. Dam *Aliovalent Ca-doping of yttrium oxyhydride thin films and implications for photochromism*, In preparation (2022).
8. Z. Wu, T. W.H. De Krom, **G. Colombi**, D. Chaykina, G. van Hattem, H. Schut, M. Dickmann, W. Egger, C. Hugenschmidt, E. Brück, B. Dam, and S. W.H. Eijt, *Formation of vacancies and metallic-like domains in photochromic rare-earth oxyhydride thin films studied by in-situ illumination positron annihilation spectroscopy*, In peer review (2022).
7. **G. Colombi**, R. Stigter, D. Chaykina, S. Banerjee, A. P.M. Kentgens, S. W.H. Eijt, B. Dam, and G. de Wijs, *Energy, metastability, and optical properties of anion-disordered REO_xH_{3-2x} ($RE = Y, La$) oxyhydrides: a computational study*, [Phys. Rev. B **105**, 5 \(2022\)](#).
6. D. Chaykina, F. Nafezarefi, **G. Colombi**, S. Cornelius, L. J. Bannenberg, H. Schreuders, and B. Dam, and S. W.H. Eijt, *Influence of crystal structure, encapsulation, and annealing on photochromism in Nd oxyhydride thin films*, [J. Phys. Chem. C **126**, 4 \(2022\)](#).
5. D. Chaykina, T. W.H. De Krom, **G. Colombi**, H. Schreuders, A. Suter, T. Prokscha, B. Dam, and S. W.H. Eijt, *Structural properties and anion dynamics of yttrium dihydride and photochromic oxyhydride thin films examined by in situ μ^+ SR*, [Phys. Rev. B **103**, 22 \(2021\)](#).
4. **G. Colombi**, T. W.H. De Krom, D. Chaykina, S. Cornelius, S. W.H. Eijt, and B. Dam, *Influence of cation ($RE = Sc, Y, Gd$) and O/H anion ratio on the photochromic properties of REO_xH_{3-2x} thin films*, [ACS photonics **8**, 3 \(2021\)](#).
3. **G. Colombi**, S. Cornelius, A. Longo, and B. Dam, *Structure model for anion-disordered photochromic gadolinium oxyhydride thin films*, [J. Phys. Chem. C **124**, 25 \(2020\)](#).
2. S. W.H. Eijt, T. W.H. De Krom, D. Chaykina, H. Schut, **G. Colombi**, S. Cornelius, W. Egger, M. Dickmann, and B. Dam, *Photochromic YO_xH_y thin films examined by in-situ positron annihilation spectroscopy*, [Acta Phys. Pol. A **137**, \(2019\)](#).
1. S. Cornelius, **G. Colombi**, F. Nafezarefi, H. Schreuders, R. Heller, F. Munnik, and B. Dam, *Oxyhydride nature of rare-earth-based photochromic thin films*, [J. Phys. Chem. Lett. **10**, 6 \(2019\)](#).